Thermal-Mechanical Characterization and Microstructural Evolution of Lead Free Solder Alloys in Harsh Environment Applications

by

KM Rafidh Hassan

A dissertation submitted to the Graduate Faculty of
Auburn University
in partial fulfillment of the
requirements for the Degree of
Doctor of Philosophy

Auburn, Alabama
May 1, 2021

Keywords: microelectronics reliability, lead-free solder, constitutive models, harsh environment applications, bismuth content, microstructural evolution

Approved by

Jeffrey C. Suhling, Chair, Quina Distinguished Professor of Mechanical Engineering
Hareesh V. Tippur, McWane Professor of Mechanical Engineering
James S. Davidson, Gottlieb Professor (Structural) of Civil Engineering
Michael J. Bozack, Professor Emeritus of Physics

Abstract

With the emergence of the modern electronic packaging technology over the last few decades, lead free solder alloys have been the primary interconnects material used in electronic packaging industry due to their relatively high melting point, attractive mechanical properties, thermal cycling reliability, and environment friendly chemical properties. As solder joints provide mechanical support, electrical and thermal interconnection between packaging levels in microelectronics assembly systems, proper functioning of these interconnections and the reliability of the electronic packages depend largely on the mechanical properties of the solder joints. However, the mechanical properties as well as the reliability of a solder, which is the primary interconnect of electronic assemblies are strongly influenced by its microstructure, which is controlled by its thermal history including its solidification rate and thermal exposures after solidification. Environmental conditions, such as, operating temperature, aging temperature, and aging time significantly affect these properties due to the microstructural evolution of the solder that occurs during aging. Moreover, electronic devices, sometimes experience harsh environment applications including well drilling, geothermal energy, automotive power electronics, and aerospace engines, where solders are exposed to very high temperatures from T = 125-200 °C. Mechanical properties of lead free solders at elevated temperatures are limited. This research involves several projects combining finite element and experimental approaches to investigate new reliability parameters and create a database of mechanical properties for different temperature exposure and the associated microstructural changes of several conventional and new lead free solder alloys.

In the first project, a combined numerical and experimental study have been carried out to establish Poisson's ratio as a new reliability parameter for lead free solder joints. The effects of Poisson's ratio on the stress/strain behavior in the BGA components subjected to thermal cycling has been investigated by a three dimensional finite element analysis (FEA). The test vehicle from which various models were built using finite element analysis included various sizes of BGA components including 19 x 19 mm, 15 x 15 mm, 10 x 10 mm and 5 x 5 mm packages with SAC305 and SAC105 solder joints. Temperature dependent stress/strain behaviors were included for the packaging materials, with a thermal cycling between T = -40 to 125 ºC. Experimental investigations have been carried out to determine the exact Poisson's ratio of several SAC and SAC+X lead free solders. Uniaxial tensile stress-strain tests have been performed with two strain rates (0.0001, and 0.00001 (sec-1)) and four testing temperatures (T = 25, 50, 75, 100 ºC). A set of additional experiments have been performed to determine the effects of aging. In particular the samples were aged (preconditioned) at a temperature of T = 125 °C for several durations including 0, 1, 2, 3, 4, 5, 6, 12, and 24 hours at a particular strain rate of 0.00001 (sec^{-1}).

In the second project, the mechanical behavior, microstructural evolution, and reliability of several different SAC+Bi alloys with various levels of Bismuth (1.0%, 2.0%, and 3.0%) have been investigated. To examine the base mechanical behavior, stress-strain tests were performed for each SAC+Bi alloy with three strain rates (0.001, 0.0001, and 0.00001 (sec-1)), and five different testing temperatures (T = 25, 50, 75, 100, and 125 ºC). The Anand parameters were calculated for each alloy from the stress-strain data. In addition, the temperature dependent mechanical properties of the various SAC+Bi solders were measured and compared including effective modulus, yield stress, and ultimate tensile

strength. The effects of aging has been studied for the various SAC+Bi alloys using both mechanical testing and microstructure observations. For the solder mechanical response, the fabricated uniaxial specimens were aged (preconditioned) at T = 125 °C for several durations of aging including 0, 1, 5, and 20 days. Stress-strain tests on the aged specimens were then performed at a single strain rate of 0.001 (sec-1), and temperatures of 25, 50, 75, 100, and 125 °C. Microstructural evolutions of the new solder alloys (1%, and 2% Bi) were also observed for aging at T = 125 °C for the same durations of 0, 1, 5, and 20 days. In particular, aging induced coarsening of the IMCs was studied for each alloy using Scanning Electron Microscopy (SEM), and correlated to corresponding material property evolution findings.

In third project, the effect of extreme high temperature exposure has been studied using SAC305 lead free solder alloy by determining mechanical properties and Anand model parameters. In particular, uniaxial tensile stress-strain tests were carried out on SAC305 specimens using a micro tension/torsion testing machine with three strain rates (0.001, 0.0001 and 0.00001 (1/sec)), four extreme high testing temperatures (T = 125, 150, 175, and 200 ºC), and four different pre-aging conditions 0, 1, 5, and 20 days at an isothermal aging temperature of T = 125 ºC. The nine Anand parameters were determined using the uniaxial tensile tests results at several strain rates and temperatures mentioned above.

In the fourth project, the microstructural evolution of SAC305 (96.5Sn-3.0Ag-0.5Cu) BGA joints have been investigated for different aging conditions utilizing Scanning Electron Microscopy (SEM). In particular, aging induced microstructural changes occurring within fixed regions have been monitored in selected lead free solder joints to

create time-lapse imagery of the microstructure evolution. Aging was performed at T = 125, and 150 °C for several durations including 0, 1, 5, 10, and 20 days, and the topography of the microstructure of a fixed region was captured using the SEM system. This process generated several images of the microstructure as the aging progressed containing the visual and quantitative information of diffusion of copper in the β-Sn matrix, growth of the Cu_6Sn_5 IMC layer as a function of aging time and temperature at the solder joint to PCB copper pad interface, and the quantitative analysis of the evolution of Ag_3Sn IMC particles during aging.

In the final project, nanoindentation methods were utilized to explore the creep behavior, and aging effects of SAC305 solder joints at several extreme high testing temperatures from 125 to 200 °C. A special high temperature stage and test protocol was used within the nanoindentation system to carefully control the testing temperature, and make the measurements insensitive to thermal drift problems. Solder joints were extracted from 14 x 14 mm PBGA assemblies (0.8 mm ball pitch, 0.46 mm ball diameter). For all the experiments, only single grain solder joints were used to avoid introducing any unintentional variation from changes in the crystal orientation across the joint cross-section. After extraction, the single grain solder joints were subjected to various aging conditions. Nanoindentation testing was then performed on the aged specimens at four different testing temperatures (T = 125, 150, 175, and 200 °C). In order to understand creep response of the solder joints at different temperatures, a constant force at max indentation was applied for 900 sec while the creep displacements were monitored. With this approach, creep strain rate was measured as a function of both temperature and prior aging conditions. Nanoindentation pile-up effects, although insignificant at room

temperature, were observed during high-temperature testing and corrections were made to limit their influence on the test results. Finally, correlation has been shown between the nanoindentation test results and the microstructural evolution of SAC305 BGA joints.

Acknowledgments

I would like to thank a number of people who unconditionally helped me throughout the PhD journey. First of all, my sincere and deepest gratefulness to my advisor Dr. Jeffrey C. Suhling for his continuous support, innovative ideas, supervision and untiring mentorship throughout my Auburn Journey. It's an immense please to get a mentor like him and I am truly honored to be a part of his research group. He continuously and convincingly convey a spirit of pursuit of excellence and perfection in research. After that, I want to extend my sincere thanks and acknowledgement to my advisory committee members including Dr. Hareesh V. Tippur, Dr. James S. Davidson, and Dr. Michael J. Bozack for their insightful discussion about this research work. I have attended a number of theory courses from them that helped to build a strong knowledgeable background and research motivation. I am very much grateful to my seniors, friends and co-workers, and want to convey special thanks to Dr. Jordan Roberts, Dr. Munshi Basit, Dr. Md. Hasnine, Dr. Quang Nguyen, Dr. Sudan Ahmed, Dr. Mohammad S. Alam, Dr, Promod Chowdhury, Abdullah Fahim, Jing Wu, Jun Chen, Mohd Aminul Hoque, Kamrul Hasan, Mohammad Ashraful Haq, Mohammad Al Ahsan, Debabrata Mondal, Jason Smith, and John Marcell for their support.

Finally, I am heartily grateful to my family members, specially my father MD. Keshmot Khan, my mother Nazma Begum, my elder brothers KM Showkot Hassan, KM Refath Hassan, and my beloved wife Amina Nasrin for their love, sacrifice, support and understanding during my study and life in the United States. Their support and encouragement was in the end what made this dissertation possible.

Table of Contents

List of Figures

List of Tables

CHAPTER 1

INTRODUCTION

1.1 Overview of Lead Free Solders in Electronic Packaging Industry

Lead As the electronic industries started focusing on environmental concerns, lead free solders became the primary interconnect material as they provide excellent thermo-mechanical properties and thus commonly used in electronic packaging industry. As a joining material, in electronic assemblies, Solder joints provide mechanical support, electrical and thermal interconnection between packaging levels in microelectronics assembly systems. It also helps to dissipate the heat generated from the Si-chip [1].

With the recent developments of the electronic packaging industry over the last few decades, solder alloys have been the primary interconnect material used in electronic packaging. In the past, eutectic 63Sn-37Pb has been the most extensively used soldering alloy in the packaging industries. The eutectic Sn-Pb solders were very attractive due to their relatively low melting temperature (183 °C) and excellent ductility and good reliability and for their superior wettability and compatibility with most substrates and devices [2].

There is a general trend towards products that minimize harmful effects on the environment and human health. This trend is further reinforced by the RoHS ban on harmful substances and WEEE regulations on recycling and minimizing of electronic

wastes. In June 2000, the EU adopted two directives, the Waste of Electrical and Electronic Equipment (WEEE) and the Directive of the Restriction of the Use of Certain Hazardous Substances (RoHS) [3]. The WEEE directive requires that lead has to be removed from any end-of-life electrical or electronic components. The RoHS specifically bans lead from electrical and electronic components manufactured after July 1, 2006. As a result of the enforcement of the directives, all electrical or electronic equipment and devices produced in or imported to E.U. member states must comply with these lead-free standards except those items that are exempted from the bans. So due to the general push towards the eco-efficiency and green electronics, manufacturers are motivated for the adoption of lead free electronics. Therefore, the conversion to lead free solders in the global electronic market appears imminent [4].

In the United States, as soon as lead-free solder legislation was proposed, the lead-free solder project headed by the NCMS initiated research and development of lead-free solder in a program lasting 4 years [5]. The results of the project have been made available in a database and offer information on such matters as modifying equipment and processes for selecting alternative materials. The project initially selected for study 79 types of alloys considered at the time to be potential candidates for use in lead-free solder. Basic attributes considered included toxicity, resource availability, economic feasibility, and wetting characteristics. The selection process narrowed the field down to the final seven alloys, and these received secondary evaluation for reliability and ease of mounting manufacturing. Evaluation of the individual alloys did not result in the final selection of a single candidate, but three alloys, Sn–58Bi, Sn–3.5Ag–4.8Bi, and Sn–3.5Ag, were recommended as candidates. Screening comments indicated that the Sn–58Bi eutectic alloy

was not suitable for use as standard solder due to the scarcity of Bi resources. However, since this material can be used for mounting at less than 200 °C, and has chalked up a 20-year plus record of use in mainframe computers, this solder was deemed suitable for special applications. These results were used to construct a database on lead-free solder that includes the information in these tables along with other items such as (1) recommended applications for lead-free solder, (2) alloy composition guidelines reflecting price and availability, (3) database of the 7 selected alloys and comparison with Sn–Pb eutectic alloy, (4) data on the characteristics of the other 70 eliminated alloys, (5) optimal process conditions using various test PWBs, (6) strength evaluation and metallurgical reaction analysis for the selected alloys and various surface mounting process reactions, (7) predicted life (using NCMS Project proprietary life prediction software) and thermal fatigue evaluation for 4 of the selected alloys, and (8) assessment of nontoxicity and alloy composition.

1.2 Lead Free Solders Selections

In selecting suitable alternative of Sn-Pb soldering materials, it is important to take into consideration that the properties of the alternative solders are comparable or superior to Sn-Pb solders. Compatible candidates of the Sn-Pb solders must have the following behaviors [6]:

- melting temperature similar to eutectic Sn-Pb for a similar reflow profile
- sufficient wettability for good metallization process
- good electrical properties for transmitting electrical signals
- strong mechanical properties for good fatigue resistance and reliability

- inexpensive and easier manufacturability

Among various alloy systems that are considered as lead-free solder candidates, Sn-Ag-Cu alloys have been recognized as the most promising because of their relatively low melting temperature (compared with the Sn-Ag binary eutectic lead free solder), superior mechanical properties, and good compatibility with other components [7-9]. Sn-Ag-Cu alloys are widely used as lead-free solutions for ball-grid-array (BGA) interconnection in the microelectronic packaging industry as solder balls and pastes. Although no "drop in" replacement has been identified that is suitable for all applications, Sn-Ag, Sn-Ag-Cu (SAC), and other alloys involving elements such as Sn, Ag, Cu, Bi, In, and Zn have been identified as promising replacements for standard 63Sn-37Pb eutectic solder. Industries have proposed several SAC alloys which include 96.5Sn-3.0Ag-0.5Cu (SAC 305) in Japan, 95.5Sn-3.8Ag-0.7Cu (SAC 387) in the EU, and 95.5Sn-3.9Ag-0.6Cu (SAC 396) in the USA. The International Printed Circuit Association has suggested that 96.5Sn-3.0Ag-0.5Cu (SAC305) and Sn-3.9Ag- 0.6Cu (two near-eutectic alloys) will be the most widely used alloys in the future [10]. This prediction is attributed to their good mechanical properties, acceptable wetting properties, and suitable melting points [8, 11, 12].

A relatively large number of lead free solder alloys have been proposed so far, including binary, ternary and even quaternary alloys. More than 70 alloys have been identified in the literature. Among them, the majority of the alloys are Sn-based alloys, that is, Sn is the preferred major constituent. In fact, Sn-rich lead free alloys have occupied more than 80% in the wave solder market share and more than 90% in the reflow solder market share (Figure 1.1). The main benefits of the various SAC alloy systems are their

relatively low melting temperatures compared with the 96.5Sn–3.5Ag binary eutectic alloy, as well as their superior mechanical and solderability properties when compared to other lead-free solders. There are some major challenges for the current series of lead-free solders. SAC series alloys have a higher melting temperature, around 217 °C, compared to 183 °C for the eutectic Sn-Pb solders. They thus require higher reflow temperature during the manufacturing process, which can lead to reliability problems. The excessive buildup of intermetallic formed at the interface between the solder joints and the copper pad can also cause reliability problems. High costs are another issue for lead-free solders.

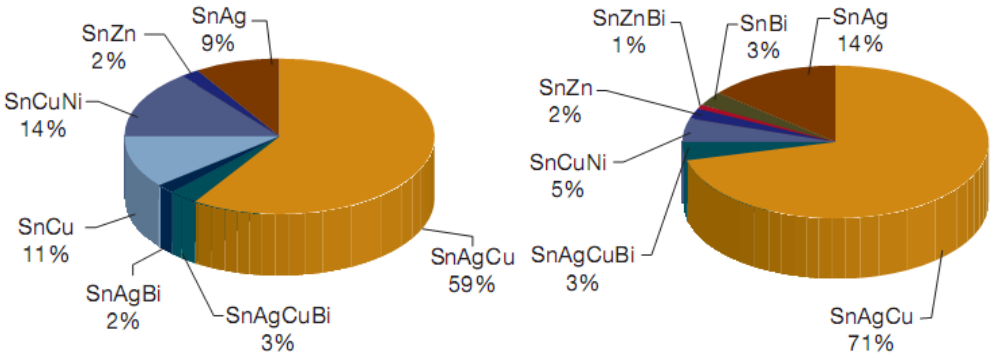

(a) Wave Solders (b) Reflow Solders

Figure 1.1 Lead Free Solder Market Share

1.3 Alternative Candidates for Lead Free Solders

About 70 different alloys were proposed as an alternative to the Sn-Pb solder. Most of these are Sn based solder where Sn is the main constituent along with one, two or even three other minor elements. These minor elements are added mainly to 1) decrease the melting temperature and 2) improve wetting and reliability of the solder [1]. The properties

of Sn and the effects of different alloying elements on the Sn based solder alloys are described below:

1.3.1 Tin

The melting temperature of elemental Sn is 231 °C. One of the main reasons of choosing Sn as the principle component in the lead free solder for electronic applications is its ability to spread and wet a number of various different substrates. In the solid state, tin can have two different phases or crystal structures 1) white or β-Sn with tetragonal crystal structure and 2) gray or α-Sn with diamond cubic crystal structure. At the room temperature the thermodynamically stable phase is β-Sn. Upon cooling, when the temperature goes below 13 °C (allotropic transformation temperature), α-Sn becomes the thermodynamically stable phase. The allotropic transformation of β-Sn to α-Sn, results a significant volume change (around 27%) causing blistering of the tin surface, cracking or disintegration. This phenomenon is mainly a surface event and often referred as 'tin pest'. The low ductility of α-Sn is another reason of causing blistering and cracking of the tin after the transformation [1, 13, 14]. Although the equilibrium temperature for β-Sn to α-Sn is 13 °C, the transformation occurs only after a significant undercooling and an extensive incubation period as long as several years. For example, no 'tin pest' was found on a SAC387 bulk sample after storing at -40 °C for 5 years [14]. Presence of heterogeneous nuclei, also known as seeding, can considerably accelerate the kinetics of the transformation. The possibility of $\beta \rightarrow \alpha$ transformation in an actual solder joint is even limited due to the constraints (component and substrate) on the both side of the joint [13, 14].

Addition of other elements, as an impurity, can affect the allotropic transformation. For example, the presence of Pb, Bi, Sb, Cu, Ge and Si inhibit β → α transformation while the presence of As, Zn, Al and Mg promote the transformation [13, 14].

Sn has a body centered tetragonal crystal structure (β-Sn), at room temperature, which is anisotropic. Hence, tin shows an anisotropic thermal (e.g. CTE) and mechanical (e.g. elastic modulus) properties as shown in Figure 1.2. As a result, during thermal cycling experiment, cracking occurs along the grain boundaries [1].

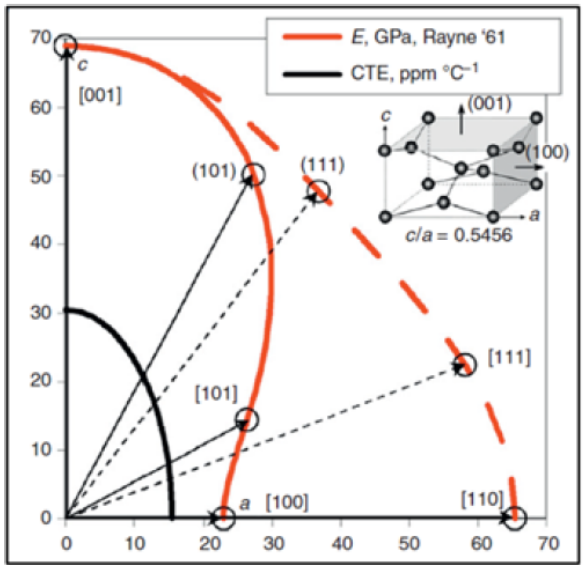

Figure 1.2 Elastic Modulus and Coefficient of Thermal Expansion (CTE) of Tin as a Function of Crystal Orientation [1]

1.3.2 Chromium (Cr)

Cr helps to improve shear ductility after long term aging. Besides, it also suppress kirkendall void formation in the solder joints [15].

1.3.3 Nickel (Ni)

Among all the micro-alloy additives, Ni is one of the most common element. Addition of Ni improves fluidity of SAC solders. Ni also improves the high strain rate

properties of solder joints. For example, the drop strength of SAC alloys can be significantly improved by Ni addition. Although Ni does not have any significant influence on the creep properties of the solder, it inhibits Cu diffusion and thus reduce the thickness of Cu_3Sn intermetallic compound (IMC). The Ni addition greater than 0.01 wt% could suppress the growth of Cu_3Sn IMC even after long term (2000 hours) aging. Since Cu_3Sn IMC is very brittle, the growth of Cu_3Sn layer is very critical for the brittle failure of the solder joints. Addition of Ni on SAC solder causes to form more stable $(Cu, Ni)_6Sn_5$ IMC which act as a barrier layer and suppress the growth of Cu_3Sn layer. Therefore, by reducing the thickness of brittle Cu_3Sn layer, Ni helps to improve strength of the solder joints. Ni also helps to improve strength by refining solder microstructure [16].

1.3.4 Zinc (Zn)

While Ni reduces only the formation Cu_3Sn, Zn doping can retard both Cu_3Sn and Cu_6Sn_5 IMC's in SAC solders. Zn also helps to improve the interface quality after multiple reflow and high temperature aging. Addition of 1.5% Zn in SAC207 solder could refine Ag_3Sn and Cu_6Sn_5 IMC's and hence increase strength by dispersion strengthening [15].

1.3.5 Cobalt (Co)

Co helps to reduce the growth of Cu_3Sn layer during high temperature aging. Addition of small amount of Co (<0.1 wt%) can improve the properties of SAC solders. Co increases the number of nucleation sites and hence significantly refine the grains of SAC305 solder. Thus it helps to improve shear strength of the solder joints [15].

1.3.6 Bismuth (Bi)

If added in small amount, Bi can improve the wetting ability and reduce melting temperature of lead free solder alloys. It also increases strength of the bulk solder and

inhibit the large Ag_3Sn formation in the bulk solder. It is recommended to avoid Pb contamination in the solder before using Bi as an additive. Because Bi can react with Pb to form a brittle IMC at the grain boundary and reduce strength significantly. If present in excess amount, Bi can cause solidification crack due to the increase in the gap between solidus and liquidus temperature [15].

1.3.7 Antimony (Sb)

Sb improves mechanical properties of lead free solders but it is toxic in nature. A small percentage (0.5 wt%) of Sb can improve drop test reliability of SAC solder joints [16]. Besides, Sb also helps to enhance strength of the solder by solid solution strengthening [17].

1.3.8 Germanium (Ge)

Ge doped solders shows low Cu dissolution from the Cu pad and hence suitable for the wave soldering process. Ge significantly improve wetting properties of the lead free solders and refine the solder microstructure. As a result, Ge addition improves the strength and ductility of the lead free solder [16].

1.3.9 Sn-Ag-Cu System

As shown in Figure 1.1, Sn-Ag-Cu (SAC) has been the most popular, widely used lead free solder in today's market. Although they are still not identified as the "drop in" replacement for all applications, a variety of SAC alloys with different chemical compositions have been the proposed by various user groups and industry experts. These include: SAC105 (98.5Sn-1.0Ag-0.5Cu), SAC205 (97.5Sn-2.0Ag-0.5Cu), SAC305 (96.5Sn-3.0Ag-0.5Cu), and SAC405 (95.5Sn-4.0Ag-0.5Cu), known as the SACN05 series; SAC387 (95.5Sn-3.8Ag-0.7Cu), SAC396 (95.5Sn-3.9Ag-0.6Cu), and SAC357 (95.2Sn-

3.5Ag-0.7Cu), identified as near eutectic SAC choices; SAC3810 (95.2Sn-3.8Ag-1.0Cu), SAC3595 (95.55Sn-3.5Ag-0.95Cu), SAC0307 (9Sn-0.3Ag-0.7Cu), and SAC107 (98.3Sn-1.0Ag-0.7Cu), designed for special needs such as high temperature application, drop and shock optimization, etc. The main benefits of the various SAC alloy systems are their relatively low melting temperatures compared with the 96.5Sn-3.5Ag binary eutectic alloy, as well as their superior mechanical and manufacturability properties when compared to other lead free solders [18].

Figure 1.3 shows a typical 3-D ternary phase diagram. The contours on the top surfaces of the figure represent the isothermal lines. Each of the 3 sectors represents the binary phase diagram of two of the three elements. The center of the diagram, where the isothermal lines reach the common, lowest point, is the eutectic point of the ternary system. Figure 1.4 is the top view (2-D) of the ternary phase diagram of Sn-Ag-Cu.

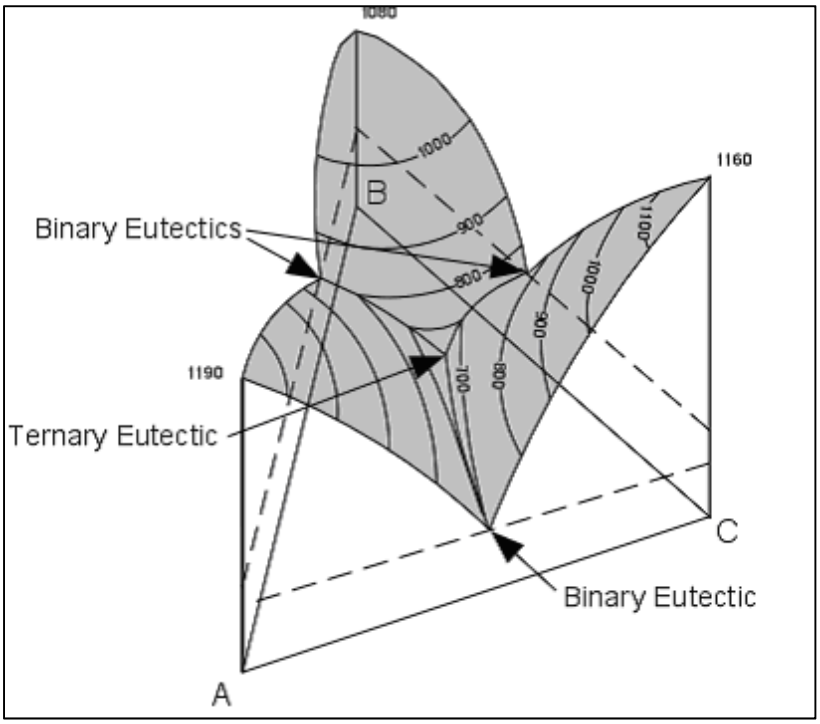

Figure 1.3 Typical 3-D Ternary Phase Diagram

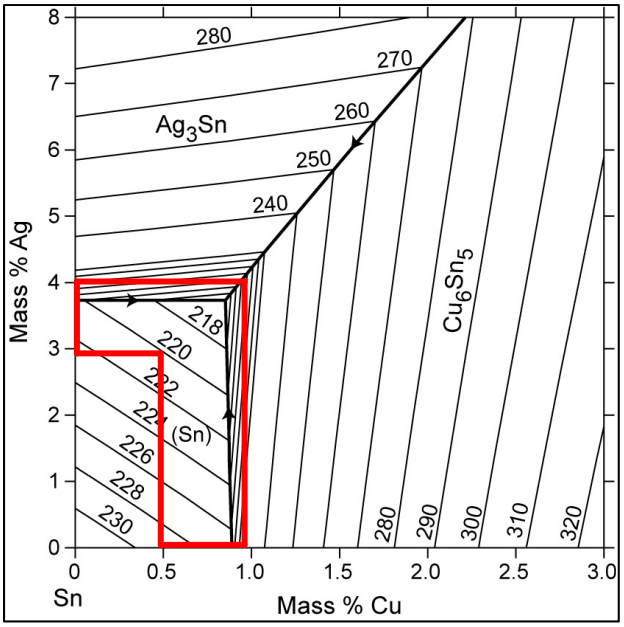

Figure 1.4 Sn-Ag-Cu Ternary Phase Diagram

The area indicated in the red box is the near eutectic region. Most of the SAC alloy compositions currently on the market are within this region. The eutectic and near eutectic melting temperature has been determined to be 217 °C, although the precise eutectic point is not known [19].

In SAC alloys, the formation of intermetallic compounds between the primary elements Sn and Ag, and Cu affect all the properties of the alloys. There are three possible intermetallic compounds that may be formed: Ag_3Sn forms due to the reaction between Sn and Ag (Figure 1.5) and Cu_6Sn_5 forms due to the Sn and Cu reaction. The compound Cu_3Sn will not form at the eutectic point unless the Cu content is high enough for the formation of Cu_3Sn at higher temperatures, so in bulk specimens Cu_3Sn is not presented. There is no reaction between Ag and Cu to form any kind of intermetallic compounds. The particles of intermetallic compounds possess much higher strength than the bulk material. Fine intermetallic particles in the Sn matrix can therefore strengthen the alloys. The intermetallic compounds can also improve the fatigue life of the solders, as SAC alloys are

reported to be 3-4 times better fatigue properties than the Sn-Pb eutectic solders. The higher fatigue resistance is believed to be contributed by the interspersed Ag_3Sn and Cu_6Sn_5 particles, which pin and block the movement of dislocations. The many patents that have been granted for SAC systems have limited their use and hindered research on several of the SAC alloys. However, many familiar alloy such as SAC305 and SAC405 are not patented to avoid excessive licensing and fees [18].

Despite the benefits mentioned above, SAC family solders sometimes are still questionable as complete substitutes for eutectic Sn-Pb because of costs, some patent issues (particularly outside Europe), aesthetic consideration (dross problem of SAC solders), and relatively high melting temperature (217 °C vs. 183 °C).

1.3.10 Sn-Ag-Cu + X System

Sn-Ag-Cu alloys have shown potential to be successful substitutes for eutectic Sn-Pb, however, the industry is still looking for a "perfect" solution. According to the results of many recent studies, performance characteristics of solder alloys are able to be optimized by doping, that is, by adding a small amount of other alloying elements into the SAC solder alloys.

The proposed doping element candidates include Bi, Ni, Co, Ge, Zn, La, Mg, Mn, Ce, Ti, Fe, In, B, etc. For example, adding 0.05% (wt.) Ni can successfully stabilize the microstructure, inhibit the excessive consumption of metal base and thus increase the reliability of the solder joints [20-22]. In addition, doping rear earth (RE) elements can significantly enhance wettability, refine microstructure and improve ductility of SAC alloys [23-26].

Even though dopants can greatly alter the mechanical, electrical and physical behavior of SAC solders, the effect on melting temperature, however, is found to be negligible. This is another advantage for doped solder alloys because manufacturers can still use the same processing conditions as conventional SAC alloys.

Meanwhile, the known issues for SAC-X solders are also apparent. For instance, the material properties and interfacial behavior of solder alloys have been demonstrated to be very sensitive to the quantity of the X-additive. As a result, it takes much more time and cost to figure out the optimal composition levels for the dopants.

1.4 Characteristics and Applications of Sn-Ag-Cu Solder Material

The advantages of SAC series over other Pb-free systems include relatively low melting temperatures, superior mechanical and solderability properties, and good tolerance for Pb contamination. These characteristics give SAC alloys good compatibility with existing electronics packaging infrastructure. In fact, there is a long history of using 95.5Sn–4.0Ag–0.5Cu (SAC405) to form solder joints for BGA packages. The high market share (≈ 70%) by SAC series alloys on a global scale provides strong evidence of its world-wide acceptance. Also, nanoscale lead-free solders ("nano-solders") have been proposed and investigated in the development of nano-soldering technique for nanoscale assembly and integration. Tin (Sn)-based and indium (In)-based lead-free nano-solders have been synthesized directly onto multisegmented nanowires using electro deposition method in nanoporous templates. Furthermore, high temperature lead free solders are being used in medical industries today where a variety of intrusive procedures used requiring tools, instruments, sensors and components in materials that are inert with respect to reactions

with the body [27]. Also, new surgical techniques have been developed to improve the quality of operations, reduce the risk to patients and reduce the pain experienced by patients. Environmental concerns and the concern about toxicity and health hazards indicate that there is a drive to develop and use lead-free solders.

1.5 Mechanical Properties of Lead Free Solders

In an electronic device, a number of different types of engineering materials exists in a close proximity. For example, a printed circuit board (PCB) is typically a glass fiber reinforced polymer (composite material), a die is a semiconductor material which is often encapsulated in a plastic or a ceramic, and the tracking and the solder joints are metallic materials. Solder joints are used to create an electrical circuit by mounting chips and components on the PCB. Hence an ideal solder joint should have a good conductivity to transmit electrical signals and at the same time, adequate strength to provide mechanical support and connection. Hence, mechanical properties of solder joints are critically important to ensure reliability of the electronic products. Among all the mechanical properties, tensile, fatigue, and creep performance of the solder are critically important. Thus an accurate measurement of mechanical properties and development of constitutive equations for solder materials are required in mechanical design, process optimization and reliability assessment.

1.5.1 Tensile Properties (Stress-Strain Behavior)

Under the action of an increasing stress, metals usually exhibit elasticity, plasticity, and a maximum in stress is followed by necking and fracture. The slope of the linear elastic portion of the stress vs. strain plot is the modulus, and the stress at termination of elastic

behavior is the yield stress. The extent of deformation prior to fracture is known as ductility. Ceramics display only elastic behavior until fracture, which is associated with cracking and very limited deformation (brittleness). Polymers may exhibit both characteristics above according to the temperature. Above the glass transition temperature, T_g, extensive deformation due to mechanisms quite unlike those in metals may follow a small degree of elasticity. Below this temperature, polymers exhibit ceramic-like behavior. In all material categories, the maximum stress attained is the tensile/compressive/shear strength according to the mode of stressing employed. Composites are physical mixtures and exhibit the average properties of their components, taking into account the proportions of each. These characteristic features of monotonic behavior are summarized in Figure 1.5. The fracture strains of brittle materials and the yield strains of metals are generally less than 1% (the yield strain of solders is around 0.1–0.2%). The amount of deformation prior to the attainment of maximum strength is between about 3% and 7% for common solder alloys.

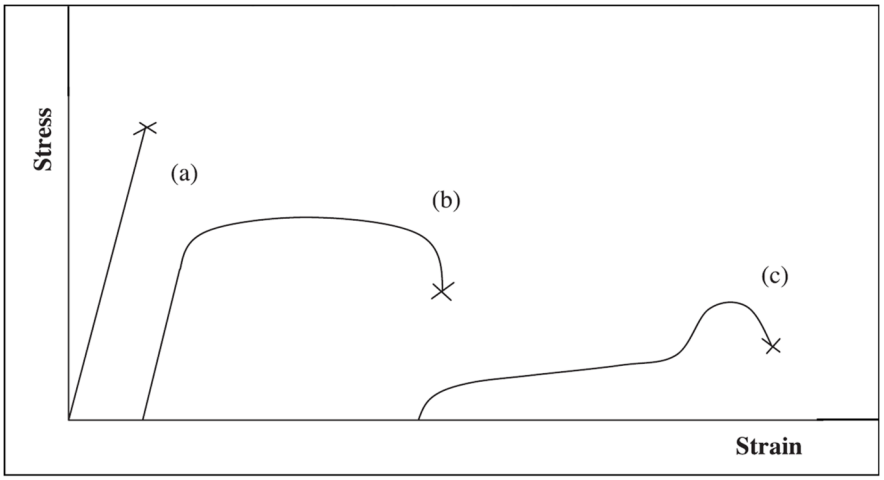

Figure 1.5 Schematic Overview of Mechanical Behavior of a) Ceramics, Polymers below their Glass Transition Temperature (Tg) and Non Ductile Material b) Ductile Materials c) Polymers above Tg

Tensile properties indicate how the material will react to forces being applied in tension. Although solder joints are rarely under pure tensile/compressive loading, tensile properties are still crucial indicators for design purposes. Through tensile tests, several material properties can be determined, such as effective modulus, yield stress (YS), ultimate tensile strength (UTS), elongation, etc. In most of the cases that engineering stress-strain curves are employed by neglecting the change in cross sectional area.

Tensile properties are generally described by stress-strain curves. Figure 1.6 shows a typical engineering stress strain curve. A typical engineering stress-strain curve for solder alloys consists of an elastic region and a plastic region. In the elastic region, when the stress is reduced, the material will return to its original shape. In this linear region, the material obeys the relationship defined by Hooke's Law. However, since the effective modulus includes small inelastic deformations or time-dependent deformations such as creep, it is usually smaller than the dynamic modulus measured by the acoustic or ultrasonic wave method, which largely eliminates the inelastic deformation due to rapid wave propagation [28-30]. Also, Ralls, et al. showed that the elastic modulus of metal will decrease with increasing temperature [31]. The underlying reason for this is because the distance between adjacent atoms increases at higher temperatures which in turns decrease the elastic modulus.

When the load is high enough to exceed the elastic limits the material will experience plastic deformation, which is permanent. At this stage the material is undergoing a rearrangement of its internal molecular or microscopic structure, in which atoms are being moved to new equilibrium positions. Specimens subject to plastic deformation will simultaneously elongate and decrease in diameter. The Yield Stress (YS)

is defined as just enough stress to cause the onset of plastic deformation. However, YS is difficult to determine. In engineering practice, a specified small amount of plastic deformation is used, with 0.2% being the widely accepted value [32]. This is determined by a parallel line drawn at 0.2% of the strain to the elastic slope (Figure 1.6). When the load is removed at a point above the yield stress, the stress-strain curve will be approximately parallel to the initial modulus.

The ultimate tensile strength (UTS) is the maximum engineering stress level reached in a stress-strain test. In ductile materials similar to solders, the UTS are usually well outside of the elastic portion and the elastic strain is very small comparing to the plastic strain. When necking occurs, the engineering stress decreases and the specimen eventually fail.

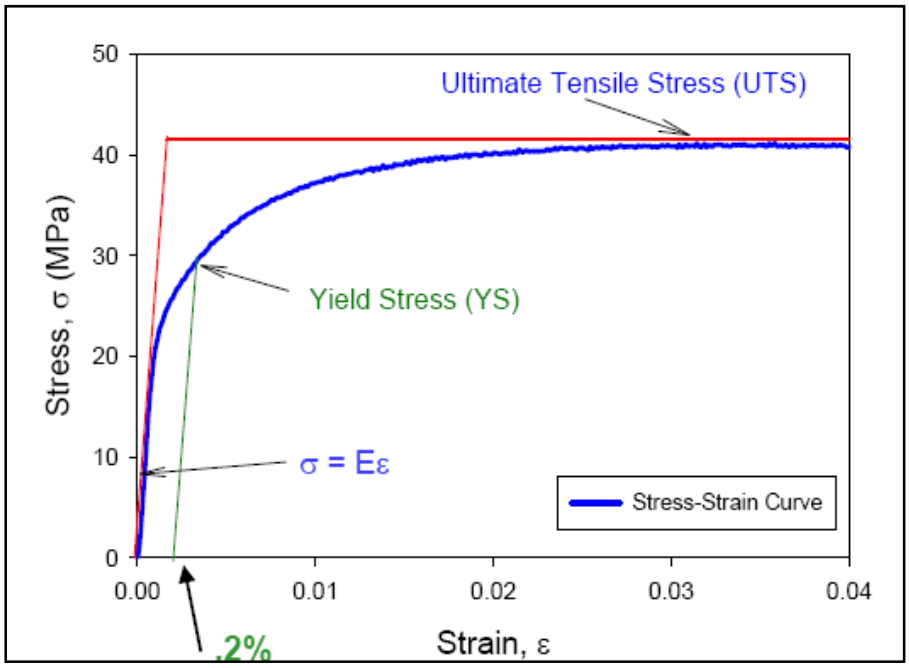

Figure 1.6 Typical Stress-Strain Curve.

1.5.2 Creep Properties

Creep deformation refers to the time dependent plastic flow or deformation of a material that occurs when the material is exposed to a constant load, typically below yield stress, for a long period of time. Creep deformation becomes significant when the material operates at a high homologous temperature (T_h), which is defined by the ratio of operating temperature (T) and the melting temperature (T_m) of the material.

$$T_h = \frac{T}{T_m} \tag{1.4}$$

Creep deformation becomes the dominant failure mode in a metallic material if T_h is greater than $0.5T_m$ [33]. The melting temperature of lead free SAC solder is around 217 °C (490 K) causing T_h for the alloys, for room temperature (298 K) operating conditions, is $0.61T_m$. As a result, lead free SAC solder alloys display creep deformation even in room temperature operating condition. Due to the mismatches of the coefficient of thermal expansion (CTE) of silicon chip and other assembly materials used in an electronic package, solder joints are remain under mechanical stress. These mechanical stresses can cause time dependent creep deformation of solder materials. In microelectronic packaging, creep deformation is regarded as one of the major failure mechanisms of solder joints [34].

Creep test is typically conducted by applying a constant uniaxial load on the test specimen at a particular temperature. During the test, deformation of the test specimen is recorded as a function of test time and the result of the creep test is presented as a 'creep strain' vs. 'time' plot. The extent of creep deformation significantly depends on the applied stress level and the test temperature. Figure 1.7 represents a typical creep curve which consists of three distinct regions, after the initial jump, namely, primary, secondary, and tertiary regions.

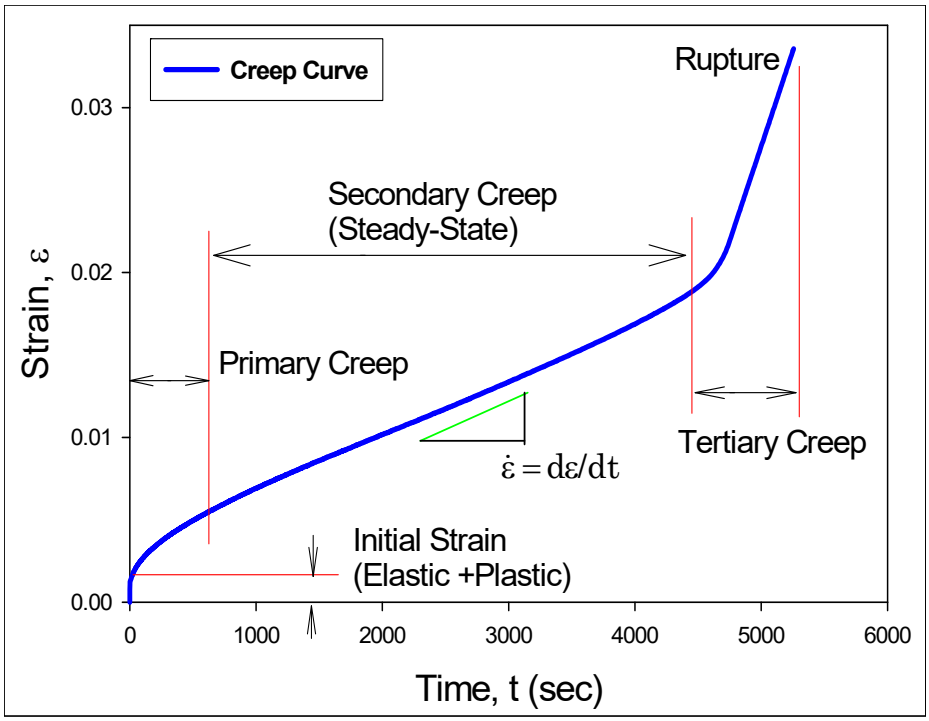

Figure 1.7 Typical Creep Curve.

Every creep test begins with an initial strain which corresponds to the instantaneous response (mostly elastic) of the material due to the applied force/load. In the primary creep stage, the material starts to deform with at a high strain rate (high slope at the beginning of the primary region) and then the strain rate decrease gradually with increasing time. This is due to the work hardening of the material which resists deformation. Eventually, with increasing test time, the creep strain rate reaches to a steady state stage which is known as steady state creep or secondary creep region. The constant creep rate, in the secondary stage, is due to the dynamic balance between strain hardening and recrystallization [32]. The strain rate in the secondary stage is very important since very often researchers use this parameter in the finite element simulations to predict reliability of the solder joints under different test conditions. After secondary creep, the material enter into the tertiary creep region followed by an immediate rupture. Tertiary region begins when the strain rate start increasing abruptly from the constant value.

1.5.3 Mechanisms of Creep Deformation

Several creep mechanisms have been proposed such as dislocation glide, dislocation creep, grain boundary diffusion, and lattice diffusion which can be summarized in a creep deformation map, as shown in Figure 1.8 [35, 36]. The deformation diagram was first introduced by Ashby in 1972 [36], and has been widely accepted and studied by other researchers in the area. In the deformation map show in Figure 1.8, the abscissa is the homologous temperature and the ordinate is normalized tensile or shear stress. The top of the map is bounded to the theoretical or ideal stress, below which is the onset of dislocation glide. Dislocation glide occurs at high stress levels over the entire homologous temperature range. In this case, the dislocation moves along the slip planes [37]. Dislocation creep is characterized by a high-temperature deformation mechanism with homologous temperatures greater than $0.5T_m$ and requiring intermediate high stress. The deformation results from diffusion controlled dislocation movement, with dislocations climbing away from barriers.

Coble proposed a grain boundary based diffusion mechanism, which involves the atomic or ionic diffusion along the grain boundaries [38]. The deformation occurs at intermediate low stress levels over an intermediate to low temperature range. Nabarro-Herring Creep or lattice or bulk diffusion occurs at low stress level and high temperature. In this case, interstitial atoms and lattice vacancies along the gradient of a grain boundary migrate in reversed directions in the presence of tension or compression pressure. Lattice or bulk diffusion becomes the primary deformation mechanism under this circumstance [39]. If there is no pressure, interstitial atoms and lattice vacancies will migrate in proportion to the gradient of their concentrations. Under pressure, the lattice defects tend

to move in directions to relieve the imbalance of pressure. The movement will eventually cause creep deformation.

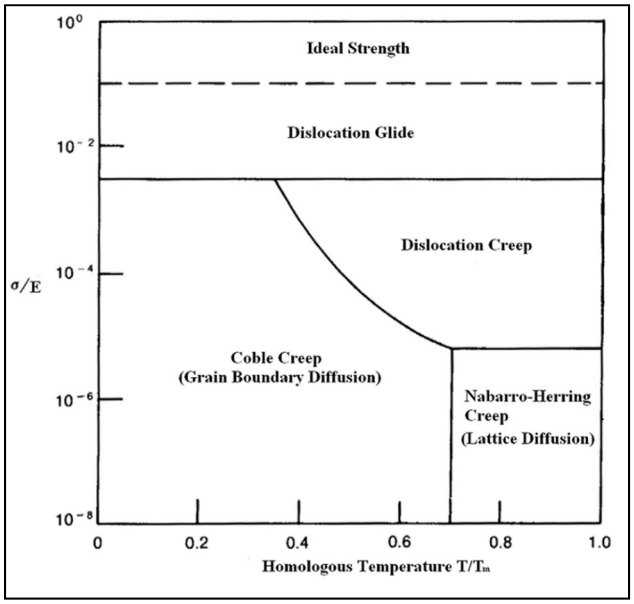

Figure 1.8 A Typical Creep Deformation Map

Grain-boundary sliding may also be involved in the creep deformation at high temperatures [30] where the displacement of grains can be induced by stress at high temperatures. However, this is not an independent deformation mechanism, but may accompany one or more of the above deformation mechanisms.

Due to the high homologous temperature ($> 0.5T_m$) of most solder alloys under normal operating conditions, the stress level determines the creep deformation mechanism. At low stress levels, the controlling mechanism is lattice diffusion and grain-boundary diffusion. As the stress rises to intermediate levels, dislocation creep takes over, and at high stress level, dislocation gliding becomes dominant. Additionally, the contribution of grain boundary gliding to creep deformation should be taken in account at all stress levels.

1.6 Nanoindentation

Indentation testing is a technique where a hard tip, with known mechanical properties, is pressed into the surface of a test sample to extract the test sample's properties. The load applied on the indenter tip caused it to penetrate into the test sample surface. When the applied load reaches to the user specified value, it can be held for a certain period of time (for creep properties) or remove instantaneously (for hardness and elastic modulus). Removal of the applied load leaves an impression or indent on the sample surface.

Nanoindentation (NI) is a kind of indentation testing where the penetration length is measured in nanometer. The development of the NI technique has been motivated by the miniaturization of the engineering materials as well as the development of the nanostructured materials. Since the area of the indenter tip is well defined (known geometry), the indent area can be easily determined from the tip penetration depth from the sample surface. Elastic modulus, hardness and creep properties of a material can be obtained from indentation load displacement data [40].

Because of having very high hardness and elastic modulus, diamond is typically used to make indenter tip Indenter tips are available in different shape and the choice of indenter tip shape depends on the type of required information from a NI test. Berkovich tip is used in this study (Figure 1.9).

This is the most common indenter tip and used to measure mechanical properties using a NI technique. The shape of a Berkovich tip is similar to a three sided pyramid where the faces meet at a single point (Figure 1.5). The tip can maintain its self-similar geometry to a significantly small scale. The center to face angle of the tip is 65.3^{o}.

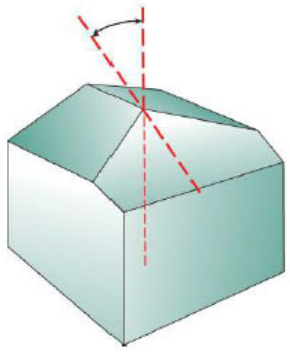

Figure 1.9 Berkovich Tip.

1.7 Harsh Environment applications of Electronics

The reliabilities of electronic products depend strongly on the environmental conditions experienced during field use. Consumer electronics typically experience maximum operating temperatures of 100 °C. However, there are several harsh environment applications such as oil and gas exploration, avionics, automotive, and defense applications where electronics are exposed to much higher temperatures than those experienced by consumer electronics [41, 42]. The electronic systems used in under-the-hood automotive applications can be operated at temperatures over 150 °C [43, 44]. For example, engine control modules mounted directly onto the engine experiences high-temperature excursions while in operation. In vehicles, when the engine is turned on, it continues to ramp up to the maximum operating temperature from the ambient temperature while the engine continues to be in operational state. Electronics experience extremely high temperatures during this period, and there can be fluctuation in the temperature conditions.

The electronic systems used in oil and gas exploration applications, also experiences ambient temperatures above 150 °C, even in some applications, 200 °C or

higher [45]. Wireline logging represents a typical application in oil and gas drilling where the electronics are exposed to very high temperatures. During this application, the logging tool is lowered into the wellbore, and the electronics experience extremely low or high temperatures depending on the location and type of the oil well. The reliability of electronics is an important concern here since the wireline logging usually lasts 2 to 6 hours.

Electronics used in commercial and defense aircrafts and ground military vehicles also experience extremely high temperatures. In high-speed civil transport and supersonic aircraft, the highest ambient temperature experienced by actuator-mount electronics (without cooling) are ≈ 193 °C and 200 °C respectively [41]. Also, temperatures in electric propulsion system in the battle tank and other mobile ground defense applications can reach up to 200 °C.

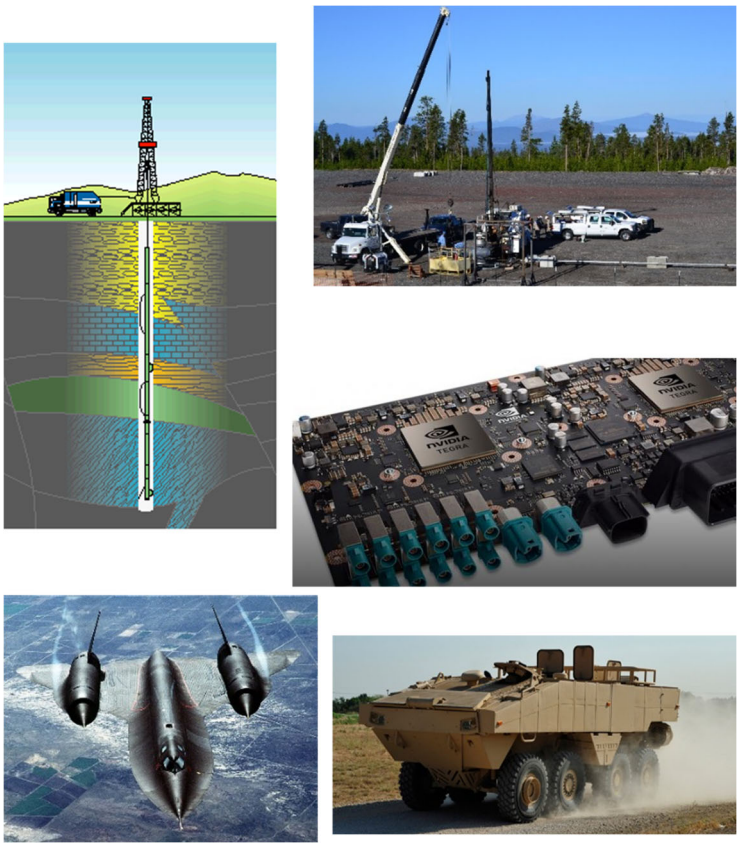

Figure 1.10 High Temperature Application of Electronics

1.8 Objectives of This Research

The goals of this research are to explore different temperature dependent mechanical behavior and microstructural evolution of lead free solder alloys for different harsh environment applications, and to develop new constitutive equations and reliability models that include aging effects to predict solder joint reliability in microelectronic packaging. The Primary objectives of this research involve:

(1) Investigate the Effect of the Value of the Solder Joint Poisson's Ratio on the Finite Element Results for BGA Components Subjected to Thermal Cycling.

(2) Establish the Fact that the Specified Poisson's Ratio Strongly Affects the Mechanical Response and Simulation Results.

(3) Experimental Characterization of Poisson's Ratio for Different SAC Alloys at Different Temperatures, Strain Rates, Solidification Profiles and Aging Conditions.

(4) Investigate the Uniaxial Tensile Properties of Different New SAC+Bi Alloys with Various Bismuth (1%, 2%, and 3%) Levels at Different Temperatures (up to 125 °C) and Different Strain Rates and Compare the Mechanical Properties with Conventional SACN05 (N = 1,2,3, and 4).

(5) Determine Anand Model Parameters Using Experimental Results and Investigate the Correlation with Experimental Results.

(6) Study the Effects of Isothermal Aging for the Various New SAC+Bi (1%, and 2%) Alloys Using both Mechanical testing and Microstructural Evolution.

(7) Determine the Isothermal Aging Dependent Anand Model Parameters of SAC305 at Extreme High Temperature (125, 150, 175, and 200 °C) Testing.

(8) Investigate the Microstructural Evolution of SAC305 BGA Joints by Visualization and Quantitative Analysis of Diffusion of Copper, Growth of IMC Layer at Solder Joint and PCB Interface, and Evolution of IMC Particles Subjected to Extreme High Temperature Aging.

(9) Determine the effects of test temperature and aging time on the mechanical response of SAC305 BGA joints using Nanoindentation method and Correlate with the Microstructural Evolution.

1.9 Organization of the Dissertation

This dissertation mainly focuses on investigating the thermal-mechanical characterization and aging dependent mechanical response and microstructural evolution of lead-free solder alloys and is presented in the following chapters:

Chapter 1: Introduction to lead free solders alloys and mechanical properties of solder materials.

Chapter 2: Literature review on isothermal aging effects, mechanical properties, nanoindentation on SAC solder joints, nanoindentation at elevated temperature, microstructural evolution during aging of SAC alloys, finite element based life prediction and reliability models of electronic packages combined with the coarsening of IMC particles.

Chapter 3: Description of experimental procedure, sample preparation, strain gage mounting, uniaxial tensile tests, raw data processing, measurement of Poisson's ratio, determination of Anand model parameters, nanoindentation measurement technique, and quantitative analysis of Scanning Electron Microscopy (SEM) images.

Chapter 4: Study on the influence of Poisson's ratio on the reliability of SAC lead free solder joints by finite element analysis.

Chapter 5: Study on the dependence of SAC lead free solder Poisson's ratio on temperature, strain rate, solidification profile, and isothermal aging by experimental characterization.

Chapter 6: Study on the mechanical behavior and reliability of SAC+Bi lead free solders with various levels of Bismuth.

Chapter 7: Study on the isothermal aging dependent mechanical response and Ananad model parameters of SAC305 solder at extreme high temperatures.

Chapter 8: Study on the visualization and modeling of microstructural evolution in SAC305 BGA joints during extreme high temperature aging.

Chapter 9: Study on the effect of high temperature on the mechanical behavior of SAC305 BGA joints using nanoindentation.

Chapter 10: Summary and conclusions of the dissertation.

CHAPTER 2

LITERATURE REVIEW

2.1 Introduction

The motivation of adopting techno-economically feasible and environmental friendly concepts in electronic industries accelerating the rapid transition to lead free soldering area. To cope with the environmental concerns, legislative mandates, and market differentiation, great efforts have been undertaken to develop desirable lead free solders and establish a corresponding database of material properties. Many researchers have attempted to measure the key mechanical properties of lead free solders. However, large discrepancies have been found in the published data from various groups. There are several reasons for these discrepancies. Firstly, the differences in specimen preparation methods among the researchers cause different microstructures in the specimens that directly affect the experimental results significantly. Secondly, the testing methods and the test conditions may also be different which will again affect the results. Thirdly, mechanical properties obtained from the bulk solders might be different from the measured properties of solder joints. Finally, the lack of standardization in the data acquisition and processing of mechanical properties makes it difficult to obtain good laboratory-to-laboratory comparisons.

Apart from the above mentioned reasons for the discrepancies in solder material properties, another critical factor is aging effects. Aging is mostly neglected in the majority

of prior studies, which will further exacerbate these problems. It has been observed from recent studies that isothermal aging leads to large reductions (up to 50%) in several key material properties for lead free solders including stiffness (modulus), yield stress, ultimate strength, and strain to failure [33]. Even more dramatic evolution has been observed in the creep response of aged lead free solders, where up to 100X increases were found in the steady state (secondary) creep strain rate (creep compliance) of SAC solders that were simply aged at room temperature [46, 47]. For elevated temperature aging at 125 °C [48], the creep strain rate was observed to change even more dramatically (up to 10,000X increase for SAC105).

In real applications, solder joints are continuously exposed to aging/thermal cycling during service. It has been well documented that the microstructure, mechanical response, and failure behavior of solder materials are constantly evolving under such circumstances [49-84]. It has also been demonstrated that aging effects are universally detrimental to reliability and cause reductions in stiffness, yield stress, ultimate strength, and strain to failure, as well as highly accelerated creep. Solder joints with highly degraded microstructure and material properties are so vulnerable that the service life of the package is often severely shortened.

The components of electronic packages undergo complex stress-strain conditions during the assembly process as well as when subjected to thermal or power cycling. This happens due to the CTE mismatch of different parts of the components so for a reliable product design, it is very important to have well-established and reliable constitutive models for lead free solder alloys to perform accurate solder joint stress-strain analysis or creep analysis. Among all the widely used constitutive models, however, none of them

take aging effects into account. In addition, current finite element prediction methods for solder joint reliability do not take into account for the effect of Poisson's ratio on reliability predictions which are very important for lead free solders as they are viscoplastic. Thus, it is necessary to study constitutive models for solders that include aging effects and to also incorporate the temperature dependent material properties including Poisson's ratio in FEA analysis for the better predictions of solder joint reliability.

2.2 Aging Effects on Tensile Properties

Studies on the effects of aging on solder material properties are primarily divided into two groups, which are aging effects on bulk solders and aging effects on solder joints. These are described in subsequent sub-sections.

2.2.1 Aging Effects on Bulk Solders

Evolution of mechanical properties with aging in both Sn-Pb and lead free solders has been reported in recent years. Researchers have done numerous studies on the effects of aging on bulk solder properties as well as some studies on solder joints in actual components. Most studies show aging has significant effects on the mechanical properties of solder materials. In 1956, Medvedev [62] reported a 30% loss of tensile strength for bulk Sn-Pb solder after 450 days of room temperature (RT) aging, and a 23% loss in tensile strength for solder joints under a similar exposure. Room temperature aging effects on solder alloys has been presented by Lampe [60]. He showed that after 30 days of room temperature aging, the shear strength and the hardness of Sn-Pb and Sn-Pb-Sb solders reduced by approximately 20%. Miyazawa [77] reported reduction of hardness and microstructural coarsening for Sn-Pb solders aged at 25 and 100 °C for 1000 hours.

Xiao, et al. [66] investigated the stress-strain behavior of SAC396 solder alloy which were subjected to aging at 25 and 180 °C for various amount of time. They have shown that the strength reduces by 25% for aging at room temperature for 35 days and a 33% reduction for aging at 180 C for 9 days. Ding, et al. investigated the influence of aging on fracture behavior of Sn-Ag solder in tensile tests [56]. They have shown that the solder samples tensile strength reduce very quickly for isothermal aging at 180 °C for 120 hours. Ma, et al. [85] studied the evolution of Young's modulus, yield stress, and ultimate tensile strength of SAC305 and SAC405 solder alloys under various aging conditions. A linear-exponential model was developed to describe the material property evolution. They have shown that the material properties decreased dramatically in the first 20 days for both room temperature aging as well as elevated temperature aging. After 20 days of aging, the properties change slowly and linearly and it continues for longer aging time.

Zhang, et al. [86] also studied the aging effects on tensile properties of SACN05 (N = 1%, 2%, 3% and 4% silver) series solders for different amount of aging at temperatures 25-125 °C. They have demonstrated that the mechanical properties degraded more dramatically when the aging temperature was increased. The data also shows that the degradation becomes linear with longer aging time. Cai, et al. [51] have also shown that the aging effects are significant for lead free solders (SAC105, SAC205, SAC305 and SAC405) for room temperature aging as well as elevated temperature aging. They have also shown that the aging effects can be reduced by using certain dopants to (e.g. Bi, In, Ni, La, Mg, Mn, Ce, Co, Ti, Zn, etc.) SAC solder alloys to enhance the reliability of lead free solders. Finally, Mustafa, et al. [78] have demonstrated that the hysteresis loop area in cyclic (tension/compression) loading of various SAC solder alloys changes significantly

with aging. For strain controlled tests, the hysteresis loop area deceases and for the stress controlled tests, the loop area increases with aging time.

2.2.2 Aging Effects on Solders Joints

Isothermal aging effects have also been reported to lower the strength and to reduce reliability of solder joints. The mechanical response of solder joints to external loading can be different from the bulk solders due to fine microstructure, grain orientation (single grain/ multigrain), and the presence of intermetallic compounds at joint boundaries.

Coyle, et al. [87] reported 20% shearing strength reduction of BGA solder joints after 240 hours of aging at room temperature. A 10% shearing strength reduction has been reported by Lee, et al. [88] for the BGA packages just after 3 days room temperature aging. Chilton, et al. [89] reported a 15% fatigue strength reduction of Sn-Pb solder joints of a SMD test package which were aged for 60 days at room temperature. Li, et al. [90] studied the elevated temperature aging effects on flip-chip packages with SAC solders. They have shown that the shear strength of solder bumps subjected to aging at 80 °C decreased gradually with aging. Also for the aging temperatures 150 and 175 °C, the degradation of shear strength of the bumps were much faster. They also reported that the fracture of the solder bumps occurred at the bulk solder. Koo, et al. [91] found that 63Sn-37Pb solder joint strength on electroplated Ni/Au BGA substrate was significantly affected by aging at 170 °C for up to 21 days, while the deterioration of shear properties of Sn-3.5Ag was much smaller. Darveaux [92] indicated that after 24 hours of aging at 125 °C, all alloys showed a 10% to 30% reduction in solder joint strength. All of the solder joints failed within the bulk solder and exhibited high ductility. In addition, the ductility of all of the Pb-free solder joints decreased with increased aging [66]. Oliver et al. [93] reported that the joint strength

of Sn-3.5Ag and SAC325 solder on both Ni/Au and Sn/Pb pad metallizations were unchanged after aging at room temperature as well as elevated temperature for 1000 hours. However they found reduction in shear strength of solder joint in Sn-Pb solders.

Pang, et al. [94] studied the aging effects on the mechanical properties and fatigue life of Sn-Pb solder joint specimens that were subjected to thermal cycling conditions from -40 to 125 °C. They have shown that the shear strength reduces significantly for specimens that were subjected to 1000 thermal cycles. They have also shown that the fatigue life of the specimens dropped by 6 times compared to non-cycled specimens. Zhou, et al. compared the joint strengths of SAC387 on both Cu and Ag substrates at an aging temperature of 170 °C, and concluded that aging had little effect on the SAC/Ag interface, but dramatically softened the SAC/Cu joint. The softening difference was said to be due to lower residual stresses at the SAC/Ag joint interface. Chen, et al. [73] studied the effects of aging on the solder bump shear strength for both Sn-Pb and Sn-3.5Ag solders. They reported that shear strength for both solder materials decreases after aging at 150 °C for 1500 hours, 8.9% for Sn-Pb solder bumps and 5.3% for Sn-3.5Ag. Kim, et al. [59] also reported similar results in which they reported an average 5% decrease in joint strength in stud bump samples for aging at 150 °C for 300 hours.

The degradations of the stiffness, strength, and creep compliance with aging are expected to be universally detrimental to reliability of solder joints in lead free assemblies. This has been demonstrated explicitly in the recent investigation of Lee and coworkers [88], where aging has been shown to degrade the Thermal Cycling Reliability (TCR) of lead free Plastic Ball Grid Array (PBGA) assemblies subjected to Accelerated Life Testing (ALT). They have shown dramatic degradation in fatigue life of BGA components with

SAC 305 solders, which were subjected to thermal cycling from 0 to 100 °C with prior aging at either 100 or 150 °C. The amount of life degradation was found to be dependent on the surface finish of the PCB substrates, with 44% degradation observed for ENIG surface finish and 20% degradation observed for OSP surface finish under the most severe aging conditions (1000 hours at 150 °C) prior to thermal cycling accelerated life testing.

In a similar study, Lee, et al. [95] showed that the lifetime of wafer-level chip scale packages with SAC305 solder interconnects was reduced by 29% for 500 hours of aging at 150 °C. Zhang, et al. [81] have investigated the correlation between the effects of isothermal aging on the reliability of PBGA components. They have shown that for 6 months aging at 125 °C that the reliability of SAC105 components dropped by 53%. Smetana, et al. [96] have performed an extensive study on the effects of prior isothermal preconditioning (aging) on the thermal cycling lifetime for a variety of components. Similar to the investigations discussed above, it was observed that prior aging reduced the thermal cycling characteristic life of SAC BGA assemblies subjected to 0 to 100 °C cycling. It was also found that changes occurred in the Weibull slope, suggesting other failure modes were created by aging. They also found that prior aging increased the thermal cycling reliability of certain components (e.g. 2512 chip resistors and certain QFNs). Similar results of improved reliability with aging were found for components subjected to a smaller thermal cycling range of 20 to 80 °C. This led them to conclude that aging does not universally reduce solder joint fatigue life.

The effects of aging on the degradation of the thermal cycling reliability of lead free BGA assemblies have been studied recently by Zhang, et al. [81]. In their studies, PBGA daisy chain test assemblies were subjected to up to 2 years of aging (25, 55, 85, and

125 °C), followed by thermal cycling from -40 to 125 °C or -40 to 85 °C to failure. They have shown that for all component sizes and lead free solder alloys, the solder joint thermal cycling reliabilities of the BGA components were severely reduced by prior aging. For up to 12 months prior aging for the components with Im-Ag PCB surface finish and thermal cycling from -40 to 125 °C, they have observed clear degradation in life for aged components relative to non-aged components and the amount of degradation was exacerbated with higher aging temperatures. Using the 63.2% Weibull characteristic life (η) as a failure metric, the reliability was observed to decrease by 37% (6 months aging) and 53% (12 months aging) for the 19 mm BGA components subjected to aging at 125 °C prior to thermal cycling.

Gradual aging also occurs during thermal cycling tests due to the high temperature dwells at the top of each thermal cycle. Several recent studies [97-101] have demonstrated that there is a strong dwell time effect on thermal cycling reliability for lead free electronics; with longer dwell times leading to reductions in the thermal cycling life.

2.3 Aging Effects on Creep Properties

It has been found in the literature that aging at room temperature as well as elevated temperatures have significant effects on creep deformation of lead free solder alloys. Darveaux, et al. [92] reported a faster creep rate for aged solder specimens than non-aged specimens. For both SAC305 and SAC405 solders and for aging at 125 °C for 1 day, they found 20 times increase in the creep rate for aged specimens. Xiao, et al. [66] found that SAC396 showed much lower absolute creep rates compared with eutectic Sn-Pb and ascribed this increase in creep resistance to the finely dispersed intermetallic compound

(IMC) precipitates in the Sn matrix. Wiese, et al. [65, 102] investigated the creep behavior of SAC 387 solder with short (1 day at 125 °C) and long (49 days at 125 °C) thermal storage times. They found that the creep rate of solder increase significantly for short time aging at 125 C but relatively smaller changes occurred for longer aging times.

Ma, et al. [103] studied the evolution of secondary creep rate with aging for SAC305 and SAC405 solders. They showed that the secondary creep rates for SAC solders increase with aging at either room temperature or elevated temperature. Also, for both SAC solders exposed to elevated temperature aging, the effects were much higher than those for room temperature aging. A more detailed investigation was conducted by Zhang, et al. [86] on aging effects on the creep behavior of lead free solders. They reported that for 6 months aging at 125 °C, the secondary or steady state creep rate of SAC105 solder increased by about 10000 times. Also, for other aging temperatures (25 to 125 °C), they found that the both the primary and secondary creep rates increase with 6 months aging. Finally, Cai, et al. [51] demonstrated that by using certain types of dopants in SAC solders, the aging effects on steady state creep rate can be reduced. They showed that for no aging the creep rates of doped solders were higher than SAC105 and SAC205 due to lower silver contents of the doped solders compared to SAC105. However, with 6 months aging at temperatures 25 to 125 °C, the secondary creep rates of the doped solders were smaller than the creep rates of SAC105.

2.4 Constitutive Modeling for Solder Materials

In microelectronics packaging, complex stresses and strains are usually generated in the components due to the CTE mismatch of different materials. Solder interconnects

are usually subjected to deformations that lead to three-dimensional stress and strain states. The solder material constitutive law plays an important role in the development of thermo-mechanical models for microelectronic assemblies. Under thermo-mechanical loading, the solder material undergoes elastic and in-elastic deformations. Elastic deformations are recoverable, while inelastic deformations consist of time-independent plastic deformations and time-dependent creep deformations, which are not recoverable. Solder constitutive behavior can be represented by a combination of elastic, plastic (isotropic or kinetic hardening), and viscoplastic/creep models.

2.4.1 Constitutive Modeling for Stress-Strain Tests

The linear elastic region in a uniaxial stress-strain curve can be modeled by Hooke's law where stress and strain are related by an elastic modulus (E). The plastic strain hardening region can be modeled by a time-independent non-linear stress-strain relationship based on either isotropic or kinematic strain hardening. Isotropic hardening assumes that the origin of the von Mises yield surface remains stationary in the stress space and the size of its yield surface expands resulting from strain hardening. In kinematic hardening, the von Mises yield surface does not change in size, but the origin of the yield surface is allowed to translate in the stress space to model strain hardening effects of increasing plastic flow stress. For solder materials, the tensile stress and strain curves are dependent on the test temperature and strain rate. The elastic modulus (E), yield stress (YS) and the tensile strength (UTS) properties vary with temperature and strain rate.

For a typical thermal cycling temperature range from -40 to 125 ^{o}C, these mechanical properties reduce with the increase in temperature. The solder material has a homologous temperature from 0.5 to 0.8 for this temperature range. Also, the creep

deformation in a solder material is highly dependent on the stress and temperature state. Thus, a time-dependent elastic-plastic-creep constitutive model, or viscoplastic constitutive model, is needed to facilitate finite element modeling for simulation of solder joint reliability during thermal cycling tests. High temperatures induce transitions in macroscopic fracture, and these transitions parallel the changes in the strength and ductility of materials [104]. Materials lose strength at higher temperatures. Hertzberg stated that the material strength increases with the testing strain rate, following a form similar to Holloman's Equation [104], where stress is related to strain rate through some strain hardening exponent.

Solder alloys possess very high homologous temperatures. The properties of solder alloys are strongly dependent on both the temperature and strain rate. Jones, et al. [105, 106] have observed an approximately linear relationship between the strength and temperature. Pang, Shi and co-workers [107] have observed similar experimental results, with a near linear relationship with temperature and a power law relation with the strain rate. Several other studies have also observed similar material behavior for both Sn-Pb eutectic and lead-free solder alloys [108-111].

The Ramberg-Osgood model describes the elastic-plastic behavior of materials, and can be used to describe to describe the stress-strain curve of solder materials [112]. In prior work, the Ramberg-Osgood model hardening exponent n and the stress coefficient σ_o were modified to be temperature and strain rate dependent. The temperature and strain-rate dependent modified Ramberg-Osgood model was also applied by Pang, et al. [112].

2.4.2 Constitutive Modeling for Creep

In general, the creep behavior of materials consists of three different stages: primary creep, secondary creep, and tertiary creep. In the primary creep regime, the material undergoes strain hardening, resulting in a decreasing strain rate with time. In the secondary stage, also known as steady-state creep regime, the creep strain rate is essentially constant, showing a very slow decrease. In tertiary stage, strain rate increases with time and ultimately results in failure of the material. Solder alloys are often subjected to steady-state creep regime under typical thermo-mechanical loading conditions. Constitutive modeling of creep deformation is needed to predict the end-of-life of electronic components by using finite element analysis. A constitutive creep model is established by conducting creep tests at different temperatures and stress levels. The materials constants are important in determining the accuracy of end-of–life predictions for solder joints using finite element analysis. Large discrepancies between the creep model and experimental data would degrade the accuracy of these predictions.

The minimum creep rate may be linked with the applied stress, σ, by a series of equations according to the dominant creep mode. There are mainly three types of creep modes, namely, power law creep, exponential creep, and combination creep. Creep is highly sensitive to both applied stress level and to test temperature. As a thermally activated process, the creep rates increase exponentially with temperature. The effect of stress is dependent upon the controlling creep mechanism. The two widely used creep models are the Dorn power law model [113], and the Garofalo hyperbolic sine model [114]. In logarithmic coordinates, the Dorn power law model yields a linear relationship between the creep strain rate and applied stress for a specified temperature. Nonlinear experimental

curves for creep, however, have been found over the entire stress range. The high stress regime exhibits the largest stress exponent n, and the low stress regime exhibits the smallest n value for any given temperature. This phenomenon is referred to as "power law break down" and indicates that the Dorn model is not suitable for fitting data obtained over large stress ranges.

The Garofalo model was established for matching creep behavior at both low and high stresses. At low and medium stresses, the creep strain rate depends on stress to the power n. At high stresses, the creep strain rate is an exponential function of stress. The model is able to predict the creep deformation over intermediate temperature regimes for the entire stress range, but it underestimates the creep deformation at both low (-40 °C) and high (125 and 150 °C) temperatures.

Ma and Suhling [33] have evaluated the creep parameters in the two models for various Pb-containing and Pb-free solder alloys and found large discrepancies in the creep data for solder alloys of the same chemical composition. There are several reasons that could explain the differences, including the specimen design, variations in testing method and test conditions used by different researchers, and storage time and temperature before the creep test. Moreover, it is important to recognize that the creep behavior of bulk solder significantly differs from solder in a joint due to the effects of microstructure evolution, intermetallic compound formation, and constraint due to different methods of assembly. Since creep modeling is often to be incorporated in finite element analysis to predict the end-of-life of electronic package, the discrepancies in material constants will directly affect the accuracy of prediction.

A third widely used creep constitutive model was proposed by Weise, et al. [102], and is often referred to as the double power law. They identified two mechanisms for steady state creep deformation for the bulk and PCB samples. They attributed them to climb controlled (low stress process) and combined gliding/climbing (high stress process) behavior and represented steady state creep behavior using two power law terms. In electronic packages, thermal mismatch induced stresses can result in extensive plastic deformation at solder joints, which is responsible for the low cycle thermal fatigue failure of solder materials. An expression for the strain was proposed by Yang, et al. [100] where total strain was divided into elastic, plastic, and creep strains.

Apart from these models, several other creep constitutive models have been proposed by researchers. Shi, et al. [101] established a unified dislocation-controlled creep constitutive model that described the creep deformation of solder alloy over a wide temperature range (-40 to 150 °C) and explained the temperature dependencies of the stress exponent n and activation energy Q. For creep strain rates at very low stress levels, they further developed a unified diffusion-controlled creep constitutive model to describe low temperature Coble creep and high temperature Nabarro-Herring creep. Clech [99] established obstacle-controlled creep models for both Pb-containing and Pb-free solder alloys. Creep deformation is impeded by discrete obstacles (phases, precipitates, grain boundaries, and other defects) distributed throughout the Sn-matrix in Sn-based solders. By taking these impeding elements into consideration, the rate-dependent obstacle-controlled creep models are able to resolve the anomalies observed in the classical analysis of creep data including stress and/or temperature dependences of activation energies and stress exponents in the Power Law or Hyperbolic Sine models.

2.5 Anand Viscoplastic Constitutive Model for Solder Joint

In the electronic packaging industry, it is important to be able to make accurate predictions of board level solder joint reliability during thermal cycling exposures. The Anand viscoplastic constitutive model is often used to represent the material behavior of the solder in finite element simulations. This model is defined using nine material parameters, and the reliability prediction results are often highly sensitive to the Anand parameters. The viscoplastic constitutive equations proposed by Anand [115] have become popular for rate-dependent deformation of metals at high temperatures. The Anand model is implemented in both the ANSYS and ABAQUS commercial finite element packages. They were initially developed for structural metals, but have been adopted for microelectronic solders (Sn-Pb and lead free) for homologous temperatures in excess of $0.5T_m$. The so-called Anand model has been widely applied for the solder stress-strain relations in finite element simulations of electronic packages, where solders undergo small elastic deformations and large viscoplastic deformations. For example, Che, et al. [116] have considered multiple constitutive theories, and then demonstrated that the Anand equations were well matched with predictions of lead free solder fatigue life. In addition, Pei and coworkers [117] have calculated the nine parameters of the Anand model by conducting tensile testing of Sn3.5Ag and Sn3.8Ag0.7Cu lead free solders at several temperatures and strain rates.

Mysore, et al. [118] have found the Anand material parameters for SAC305 (Sn3.0Ag0.5Cu) lead free solder alloy by performing double lap shear tests. They suggested that the Anand parameters for solder joint samples are significantly different

than those measured by testing of bulk solder specimens. In addition, Motalab, et al. [119] have evaluated the Anand parameters for SAC305 solder using two approaches, including stress-strain testing and creep testing. Bai and coworkers [120] suggested a modified approach for SAC305 (Sn3.0Ag0.5Cu) lead free solder where strain rate and temperature dependent values were included for Anand model parameter h_o. The Anand model constants for SAC105 (Snl.0Ag0.5Cu) lead free solder have been reported by Amagai, et al. [121] and Kim, et al. [122].

2.6 Reduction of Aging Effect by Dopant

Addition of 4th element in the SAC solder is known as doped SAC alloy. Dopants play an important role to control microstructure and mechanical properties of the alloy. Dopants have been found to strongly influence the properties and behaviors of lead free solders. For example, addition of Bismuth (Bi) as a dopant has been demonstrated to have several beneficial effects. Bi helps to reduce solidification temperature, increases strength by means of precipitation hardening, and also helps to reduce IMC (Intermetallic Compound) layer thickness in lead free solder materials [123]. The Effect of Bi on the mechanical properties of a SAC (Sn3.5Ag0.9Cu) alloy was investigated by Matahir and coworkers [124]. They reported that the shear strength increased with increasing Bi addition up to 2 wt%. Beyond that point, the shear strength decreased with increasing Bi%. Improved shear strength might attribute to the role of Bi on the morphology of microstructure and distribution of dominant IMC (Ag_3Sn). Reduction of strength at higher Bi content was due to the evolution of Bi rich phase and fragmentation of the IMC.

Pandher, et al. [125] also reported that addition of 2% Bi in SAC alloys improves wetting and alloy spreading.

Zhao, et al. [126] found that addition of 0.02% Ni to SAC105 increased the formation of NiCuSn IMC and reduced the localized grain size at solder/NiAu pad interface. In addition, the effects using various doped elements (i.e. Co, Fe, In, Ni, Zn and Cu) in SAC305 BGA solder joints on Cu pads were studied by Sousa, et al. [127]. They concluded that addition of low levels of Zn had a significant beneficial effect on the interfacial IMC. Lee and coworkers [128] found that micro-alloying SAC alloys with Ni and Bi improved thermal fatigue life and drop impact resistance. Yeung, et al. [129] studied a novel lead-free solder SAC_Q. Based on drop test, thermal cycling, and finite element simulation, they conclude that the doped alloy has improved board level reliability when compared to SAC105. Additional literature publications on the effects of dopants have been reviewed in reference [51].

Sun et. al. [130]reviewed the effects of different alloying elements (Mn, Fe, Bi, Ni, In, Zn, Ga, Sb, Mg), Rear Earth (RE) Elements (Ce, La, Y, Er, Pr, Nd, Yb), and nanoparticles (Al_2O_3, Al, TiO_2, ZnO, ZrO_2, CNT, Graphene, CeO_2, TiB_2, Ni-Coated CNT, Mo, SiC, $SrTiO_3$, Co) on melting temperature, wettability, mechanical properties, microstructure, interfacial reaction and Sn whiskers.

For SAC305 solder, average width of eutectic region was found as 6.8±2.8 μm and grain size of β-Sn was 24.8±5.9 μm. Indium (In), helps to refine IMC and Sn-rich phase as well as makes the microstructure more uniform. Titanium (Ti) can significantly reduce Sn grain size and width of eutectic region by heterogeneous nucleation of IMC's. Iron (Fe) forms large $FeSn_2$ IMC which has a weak interface with β-Sn matrix. Magnesium (Mg)

helps to coarsen eutectic region. Addition of Al in SAC105 refines β-Sn dendrites and enlarge eutectic regions. Besides, it also prevent Ag_3Sn and Cu_6Sn_5 and forms two new IMC Ag_3Al and Al_2Cu. Zn also helps to refine β-Sn dendrites significantly. Ni was found to reduce the size of Sn-rich phase and refine the microstructure. Since Antimony (Sb) has higher affinity towards Sn, presence of Sb reduces the driving force to form Cu-Sn IMC's resulting a narrow IMC layer in the solder joint. Sb also helps to refine IMC grain size.

RE elements can significantly refine the microstructure of SAC solders. Er can reduces the particle size of Ag_3Sn and Cu_6Sn_5 whereas Pr and Nd refine β-Sn dendrites and IMC particle size by forming uniformly dispersed fine $RESn_3$. These fine particles act as heterogeneous nucleation sites during solidification. However, excessive amount of RE elements will cause to form bulk $RESn_3$ phase which has a negative effect on mechanical properties. La, Ce, and Y also have a similar effect on solder microstructure.

Al and Ni nanoparticle was found to reduce IMC particle size, spacing and IMC layer thickness by forming very fine and uniformly dispersed Sn-Ni-Cu and Sn-Sg-Al IMCs. Addition of small amount of Fe nanoparticles refine the microstructure and forms $FeSn_2$ phase. Al_2O_3 nanoparticles increase the size of eutectic region and reduce Ag_3Sn particle size. TiO_2 and SiC nanoparticle reduces the size and spacing between Ag_3Sn particles. $SrTiO_3$ nanoparticle reduces the size of Ag_3Sn and Cu_6Sn_5 particles by promoting the rate of nucleation during solidification. ZnO suppresses Ag_3Sn and Cu_6Sn_5 IMC formation and reduces β-Sn grain size by 22%.

The Effect of dopants on the aging induced changes in microstructure was also studies by a number of scientists. Sadiq et al. [131] worked with different Lanthanum (La) doped SAC305 alloys and recorded the changes in microstructure and mechanical

properties during isothermal aging at 150 °C for 6 different aging conditions (i.e. 0 , 10, 25, 50, 100 and 200 hours). They reported that La drastically reduces the IMC particle size and also significantly inhibit the growth of IMC particles during isothermal aging. Based on polarized light image they found that in as cast condition, grain size of SAC305 was ~8 mm and was significantly reduced (~1 mm) after La addition. From the graph presented in that paper, it is also clear that aging doesn't have any significant influence in average grain size.

In another study, Lee et al. [132] studied the effect of Lanthanum (La) addition and high temperature storage on the microstructure and microhardness of Sn-3.5Ag solder joints. Their experimental results confirms that addition of La refine the solder microstructure. They explained that during solidification of the solder, $LaSn_3$ compounds form at the beginning and provide extra nucleation sites for Ag_3Sn IMC to grow resulting a refine microstructure. Addition of La was also found to reduce the thickness of IMC layer after soldering as well as isothermal aging. They also reported that La addition helps to improve microhardness and thermal resistance of solder joints.

Hao et al. [133] studied the effects rare earth element Er addition on the evolution of microstructure of lead free eutectic SAC (Sn-3.8Ag-0.7Cu) solder joints during isothermal aging. Aging was conducted at 170 °C for 4 different holding periods (i.e. 0, 200, 500 and 1000 hours). The authors measured the thickness of IMC layer of Sn-3.8Ag-0.7Cu and Sn-3.8Ag-0.7Cu-0.15Er alloy after different aging duration. They found that Er addition reduces the thickness of IMC layer in as reflowed condition and also significantly reduces the growth during aging. They argued that Er combines with Sn to form $ErSn_3$ IMC and reduces the activity of Sn which subsequently suppress the formation of Cu_6Sn_5

IMC layer. They also observed that $ErSn_3$ IMCs formed during solidification of solder act as a heterogeneous nucleation site for Ag_3Sn and Cu_6Sn_5 precipitates. The increase in nucleation sites results a refinement of Ag_3Sn and Cu_6Sn_5 particles. Addition of Er also found to make the microstructure more uniform and reduce the coarsening rate of the IMCs during isothermal aging.

Witkin [134] and Delhaise et al. [135] studied the effect of aging of Bi doped SAC alloys. In both study, the authors reported an elimination or at least reduction of aging induced degradation in SAC-Bi alloys.

2.7 Nanoindentation Tests on SAC Solder Joints

Most prior work on solder mechanical behavior and aging effects has involved tension, compression, and shear testing of miniature bulk solder specimens. Sample geometries have included traditional uniaxial tensile specimens, small cylinders in compression, lap shear specimens, and Iosipescu shear specimens. A more limited number of researchers have examined aging effects by mechanical loading of solder joints [57, 64, 65, 92]. These studies have involved shearing of custom fabricated solder ball arrays [64, 65, 92], as well as impression creep experiments [57].

Nanoindentation techniques [40] have recently become popular for measuring mechanical properties and creep deformation behavior of extremely small material samples, and several investigators [75, 136-148] have applied them to lead free solders. Early solder nanoindentation studies included room temperature measurements of the elastic modulus E and hardness H of β-Sn dendrites, eutectic phases, and individual Ag_3Sn and Cu_6Sn_5 intermetallic compounds [136, 137, 146, 148]. Hasnine et al. [75, 140-142],

have examined aging effects in SAC solder joints extracted from PBGA assemblies using nanoindentation. Their results showed that the aging induced degradations of the room temperature mechanical properties (modulus, hardness) of single grain SAC joints were of similar magnitudes to those seen previously by testing of larger "bulk" solder specimens with hundreds of grains. However, the degradation of the creep response, while still significant (15-100X increase), was less in the solder joints relative to larger uniaxial tensile specimens (200-7500X increase). This was due to the single grain nature of the joints considered, and the lack of the grain boundary sliding creep mechanism. They also tested very small tensile specimens (10 mm long) with 10-20 grains, and the creep degradation results were similar to the single joint specimens.

Knowledge of elevated temperature behavior, especially creep behavior, is critical to understanding solder joint reliability in thermal cycling and accelerated life testing. Elevated temperature nanoindentation measurements of modulus and hardness of bulk SAC305 and SAC357 solder samples were performed by Gao, et al. [138], and Han and coworkers [139]. In addition, the latter authors also examined the sensitivity of the creep response of lead free solder to temperature. Sadiq, et al. [147]have investigated the nanoindentation elastic modulus and hardness of β-Sn and eutectic phases within a SAC305 solder joint at temperatures ranging from 45-85 °C. Another solder nanoindentation study over a larger temperature range (25-150 °C) was performed by Lotfian, et al. [143], where they reported the mechanical properties of the constituent phases of SAC397 solder joints. Marques, et al. [144, 145] used nanoindentation to study mechanical properties and creep behavior of SAC305 solder joints over a wide temperature

range (25-175 °C). Based on finite element simulations, they also developed a method to correlate nanoindentation creep results with uniaxial creep data.

Nanoindentation pile-up, defined by an uplift of material near the edges of an indent, is often observed in testing of solders [136, 137, 143, 147, 148]. Pile-up depends significantly on the work hardening ability of the material [149]. For a material that easily work hardens, the top surface near the indent will be hardened during the deformation and thus will prevent pile up by resisting upward flow of the material. Prior researchers have used different techniques to include the pile-up area in their measurement. Kese, et al. [150] proposed a semi ellipse method for pile up correction, which was based on the assumption that the pile-up contact area had a semi-elliptical shape. While some researchers [147, 148, 151] have used the Kese, et al. method, others [137] have used FEA simulations to guide pile-up corrections.

2.8 Effects of Aging on the Microstructure of Solder

Due to their low melting temperatures, solders are exposed to high homologous temperatures in most product applications. Thus, there is a continuous state of active diffusion processes in the solder alloys, and their microstructures are inherently unstable and will continually evolve during normal operating temperature conditions of electronic packaging assemblies. High temperature storage, which is also known as isothermal aging, of the solder alloys causes a significant change in the microstructure leading to a degradation of mechanical properties. Chou [152] studied the effect of isothermal aging on microstructure of Sn-Pb and lead free SAC solder joints. He reported a significant phase coalescence of eutectic Sn-Pb solder joint after aging.

Xu et al. [61] measured the thickness of IMC layer of different Sn-Pb alloys with different surface finishes after isothermal and thermal cycling aging. Based on their experimental results they had proposed an integrated model to predict the IMC layer growth under different isothermal aging and thermal cycling environment.

Ubachs et al. [153] developed a model to predict microstructural evolution during isothermal aging of Sn-Pb alloy by numerical simulation. They focused their study on a fixed region and compared experimental observation of phase growth during isothermal aging at 150 °C, for 0 to 15 hours, with the predicted phase growth by simulation.

In recent days, electronic industries are moving towards lead free solders due to the growing concern about environment. Effect of aging in lead free solder is even more significant. Sahaym et al. [154] examined the evolution of microstructure of bulk SAC105 and SAC305 solder during isothermal aging at 150 °C. They observed the changes of identical region after 4 different aging durations (0, 110, 194, and 310 hours). In as reflowed condition, they found that the microstructure is consisted of several pro-eutectic colonies of β-Sn grains surrounded by eutectic regions. Most of the grains in a pro-eutectic colony has low angle ($<15^{o}$) boundaries with the neighboring grains. They reported that after 310 hours of aging, the average size of IMC precipitates has increased from 0.35 μm to 2.5 μm and the average grain size has increase from 4.5 μm to 7.5 μm.

The authors also observed that a small percentage (~10%) of β-Sn grains, especially those near the eutectic region, has went through recrystallization during isothermal aging. They claimed the stress on the β-Sn grains, due to the growth of IMC particle, is responsible for the recrystallization. The extent of recrystallization was less in SAC105 than in SAC305 due to the relative difference in IMC volume fraction. Although not mentioned

clearly in the text, it is evident from their graph that the number of high angle grain boundary has been reduced and low angle grain boundary has been increased after aging for 100 hours.

Maleki et al. [155] studied the evolution of microstructure of SAC405 and pure Sn during isothermal aging at 150 °C after 144 hours and 296 hours. They also performed Mechanical testing (shear test) to correlate changes in microstructure and mechanical properties. Sample size was approximately 1 × 0.3 × 0.3 mm and it was attached to Cu-pad. They reported that in as-reflowed condition, the microstructure of SAC405 was consisted of ~70 vol% of eutectic phase and ~30 vol% of β-Sn dendrite, whereas the mean diameter of IMC particles and interparticle distance was ~250nm and ~630 nm, respectively. Average particle size increases with aging time due to Ostwald ripening. During IMC growth, they attributed bulk diffusion to be the main rate controlling mechanism. On the other hand, aspect ratio decreases and interparticle spacing increases with aging due to the driving force to reduce surface energy. Electron backscatter diffraction (EBSD) analysis confirmed the presence of large grains (~200 μm) in SAC405 solder before aging. After 296 hours of aging at 150 °C they didn't find any significant change in grain size and orientation. On the other hand, pure tin has a fine grain (~10 μm) microstructure before aging which grows significantly during aging and become ~200 μm after aging. They attributed the reduction of mechanical properties during aging for SAC 405 to the IMC's coarsening whereas for pure Sn to the grain coarsening.

Telang et al. [156] worked on the effects of aging at 150 °C on microstructure, especially grain size and grain-boundary misorientation, of several alloys including Pure Sn (ingot and reflowed), Eutectic Sn-3.5Ag (ingot), Eutectic Sn-3.8Ag-0.7Cu (ingot), Sn-

1.6Ag (solder ball), Sn-3.0Ag (solder ball), and Sn-3.0Ag-0.6Cu (solder ball). For Sn-3.5Ag alloy they studied three different aging conditions (i.e. 0, 200, and 400 hours.) whereas for rest of the alloys they studied two different aging conditions (i.e. 0. and 200 hours). Before aging, grain size of pure Sn ingot and Reflowed Pure Sn was 50-150 μm (equiaxed) and 100-250 μm (equiaxed), respectively. After aging for 200 hours, the grain size of pure Sn for both condition was >500 μm with irregular shape. They found ledges, in SEM image, along the grain boundary (confirmed by polarized light microscopy) of sample after aging. According to the authors, these ledges were formed due to anisotropic nature of thermal expansion coefficient (CTE) of Sn grain. After aging, when the sample was taken out from the oven, different grains contracted with different magnitudes leading to the ledges. They also argued that the extent of contraction depends on the size and the orientation of the grain. Before aging, the sample had smaller grain size. As a result, when the sample was kept inside the oven, difference in expansion of different grains was relatively small. This resulted small ledges along the grains of as reflowed sample. Although the grain boundaries moved during the aging process, these ledges were retained throughout the experiment.

After comparing the microstructure of eutectic Sn-Ag (3.5% Ag) ingot with pure Sn ingot, they found that Sn-Ag alloy has a much finer (10-30 μm) grain size, which was very stable. Aging of Ag-Sn alloy did not cause any significant grain growth due to the pinning effect of Ag_3Sn IMC particles. On the other hand, the grain size of SAC (Sn-3.8Ag-0.7Cu) ingot was similar to that of Sn-Ag ingot (10-30 μm). But, aging for 200 hours caused a significant growth in the grain size (~120 μm) of the alloy. Although not stated clearly in the text, it is evident from the misorientation histogram that the extent of

misorientation, among the grains, for the both alloys decrease with increasing aging time. From their experimental observations the authors also have discussed the effect of Ag and Cu on preferred grain orientation and grain size.

Allen et al. [70] studied two near eutectic lead free SAC solders (bulk Sn-3.5Ag-0.9Cu and SAC405 joint). They used 3 different aging temperatures (152, 177, and 201 °C) and 5 different aging durations (0, 1, 2, 4, and 8 weeks). They measured the density of IMC particle after different aging conditions and based on their experimental results they conclude that the rate controlling mechanism for coarsening is volume diffusion (n=3). They also reported that the coarsening kinetics of eutectic SAC solder is slower than that of eutectic Sn-Pb solders.

Kumar et al. [157] worked with SAC105 and SAC305 alloys. For isothermal aging experiments, they polished a bulk reflowed solder samples and then aged the samples at 150 °C in high vacuum (to prevent oxidation). After different aging intervals (i.e. 0, 110, 194, 220, and 330 hours) they captured the SEM image of the same region, of any particular sample, to quantify the coarsening behavior of the IMC's. They found that the growth rate of Cu_6Sn_5 particles are much faster than Ag_3Sn particles, due to the higher diffusivity of Cu than Ag in Sn matrix. Besides, the fraction of Ag_3Sn particles was significantly higher than Cu_6Sn_5 particles. Hence, they decided to focus their study on the coarsening of Ag_3Sn particles only. The authors introduced a new parameter named as explicit parameter '$C_{Ag}D_{Ag}t/T$', where C_{Ag} and D_{Ag} are solubility and diffusivity of Ag in Sn matrix, respectively, to capture the thermomechanical history of a lead free solder during isothermal aging. Utilizing this parameter, they predicted coarsening rate of Ag_3Sn particles, during isothermal aging, and then compared with the experimental observations.

They conclude that the model could efficiently measure thermomechanical history during isothermal aging and thermomechanical cycling (TMC) below 200 cycles. After 200 cycles the IMC particles undergo dissolution and re-precipitation/redistribution which can't be captured properly by this model. In addition to coarsening, during isothermal aging, they also had observed recrystallization near the eutectic region. They explained that the growth of IMC particles might play an important role in recrystallization.

Besides bulk solder samples, researchers have also explored the effect of aging on the actual solder joints. Chauhan et al. [158] monitored the effect of isothermal aging at 100 ^{o}C on phase coarsening and evolution of SAC305 solder joint. They used image processing software to quantify size, interparticle spacing and volume fraction of Ag_3Sn and Cu_6Sn_5 IMC's. Impact of these changes on secondary creep response was modeled using multiscale creep model. The authors performed their experiments in 4 different aging conditions (0, 24, 600, and 1000 hours.) and presented average results of 3 samples (solder joint) for each aging condition. They found that the size of Ag_3Sn increases monotonically with increasing aging time whereas the size of Cu_6Sn_5 decreased after 600 hours of aging. They didn't find any significant change in Sn grain morphology after 1000 hours (41 days) of aging.

Yang et al. [159] prepared solder joints using 2 different soldering methods (laser and infrared soldering) and captured the evolution of microstructure during aging up to 190 ^{o}C for times up to 300 days. They reported that the evolution is consisted of the growth of IMC's and the Cu-Sn layer near the interface. Although they had studied two different initial microstructure, obtained from 2 different soldering methods, aging at 190 ^{o}C caused the final microstructures to be the same.

Chiu et al. [160] examined the effect of aging time and temperature on the board level reliability during the drop test of lead free SAC solder joints. They reported that kirkendall void formation, at the interface of Cu pad and Cu_3Sn IMC, is the main reason for getting lower drop reliability during drop test.

Fix et al. [79] explored the effect of aging time (0 to 1000 hours) and temperatures (125 to 175 °C) on the microstructure of SAC405 solder joint. They have confirmed a significant growth of Ag_3Sn and Cu_6Sn_5 IMCs with aging time. The authors modeled phase growth based on Ostwald ripening mechanism. They conclude that a growth exponent n = 3, which indicated volume diffusion as the growth rate controlling mechanism, matches very well with the experimental growth rate data.

The effect of aging at 150 °C on the evolution of eutectic Sn-Ag solder joint for up to 800 hours was studied by Ahat et al. [161]. From experimental results, they conclude that the thickness of IMC layer increases linearly with square root of aging time. Choi et al. [162] investigated the effect of different soldering and aging time on the interface layer of Sn-3.5Ag solder and Cu substrate. They used the same solder joint to age at 130 °C for different time duration up to 800 hours They found that thickness of IMC layer continue to grow with increasing aging duration. However, the growth behavior of IMC layer during aging strongly depends on the initial morphology and hence on the soldering time.

Akhtar et al. [163] studied the evolution of microstructure near the interface of a solder joint during isothermal aging at 150 °C, for four different aging duration (0, 250, 500, and 1000 hours). They used SAC305 solder joint (ball diameter 500 μm) with two different surface finish (Immersion Gold (ImAu) and Immersion Tin (Sn)). Image analysis software ImageJ was used to measure the thickness of the IMC layer. They also calculated

the activation energy based on the measured thickness data. They found that the thickness of the IMC layer increases with increasing aging time. Besides, the morphology of the IMC layer, for both surface finishes, change from scallop type to layer type after the aging treatment. Based on their calculations they found that the activation energy of SAC305/ImSn system was less than SAC305/ImAu system resulting a higher IMC layer growth rate in SAC305/ImSn system.

A comparative study was performed by Berthou et al. [164] where the authors compared the failure mechanism of BGA packages with SAC305 solder joints subjected to two different conditions: (a) accelerated thermal cycling (ATC) between -55 to 125 °C and (b) thermal storage at 80, 125, and 150 °C for 1000 hours. During ATC, they found recrystallization of big Sn grains to small grains in the regions of high stress accumulation. Cracks initiates and grows at interface of the new recrystallized grains. On the other hand, thermal storage for 1000 hours caused a significant growth of IMC layer near the interface as well as the IMCs in the bulk. They didn't reported any recrystallization after thermal storage.

2.9 Finite Element Modeling of Solder Joint Reliability

In order to make faster, cheaper, and more reliable electronic products, it is very important for the packages to be evaluated at early design stages by simulation tools. Solder joint reliability models based on actual test data, accurate constitutive modeling, dominant damage mechanisms, and appropriate simulation, are needed to perform this task. Electronic packages often undergo thermal and/or power cycling conditions throughout their service life. CTE mismatch induced stresses/strains are the root cause of most solder

joint failures. Solder joints fail mostly due to the fatigue caused by the thermal or power cycling operations. The procedure of reliability modeling can be divided in two major steps:

(1) Finite element modeling to predict stresses, strains, and deformations of the solder joints during thermal cycling. The required output parameters (e.g. plastic strain or energy density per cycle) are extracted by post-processing the finite element analysis results.

(2) Application of a solder life prediction model to the output parameters of the finite element analysis to calculate the number of cycles until failure of the solder joint. The material constants in the life prediction model for the solder need to be evaluated from the experimental crack growth data for components having similar geometric form factors.

Syed [185] has used double power law and hyperbolic sine creep equations to predict the reliability of solder joints in BGA assemblies. He showed that failure criteria based on accumulated strains and dissipated energy density per cycle can provide good predictions of the measured mean life of solder joints. In addition, it was demonstrated that the energy density approach better captures low temperatures and high stress effects than the accumulated creep strain approach. Schubert, et al. [186] have presented thermo-mechanical analyses that predicted the life of solder joints in flip chip on board (FCOB) and PBGA assemblies for both SnPb and SnAgCu solders. They have also used double power law and hyperbolic sine creep constitutive equations, as well as accumulated creep strain and strain energy density methods for the fatigue life models. Both fatigue models

were found to fit their experimental failure data reasonably well. Also, SAC solders were shown to perform poorer for stiffer components and higher strain levels.

Zahn [187] used a volume average energy density method to predict the life of 63Sn37Pb and SAC405 solder joints. He also explored model simplifications based on symmetry, and found that one-eighth models are the smallest that can yield correct results, and that diagonal slice symmetry models yield different accumulated energy per cycle values than the true three-dimensional case.

Lee and coworkers [188] have classified solder fatigue models into five categories: stress based, plastic strain based, creep strain based, energy based, and damage based. Other methods have been classified as empirical models. They have shown a general procedure to choose an appropriate fatigue model based on the package conditions and limited finite element analysis times. They identified 14 models in the literature, which were developed based upon various assumptions, including the manner in which the physical and metallurgical aspects of fatigue are taken into account. The characteristics of the 14 identified fatigue models are presented in Table 2.1.

Table 2.1 Summary of Solder Joint Fatigue Models [186]

Fatigue Model	Model Class	Parameters	Coverage	Applicability
Coffin-Manson	Plastic strain	Plastic strain	Low cycle fatigue	All
Total Strain	Plastic + elastic strain	Strain range	High and low cycle fatigue	All
Solomon	Plastic shear strain	Plastic shear strain	Low cycle fatigue	All
Engelmaier	Total shear strain	Total shear strain	Low cycle fatigue	Leaded & leadless, TSOP
Miner	Superposition (plastic and creep)	Plastic failure & creep failure	Plastic shear and matrix creep	PQFP, FCOB
Knecht & Fox	Matrix creep	Matrix creep shear strain	Matrix creep only	All
Syed	Accumulation of creep strain energy	gbs energy and mc energy	Implies all coverage	PBGA, SMD, NSMD
Dasgupta	Total strain energy	Energy	Joint geometry accounted for	LLCC, TSOP
Liang	Stress/strain energy density based	Energy	Constants from isothermal low cycle fatigue tests	BGA and leadless joints
Heinrich	Energy density based	Energy	Hysteresis curve	BGA
Darveaux	Energy density based	Damage + energy	Hysteresis curve	PBGA, leadless
Pan	Strain energy density	Strain energy density and plastic energy density	Hysteresis curve	LCCC
Stolkarts	Damage accumulation	Damage	Hysteresis curve & damage evolution	All
Norris & Landzberg	Temperature and frequency	Temperature frequency	Test condition vs. use conditions	All

Ridout, et al [189] have classified the methods of calculating solder cycles to failure into three categories, analytical methods, combined constitutive law and fatigue methods, and damage mechanics methods (Figure 2.1). They have reported that the constitutive law and fatigue law class of methods (encompassing FEA and other alternatives) are very popular, providing more accurate predictions with fewer restrictions than analytical methods. However, they have with increased set up time and computational cost. The damage mechanics based methods require considerably more effort both in implementation and computational cost and their predictive capability is unproven.

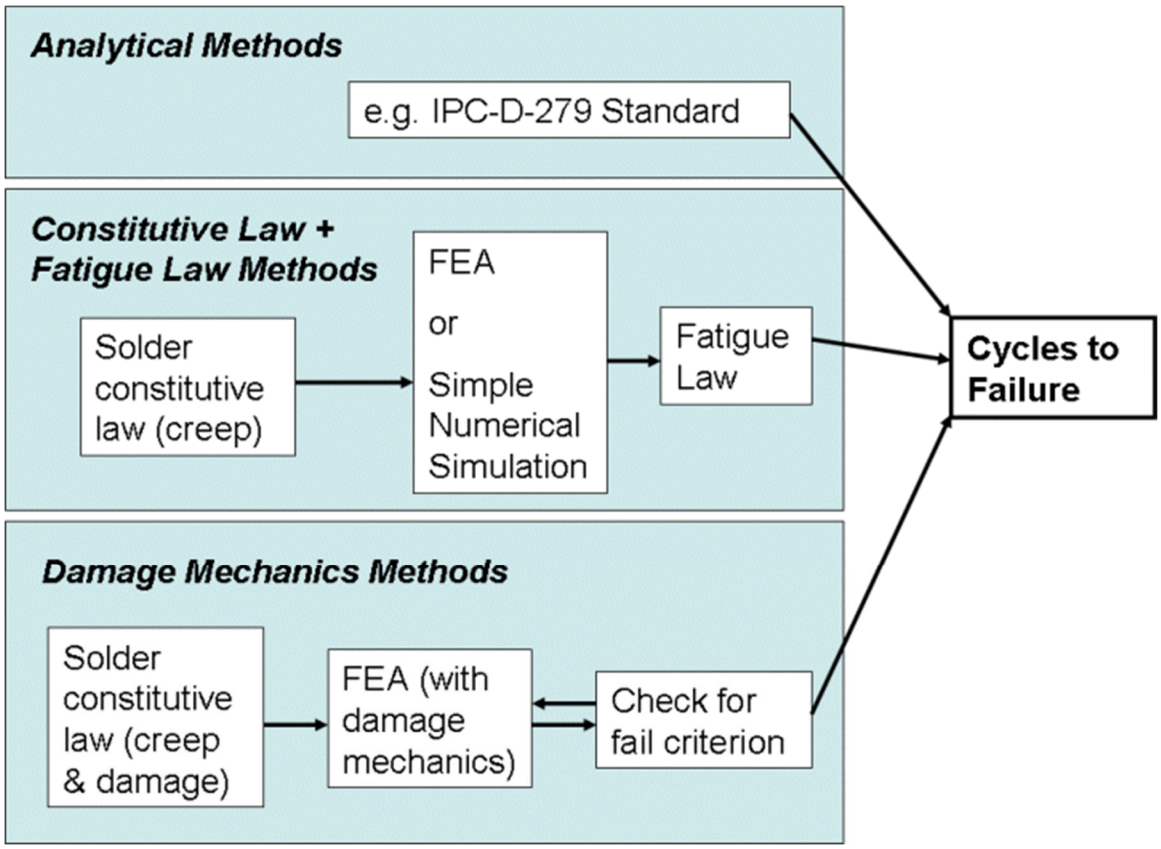

Figure 2.1 Modeling Methods to Calculate the Cycles to Failure [189]

A damage mechanics based fatigue life model has been presented by Tang and Basaran [142]. They have coupled an internal damage variable with a unified viscoplastic model to characterize the response of solder alloys. Gustafsson, et al. [143] have used the

volume average energy method to predict the life of BGA solder joints and have shown that a linear global model with a nonlinear submodel drastically overestimates the life in comparison with the nonlinear global models.

Pang, et al. [192] have predicted flip chip solder joint reliability by using dwell creep (creep during dwell times) and full creep (creep during the whole analysis) methods. They have shown that the dwell creep method predicts much longer fatigue life of the solder joints than the full creep method. Shnawah, et al. [193] have studied the thermal cycling and drop impact reliability of SAC solder joints. A significant thermal cycling performance improvement was found for assemblies made from SAC305/SAC405 solders relative to those assembled with lower silver content SAC105 solder. Liu, et al. [194] have used finite element analysis to examine pad design and found that the fatigue lifetime of BGA solder joints with dent pad OSP surface finish is 25% lower than that for flat pad Ni/Au surface finish. Thermal cycling reliability of a BGA SiP has been investigated by Yu, et al. [195]. They have found that the failure position changed relative to conventional BGA packages. Vasudevan and Fan [196] have incorporated acceleration terms into conventional fatigue models to examine the effects of thermal cycling range and frequency.

Darveaux [197] has presented energy dissipation based models for crack initiation and crack growth rate in solder joints. These types of models have been subsequently used by many researchers for life prediction of the SnPb and SAC solders. The four constants in the failure models are determined by curve fitting using the experimental failure data, where the energy dissipation per cycle is found from FEA simulations.

2.10 Summary

In this chapter, the theoretical background behind the motivation of this work has been discussed briefly. A number of existing literature on the effects of aging on the mechanical properties and the microstructure of lead free solder was extensively discussed here. The mechanical properties of a solder are strongly influenced by its microstructure, which is controlled by its thermal history including its solidification rate and thermal exposures after solidification. Isothermal aging has been found detrimental to the mechanical properties and the reliability of lead free solder materials. The dramatic changes in the material properties, constitutive and failure behavior of bulk solder materials as well as solder joints have been reported in the literature. For example, research in the literature has shown that aging leads to large reductions in solder material properties including shear strength, elastic modulus, nanoindentation joint modulus and hardness, high strain rate mechanical behavior, creep response, and Anand model parameters. Other studies have shown that aging causes severe degradations in uniaxial cyclic stress-strain curves and fatigue life, shear cyclic stress-strain curves and fatigue life, fracture behavior, drop reliability, and thermal cycling reliability.

In a large number of literatures, dopants have been found to strongly influence the properties and behaviors of lead free solders. For Example, Bi helps to reduce solidification temperature, increases strength by means of precipitation hardening, helps to reduce IMC (Intermetallic Compound) layer thickness, and also reduce aging induced degradation of mechanical properties in lead free solder materials. Ni helps to improve thermal fatigue life and drop test performance by refining Sn grain size and reducing the

IMC layer formation near the Cu pad. The effects of rear earth (RE) elements and nanoparticle addition on the properties of lead free solder was also discussed in this chapter.

As a relatively newer tool, nanoindentation methods have shown great potential for characterizing solder materials and aging effects at the joint scale. Nanoindentation is mainly used to extract elastic modulus and hardness of solder joints. Some of the prior works have also used nanoindentation technique to characterize the creep properties although most of the nanoindentation experiments, on solder joints, were conducted at room temperature.

The changes in solder mechanical behavior are a result of the evolution of the SAC solder microstructure that occurs during aging. The most well-known and widely observed changes are coarsening of the Ag_3Sn and Cu_6Sn_5 intermetallic compounds (IMCs) present in the eutectic regions between beta-Sn dendrites. Several researchers have proposed empirical models to describe the growth of these secondary phase particles as a function of aging temperature and aging time, and related this growth to mechanical property changes.

Traditional finite element based predictions for solder joint reliability during thermal cycling accelerated life testing are based on solder constitutive equations (e.g. Anand viscoplastic model) and failure models (e.g. energy dissipation per cycle model) that do not evolve with material aging. Thus, there will be significant errors in the calculations with lead free SAC alloys that illustrate dramatic aging phenomena. A modification in finite element modeling approach is thus necessary incorporating temperature and rate dependent mechanical properties and effects of isothermal aging.

CHAPTER 3

EXPERIMENTAL PROCEDURE, DATA PROCESSING AND CONSTITUTIVE MODELING

3.1 Introduction

In this chapter, a novel specimen preparation technique is presented for mechanical testing. Micro-scale uniaxial tensile specimens were prepared in a rectangular shaped hollow glass tube using a vacuum suction method. The test specimens were then cooled either by a water quenched profile or an industry standard SMT reflow profile. Typical dimension of the uniaxial tensile specimens were 80 (length) ×3 (width) ×0.5 (height) mm. Strain gage mounting technology has been used to mount gages in the prepared rectangular sample to measure the Poisson's ratio. Uniaxial tensile tests were performed using a micro tension torsion testing system. Empirical constitutive model was adopted to represent the collected raw data and to extract the desired mechanical properties of different SAC and SAC+X lead free solder materials. The Anand viscoplastic constitutive model is the most widely used material model build in many popular finite element analysis codes like ANSYS and ABAQUS. It has nine parameters which are typically determined from uniaxial stress-strain tests at several strain rates and temperatures using a multistep parameter determination procedure presented in following sections.

For microstructural and nanoindentation study of solder joints, SAC305BGA joints were extracted from 14 x 14 mm PBGA assemblies (0.8 mm ball pitch, 0.46 mm ball diameter) that are part of the iNEMI Characterization of Pb-Free Alloy Alternatives Project. After extraction, a typical sample mounting and polishing procedure was followed to make the solder joints suitable for scanning electron microscopy and nanoindentation tests. For nanoindentation study, only single grain solder joints were used as the properties of SAC solder joints are highly dependent on crystal orientation. Polarized light microscopy techniques was utilized to determine the orientation of the tested joints.

3.2 Uniaxial Test Sample Preparation

Use of a bulk solder bars is undesirable, because they will have significantly different microstructures than those present in the small solder joints used in microelectronics assembly. In addition, machining can develop internal/residual stresses in the specimen. The unique technique developed here is able to make micro-scale uniaxial tensile specimens with no requirement of further machining/cutting. First of all, bulk solder material was sliced using a shear cutter and then melted in a quartz crucible using circular heating elements (see Figure 3.1). The heater in the melting process is excited using a digital controller, which uses feedback from a thermocouple attached on the crucible. The solder is drawn into the glass tube by inserting one end into the molten solder in the crucible, and then applying suction to the other end using a rubber tube connected to a vacuum source. The amount of solder drawn into the tube is controlled using a regulator on the vacuum line. After the desired amount of solder fills the tube, it is solidified by quenching in a room temperature water bath.

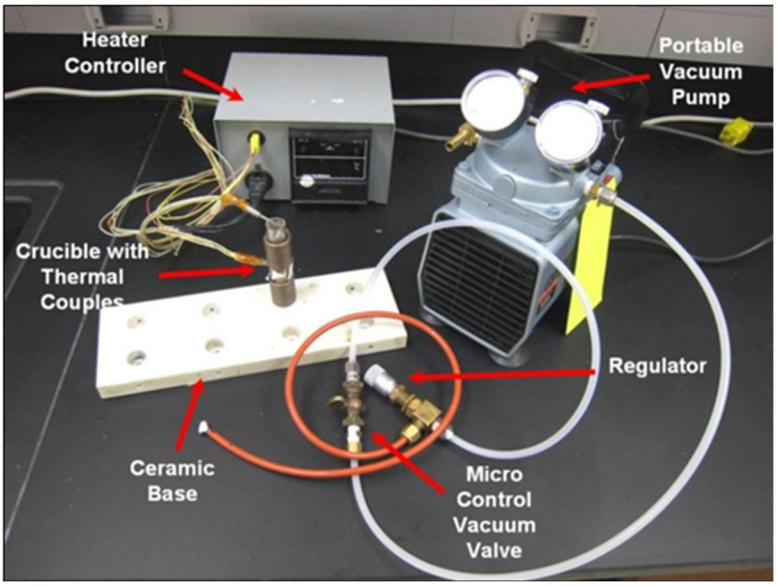

Figure 3.1 Equipment used for Specimen Preparation

Solidification was done using following two profiles that produced two different microstructures:

1) Water quenched (WQ) microstructure: Here the solidification/cooling rate was faster, almost instantaneous from melting to room temperature. This process generated fine microstructures and resulting the upper limits of the mechanical properties for each SAC and SAC+X alloy. The temperature vs. time variations for the WQ profile is shown in Figure 3.2.
2) Reflowed (RF) microstructure: Here the solidification/cooling was sequential as the WQ tubes were sent through a 9 zone Heller 1800EXL SMT reflow oven (Figure 3.3) to re-melt the solder in the tubes and subject them to the desired temperature profile (i.e. same as actual solder joints). This process generated a coarse microstructure very similar to an actual solder joints. The reflow temperature profile used in this study is presented in Figure 3.4.

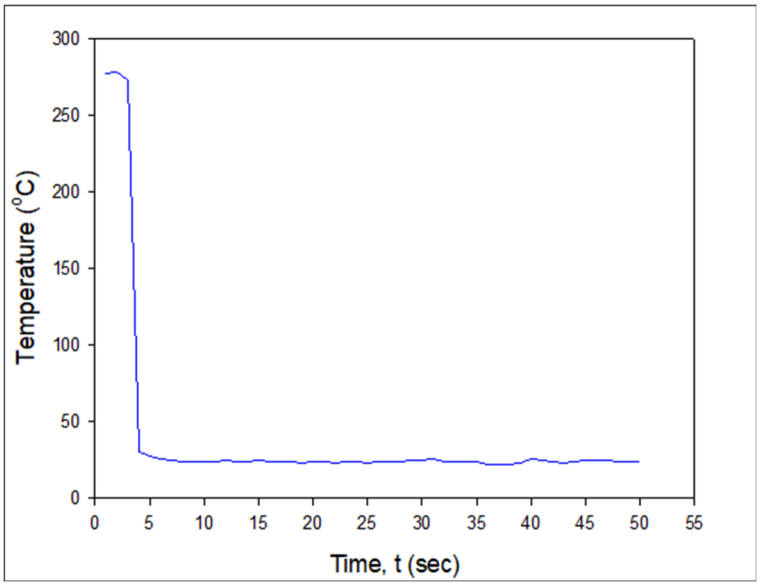

Figure 3.2 Water Quenched (WQ) Cooling Profiles

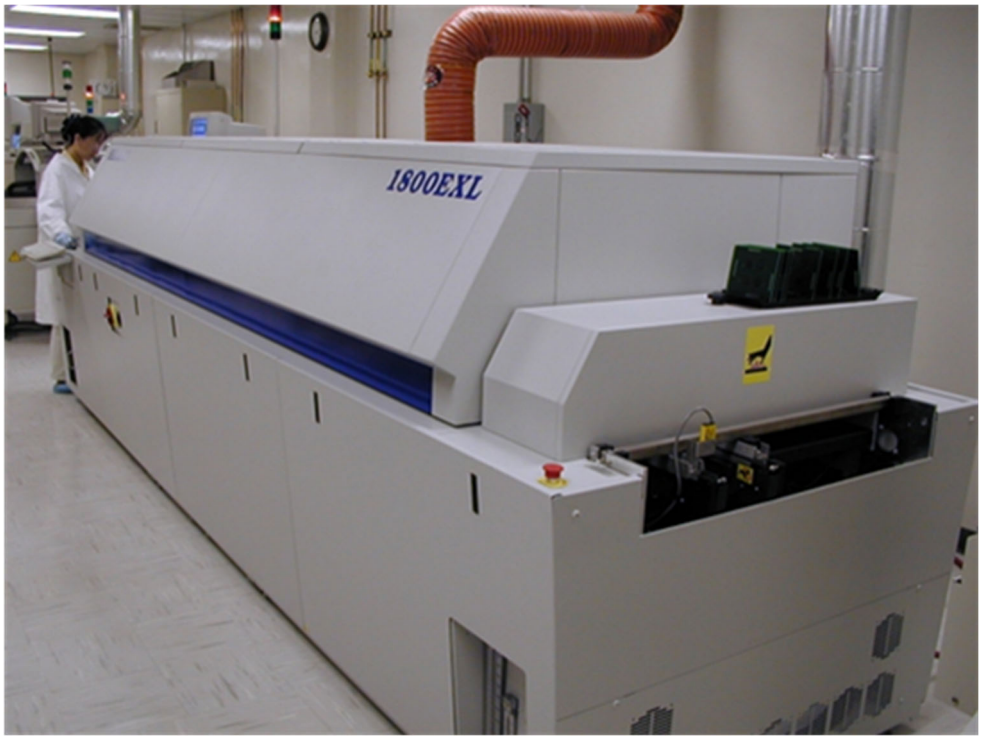

Figure 3.3 Heller 1800EXL Reflow Oven

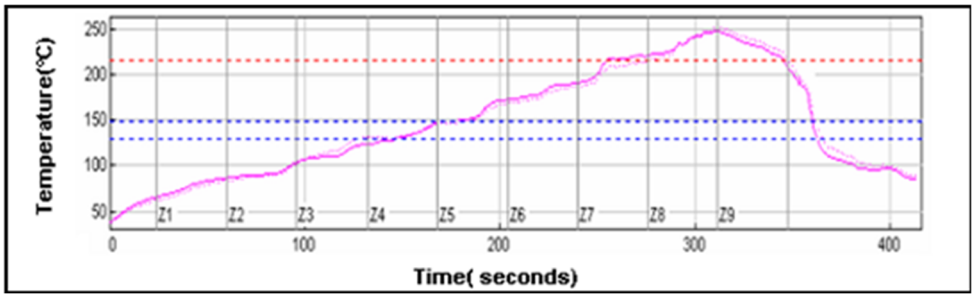

Figure 3.4 Reflow (RF) Cooling Profiles

A typical glass tubes filled with solder and final solder samples after extraction from the glass tubes are shown in Figure 3.5. The rectangular solder sample can be extracted from the glass tubes by a number of ways. Such as:

1) Using the CTE mismatch: Glass has lower coefficient of thermal expansion (CTE) compared to solder. As a result, for some solder alloy and cooling rate combinations, solidified solder samples were easily pulled out from the glass tube due to the difference is the CTE of glass and solder.
2) Breaking the glass tube: Another way followed to extract the solder sample from the glass tube is by carefully breaking the glass.

The dimensions of tubes in this work had a length of 120 mm, and a cross-sectional area of 3.0 x 0.5 mm. A thickness of 0.5 mm was chosen since it matches the height of typical BGA solder joints. The nominal dimensions of the final test samples were 80 x 3 x 0.5 mm. The specimens were stored in a low temperature freezer (-40 °C) after the water quenched/reflow process to minimize any aging effects. The solder microstructure has been verified to be consistent throughout a specimen volume, and from specimen to specimen by cross-sectioning. A micro-focus x-ray system was used to inspect the samples for the presence of flaws (e.g. notches and external indentations) and/or internal voids (non-

visible). Specimens with no flaws and voids were generated using proper experimental techniques, and Figure 3.6 illustrates x-rays scans for good and poor specimens.

(a) Within Glass Tubes

(b) After Extraction

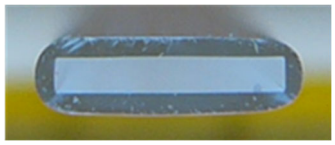

(c) Cross-Section

Figure 3.5 Solder Uniaxial Test Specimens

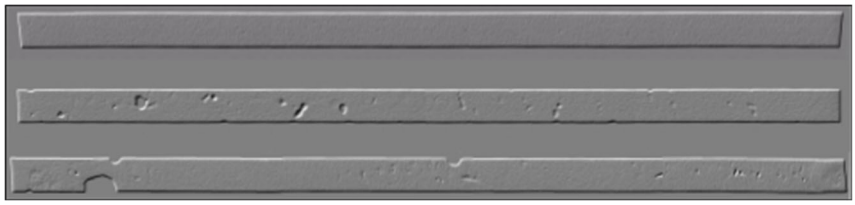

Figure 3.6 X-Ray Inspection of Solder Test Specimens (Good and Bad Samples)

3.3 Mounting Strain Gages on Solder Specimen

To determine the value of Poisson's ratio for different SAC and SAC+X lead free solder alloys experimentally strain gages were mounted on solder specimens. The gage used for experimental characterization was very specially designed by Micro-Measurements (C2A-13-015LW-120) with a gage resistance of 120 ± 0.6% Ohms. 0.5 mm.

Figure 3.7 shows the sequential flow diagram of the gage mounting steps and Figure 3.8 shows one complete assembly of mounted gage on a real solder specimen.

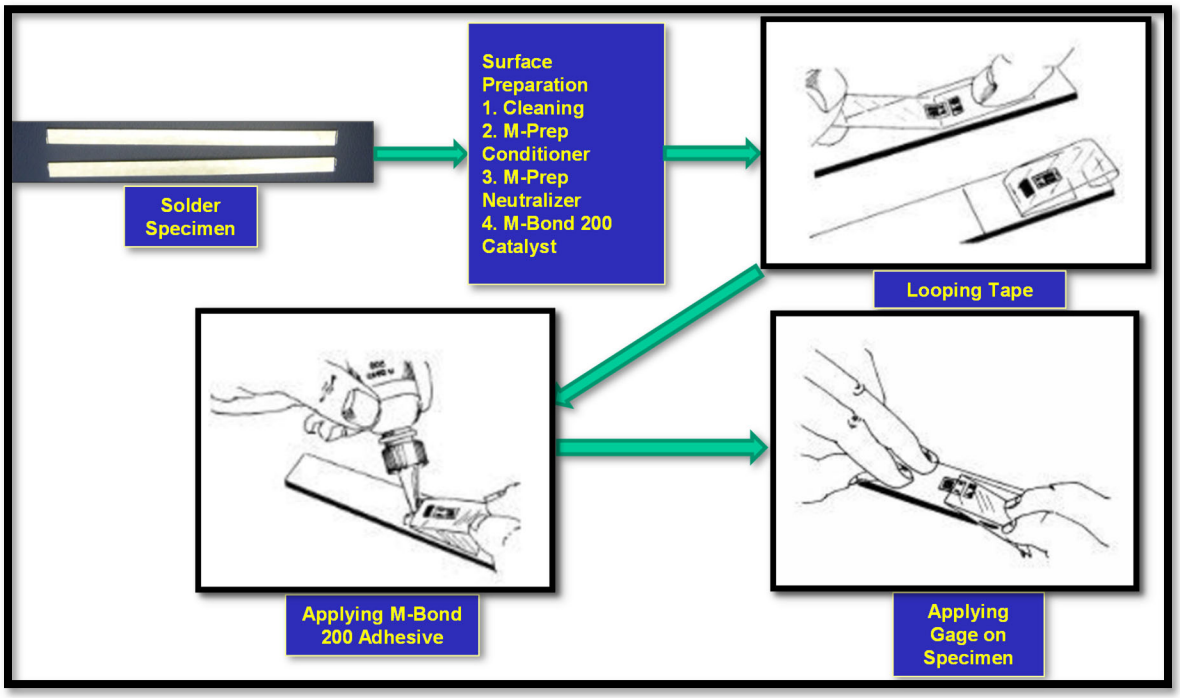

Figure 3.7 Flow Diagram of Strain Gage Mounting Steps

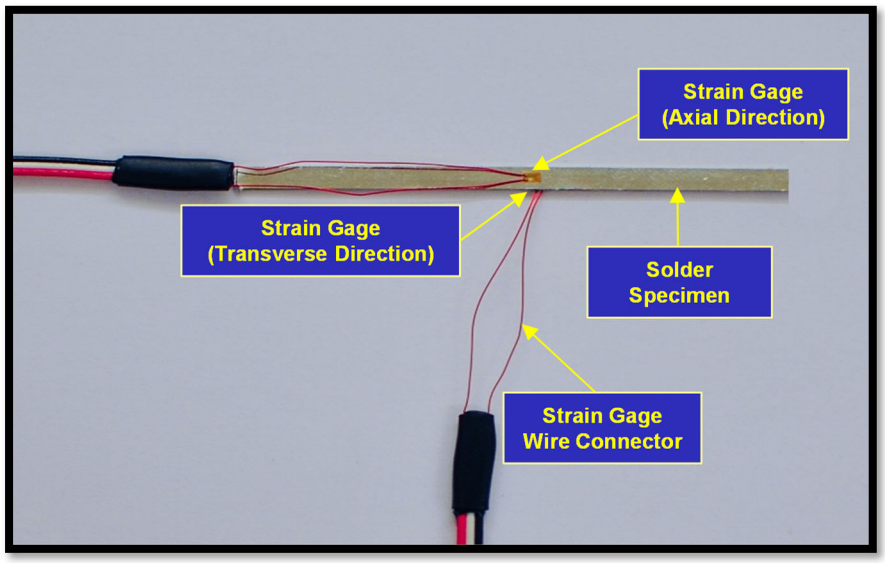

Figure 3.8 Strain Gage Mounted on a Solder Specimen

The geometrical specifications of the gage (gage length: 0.38 mm, overall length: 1.32 mm, grid width: 0.5 mm, overall width: 0.86 mm, matrix length: 1.90 mm, matrix width: 1.37 mm) comfortably fits on the rectangular solder specimens with nominal dimensions of 80 x 3 x 0.5 mm. Micro-Measurements certified M-Bond 200 was used as the adhesive for bonding the gage on the specimen surface for its excellent general-purpose features like fast room-temperature cure and ease of application. Before applying the gage to the specimen surface a standard surface preparation technique [198] was applied including cleaning, applying M-Bond preparation conditioner, neutralizer, and catalyst as shown in Figure 3.7.

3.4 Uniaxial Tensile Testing System

Wisdom Technology MT-200 tension/torsion thermo-mechanical test system was used to perform the stress-strain tests in this study as shown in Figure 3.9. This instrument is optimized for loading small specimens such as thin films, solder joints, gold wire, fibers, etc. It provides an axial displacement resolution of 0.1 micron. Samples can be tested over a temperature range of -185 to +300 °C using supplemental environmental chambers added to the system. However, the high temperature system has been calibrated to accurately control the specimen temperature. Appendix A.1 represents the variation in set temperatures and specimen temperatures. The calibrated temperature table has also been included in Appendix A.1.

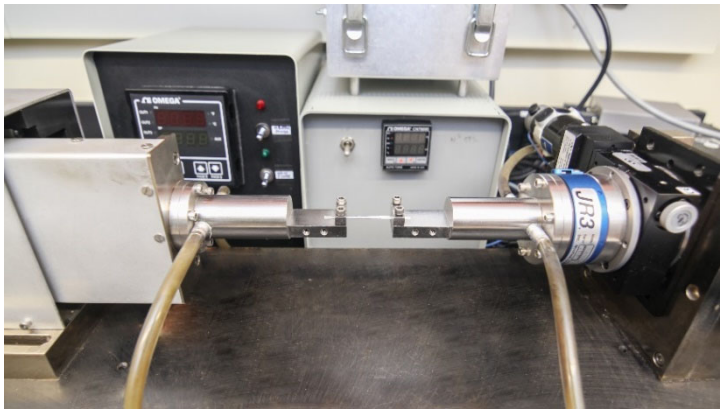

(a)

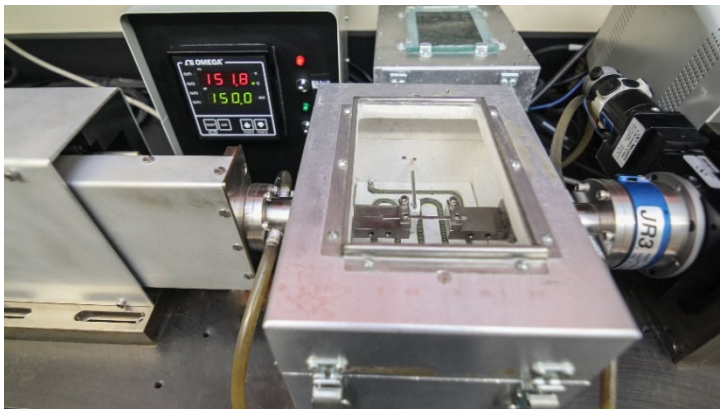

(b)

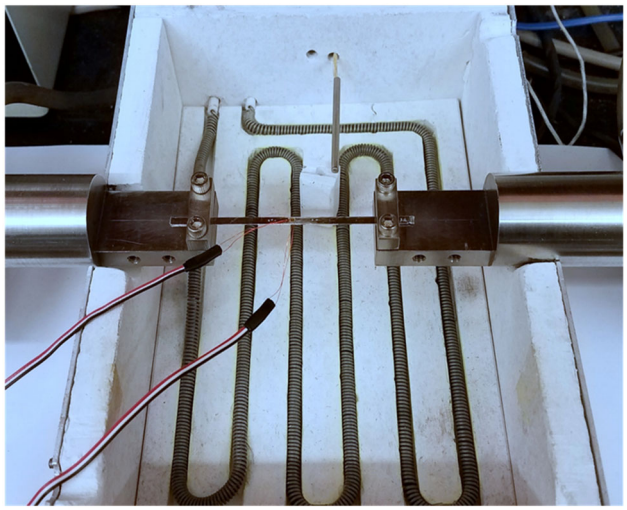

(c)

Figure 3.9 Mechanical Test System with Uniaxial Sample

Forces and displacements were measured in the uniaxial tests, and the axial stress and axial strain were calculated using

$$\sigma = \frac{F}{A} \qquad \varepsilon = \frac{\Delta L}{L} = \frac{\delta}{L} \tag{3.1}$$

where F is the measured uniaxial force, δ is the measured crosshead displacement, σ is the uniaxial stress, ε is the uniaxial strain, A is the original cross-sectional area, and L is the chosen specimen gage length (initial length between the grips). The gage length of the specimen was kept as 60 mm (thus the length to width ratio was 20 to 1).

3.5 Typical Testing Data and Data Processing

3.5.1 Typical Uniaxial Tensile Test Data

A typical SAC solder tensile stress strain curve is illustrated in Figure 3.10. The standard material properties are labelled on the graph including the effective elastic modulus E (initial slope of the stress-strain curve). This effective modulus is rate dependent since solder behavior is viscoplastic. The value of the effective modulus will become the true elastic modulus as the testing speed is increased to the limit of infinite strain rate. The yield stress σ_Y (YS) is defined using the typical definition of the stress level that results in a permanent strain of $\varepsilon = .002 = 0.2\%$ upon unloading. The maximum (saturation) stress on the stress-strain curve is the ultimate tensile strength σ_u (UTS). As shown the figure, the stress-strain curve for the solder material has an elastic region at the beginning, a small transition region followed by a plastic region. As the strain becomes significantly high, localized deformation takes place which is also known as necking.

Necking causes a visible reduction in cross-sectional area and a drop in the applied load, near the end of the stress strain curve, leading towards a rupture.

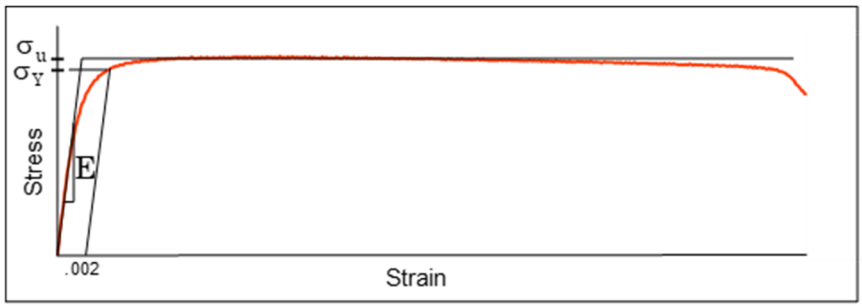

Figure 3.10 SAC Stress-Strain Curve and Material Properties

3.5.2 Stress-Strain Data Processing

For the uniaxial stress-strain tests, a total of 10 specimens have been tested at a specific aging/testing condition. From the recorded stress-strain data, a set of averaged material properties were extracted. Figure 3.11 illustrates the data processing steps where the entire stress-strain curves were truncated to a certain strain limit (2%) so that all solder materials can be compared uniformly. In this work, a single "average" curve was generated using a four parameter hyperbolic tangent empirical model (red curve in Figure 3.9 (c)) to represent a set of 10 recorded stress-strain curves for a certain testing configuration.

$$\sigma = C_1 \tanh(C_2\varepsilon) + C_3 \tanh(C_4\varepsilon) \tag{3.2}$$

Material constants C_1, C_2, C_3, and C_4 are determined through regression fitting of the model to experimental data. The effective elastic modulus E at zero strain is calculated from the model constants using

$$E = \sigma'(0) = C_1C_2 + C_3C_4 \tag{3.3}$$

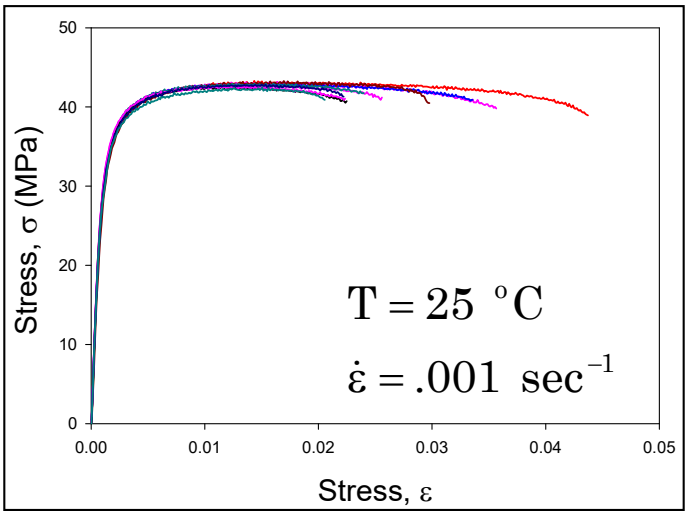

(a) Entire Curve

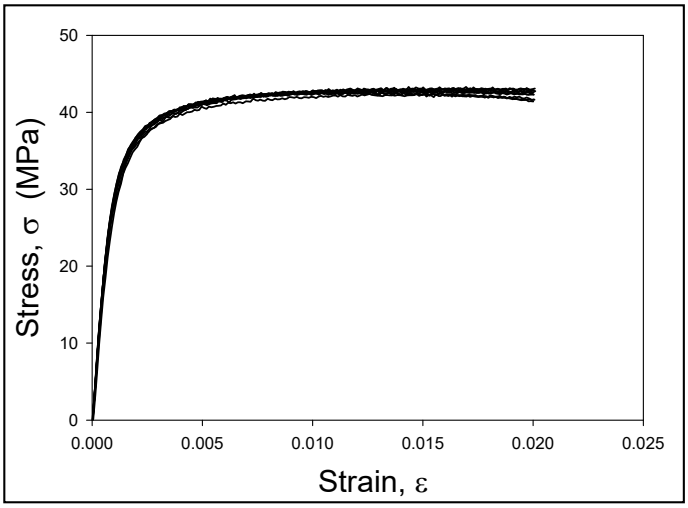

(b) Initial Region

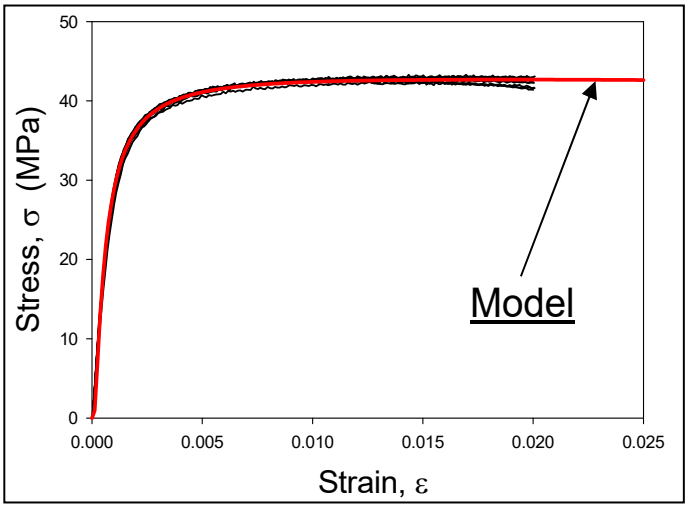

(c) Empirical Model Fit

Figure 3.11 Solder Stress-Strain Curves Data Processing

When consider extreme large strain situation ($\varepsilon \to \infty$), the ultimate tensile strength (UTS) can be obtained by:

$$\lim_{\varepsilon \to 0} \sigma(\varepsilon) = C_1 + C_3 \tag{3.4}$$

3.5.3 Data Acquisition and Processing to Measure Poisson's Ratio

To measure the Poisson's ratio experimentally, some additional arrangements were made for data acquisition from the MT-200 tension/torsion thermo-mechanical test system. Data acquisition was performed using a National Instruments NI-9237 strain gage bridge module along with NI-9944 connector hardware. The experiments were controlled using LabVIEW software, and the strain gage data from each test were stored for subsequent analysis. Post processing consisted of performing a linear regression fit to the recorded transverse vs. axial strain data from each test. From the definition of a linear Poisson's ratio, the relationship between the two strains is:

$$\varepsilon_y = -\nu\varepsilon_x \tag{3.5}$$

Or

$$\left|\varepsilon_y\right| = +\nu\varepsilon_x \tag{3.6}$$

where, ε_y is the transverse strain, ε_x the axial strain, and ν is the Poisson's ratio.

Typical transverse strain vs. axial strain raw data for an example test for SAC305 is shown in Figure 3.12 along with the corresponding linear regression fit represented by the blue line. The variation of the raw data was quite linear, and the slope is the desired Poisson's ratio for a particular test. A total of 6-8 specimens were tested and numerical average along with the standard deviations were recorded at a specific aging/testing condition.

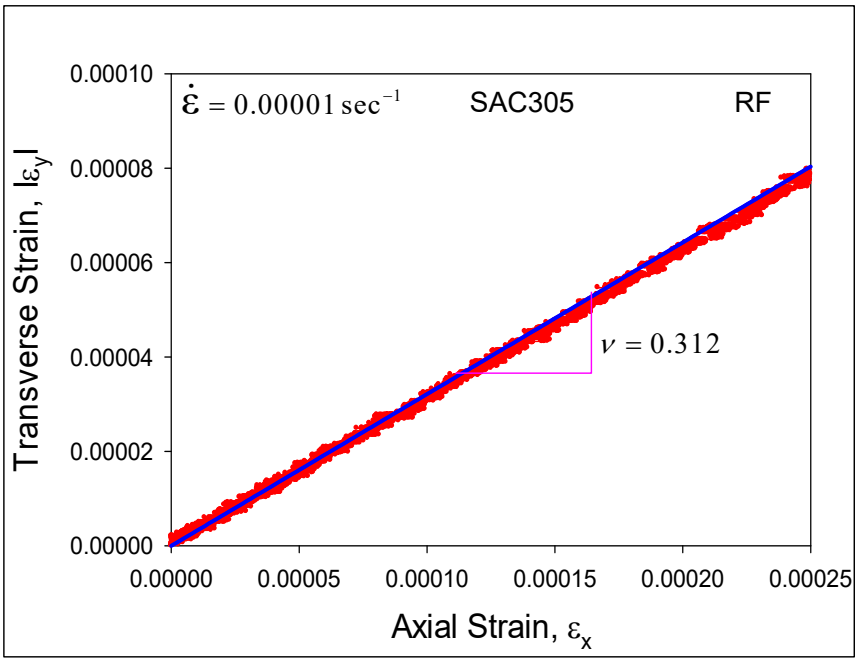

Figure 3.12 Linear Regression Fitting to Measure Poisson's Ratio

3.6 Anand Viscoplastic Constitutive Model

Anand, et al. [115] proposed a popular set of viscoplastic constitutive equations for rate-dependent deformation of metals at high temperatures (e.g. in excess of a homologous temperature of $0.5T_m$). This model is defined using nine material parameters, and the reliability prediction results are often highly sensitive to the values of the Anand parameters. Although it was originally aimed at hot working of high strength aluminum and other structural metals, the so-called Anand model has been adopted successfully to represent isotropic materials such as microelectronic solders (SnPb and lead free) with small elastic deformations and large viscoplastic deformations.

3.6.1 Review of Elementary Equations of Anand Viscoplastic Constitutive Model

Several authors [167, 168, 172] have previously reviewed the general equations of the Anand constitutive model for one-dimensional (uniaxial) stress states. The theoretical approach is based on a scalar internal variable s, which represents the material resistance to plastic flow. The model includes three equations: (1) stress equation, (2) flow equation, and (3) evolution equation. These expressions unify the rate-independent plastic behavior of the material. The Anand model does not contain an explicit yield condition or a loading/unloading criterion.

For the one-dimensional case (uniaxial loading), the stress equation is given by

$$\sigma = cs; \; c < 1 \tag{3.7}$$

where s is the internal valuable and c is a function of strain rate and temperature which can be expressed as:

$$c = c\left(\dot{\varepsilon}_p, T\right) = \frac{1}{\xi}\sinh^{-1}\left\{\left[\frac{\dot{\varepsilon}_p}{A}e^{\left(\frac{Q}{RT}\right)}\right]^m\right\} \tag{3.8}$$

where $\dot{\varepsilon}_p$ is the inelastic (plastic) strain rate, T is the absolute temperature, ξ is the multiplier of stress, A is the pre-exponential factor, Q is the activation energy, R is the universal gas constant, and m is the strain rate sensitivity. Substituting Equation 3.8 into Equation 3.7, the stress equation can be expressed as:

$$\sigma = \frac{s}{\xi}\sinh^{-1}\left\{\left[\frac{\dot{\varepsilon}_p}{A}e^{\left(\frac{Q}{RT}\right)}\right]^m\right\} \tag{3.9}$$

The Anand model flow equation is found by rearranging Equation 3.9 and can be expressed as:

$$\dot{\varepsilon}_p = A\, e^{-\left(\frac{Q}{RT}\right)}\left[\sinh\left(\xi\frac{\sigma}{s}\right)\right]^{\frac{1}{m}} \tag{3.10}$$

The differential form of the evolution equation for the internal variable s is assumed to be of the form

$$\begin{aligned} \dot{s} &= h(\sigma, s, T)\dot{\varepsilon}_p \\ \dot{s} &= \left[h_o\left(1-\frac{s}{s^*}\right)^a \operatorname{sign}\left(1-\frac{s}{s^*}\right)\right]\dot{\varepsilon}_p ; \quad a > 1 \end{aligned} \tag{3.11}$$

where, the term $h(\sigma, s, T)$ in Equation 3.11 is associated with the dynamic hardening and recovery processes. Parameter h_o is the hardening constant, a is the strain rate sensitivity of the hardening process, and the term s* is expressed as

$$s^* = \hat{s}\left[\frac{\dot{\varepsilon}_p}{A} e^{\left(\frac{Q}{RT}\right)}\right]^n \tag{3.12}$$

where $\hat{s}$ is a coefficient and n is the strain rate sensitivity of the saturation value of the deformation resistance. Equation 3.11 can be expressed as:

$$ds = h_o\left(1-\frac{s}{s^*}\right)^a d\varepsilon_p \tag{3.13}$$

for s < s*, and then integrated resulting in an evolution expression for the internal variable s:

$$s = s^* - \left[\left(s^* - s_o\right)^{(1-a)} + (a-1)\left\{(h_o)\left(s^*\right)^{-a}\right\}\varepsilon_p\right]^{\frac{1}{1-a}} \tag{3.14}$$

where the initial value is $s(0) = s_o$ at time $t = 0$. Combining Equations 3.12 and 3.14 results in an evolution equation for the internal variable s in terms of the plastic strain and plastic strain rate:

$$s = \hat{s}\left[\frac{\dot{\varepsilon}_p}{A}e^{\left(\frac{Q}{RT}\right)}\right]^n - \left[\left(\hat{s}\left[\frac{\dot{\varepsilon}_p}{A}e^{\left(\frac{Q}{RT}\right)}\right]^n - s_o\right)^{(1-a)} + (a-1)\left\{(h_o)\left(\hat{s}\left[\frac{\dot{\varepsilon}_p}{A}e^{\left(\frac{Q}{RT}\right)}\right]^n\right)^{-a}\right\}\varepsilon_p\right]^{\frac{1}{1-a}} \quad (3.15)$$

Or,

$$s = s(\dot{\varepsilon}_p, \varepsilon_p) \quad (3.16)$$

The final equations in the Anand model (1D) are the stress equation in Equation 3.9, the flow equation in Equation 3.10, and the integrated evolution equation in Equation 3.15. These expressions include 9 material parameters (constants): A, ξ, Q/R, m in Equations 3.9, and 3.10; and constants h_o, a, s_o, $\hat{s}$, and n in Equation 3.15.

3.6.2 Uniaxial Stress-Strain Theoretical Response

The post yield uniaxial stress-strain relations predicted by the Anand model are obtained by combining Equations 3.9 and 3.15 and can be expressed as:

$$\sigma = \frac{1}{\xi}\sinh^{-1}\left\{\left[\frac{\dot{\varepsilon}_p}{A}e^{\left(\frac{Q}{RT}\right)}\right]^m\right\}\left(\hat{s}\left[\frac{\dot{\varepsilon}_p}{A}e^{\left(\frac{Q}{RT}\right)}\right]^n - \left[\left(\hat{s}\left[\frac{\dot{\varepsilon}_p}{A}e^{\left(\frac{Q}{RT}\right)}\right]^n - s_o\right)^{(1-a)} + (a-1)\left\{(h_o)\left(\hat{s}\left[\frac{\dot{\varepsilon}_p}{A}e^{\left(\frac{Q}{RT}\right)}\right]^n\right)^{-a}\right\}\varepsilon_p\right]^{\frac{1}{1-a}}\right)$$

$$\sigma = \sigma(\dot{\varepsilon}_p, \varepsilon_p) \quad (3.17)$$

For a uniaxial tensile test performed at fixed (constant) strain rate $\dot{\varepsilon}_p$ and constant temperature T, this expression represents highly nonlinear stress-strain behavior (power law type function) after yielding:

$$\sigma=\sigma(\varepsilon_p) \tag{3.18}$$

Anand model predictions for the yield stress (σ_Y) and the Ultimate Tensile Strength (UTS = maximum or saturation stress) can be obtained from Equation 3.17 by taking the limits for small and large plastic strains. The yield stress is given by the limit as ε_p goes to 0:

$$\sigma_Y = \sigma\big|_{\varepsilon_p \to 0} = c s_0 = \frac{1}{\xi}\sinh^{-1}\left\{\left[\frac{\dot{\varepsilon}_p}{A}e^{\left(\frac{Q}{RT}\right)}\right]^m\right\} \; s_0 = c s_0 \equiv \sigma_0 \tag{3.19}$$

while the UTS is given by the limit as ε_p goes to ∞:

$$\text{UTS}=\sigma\big|_{\varepsilon_p \to \infty} = \frac{\hat{s}}{\xi}\left[\frac{\dot{\varepsilon}_p}{A}e^{\left(\frac{Q}{RT}\right)}\right]^n \; \sinh^{-1}\left\{\left[\frac{\dot{\varepsilon}_p}{A}e^{\left(\frac{Q}{RT}\right)}\right]^m\right\} \equiv \sigma^* \tag{3.20}$$

Using the saturation stress (σ^* = UTS) relation in Equation 3.20, the post yield stress-strain response (power law) in Equation 3.17 can be rewritten as:

$$\sigma = \sigma^* - \left[\left(\sigma^* - c s_0\right)^{(1-a)} + (a-1)\left\{\left(ch_0\right)\left(\sigma^*\right)^{-a}\right\}\varepsilon_p\right]^{1/(1-a)} \tag{3.21}$$

3.6.3 Determination of the Anand Model Parameters from the Uniaxial Stress-Strain Data

Anand [115] suggested using stress-strain data measured over a wide range of temperatures and strain rates to determine the 9 parameters(A, ξ, Q/R, m, h_o, a, s_o, $\hat{s}$, and n) in the viscoelastic constitutive relations presented above. Several previous studies [167, 168, 172], have outlined a procedure for performing this task. . From the measured data, the value of the saturation stress (σ^* = UTS) can be obtained for several strain rates and temperatures. In addition, the stress-strain (σ, ε) data for each temperature and strain rate can be recast as stress vs. plastic strain data ($_{\sigma, \varepsilon_p}$) by using

$$\varepsilon_p = \varepsilon - \frac{\sigma}{E} \tag{3.22}$$

where E is the initial elastic modulus of the material at the specific temperature and strain rate being considered. The Anand model parameters can be obtained by following procedure

1. Out of nine Anand parameters, the values of six parameters $\hat{s}$, ξ, A, Q/R, n and m are determined by non-linear regression (least squares) fitting of Equation 3.20 to the recorded saturation stress vs. strain rate and temperature data.
2. The value of the remaining three parameters s_o, h_o, and a are determined by non-linear regression (least squares) fitting of Equation 3.21 to the recorded stress vs. plastic strain data at several strain rates and temperatures.

3.6.4 Correlation between Anand Model Predictions and Experimental Results

Once the Anand constants are determined for each alloy, it is possible to predict the stress (σ) vs. plastic strain (ε_p) curve at a particular set of temperature, strain rate, and

alloy using Equation 6.11. This result can be adjusted to a stress (σ) vs. total strain curve (ε) by adding the elastic strain to the plastic strain:

$$\varepsilon = \varepsilon_e + \varepsilon_p \qquad \varepsilon_e = \frac{\sigma}{E} \tag{3.23}$$

where E is the initial elastic modulus at the particular temperature, strain rate, and aging conditions.

3.7 Study of the Microstructural Evolution

3.7.1 Sample Preparation for Scanning Electron Microscopy (SEM)

To identify the physical mechanism behind the mechanical property changes, microstructural study was done for different SAC and SAC+X alloys and for SAC305 BGA joints. The sample preparation involved different steps, such as:

1. First of all, the fabricated solder samples, and BGA packages were cut into small pieces and potted in epoxy.
2. After that, the surface preparation was done by mechanical grinding with several grades of SiC papers (#320 to #400, #600, #800 and #1200) in a rotating metallographic disc as shown in Figure 3.13. The final polishing was conducted with 0.02 μm colloidal silica suspensions (BUEHLER MasterMet 2) and BUEHLER ChemoMet polishing cloth.
3. After several duration of grinding the topography was checked using OLYMPUS BX60 Optical Microscope shown in Figure 3.14 to confirm the desired surface appearance, otherwise grinding was continued for longer durations for better topography.

This procedure resulted in mirror finish samples suitable for optical microscopy, Scanning Electron Microscopy (SEM), as well as nanoindentation.

Figure 3.13 Grinding and Polishing Machine

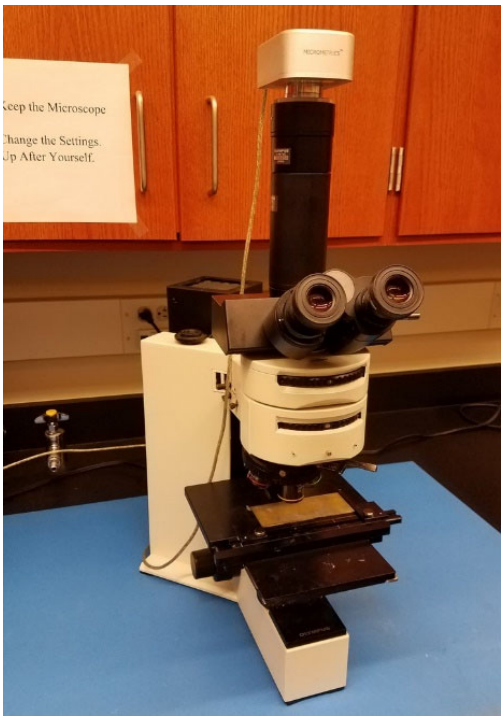

Figure 3.14 OLYMPUS BX60 Optical Microscope

3.7.2 Capturing Images Using Scanning Electron Microscopy (SEM)

Microstructure analysis of the solder alloys was performed on the mounted and polished testing specimens by using a Zeiss Crossbeam 550 SEM (Figure 3.15). In

addition, EDS (Energy-Dispersive X-ray Spectroscopy) was employed to explore the chemical composition of different phases in the microstructure. As shown in Figure 3.16 small indentation marks were added to the cross-sections to facilitate subsequent locating of the same regions in the solder joints. Pyramidal idents were placed near the corners of the regions of interest using a nanoindentation system shown in next section. As shown in Figure 3.16, the indents were placed suitably away from the region of interest to minimize any influence on the microstructure evolution. In this case, the region of interest was approximately 60 x 40 µm, while the center-to-center spacing between the indentation marks was approximately 90 µm. SEM analysis of the selected regions was then performed on the non-aged as-polished samples. The same samples were then aged and microstructures of the selected regions were captured using the SEM after each aging interval as shown in Figure 3.16.

Figure 3.15 Zeiss Crossbeam 550 SEM

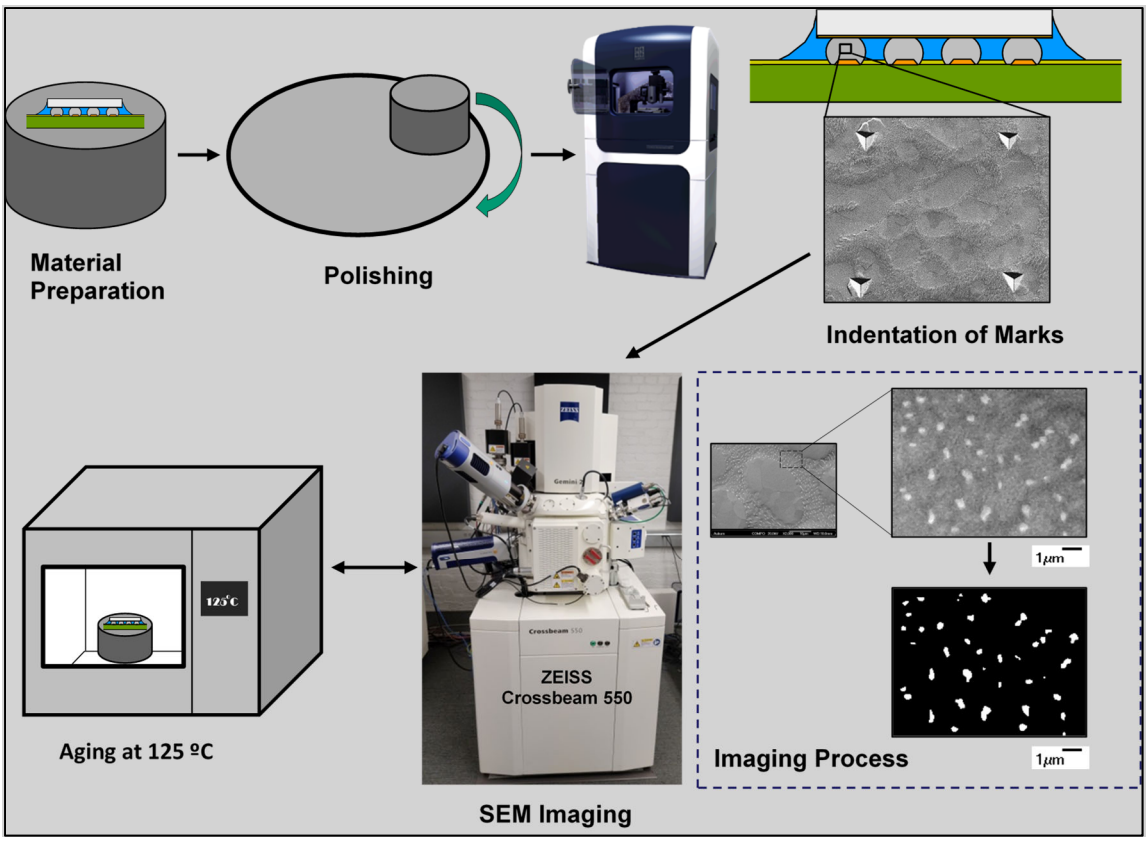

Figure 3.16 Flow Chart of SEM Imaging Procedure (Including Zeiss Crossbeam 550 and Hysitron TI 950)

3.7.3 Measurement of Area and Number of IMC Particles by Image Processing

After capturing the images for different durations and temperatures of isothermal aging, quantitative analyses of the size metrics of the IMC particles were performed with all of the SEM images to study the evolution of IMC particles. The analyzed regions were typically chosen intentionally to be interdendritic regions with a rich concentration of IMC particles. The area of each particle, the total area of all of the particles, and the total number of particles in each selected region and aging time were determined using image analysis software (Adobe Photoshop) and MATLAB.

The particle size measurement process involves 3 major steps. In first step, all the IMC particles were outlined in Adobe Photoshop. After that, the gray scale images were

converted into a binary image. Finally, the average area of the particles (White spots), in the binary image, and the number of particles were calculated using MATLAB. Figure 3.17 shows an example of image processing. The particles were outlined very carefully so that all the individual particles in the field were identified and counted for analysis.

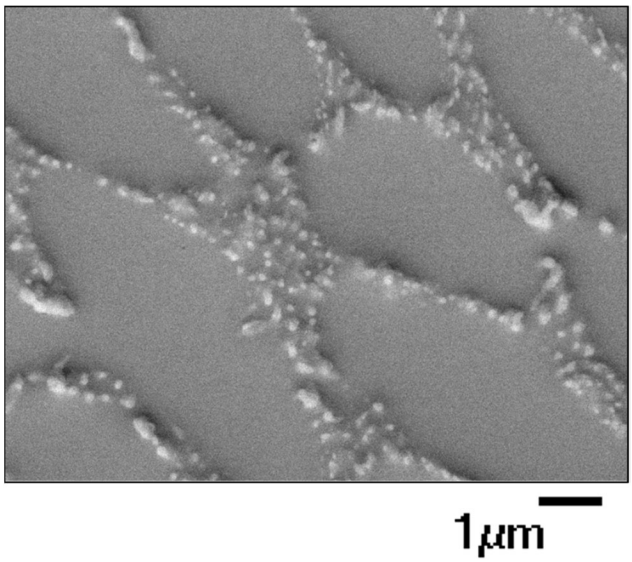

(a)

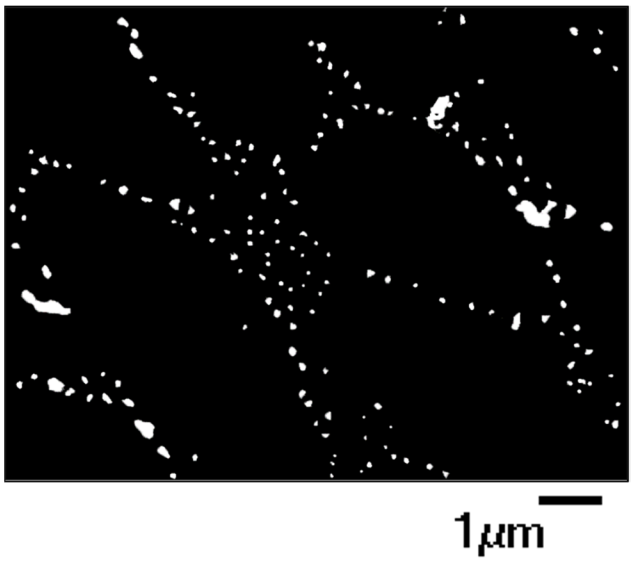

(b)

Figure 3.17 Image Processing Steps for IMC Particle Area Calculations (a) After Outlining All the Particles (b) Binary Image

3.7.4 Measurement of IMC Particle Diameter

For an ideal spherical IMC particle, the amount of the particle that is visible on the polished cross-sectional surface is actually unknown as shown in Figure 3.18. In this case, the black portion of the particle represents the portion on IMC exposed on the polished surface, while the gray shaded portion is the portion of the IMC below the surface. As indicated in Figures 3.18 and 3.19, the observed particle diameter (apparent diameter) for a particle is actually less than or equal to the actual particle diameter. Thus, the measured (apparent) average particle diameter must be adjusted to calculate the actual average particle diameter.

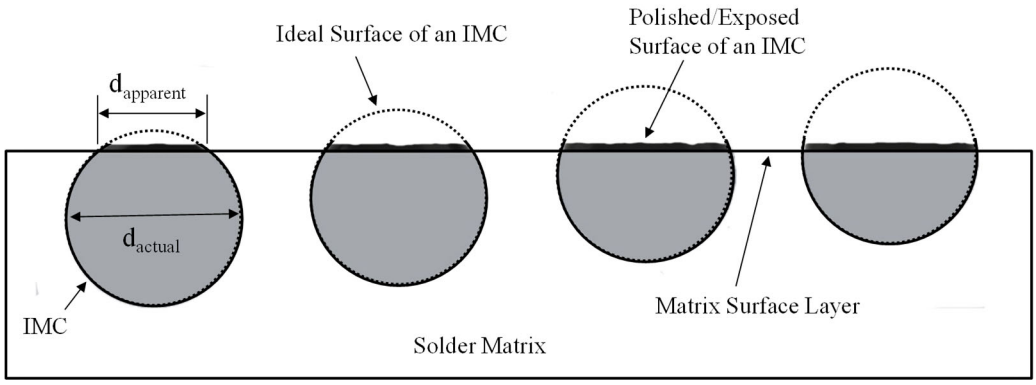

Figure 3.18 Schematic Representation of an IMC with Several Possible Exposed Area above the Surface Layer

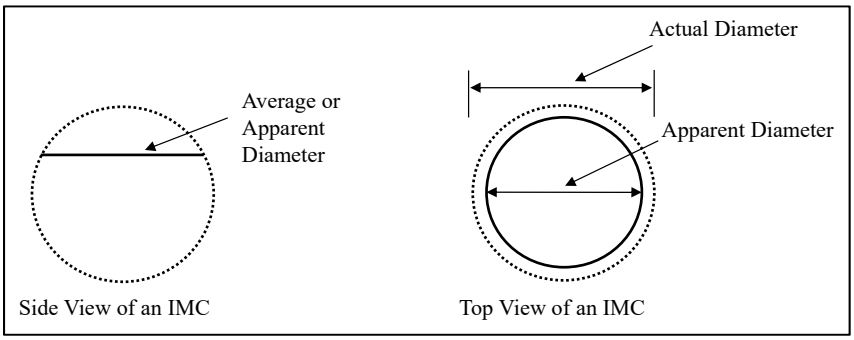

Figure 3.19 Side and Top View of an Ideal Spherical IMC Particle Showing Actual and Apparent Diameters

For a fixed particle with diameter d, the apparent/measured particle diameter $d_{apparent}$ can be several different values based on the vertical position of the particle (Figure 3.18). The average value of $d_{apparent}$ can be found mathematically by averaging all possible values obtained from all possible vertical positions for the particle:

$$(d_{apparent})_{ave} = 2 \times (R_{apparent})_{ave} = \frac{2}{R}\int_0^R \sqrt{(R^2 - x^2)}dx \tag{3.24}$$

$$(d_{apparent})_{ave} = \frac{2}{R} \times \frac{\pi R^2}{4} = \frac{\pi}{4} d_{actual} \tag{3.25}$$

$$d_{actual} = \frac{4}{\pi}(d_{apparent})_{ave} \tag{3.26}$$

Equation 3.26 was used to estimate the actual diameter of each particle by adjusting the measured (apparent) diameter.

If the particles are spherical, the apparent diameter of the exposed surface of each particle can be calculated by assuming a circular relation between particle surface area and apparent diameter:

$$A_{apparent} = \pi R^2 = \frac{\pi}{4}(d_{apparent})^2 \tag{3.27}$$

$$d_{apparent} = \frac{2}{\sqrt{\pi}}\sqrt{A_{apparent}} \tag{3.28}$$

Combining of Equations (3.26, 3.28) yields the relation for the particle diameter in terms of the measured/particle surface area:

$$d_{actual} = \frac{4}{\pi}(d_{apparent})_{ave} = \frac{8}{\pi^{3/2}}\sqrt{(A_{apparent})_{ave}} \quad (3.29)$$

Additionally, this analysis also assumes that the particle does not move vertically during the aging process.

3.7.5 Tracking the Changes in IMC Particle Diameter during Isothermal Aging

For very durations of isothermal aging at a particular temperature, three regions similar to that shown in Figure 3.17 were processes and analyzed. The evolution of the average diameter of the IMC particles and the total number of particles data were gathered for all three regions and then the data were fitted using a two term exponential relation

$$\frac{d}{d_o} = k_1 e^{k_2 t} + k_3 e^{k_4 t} \quad (3.30)$$

where d is the average diameter of all particles at time t, d_o is the average diameter of all particles at time t = 0, and K_1, K_2, K_3, and K_4 are fitting constants.

3.8 Nanoindentation Method to Perform Creep Tests on Solder Joints

3.8.1 Sample Preparation for Nanoindentation

To perform a part of microstructural study and the whole nanoindentation tests, SAC305 (96.5Sn-3.0Ag-0.5Cu) BGA joints were extracted from PBGA assemblies (Amkor CABGA, 14 x 14 mm, 192 balls, 0.8 mm ball pitch, 0.46 mm ball (diameter) that were assembled for the iNEMI Characterization of Pb-Free Alloy Alternatives Project (Figure 3.20). Prior to cross sectioning, the PBGA test assemblies were stored in a freezer at T = -10 °C to minimize any aging effects after board assembly. Figure 3.21 shows

BUEHLER IsoMet 1000 Precision Cutter that was used to cut the test boards for cross-sectioning purposes.

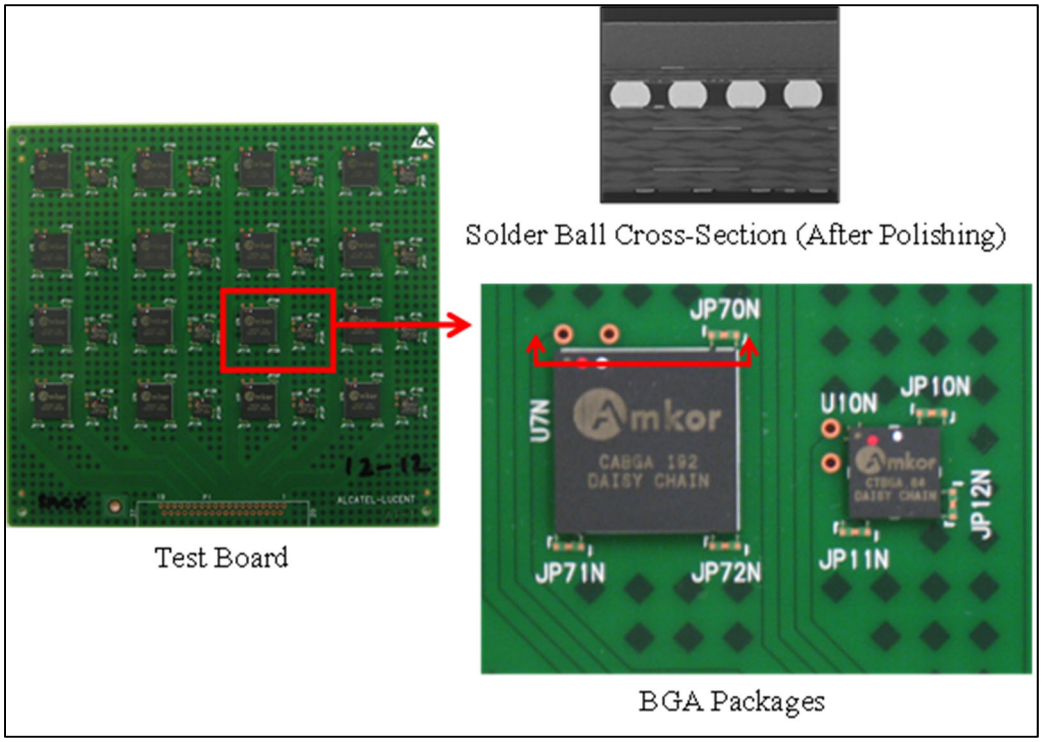

Figure 3.20 iNEMI Test Board and BGA Package

Figure 3.21 IsoMet 1000 Precision Cutter

Due to the limited space inside the high temperature stage attached with the nanoindentation system a restriction was imposed of using an epoxy mounted sample inside the stage. The maximum allowable sample height is around 3 mm, which impose a restriction of using an epoxy mounted sample inside the high temperature stage. As a result, an alternative approach was developed to polish solder joint samples without any epoxy encapsulate. As shown in Figure 3.22, cross-sectional samples were mounted on a cylindrical epoxy preform by double-sided tape to facilitate polishing. The polished solder joint array cross-sections were then carefully extracted from the preform.

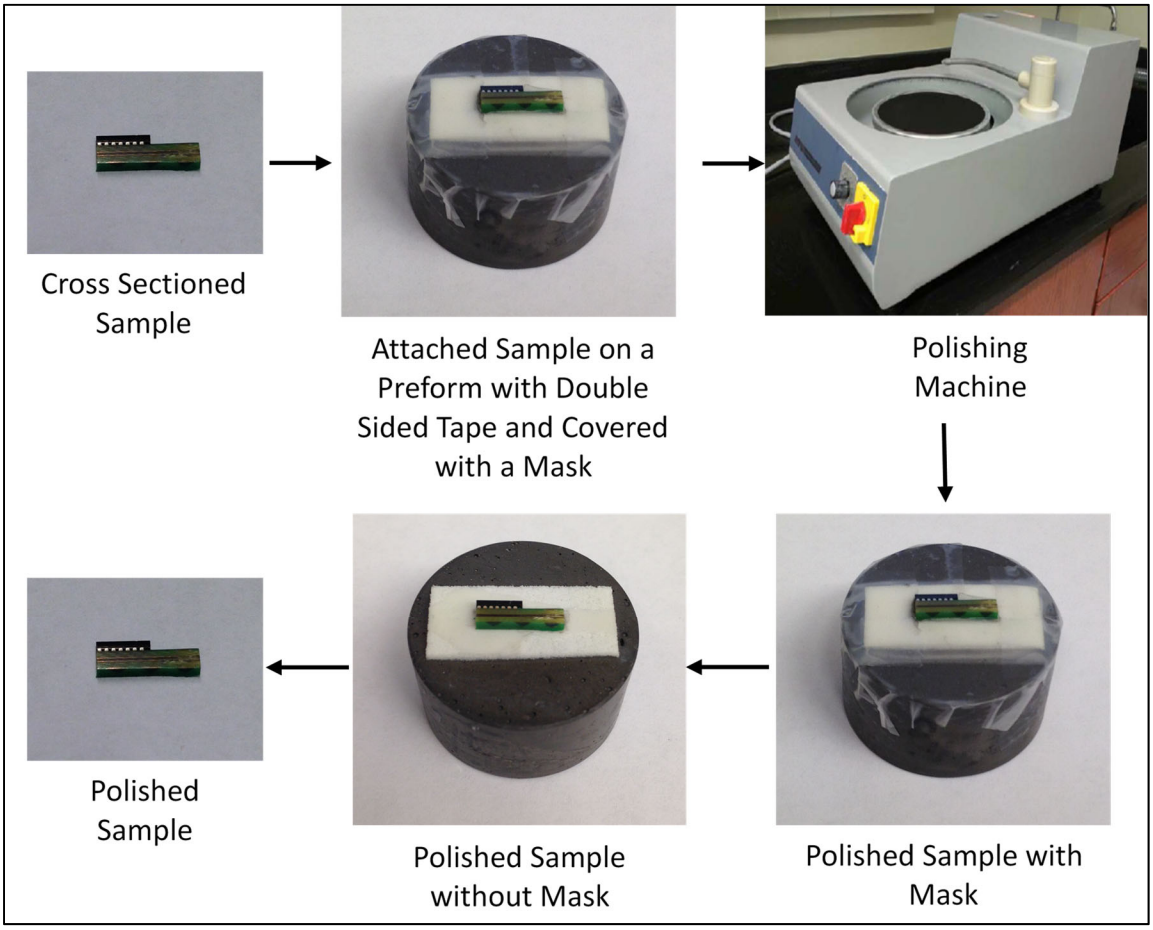

Figure 3.22 Sample Preparation Procedure for High Temperature Nanoindentation

As the mechanical properties of SAC305 BGA joints depend on the crystallographic orientation, therefore it is necessary to determine the orientation before performing nanoindentation. The orientation of the SAC305 BGA joints were initially determined using a Zeiss polarized light microscopy as shown in Figure 3.23.

Figure 3.23 Zeiss Polarized Light Microscope

3.8.2 Nanoindentation Machine and Test Procedures

Hysitron TI 950 nanoindentation system shown in Figure 3.24 was used in this work to perform creep test. A Berkovich indenter tip was employed to indent the surface of SAC305 BGA joints to extract mechanical properties. During each indentation experiment, load versus indentation displacement response of the test samples in the direction normal to the cross-sectional surface was measured.

Figure 3.24 Hysitron TI950 TriboIndenter

Figure 3.25 shows a typical cross-sectioned SAC305 lead free solder joint sample after nanoindentation testing. A set of 10-30 indents were made, and the measured test data were averaged to obtain statistically relevant results and consistency of inspection. The indents in a set were positioned at least 3b apart, where b is the width of a single indent, to avoid interactions between the plastic zones created by the indentations. Figure 3.26 shows a typical example of loading profile used during nanoindentation, for hardness and modulus testing. The loading profile has three segments 1) loading from 0 mN to 10 mN force, 2) holding 10 mN force for a few seconds, and 3) unloading from 10 mN to 0 mN. Depending on the type of the test material, the different parameters in the loading profile was adjusted to get an accurate measurement.

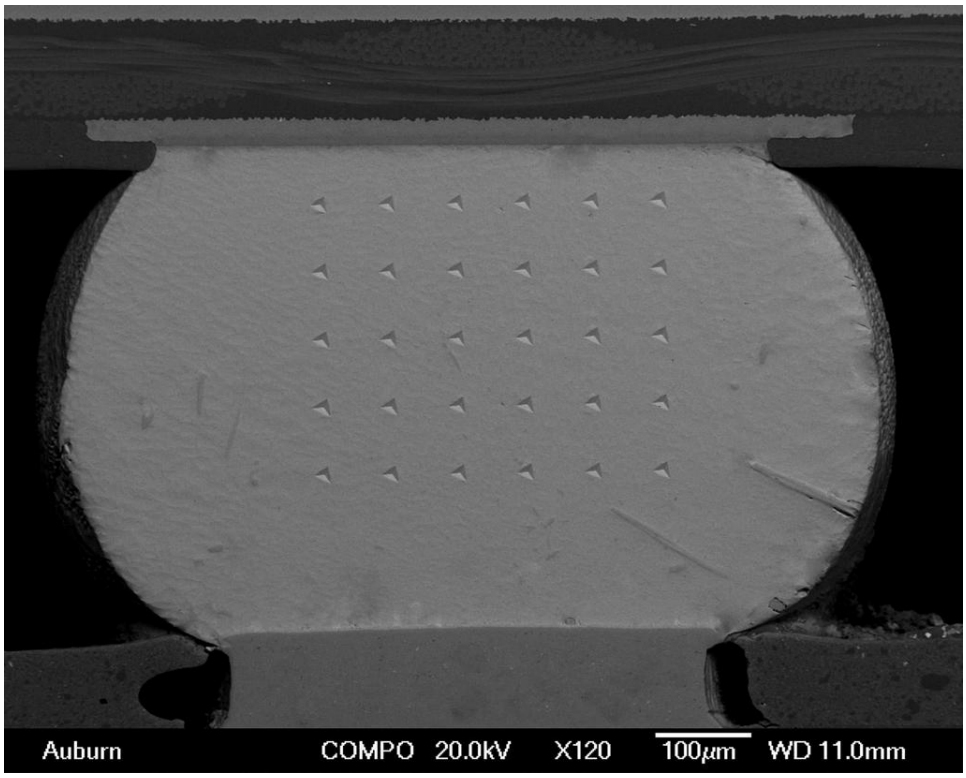

Figure 3.25 SAC305 Solder Joint after Nanoindentation Testing

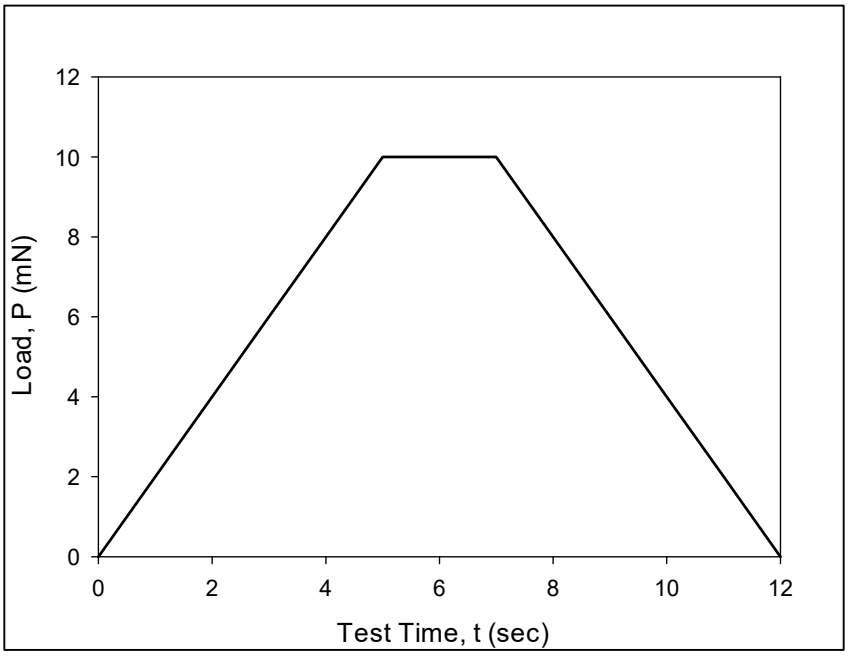

Figure 3.26 Example of the loading profile used during nanoindentation testing

3.8.3 Measurement of Elastic Modulus and Hardness

Figure 3.27 shows a typical load (P) versus displacement (h) curve obtained after a nanoindentation test. This curve has three different segments where the first, second, and third segments represent the displacements during the loading, holding and unloading period, respectively.

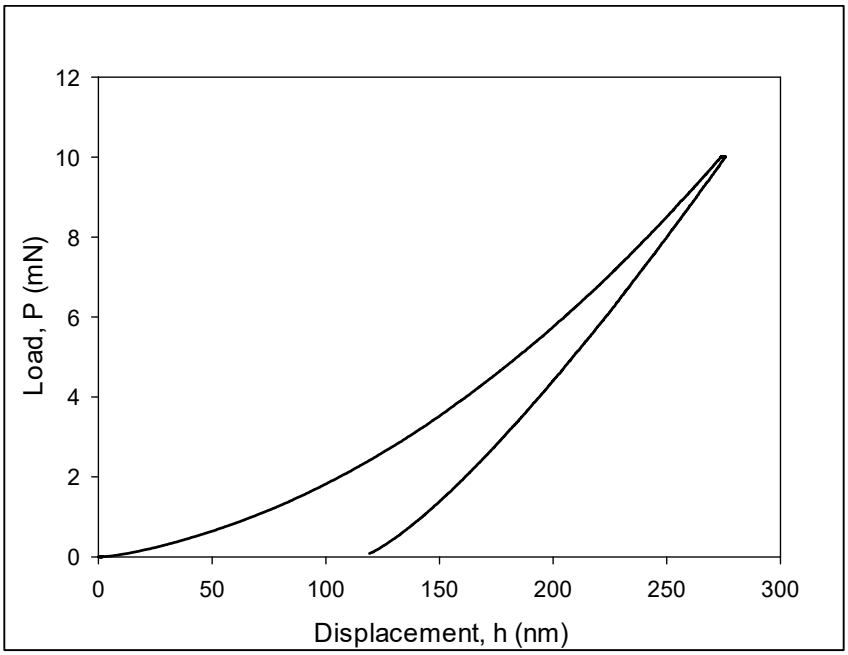

Figure 3.27 Example of load-displacement curve obtained after nanoindentation Test

During a nanoindentation experiment, the effects of the non-rigidity of an indenter, during a nanoindentation experiment, can be addressed by introducing a term called reduced modulus (E_r) through the following equation:

$$\frac{1}{E_r} = \frac{(1-\nu^2)}{E} + \frac{(1-\nu_i^2)}{E_i} \tag{3.31}$$

where E is the elastic modulus of the test specimen, E_i is the known elastic modulus of the indenter tip material, ν and ν_i are the Poisson's ratio of the test specimen and the

indenter tip, respectively. Typically the reduced modulus was measured from an indentation experiment using the following equation

$$E_r = \frac{\sqrt{\Pi}}{2} \times \frac{S}{\sqrt{A}} \tag{3.32}$$

where S is the stiffness of the test specimen at the maximum load and A is the projected contact area at the maximum load. Stiffness was determined from the initial slope $(\frac{dP}{dh})$ of the unloading segment of a load displacement curve. The contact area A was measured following the technique proposed by Oliver and Pharr [165] where they assumed the contact area to be a function of contact depth. For an ideal Berkovich tip, it can be expressed as:

$$A(h_c) = 24.5h_c^2 \tag{3.33}$$

In order to address any deviation from the ideal Berkovich geometry due to tip blunting, a modified version of Equation 3.32 was utilized.

$$A(h_c) = 24.5h_c^2 + C_1h_c^1 + C_2h_c^{1/2} + C_3h_c^{1/4} + C_4h_c^{1/8} + C_5h_c^{1/16} \tag{3.34}$$

where C_1, C_2, C_3, C_4, and C_5 are fitting constants. In order to determine the values of these constants, multiple indents were made at multiple depths on a quartz sample with known elastic modulus (69.6 GPa). The contact areas at the different known depths were determined from Equation 3.32 and these values were plotted to get A versus h_c plot. The values of constants C_1 to C_5 were determined by fitting the plot by Equation 3.34. Once the values of the constants are known for a particular tip geometry, Equation 3.32 was used to determine the value of reduced modulus (E_r) for any unknown material and Equation 3.31 was used to convert E_r to elastic modulus E.

Hardness is a material property that defines the resistance of the surface against plastic deformation. During a nanoindentation experiment, hardness H was determined by dividing the maximum load by the projected contact area.

$$H=\frac{P_{max}}{A} \tag{3.35}$$

Tabor [166] developed an approximate relationship between hardness and yield stress of which is true for many metals.

$$H \approx 3\sigma_Y \qquad \text{or} \qquad \sigma_Y \approx \frac{H}{3} \tag{3.36}$$

Equation 3.36 was used to determine stress during nanoindentation experiments.

3.9 Summary and Discussion

In this chapter, all the experimental procedure including sample preparation and data processing has been discussed in details. To measure the mechanical properties like effective modulus, yield stress, ultimate strength, Poisson's ratio, etc. uniaxial tensile specimens were prepared in a rectangular shaped hollow glass tube by an unique way using a vacuum suction method followed by an industry standard SMT reflow process. Typical dimension of the uniaxial tensile specimens were 80 (length) x 3 (width) x 0.5 (height) mm. Uniaxial tensile tests were performed using a micro tension torsion testing system. Nanoindentation experiments and a part of microstructural study were conducted on actual SAC305 BGA joints extracted from 14 x 14 mm PBGA assemblies (0.8 mm ball pitch, 0.46 mm ball diameter). Nanoindentation experiments were performed using Hysitron TI950 TriboIndenter and Zeiss crossbeam 550 scanning electron microscopy (SEM) was used for microstructural study to explain the physics behind mechanical property evolution.

CHAPTER 4

FINITE ELEMENT PREDICTION OF THE INFLUENCE OF POISSON'S RATIO ON THE RELIABILITY OF SAC LEAD FREE SOLDER JOINTS

4.1 Introduction

Finite element results to predict reliability are often very sensitive of using appropriate mechanical properties. Solder The Poisson's ratio (PR = ν) is a basic mechanical property of a material that relates the transverse contraction strain to the axial extension strain in a uniaxial tension stress-strain test. It is a required input parameter in almost all material constitutive models (e.g. elastic, elastic-plastic-creep, Anand model, etc.) used for solder in finite element simulations. Since it is more difficult to measure relative to standard stress-strain and creep curves, it is often guessed or assumed to be a fixed value (e.g. $\nu = 0.3$), independent of temperature, strain rate, and material composition.

In this chapter, it has been developed a framework for correcting this limitation and introducing Poisson's ratio as a forgotten but very important mechanical property of SAC lead free solders that should be taken into consideration. The approach involves the use of a similar three-dimensional finite element analysis (FEA) modeling approach discussed by the authors in reference [199] to investigate the effect of the value of the solder joint Poisson's ratio on the stress/strain histories in the finite element results for BGA components subjected to thermal cycling between -40 to 125 ^{o}C. Models were developed

for the 15 mm, 10 mm, and 5 mm components with SAC305 interconnects. For all three component sizes, plastic energy dissipation per cycle for the critical solder balls were determined for different values of the solder Poisson's ratio between $0.15 < \nu < 0.40$. The plastic work (DeltaW) per cycle results from the finite element calculations were then combined with the Morrow-Darveaux (dissipated energy based, DeltaW) [197] approach to calculate the number of cycles to initiate the crack in the critical solder ball for different values of solder Poisson's ratio. Correct prediction of the solder joint response is significantly dependent on the details of structural model including the mesh density, accuracy of material models used in the simulation, and adequacy of the prescribed loading and boundary conditions. The overall goal was to establish the fact that the specified Poisson's ratio strongly affects the mechanical Response and simulation results. Details of the utilized modeling procedure are now discussed.

4.2 Finite Element Reliability Models

4.2.1 Test Board for FEA Model and BGA Component Constructions

Figure 4.1 illustrates the test board from which different BGA component geometries were extracted for finite element modeling. The test board incorporated four different sizes of BGA components including 19 x 19 mm, 15 x 15 mm, 10 x 10 mm and 5 x 5 mm packages with SAC305 and SAC105 solder joints. Table 4.1 represents different component specifications. The test boards had dimensions of 100 x 67 x 1.5 mm, with a variety of surface finishes including Im-Ag, ENIG, and ENEPIG. In this study, finite element models were developed for the 15 mm, 10 mm, and 5 mm components with SAC305 interconnects which is highlighted in Table 4.1.

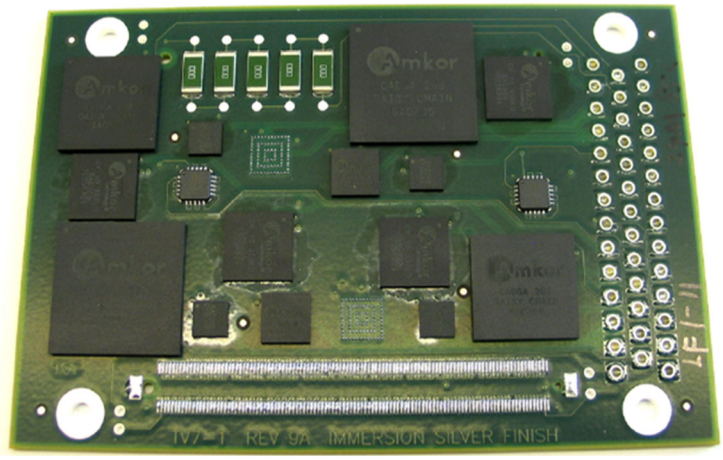

Figure 4.1 Assembled BGA Board

Table 4.1 Different Component Specifications of Assembled Board

Type	Body Size (mm)	Die Size (mm)	Ball/Lead Count	Pitch (mm)	Ball Alignment
BGA	19X19	12X12	288	0.8	Perimeter
BGA	15X15	12.7X12.7	208	0.8	Perimeter
BGA	10X10	5X5	360	0.4	Perimeter
BGA	5X5	3.2X3.2	97	0.4	Perimeter
CSP	7X7	5.9X5.9	84	0.5	Perimeter
MLP	5X5	4.5X4.5	20	0.25	Perimeter

Figure 4.2 illustrates the BGA component geometries before SMT assembly. There were 208, 360, and 97 solder balls in the 15 mm, 10 mm, and 5 mm components, respectively. The 15 mm and 10 mm packages were symmetric about horizontal and vertical center lines as shown by the red dashed lines. Using this geometrical advantage, quarter symmetry FEA models could be developed. The 5 mm package with 3 missing solder balls near the package center, and was symmetric about a diagonal as indicated by the red dashed line, therefore, a diagonal symmetry half model could be developed.

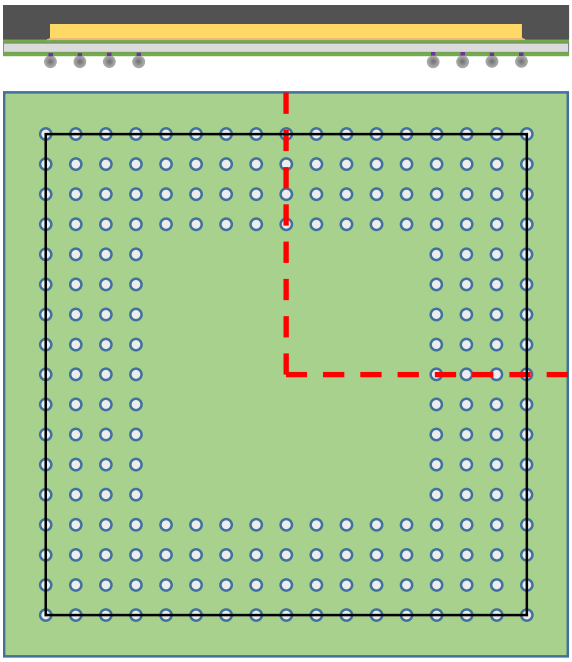

(a) 15 mm BGA

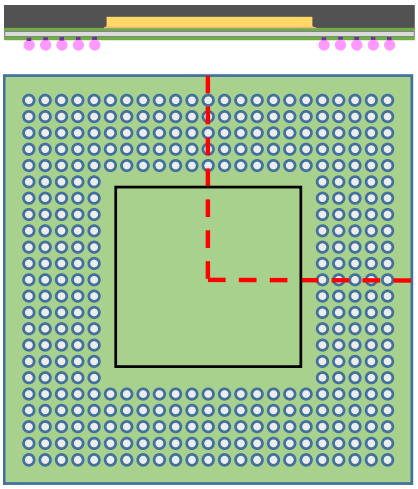

(b) 10 mm BGA

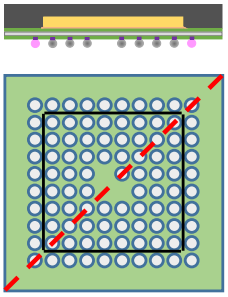

(c) 5 mm BGA

Figure 4.2 BGA Component Constructions

The die outlines are represented by black boxes in Figure 4.2, and solder balls outside of the die shadow were indicated with pink coloring on the package cross-sections. In the 15 mm package, only half of the outside row solder joints were outside of the die shadow, while the entire outside row of balls was outside of the die shadow in the 5 mm components. For the 10 mm packages, no solder balls were under the die.

4.2.2 Different Geometry and Meshing

The actual dimensions of the SAC305 solder joints, and other thin layers in the packages were extracted by cross-sectioning of several assembled PBGA components by the authors of reference [199]. Figure 4.3 shows an optical microscopy image of the region near a solder ball in one of the assembled 15 mm packages as an example.

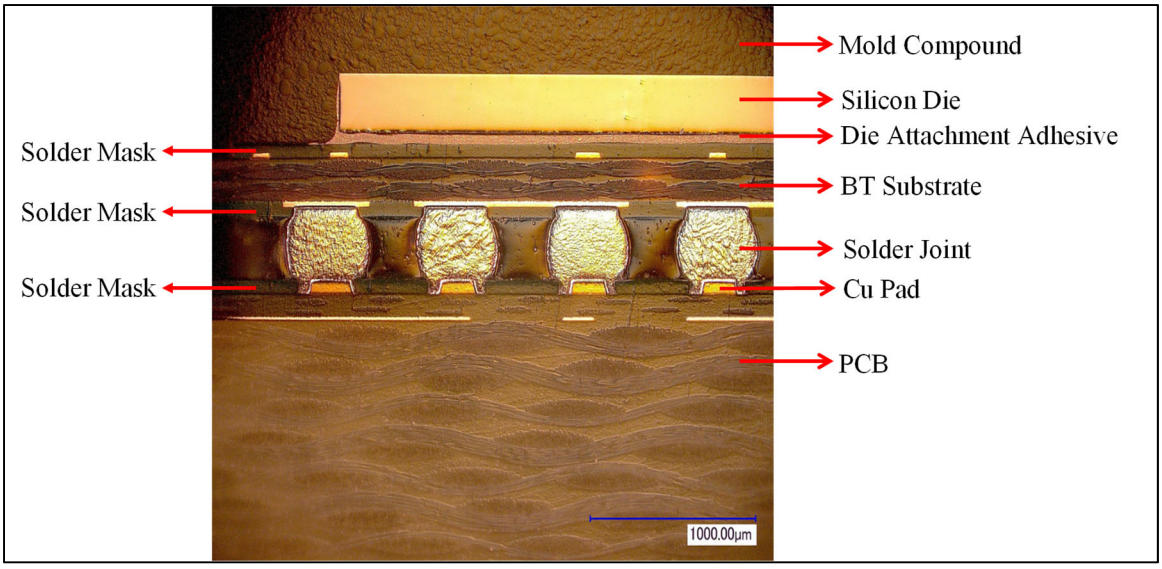

Figure 4.3 Optical Microscopy Cross-section of 15 mm BGA

A measurement microscope was used to extract dimensions from the cross-sections to build the finite element mesh design. More specifically, the thicknesses of the three solder mask (SM) layers, mold compound, die attachment layer, BT substrate, and copper pad layers were observed in each package and listed in Table 4.2. The shapes of a typical solder joints were also determined. Finally, the dimensions of the copper vias present in

the PCB under the pads of the fine pitch components (10 mm and 5 mm BGAs) were measured.

Table 4.2 Different Component Dimensions (mm) form Microscopy

Dimension	15mm BGA	10 mm BGA	5 mm BGA
Die Edge Length	12.7	5.0	3.2
Die Thickness	0.280	0.165	0.165
Mold Thickness	0.73	0.45	0.44
Die Attach Thickness	0.05	0.02	0.02
Solder Mask Thickness	0.06	0.05	0.05
BT Substrate Thickness	0.20	0.10	0.07
Copper Pad Thickness	0.025	0.025	0.025

ANSYS (APDL) finite element software was used for meshing and analyzing the PBGA packages. The meshing was done by Solid185 elements, which support viscoplasticity, hyperelasticity, stress stiffening, creep, large deformation and large strain capabilities. Brick elements were used exclusively in the meshes (no tetrahedrons), and aspect ratios were kept small. The meshes for the 15 mm, 10 mm, and 5 mm components contained are shown in Figures 4.4, 4.5, and 4.6, respectively. The mesh for the 15 mm component contained 1,134,708 elements, whereas, the 10 mm, and 5 mm components contained 1,005,120, and 764,420 elements, respectively. A close-up of the mesh of the 15 mm BGA near the solder balls with details of the various material layers is shown in Figure 4.7.

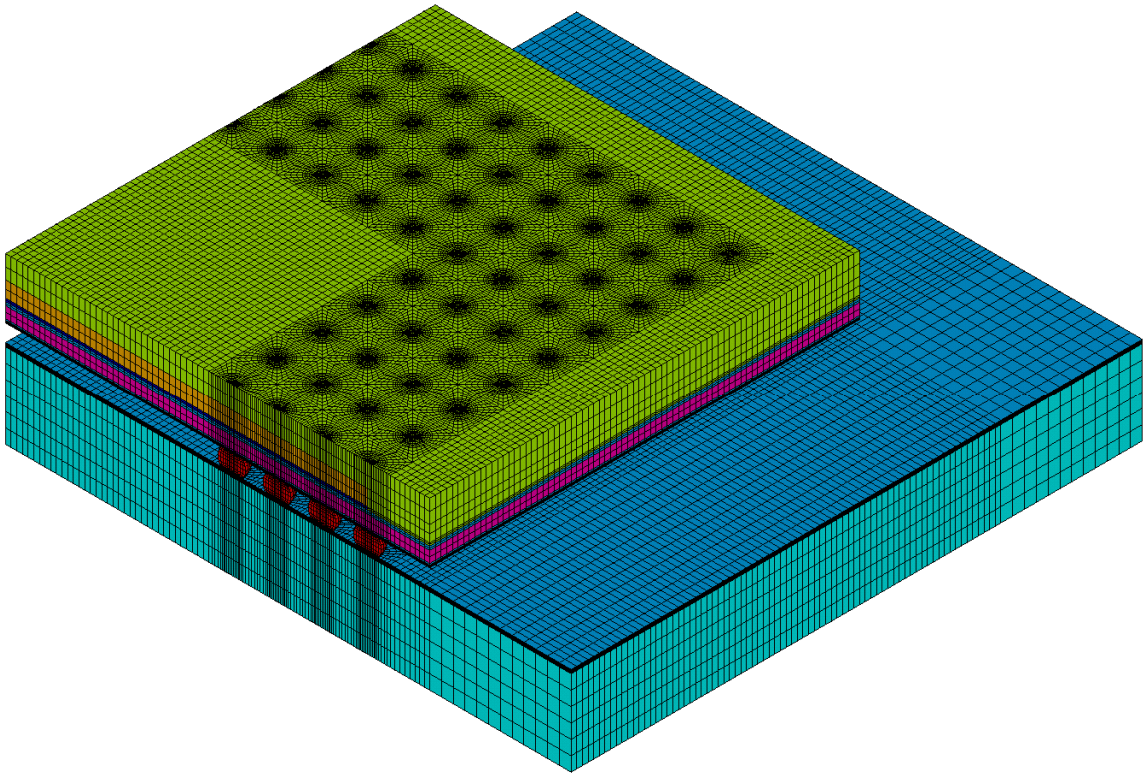

(a) Quarter model

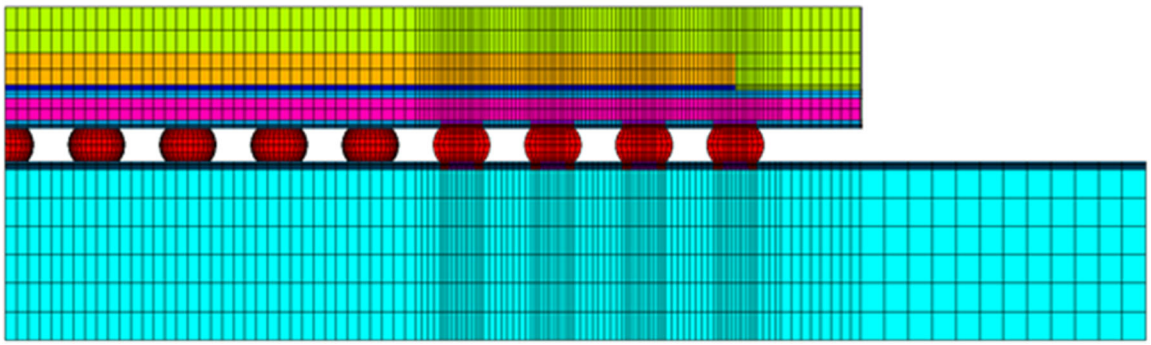

(b) Front View

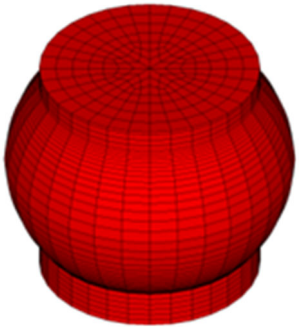

(c) Solder Ball

Figure 4.4 Finite Element Mesh (15 mm BGA)

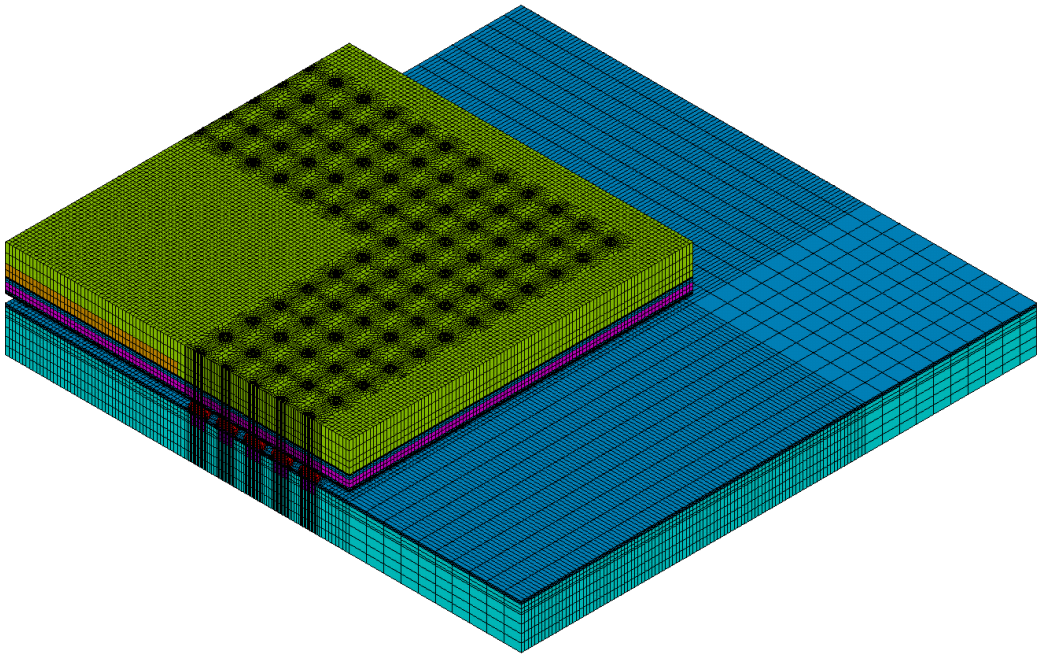

(a) Quarter Model

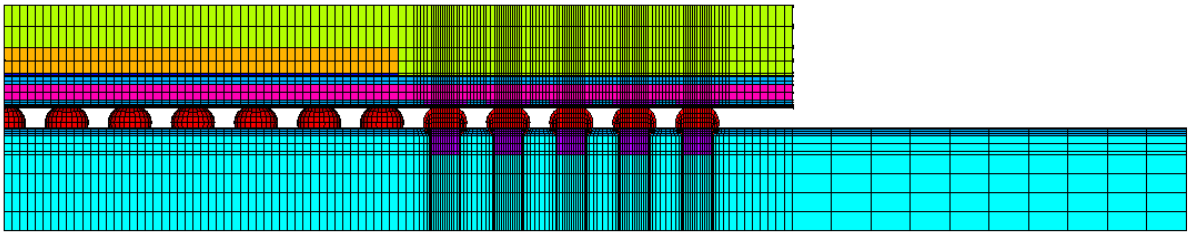

(b) Front View

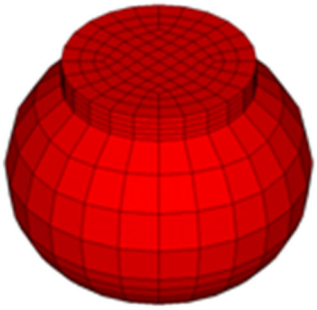

(c) Solder Ball

Figure 4.5 Finite Element Mesh (10 mm BGA)

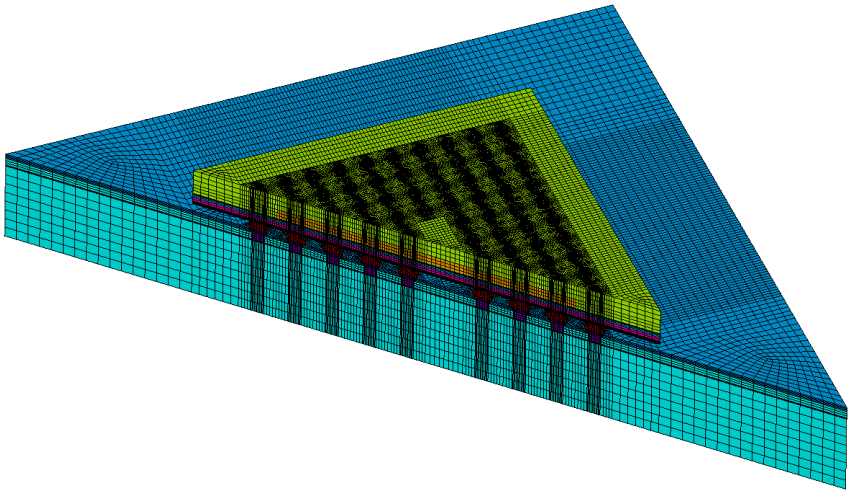

(a) Half Model

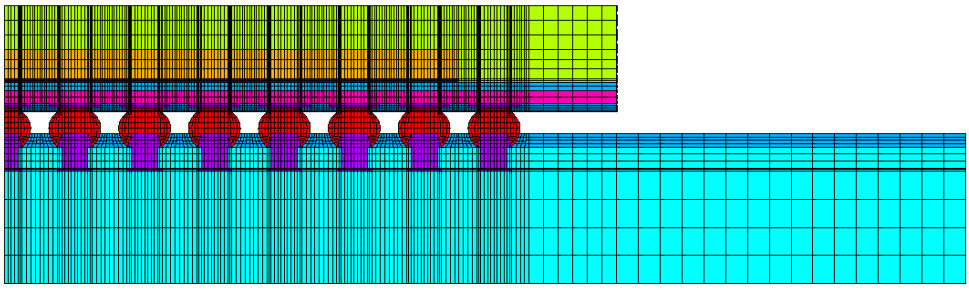

(b) Front View

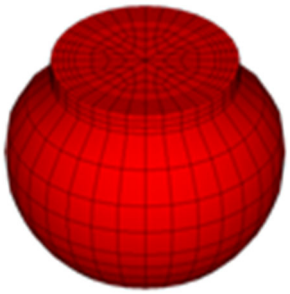

(c) Solder Ball

Figure 4.6 Finite Element Mesh (10 mm BGA)

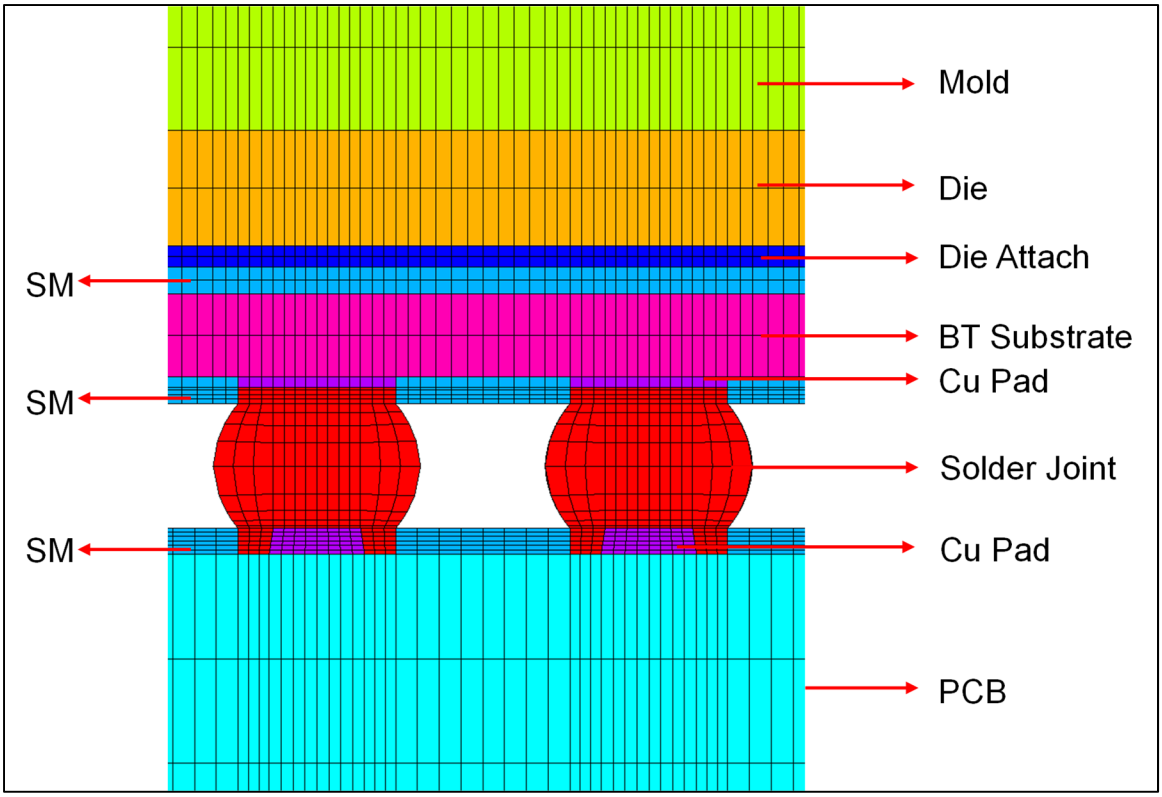

Figure 4.7 Mesh near Solder Joints (15 mm BGA)

4.2.3 Material Behavior Models and Mechanical Properties for FEA Modeling

To model the whole package different mechanical properties for different components and viscoplastic constitutive models listed by the authors in reference [199] has been utilized here. In particular, the Anand viscoplastic material model [115] was employed to accurately model the behavior of the SAC305 joints in the various FEA models for no aging condition and the values for nine parameters of the model are listed in Table 4.3. The remaining packaging materials (silicon, copper, soldermask, die attachment adhesive, mold compound, BT substrate, and PCB) were assumed to be linear elastic materials. The directional behaviors of the BT substrate and PCB were included by using orthotropic material constants including temperature dependence. The material constants were measured using stress-strain and CTE (TMA) testing [78], and are listed in Table 4.4.

Table 4.3 Anand Parameters for SAC3059 (No Aging)

Constant Number	Anand Constant	Units	SAC305 (RF)
1	s_0	MPa	21.00
2	Q/R	1/K	9320
3	A	sec^{-1}	4137
4	ξ	Dimensionless	4.00
5	m	Dimensionless	0.50
6	h_o	MPa	45,000
7	$\hat{s}$	MPa	23.97
8	n	Dimensionless	0.0323
9	a	Dimensionless	1.05

Table 4.4 Material Properties Used for FEA Modeling

Material	Elastic Modulus (GPa)	Shear Modulus (GPa)	Poisson's Ratio	CTE [1/°C]
Solder Ball (Anand Model)	54, 45, 41, 37, 34, 30 at -40, 25, 50, 75, 100, 125 °C	Isotropic	0.15/0.20/0.25/0.30/0.35/0.40	24.5×10^{-6}
Copper Pad	129.0	Isotropic	0.34	16.3×10^{-6}
Silicon Die	163.0	Isotropic	0.28	2.5×10^{-6}
Die Attachment	6.77	Isotropic	0.35	83.6×10^{-6}
Solder Mask	3.10	Isotropic	0.30	30×10^{-6}
Mold Compound	23.52	Isotropic	0.25	10×10^{-6}
PCB	19.30 (xy, -40 °C)	8.71 (xy, -40 °C)	0.11 (xy)	14.5×10^{-6} (xy)
	13.20 (xy, 125 °C)	5.95 (xy, 125 °C)		
	8.48 (z, -40 °C)	3.80 (xz, yz; -40 °C)	0.39 (xz, yz)	67.2×10^{-6} (z)
	5.84 (z, 125 °C)	2.60 (xz, yz; 125 °C)		
BT Substrate	17.89 (xy)	8.06 (xy)	0.11 (xy)	12.4×10^{-6} (xy)
	7.85 (z)	2.82 (xz, yz)	0.39 (xz, yz)	57.0×10^{-6} (z)

4.2.4 Loads and Boundary Condition

Figure 4.8 shows the applied temperature history used in this finite element simulation. The loading applied to the models consisted of a time dependent temperature distribution that matched the thermal cycling from -40 to 125 ºC experienced by the assemblies in the life testing experiments. Each cycle consists of 1.5 hour (90 minute), which featured ramp and dwell times of 30 minutes and 15 minutes, respectively to match the experimental in-chamber profile. Each ramp step was divided into 6 load steps, while each dwell step was divided into 2 load steps. Within each load step, the temperature changes were linear in time. The package assembly was assumed to be in a stress-free state at 25 ºC (room temperature), with no initial residual stresses/deformations induced in the manufacturing process. After the cooldown from 25 ºC to -40 ºC, three thermal cycles were simulated.

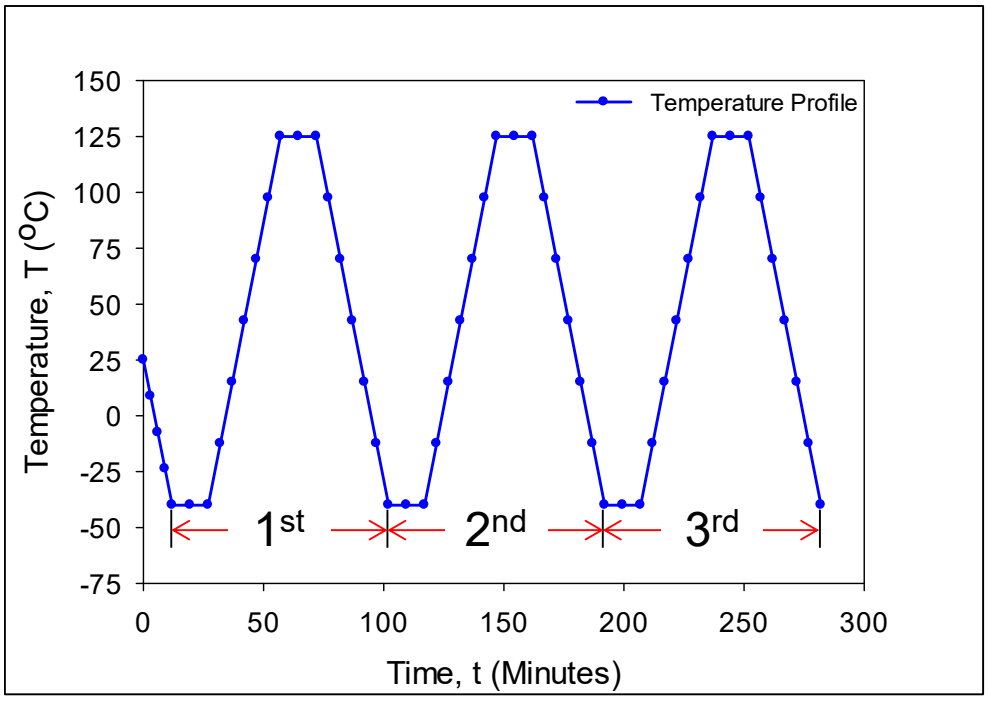

Figure 4.8 Temperature Profile of Thermal Cycling

In all of the models, it was found that the cycle to cycle variation of the solder stress/strain behavior became stable by the third cycle. The values during the third cycle were extracted to evaluate the dissipated plastic work per cycle (ΔW) that was used to predict fatigue life. The quarter model for the 15 mm and 10 mm BGA components were appropriately constrained along the axes of symmetry, so that for a node in a symmetry plane, the displacement component perpendicular to the symmetry plane was required to be zero. In addition, all three displacements were set to zero for the center node at the bottom surface of the PCB to prevent any rigid body motions. The half model for the 5 mm BGA was similarly constrained along its diagonal line of symmetry. Perfect bonding was assumed at all interfaces between different materials. Iterative solution procedures have been used due to the nonlinear material and kinematic (large deformation) characteristics of the model.

4.3 Finite Element Results

The development of inelastic strains in the solder materials leads to accumulation of plastic work (W_{pl}). In the case of thermal cycling of BGA packages, plastic work was induced in solder joints due to the mismatches of coefficient of thermal expansions (CTEs) of the different materials comprising the assembly. Figures 4.9 (a), (b) and (c) show the predicted contours of accumulated plastic work (W_{pl}) in the solder joints of the 15 mm, 10 mm, and 5 mm BGA components, respectively, after completion of three complete thermal cycles for the non-aged assemblies. For the 15 mm BGA (0.8 mm pitch), the region of highest plastic work accumulation and crack propagation was at the bottom of the solder joints (board side), whereas for the finer pitch solder interconnections (0.4 mm) in the 10 mm and 5 mm BGA components, the cracks initiated at one of the top corners of the solder

joint at the alloy/package interface where the maximum accumulated plastic work occurred, and then propagated along the top of the solder joints. This finding agreed well with the experimental measurements, where first failures were found in the corner joints of the all the BGA packages. In addition, typical crack propagation paths in failed joints from the experimental test boards are included. These crack locations agreed well with the predicted regions of highest plastic work.

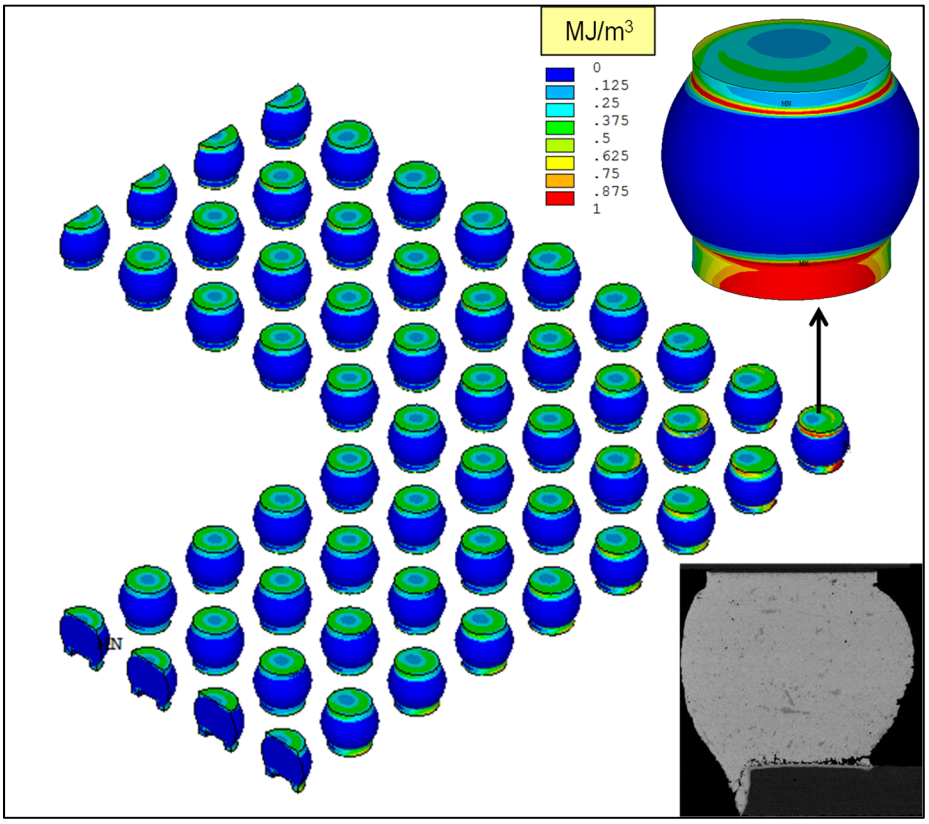

(a) 15 mm BGA

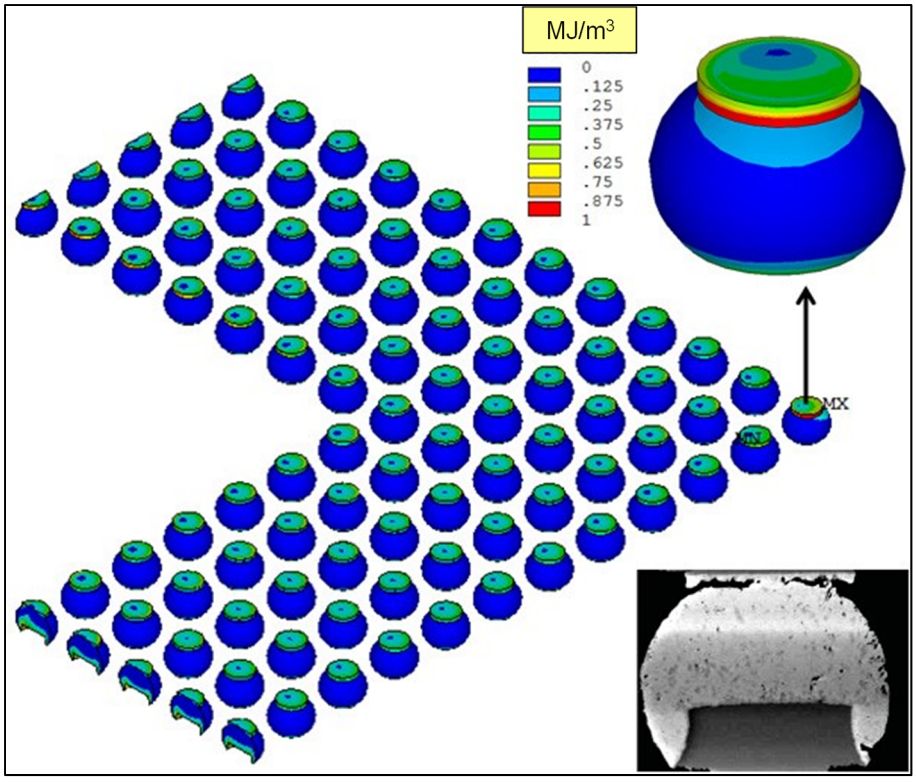

(b) 10 mm BGA

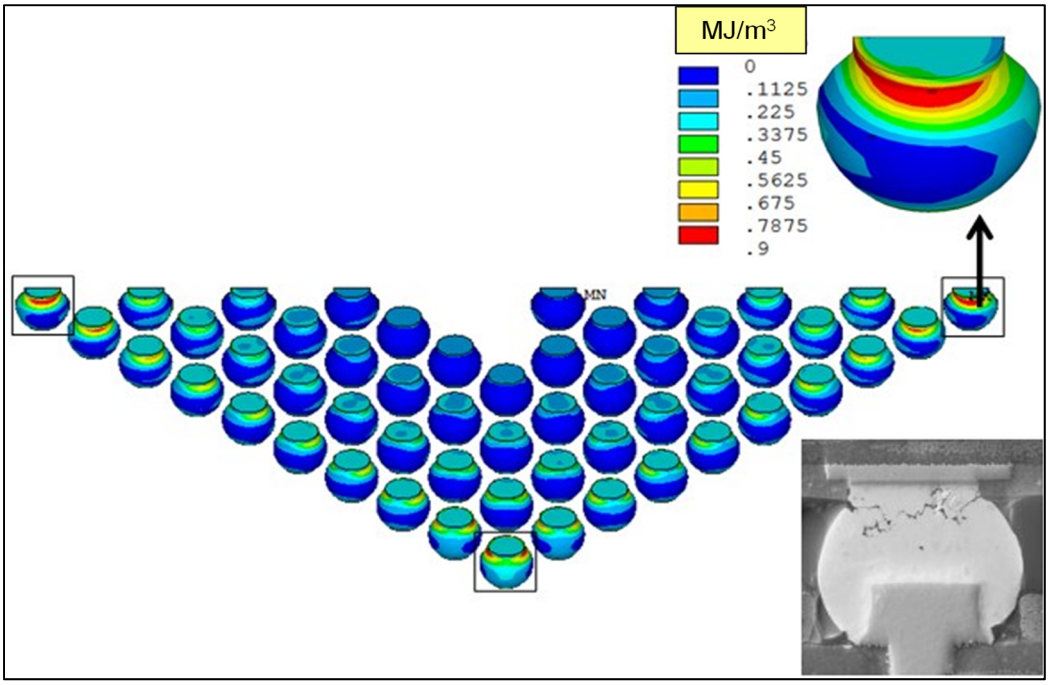

(c) 5 mm BGA

Figure 4.9 Contours of Accumulated Plastic Work (MPa)

To reduce the mesh dependency for the calculated plastic work values in the critical solder joints, volume averaged values were calculated across a set of N elements along the crack path using the following relationship:

$$\left(W_{pl}\right)_{Averaged} = \frac{\sum_{i=1}^{N}(W_{pl})_i V_i}{\sum_{i=1}^{N} V_i} \tag{4.1}$$

where $(W_{pl})_i$ are the elemental values of the accumulated plastic work and V_i are the volumes of the elements.

Darveaux [13] has developed a life prediction methodology for solder joints based on the energy dissipation (ΔW) occurring during thermal cycling. The procedure uses a power law relation for estimating crack initiation. More precisely it calculates the number of thermal cycle to initiate the crack as follows:

$$N_i = K_1 \left(\Delta W\right)^{K_2} \tag{4.2}$$

where Ni is the number of thermal cycles to crack initiation, K_1 and K_2 are material constants, and ΔW is the change in W_{pl} during one cycle. Typically, $-3 \le K_2 \le -1$, from previous experimental tests [14]. In this analysis, an example value of K_1= 120 and K_2 = -2.0 were used for the calculation of number of thermal cycles to crack initiation.

Using the FEA results for different values of the input solder Poisson's ratio, the predicted dependencies of the plastic work per cycle and the cycles to crack initiation on the solder Poisson's ratio were determined for the three types of assembled PBGA components. The results for the 15mm, 10 mm, and 5 mm components are listed in Table 4.5, and plotted in Figures 4.10, and 4.11 respectively.

Table 4.5 Predicted Plastic Work and Cycles to Crack Initiation for Various Values of the Specified Solder Joint Poisson's Ratio

Poisson's Ratio (ν) (Input to the FEA Model)	15 mm BGA		10 mm BGA		5 mm BGA	
	Plastic Work Per Cycle ΔW (MPa)	No. of Cycles to Crack Initiation (N_f)	Plastic Work Per Cycle ΔW (MPa)	No. of Cycles to Crack Initiation (N_f)	Plastic Work Per Cycle ΔW (MPa)	No. of Cycles to Crack Initiation (N_f)
0.15	0.1714	4085	0.1673	4287	0.1393	6184
0.20	0.1898	3328	0.1857	3476	0.1577	4825
0.25	0.1910	3293	0.1869	3435	0.1589	4753
0.30	0.1946	3169	0.1905	3307	0.1625	4544
0.35	0.1971	3089	0.1930	3225	0.1650	4413
0.40	0.2092	2742	0.2051	2849	0.1771	3826

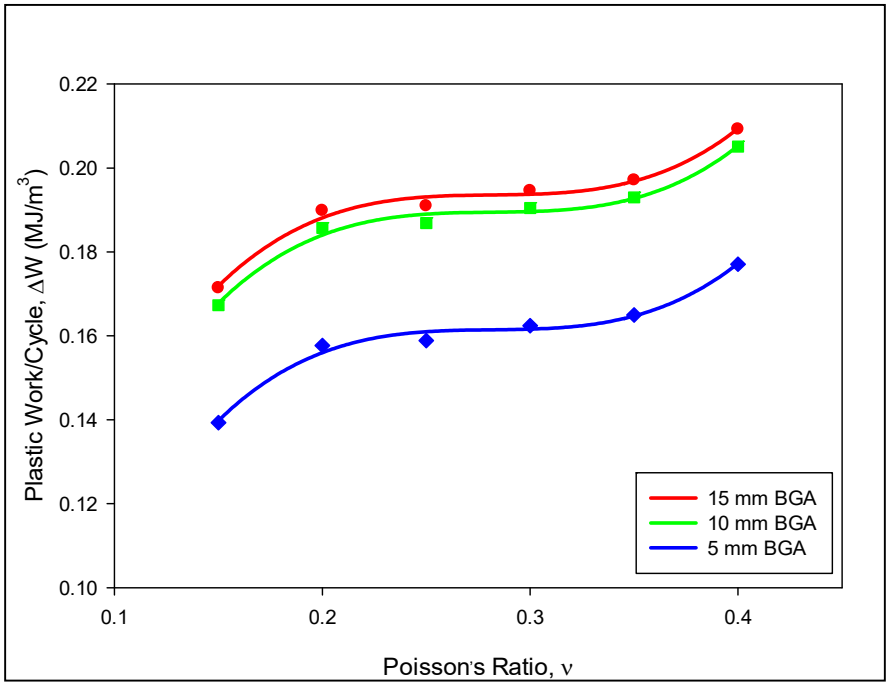

Figure 4.10 Predicted Variation of Plastic Work per Cycle with Solder Joint Poisson's Ratio

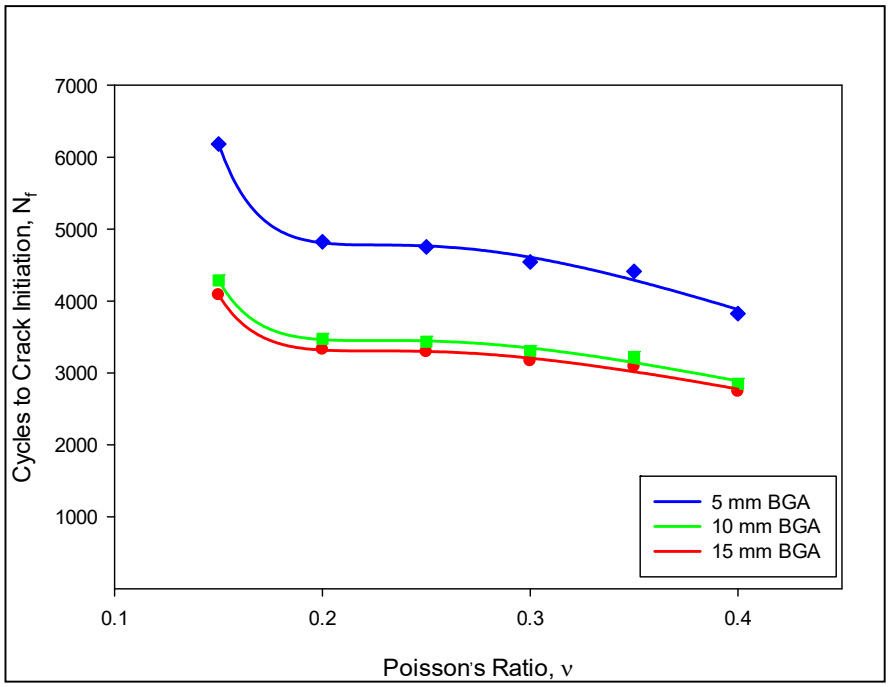

Figure 4.11 Predicted Dependence of the Cycles to Crack Initiation on the Solder Joints Poisson's Ratio

4.4 Summary and Discussion

In the current work, it has been extended the previous research on the effects of aging on lead free solder material behavior to explore the effects of prior aging on solder joint (board level) reliability in actual assemblies. The overall objective was to develop new reliability prediction procedures counting the influence of solder joint Poisson's ratio in finite element modeling to investigate its effect on reliability. The developed reliability modeling procedure has been applied to a family of assembled PBGA components. In the simulations, the packages were subjected to thermal cycling between -40 to +125 ºC.

From the finite element results shown in Table 4.5 and Figures 4.10, and 4.11, the value of the input Poisson's ratio specified in the FEA simulation affected the results for both the plastic work per cycle and the cycles to crack initiation considerably. The variations in the plastic work per cycle for different Poisson's ratio values were ~22% for

the 15 mm BGA, ~23% for the 10 mm BGA, and ~27% for the 5 mm BGA. The effect was more significant in terms of the reliability. For the predicted cycles to crack initiation, the variations for different Poisson's ratio values were ~33% for the 15 mm BGA, ~34% for the 10 mm BGA, and ~38% for the 5 mm BGA. In summary, the finite element simulation results have demonstrated that for specified values of $0.15 < \nu < 0.40$, the solder plastic work varied over 25% and the predicted reliability varied approximately 40% when using a Morrow-Darveaux energy-based fatigue model. Thus, the FEA results are highly sensitive to the specified value of the solder Poisson's ratio, so that it is important to carefully characterize the Poisson's effect in lead free solders.

CHAPTER 5

EXPERIMENTAL CHARACTERIZATION OF THE DEPENDENCE OF POISSON'S RATIO OF LEAD FREE SOLDER ON TEMPREATURE, STRAIN RATE, SOLIDIFICATION PROFILE AND ISOTHERMAL AGING

5.1 Introduction

Solder joint reliability under thermal and mechanical loading is a great concern in electronic packaging industry. Reliability testing and computational modeling are widely used methods for this assessment. From the finite element results presented in chapter 4, it is evident that the specified value of solder joint Poisson's ratio greatly affects the simulation results as the plastic work per cycle as well as the reliability (number of cycles to initiate the crack) under thermal cycling loading varied significantly with different values of solder joint Poisson's ratio between $0.15 < \nu < 0.40$. Therefore, it emphasized the fact that rather than assuming the value of solder joint Poisson's ratio for different finite element simulations and reliability prediction model, it should be experimentally determined for different test conditions.

In this work, an experimental investigation was conducted to characterize the Poisson's ratio of several SAC and SAC+X lead free solders. Uniaxial tensile stress-strain tests were carried out on SAC305 (96.5Sn3.0Ag0.5Cu), SAC405 (95.5Sn4.0Ag0.5Cu), Innolot (SAC+3% Bi), and SAC_Q (SAC+3% Bi) specimens using a micro tension/torsion

testing machine with two strain rates (0.0001, and 0.00001 (sec^{-1})) and four testing temperatures (T = 25, 50, 75, 100 ºC). Deformations and strains in the axial and transverse directions were measured using miniature strain gages with automatic data acquisition from LabVIEW software. The recorded transverse strain vs. axial strain data for each test were then fit with a linear regression analysis to determine the Poisson's ratio value. A large test matrix of experiments was developed to study the effects of temperature, strain rate, alloy composition, solidification cooling profile, and isothermal aging (Aging at T = 125 °C) exposure on the value of solder Poisson's ratio and to create a material property database for finite element simulations. The details of sample preparation including strain gage mounting, experimental procedure, data acquisition and raw data processing was discussed in section 3.5.3. Utilizing the method the experimental results are discussed now.

5.2 Alloy Composition and Experimental Test Matrix

In this study, uniaxial tensile tests were carried out on four different SAC and SAC+X lead free solder alloys. Table 5.1 represents the alloys along with their vendor recommended chemical compositions.

Table 5.1 Vendor Specified Compositions of Solder Alloys (wt%)

Alloy	Sn	Ag	Cu	Bi	Ni	Sb
SAC 305	96.50	3.00	0.50	0.00	0.00	0.00
SAC405	95.50	4.00	0.50	0.00	0.00	0.00
Innolot	90.95	3.80	0.70	3.00	0.15	1.40
SAC_Q	92.50	4.00	0.50	3.00	0.00	0.00

A large test matrix of experiments was studied here for determining Poisson's ratio experimentally. All the four solder alloys listed in Table 5.1 were tested with both water quenched (WQ) and reflowed (RF) microstructures. The experiments for water quenched (WQ) microstructure were carried out at a single strain rate (0.00001 (sec^{-1}), whereas, two strain rates (0.0001 and 0.00001 (sec^{-1})) were used for reflowed (RF) microstructure sample testing for no aging condition. The test matrix for both cases are listed in Tables 5.2, and 5.3.

Table 5.2 Test Matrix for Water Quenched (WQ) Microstructure

Alloy	Strain Rate (sec^{-1})	Test Temperature (°C)			
		25	50	75	100
SAC305	10^{-5}	√	√	√	√
SAC405		√	√	√	√
Innolot		√	√	√	√
SAC_Q		√	√	√	√

Table 5.3 Test Matrix for Reflowed (RF) Microstructure

Alloy	Strain Rate (sec^{-1})	Test Temperature (°C)			
		25	50	75	100
SAC305	10^{-4}	√	√	√	√
	10^{-5}	√	√	√	√
SAC405	10^{-4}	√	√	√	√
	10^{-5}	√	√	√	√
Innolot	10^{-4}	√	√	√	√
	10^{-5}	√	√	√	√
SAC_Q	10^{-4}	√	√	√	√
	10^{-5}	√	√	√	√

A set of additional experiments was performed to determine the effects of isothermal aging on the Poisson's ratio values. For the aging experiments, the starting point was the reflowed (RF) microstructure for each of the three solder alloys. The samples were aged at T = 125 ºC for various durations including 0 (no aging), 1, 2, 3, 4, 5, 6, 12,

and 24 hours. For each aging duration, testing was performed using the same four testing temperatures (T = 25, 50, 75, 100 ^{o}C) and a single strain rate (0.00001 (sec^{-1})). The test matrix is shown in Table 5.4.

Table 5.4 Test Matrix for Isothermal Aging with Reflowed (RF) Microstructure

Alloy	Strain Rate (sec^{-1})	Test Temperature (°C)	Isothermal Aging at T = 125 ^{o}C								
			No Aging	1 Hour Aging	2 Hours Aging	3 Hours Aging	4 Hours Aging	5 Hours Aging	6 Hours Aging	12 Hours Aging	24 Hours Aging
SAC305	10^{-5}	25	√	√	√	√	√	√	√	√	√
		50	√	√	√	√	√	√	√	√	√
		75	√	√	√	√	√	√	√	√	√
		100	√	√	√	√	√	√	√	√	√
SAC405		25	√	√	√	√	√	√	√	√	√
		50	√	√	√	√	√	√	√	√	√
		75	√	√	√	√	√	√	√	√	√
		100	√	√	√	√	√	√	√	√	√
Innolot		25	√	√	√	√	√	√	√	√	√
		50	√	√	√	√	√	√	√	√	√
		75	√	√	√	√	√	√	√	√	√
		100	√	√	√	√	√	√	√	√	√
SAC_Q		25	√	√	√	√	√	√	√	√	√
		50	√	√	√	√	√	√	√	√	√
		75	√	√	√	√	√	√	√	√	√
		100	√	√	√	√	√	√	√	√	√

5.3 Results for Non-Aged Solder Samples

Typical transverse strain vs. axial strain raw data for an example test for SAC305 is shown in Figure 3.12 in chapter 3 along with the corresponding linear regression fit of Equation 3.6. The variation of the raw data was quite linear, and the slope is the desired Poisson's ratio. Utilizing the method described in section 3.5.3 example test results from regression fitting for SAC305 solder alloy for a particular strain rate (0.00001 (sec^{-1}) are shown in Figure 5.1 (a) for water quenched (WQ) microstructure, whereas, in Figures 5.1 (b), and 5.1 (c), the results for two strain rates (0.0001 and 0.00001 (sec^{-1})) are presented for reflowed (RF) microstructure.

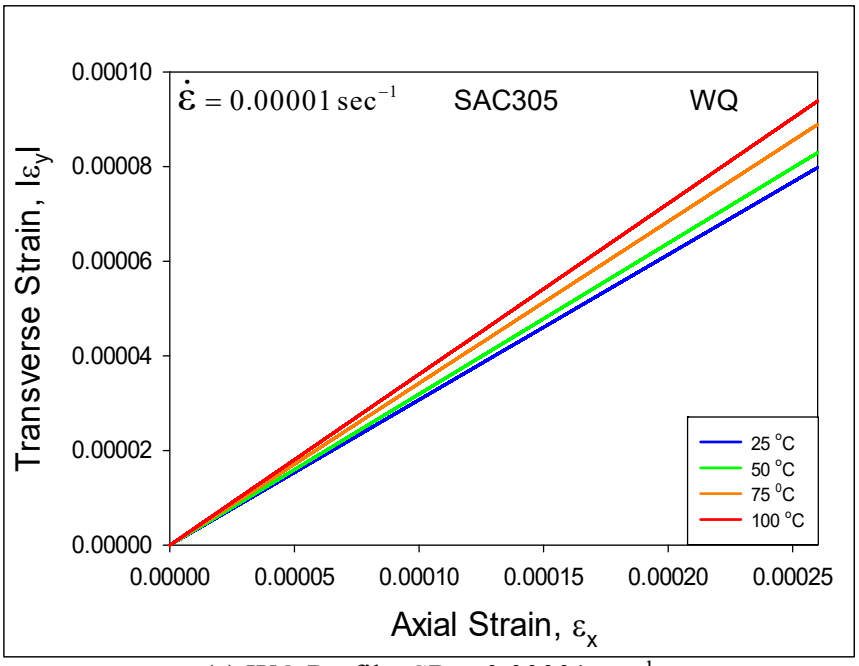

(a) WQ Profile, SR = 0.00001 sec^{-1}

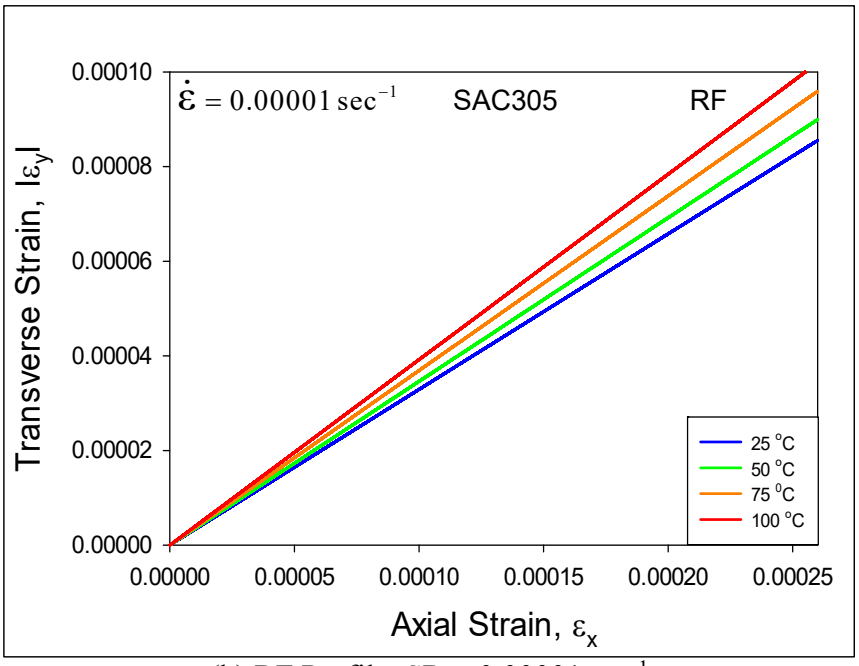

(b) RF Profile, SR = 0.00001 sec^{-1}

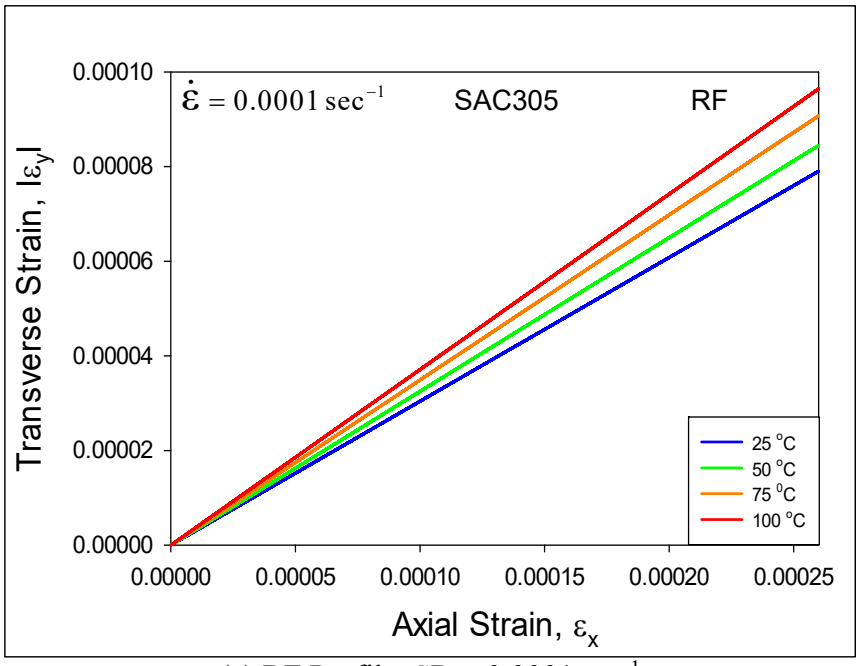

(c) RF Profile, SR = 0.0001 sec^{-1}

Figure 5.1 Example Poisson's Ratio Test Data of SAC305 Solder Alloy for Different Temperatures

In all cases, the Poisson's ratio was seen to increase significantly with temperature. Similar trends of results from the regression fitting were obtained for each leg of the test matrix presented in Table 5.2 and 5.3. The measured results are listed in Table 5.5 and 5.6 and the comparisons are shown in Figures 5.2, 5.3, and 5.4.

Table 5.5 Poisson's Ratio Values for Different Lead Free Solders with Water Quenched (WQ) Microstructure (No Aging)

Alloy	Strain Rate (sec^{-1})	Poisson's Ratio (ν)			
		25 °C	50 °C	75 °C	100 °C
SAC305	10^{-5}	0.307 (0.002)	0.319 (0.002)	0.342 (0.002)	0.361 (0.003)
SAC405		0.284 (0.002)	0.302 (0.002)	0.327 (0.003)	0.348 (0.002)
Innolot		0.265 (0.003)	0.293 (0.003)	0.319 (0.002)	0.336 (0.003)
SAC_Q		0.261 (0.002)	0.289 (0.001)	0.311 (0.003)	0.331 (0.001)

Table 5.6 Poisson's Ratio Values for Different Lead Free Solders with Reflowed (RF) Microstructure (No Aging)

Alloy	Strain Rate (sec^{-1})	Poisson's Ratio (ν)			
		25 °C	50 °C	75 °C	100 °C
SAC305	10^{-4}	0.304 (0.001)	0.324 (0.001)	0.349 (0.001)	0.371 (0.001)
	10^{-5}	0.329 (0.002)	0.346 (0.001)	0.369 (0.001)	0.383 (0.001)
SAC405	10^{-4}	0.292 (0.001)	0.308 (0.002)	0.332 (0.001)	0.351 (0.001)
	10^{-5}	0.305 (0.001)	0.322 (0.001)	0.344 (0.003)	0.364 (0.001)
Innolot	10^{-4}	0.279 (0.003)	0.301 (0.002)	0.325 (0.002)	0.341 (0.003)
	10^{-5}	0.291 (0.003)	0.314 (0.001)	0.331 (0.002)	0.353 (0.003)
SAC_Q	10^{-4}	0.274 (0.001)	0.298 (0.001)	0.318 (0.003)	0.335 (0.002)
	10^{-5}	0.289 (0.002)	0.309 (0.003)	0.326 (0.002)	0.346 (0.002)

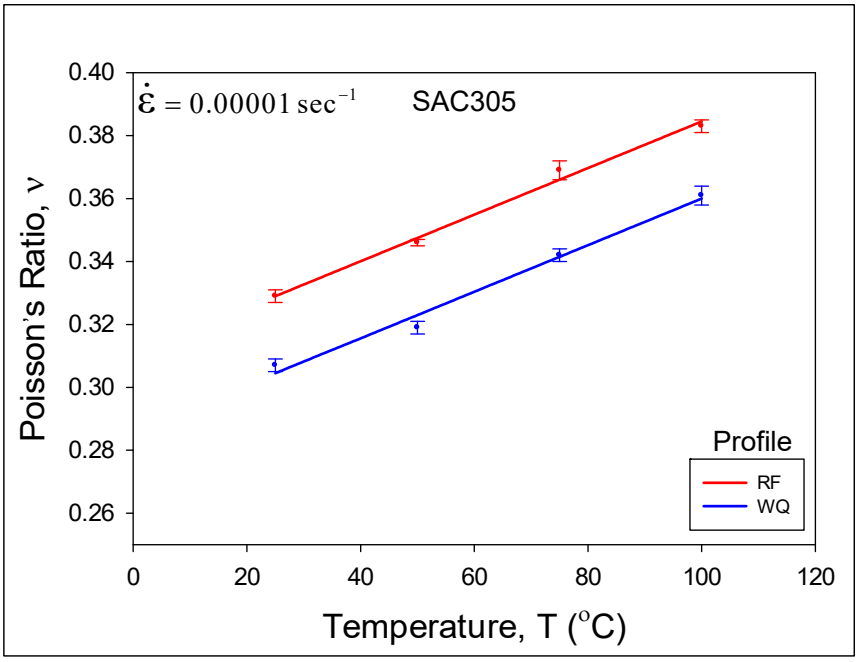

(a) SAC305

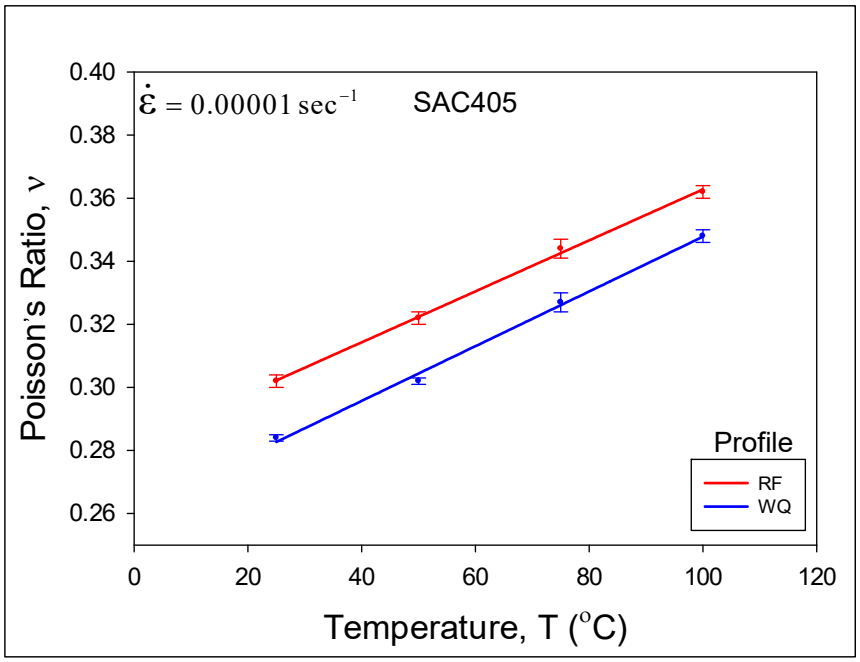

(b) SAC405

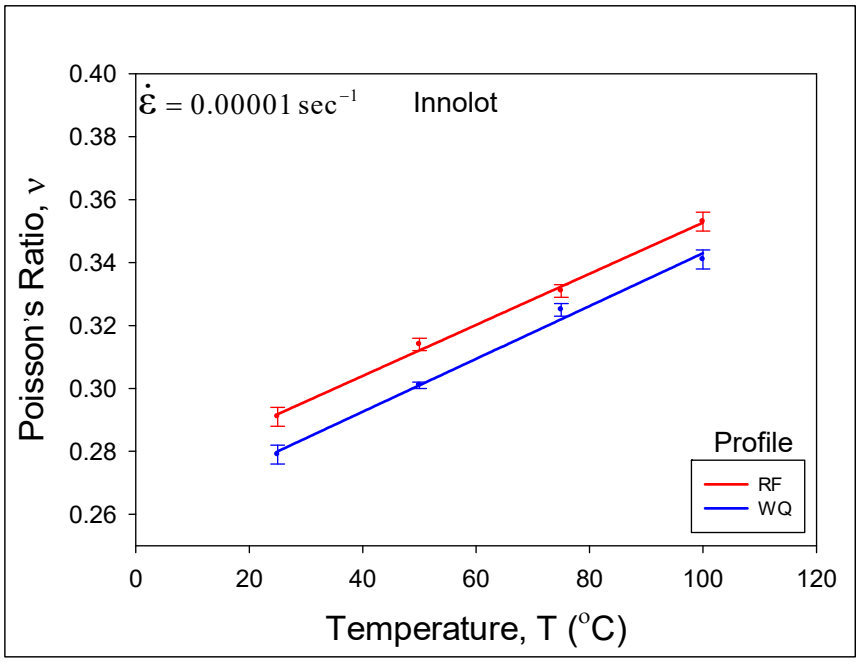

(c) Innolot (SAC+Bi)

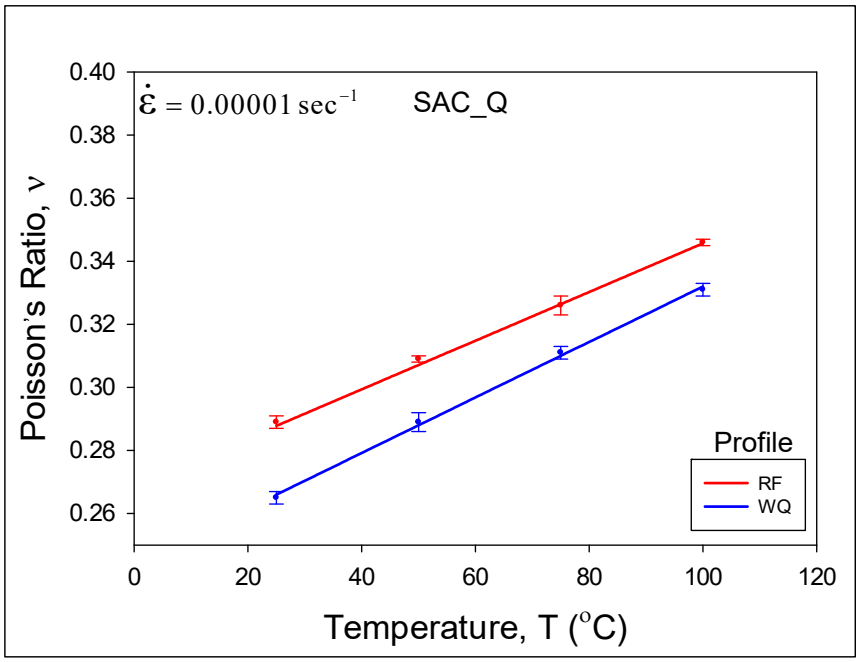

(d) SAC_Q (SAC+Bi)

Figure 5.2 Temperature Dependence of the Poisson's Ratio for Different Microstructures (WQ and RF)

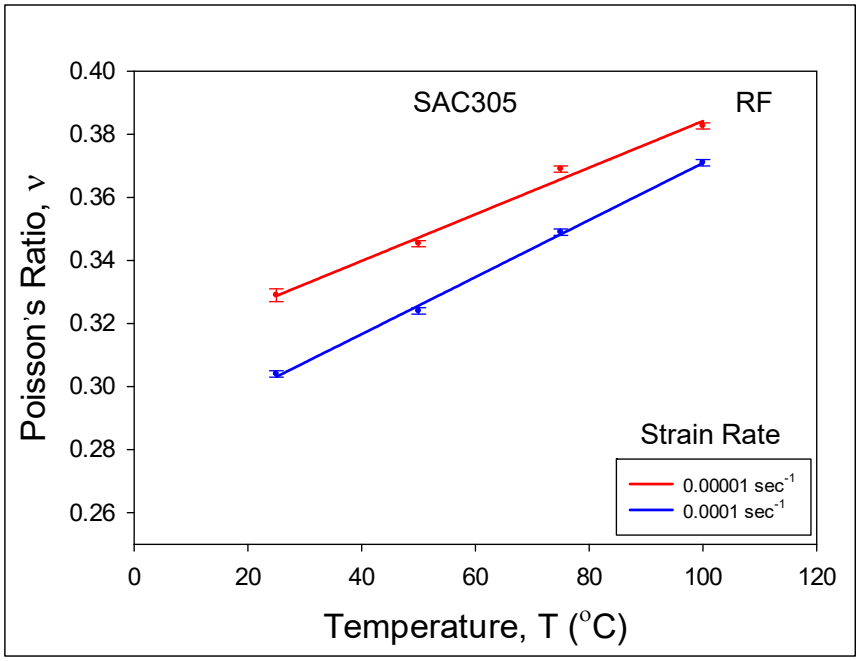

(a) SAC305

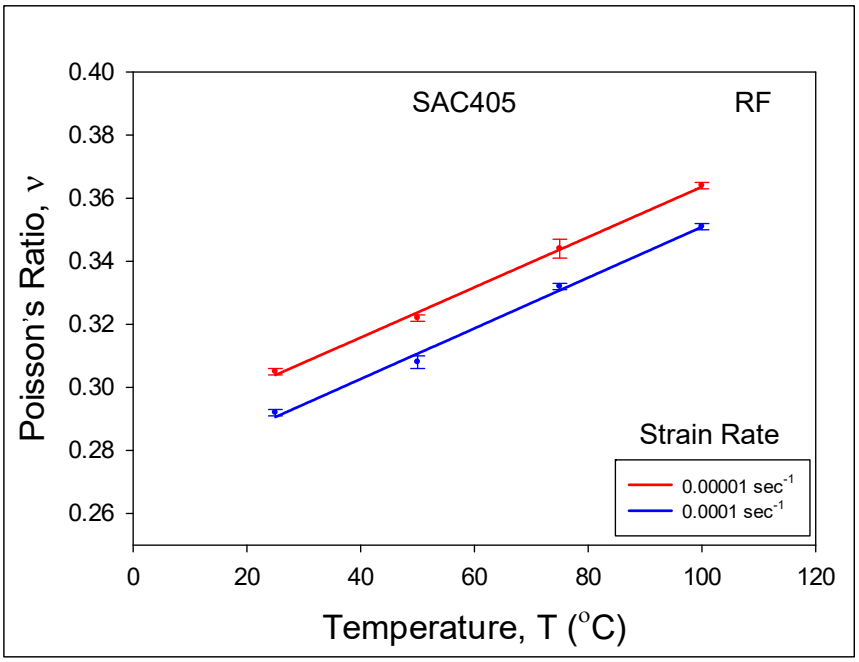

(b) SAC405

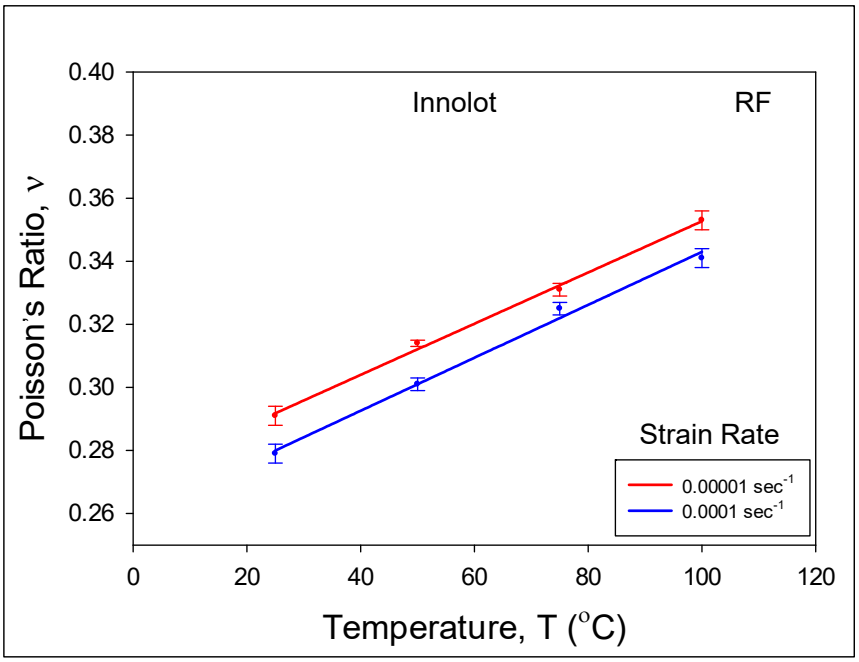

(c) Innolot (SAC+Bi)

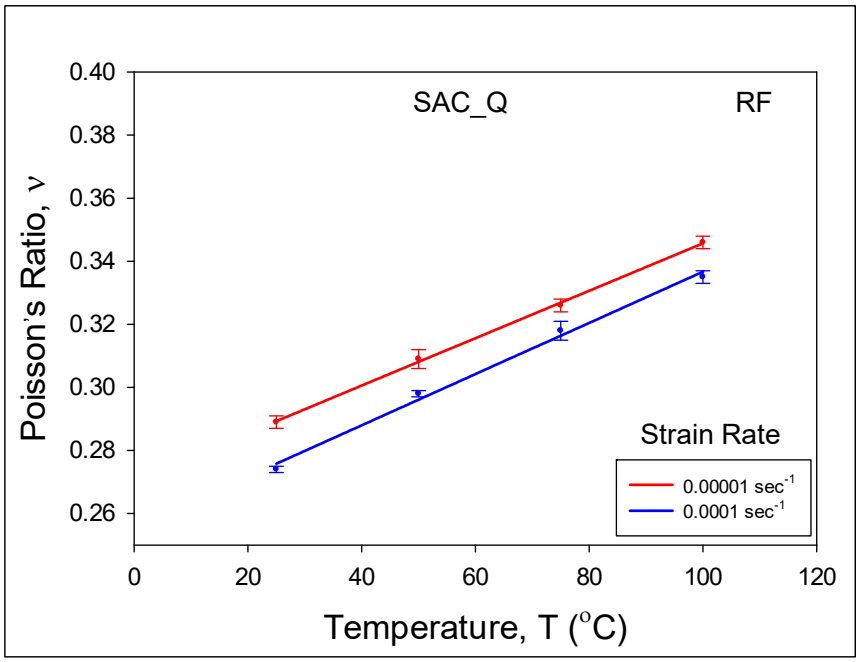

(d) SAC_Q (SAC+Bi)

Figure 5.3 Temperature Dependence of the Poisson's Ratio for Different Strain Rates (0.0001 and 0.00001 sec-[1])

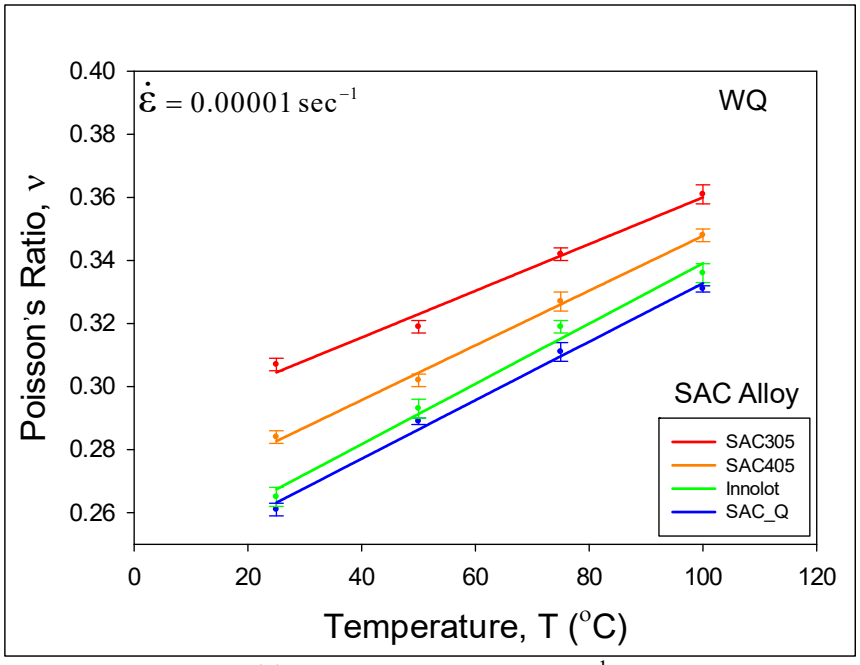

(a) WQ, SR = 0.00001 sec^{-1}

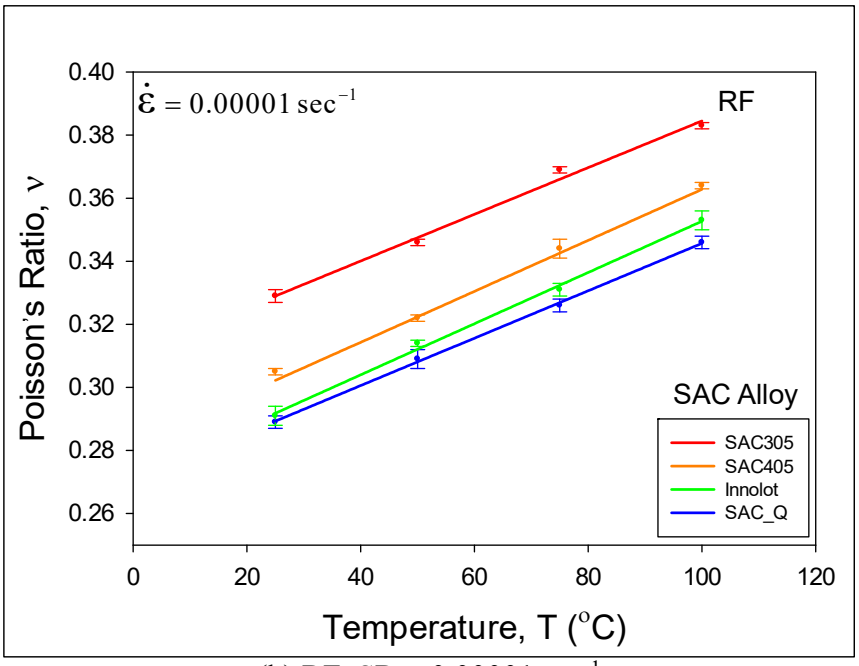

(b) RF, SR = 0.00001 sec^{-1}

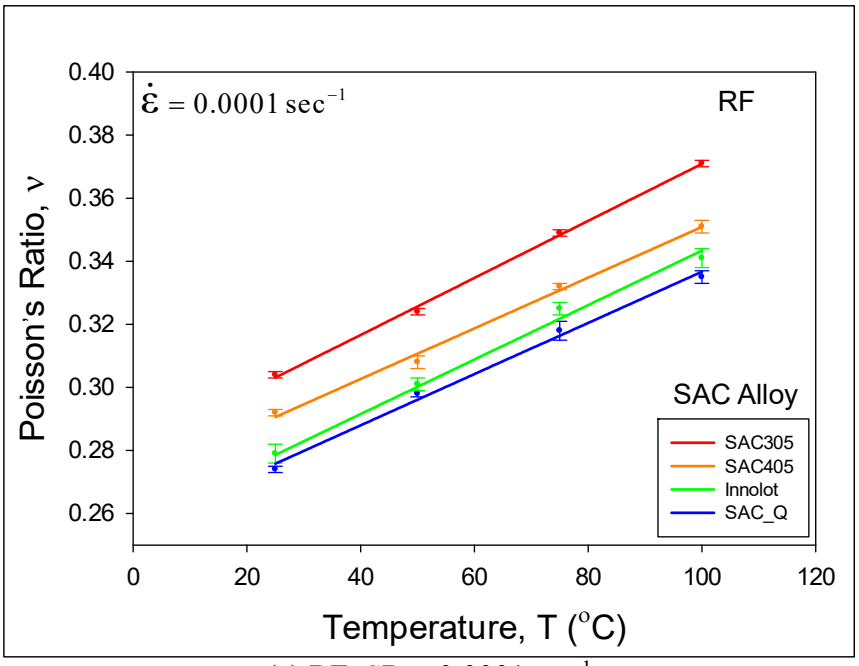

(c) RF, SR = 0.0001 sec^{-1}

Figure 5.4 Temperature Dependence of the Poisson's Ratio for Different Solder Alloys (SAC305, SAC405, Innolot, and SAC_Q)

The dependence of the Poisson's ratio on solidification profile can be visualized for each alloy using the data in Table 5.5 and the plots in Figure 5.2. In general, the Poisson's ratio value decreases when increasing the rate of cooling in the solder solidification profile. In other words, the Poisson's ratio values are lower for the very fine microstructures obtained with the WQ profile relative to the values obtained with the coarser (more realistic) microstructures obtained with the RF profile.

The dependence of the Poisson's ratio on strain rate can be visualized for each alloy using the data in Table 5.6 and the plots in Figure 5.3. In general, the Poisson's ratio decreases when increasing the strain rate. For the two strain rates considered (10^{-4} and 10^{-5} sec^{-1}), the Poisson's ratio value for the slower strain rate was typically 5-10% higher than that for the higher strain rate.

When comparing solder alloys with the same solidification profile and strain rate, the Poisson's ratio for SAC305 is the greatest, followed by that for SAC405, and Innolot, and then finally that for SAC_Q. This can be easily visualized from the plots in Figure 5.4, which show the dependence of the Poisson's ratio on temperature. In each graph, the solidification profile and strain rate are the same, and the four different alloys are represented by the different colors (red = SAC305, orange = SAC405, green = Innolot, and blue = SAC_Q). It is clear that the Poisson's ratio of a SAC solder is reduced when adding additional silver. The observed increases in the Poisson's ratio values for SAC305 relative to SAC405 are typically in the range of 5-8%. More silver (Ag) in the composition leads to more Ag_3Sn IMC particles, which stiffens to the material increases its resistance to dislocation movement. The smallest Poisson's ratio values were found for SAC_Q, which includes bismuth (Bi) in addition to tin (Sn), silver (Ag), and copper (Cu).

5.4 Effect of Isothermal Aging on Experimental Results

After exploring the effects of solidification rate, temperature and strain rates on the measured values of Poisson's ratio, a set of additional experiments was performed to determine the effects of isothermal aging (microstructural coarsening) on the Poisson's ratio values as represented by the test matrix in Table 5.4. For each aging duration, testing was performed using the same four testing temperatures (T = 25, 50, 75, 100 ^{o}C) and a single strain rate (0.00001 (sec^{-1})). The samples were aged at T = 125 ^{o}C for various durations including 0 (no aging), 1, 2, 3, 4, 5, 6, 12, and 24 hours and the extracted results are listed in Table 5.7 and the comparison plots are shown in Figure 5.5.

Typical variations in the extracted Poisson's ratio values with aging are illustrated by the numerical values in Table 5.7 for SAC305, SAC405, and SAC_Q, respectively. In this table, the measured Poisson's ratio values for 0, 1, 2, 3, 4, 5, 6, 12, and 24 hours of aging are included. With one day of aging, the PR value increases by 10-15% for SAC305 and SAC405, while only 6-8% for Innolot and SAC_Q. Figure 5.5 illustrates the evolution of the Poisson's ratio value with aging time for each of the four lead free solder alloys. The various colored curves in each graph represent the different testing temperatures. It is observed that the most dramatic changes occur in the first 5-6 hours of aging, and then the degradation rates becomes smaller. In addition, the more gradual nature of the aging induced changes for SAC_Q relative to SAC305/SAC405 are clearly evident.

Table 5.7 Poisson's Ratio Values for Different Lead Free Solders for Different Aging Conditions with Reflowed (RF) Microstructure

Alloy	Strain Rate (sec^{-1})	Test Temperature (°C)	Poisson's Ratio (ν) (Isothermal Aging at T = 125 °C)								
			No Aging	1 Hour Aging	2 Hours Aging	3 Hours Aging	4 Hours Aging	5 Hours Aging	6 Hours Aging	12 Hours Aging	24 Hours Aging
SAC305	10^{-5}	25	0.329 (0.002)	0.332 (0.001)	0.337 (0.002)	0.341 (0.002)	0.349 (0.001)	0.355 (0.002)	0.359 (0.001)	0.361 (0.002)	0.362 (0.001)
		50	0.346 (0.001)	0.349 (0.001)	0.352 (0.001)	0.361 (0.002)	0.368 (0.001)	0.376 (0.003)	0.380 (0.002)	0.382 (0.002)	0.385 (0.002)
		75	0.369 (0.001)	0.371 (0.002)	0.376 (0.002)	0.382 (0.001)	0.397 (0.003)	0.409 (0.003)	0.412 (0.001)	0.414 (0.001)	0.417 (0.003)
		100	0.383 (0.001)	0.390 (0.001)	0.395 (0.001)	0.402 (0.003)	0.413 (0.002)	0.427 (0.002)	0.431 (0.002)	0.433 (0.002)	0.437 (0.002)
SAC405		25	0.305 (0.001)	0.313 (0.002)	0.319 (0.001)	0.326 (0.003)	0.335 (0.001)	0.343 (0.002)	0.348 (0.001)	0.351 (0.002)	0.355 (0.002)
		50	0.322 (0.001)	0.332 (0.001)	0.341 (0.003)	0.349 (0.001)	0.357 (0.003)	0.366 (0.001)	0.371 (0.001)	0.376 (0.001)	0.379 (0.003)
		75	0.344 (0.003)	0.353 (0.001)	0.359 (0.002)	0.366 (0.002)	0.373 (0.001)	0.379 (0.003)	0.384 (0.002)	0.388 (0.002)	0.392 (0.002)
		100	0.364 (0.001)	0.373 (0.002)	0.379 (0.002)	0.388 (0.001)	0.397 (0.001)	0.405 (0.002)	0.411 (0.002)	0.414 (0.003)	0.416 (0.002)
Innolot		25	0.291 (0.003)	0.295 (0.002)	0.300 (0.002)	0.305 (0.003)	0.310 (0.001)	0.314 (0.002)	0.319 (0.001)	0.322 (0.002)	0.327 (0.003)
		50	0.314 (0.001)	0.319 (0.002)	0.324 (0.003)	0.330 (0.003)	0.334 (0.002)	0.340 (0.002)	0.343 (0.003)	0.348 (0.001)	0.352 (0.002)
		75	0.331 (0.002)	0.335 (0.003)	0.340 (0.003)	0.347 (0.001)	0.352 (0.003)	0.355 (0.003)	0.359 (0.002)	0.365 (0.003)	0.368 (0.002)
		100	0.353 (0.003	0.355 (0.002)	0.359 (0.001)	0.364 (0.003)	0.369 (0.003)	0.373 (0.002)	0.376 (0.002)	0.381 (0.001)	0.384 (0.003)
SAC_Q		25	0.289 (0.001)	0.292 (0.001)	0.294 (0.002)	0.298 (0.001)	0.301 (0.003)	0.304 (0.002)	0.307 (0.001)	0.308 (0.003)	0.310 (0.001)
		50	0.309 (0.003)	0.313 (0.002)	0.317 (0.001)	0.319 (0.003)	0.322 (0.002)	0.325 (0.002)	0.328 (0.001)	0.330 (0.002)	0.331 (0.003)
		75	0.326 (0.002)	0.331 (0.002)	0.334 (0.003)	0.337 (0.002)	0.340 (0.002)	0.342 (0.003)	0.345 (0.002)	0.348 (0.001)	0.351 (0.003)
		100	0.346 (0.002)	0.349 (0.001)	0.352 (0.002)	0.355 (0.002)	0.359 (0.003)	0.361 (0.001)	0.364 (0.003)	0.366 (0.002)	0.368 (0.002)

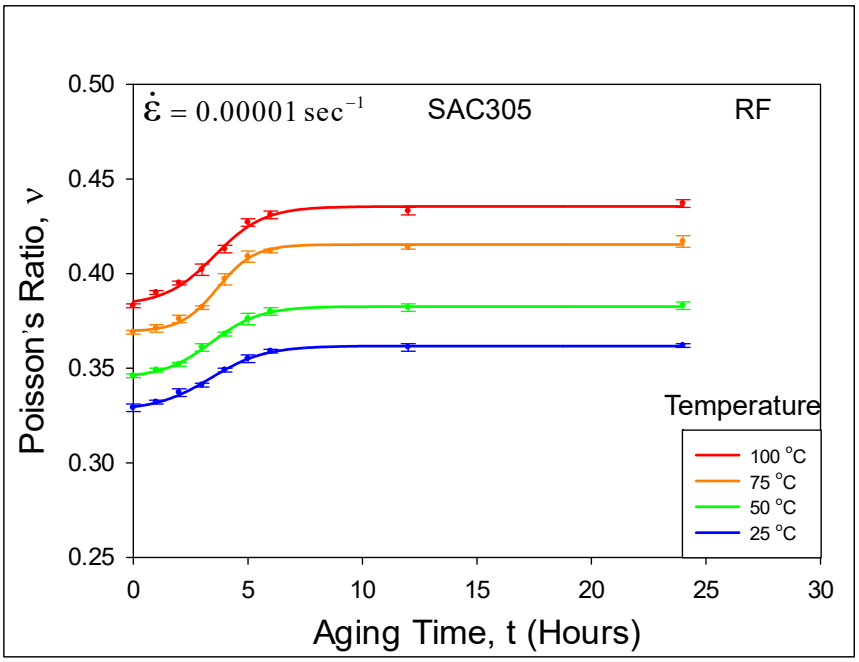

(a) SAC305

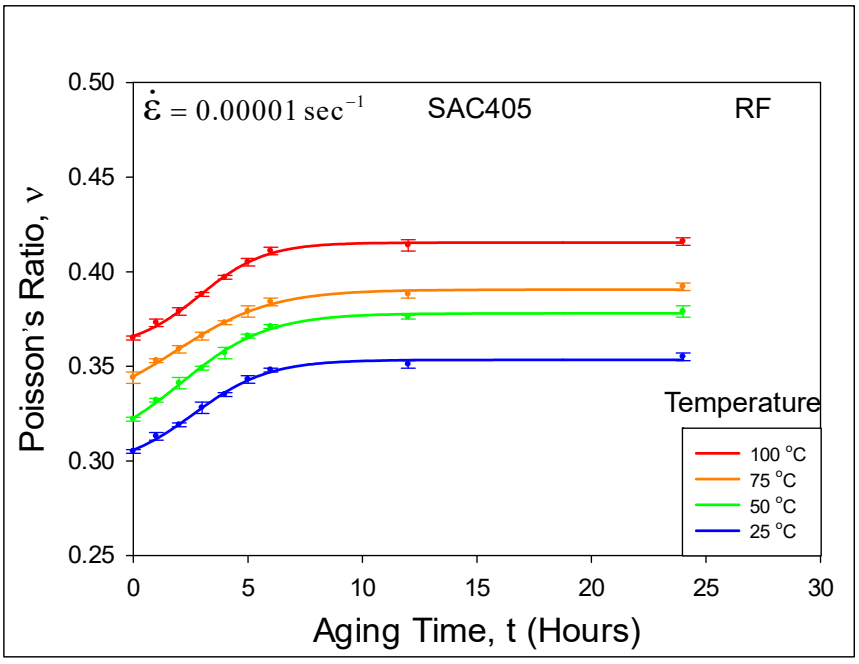

(b) SAC405

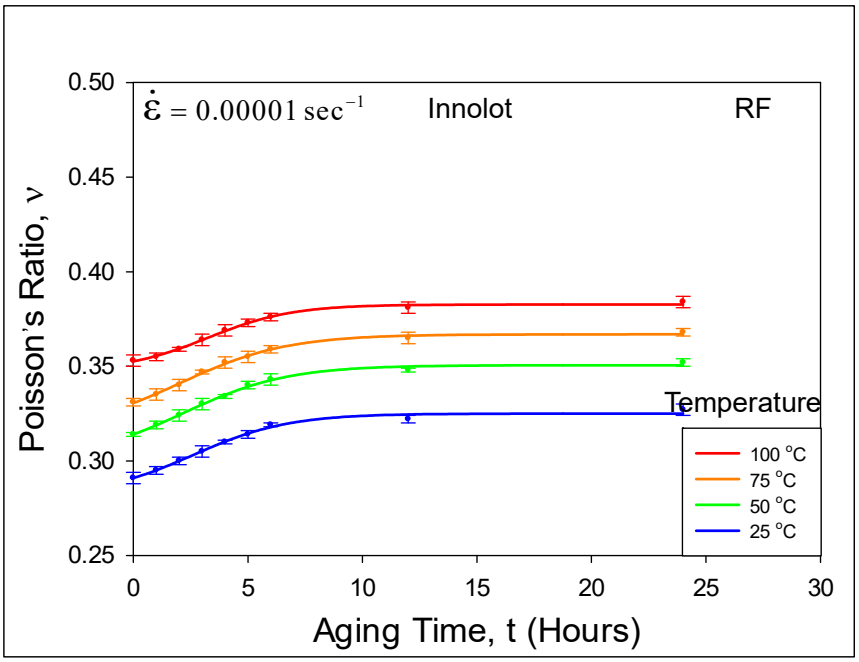

(c) Innolot (SAC+Bi)

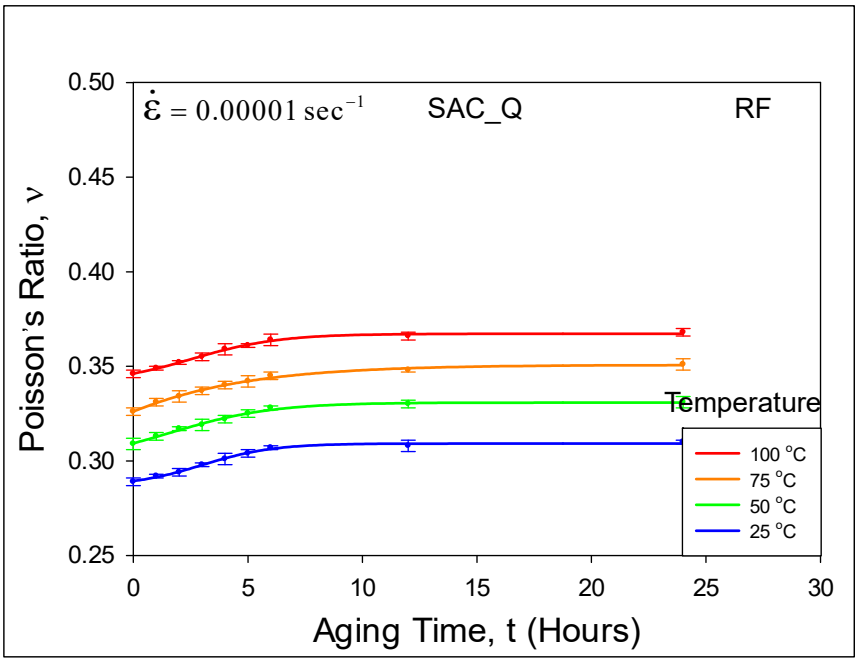

(d) SAC_Q (SAC+Bi)

Figure 5.5 Isothermal Aging Dependence of the Poisson's Ratio for Different Solder Alloys for Different Temperatures

(a)

5.5 Summary and Discussion

In this work, experimental investigations were conducted to characterize the Poisson's ratio of several SAC and SAC+X lead free solders. Uniaxial tensile stress-strain tests were carried out on SAC305 (96.5Sn3.0Ag0.5Cu), SAC405 (95.5Sn4.0Ag0.5Cu), Innolot (SAC+3% Bi), and SAC_Q (SAC+3% Bi) specimens using a micro tension/torsion testing machine with two strain rates (0.0001, and 0.00001 (sec^{-1})) and four testing temperatures (T = 25, 50, 75, 100 ^{o}C). Deformations and strains in the axial and transverse directions were measured using miniature strain gages with automatic data acquisition from LabVIEW software. The recorded transverse strain vs. axial strain data for each test were then fit with a linear regression analysis to determine the Poisson's ratio value.

A large test matrix of experiments was developed to study the effects of temperature, strain rate, alloy composition, solidification cooling profile, and isothermal aging exposure on the value of solder Poisson's ratio; and to create a material property database for finite element simulations. The Poisson's ratio was found to increase significantly (15-25%) with increasing temperature. It was also found to decrease with increasing strain rate, alloy silver content, and cooling rate after solidification. Finally, the microstructural coarsening that occurs during isothermal aging led to an increase in the Poisson's ratio (up to 15% increase with one day of aging). Considering all of the possible branches of the test matrix (temperatures, strain rates, prior aging conditions, and microstructure), the value of the Poisson's ratio of SAC305 ranged from $0.31 < \nu < 0.44$. Similarly, the Poisson's ratio of SAC405 ranged from $0.28 < \nu < 0.42$, and the Poisson's ratio of Innolot and SAC_Q ranged from $0.27 < \nu < 0.38$, and $0.26 < \nu < 0.37$ respectively.

Overall, the SAC_Q alloy had the lowest PR values for all temperatures, strain rates, solidification profiles, and durations of aging.

CHAPTER 6

MECHANICAL BEHAVIOR AND RELIABILITY OF SAC+Bi LEAD FREE SOLDERS WITH VARIOUS LEVELS OF BISMUTH

6.1 Introduction

The microstructure and mechanical properties of lead free solder joints in electronic assemblies are constantly evolving when exposed to isothermal aging. These changes lead to dramatic reductions in reliability of lead free electronic assemblies subjected to aging. The root cause of the changes in solder joint mechanical behavior is the evolution of the SAC solder microstructure that occurs during aging. This includes coarsening of the Ag_3Sn intermetallic compounds (IMCs) present in the eutectic regions between beta-Sn dendrites. Many recent studies have been conducted aiming at mitigating aging effects in SAC solders. Several have reported great improvement of properties including wettability, shock/drop reliability, melting temperature, creep properties, and microstructure [26-27] by the addition of some new elements such as Bi, Sb, Ni, Mn, In, Co, Mg, Zn, La, Ce, and Ti to the traditional SAC alloys. Researchers have suggested that Bi exists as a single phase in the SAC microstructure or goes into solid solution with Sn, especially when the solder is exposed to isothermal aging. Also, Bi doesn't form any intermetallic compounds with other constituents and copper, thus, reducing IMC layer thickness [32-33].

In this chapter, several different new SAC+Bi alloys along with popular Sn-3.5Bi solder alloy were studied to explore the mechanical behavior, microstructural evolution,

and reliability to find some alternate lead free solders for high reliability applications. Several different SAC+Bi alloys with various levels of Bismuth (1.0%, 2.0%, and 3.0%) were tested to make a database by showing comparison of these new alloys with the conventional SACN05 (N = 1, 2, 3, 4), and another popular SAC+3% Bi alloy popularly known a s SAC_Q. The chemical composition of each new SAC+Bi alloys were verified by EDS. To examine the base mechanical behavior, stress-strain tests were performed for each SAC+Bi and Sn-3.5Agalloy with three strain rates (0.001, 0.0001, and 0.00001 (sec^{-1})), and five different testing temperatures (T = 25, 50, 75, 100, and 125 ^{o}C). The Anand parameters were calculated for each alloy from the stress-strain data, and correlation was shown between the experimental curves and the model predictions. In addition, the temperature dependent mechanical properties of the various SAC+Bi solders were measured and compared including initial modulus, and ultimate tensile strength.

The effects of aging were studied for two of the new SAC+Bi (1%, and 2%) alloys using both mechanical testing and microstructure observations. For the solder mechanical response, the fabricated uniaxial specimens were aged (preconditioned) at T = 125 °C for several durations of aging including 0, 1, 5, and 20 days. Stress-strain tests on the aged specimens were then performed at a single strain rate of 0.001 (sec^{-1}), and temperatures of 25, 50, 75, 100, and 125 °C. Using the measured data, the evolutions of the stress-strain behaviors and mechanical properties were determined for the SAC+Bi alloys as a function of aging time. Microstructural evolutions of the new solder alloys were also observed for aging at T = 125 °C for the same durations of 0, 1, 5, and 20 days. In particular, aging induced coarsening of the IMCs was studied for each alloy using Scanning Electron

Microscopy (SEM), and correlated to corresponding material property evolution to explain the physics behind the mechanical response**.**

The details of tensile testing including sample preparation, mechanical testing system (MT-200 micro tension/torsion machine), data acquisition, and raw data processing were discussed in various sections (3.2, 3.4, and 3.5) in chapter 3. Utilizing the method the experimental results are discussed now.

6.2 Alloy Composition and Experimental Test Matrix

In this study, Energy Dispersive X-Ray Spectroscopy (EDX) was used to extract the chemical composition of various SAC+Bi doped alloys and another popular Sn-3.5Ag alloy. At least 10-12 regions were analyzed. The nominal vendor specified compositions are listed in Table 6.1. The EDX results showed that the sample element compositions were very close to the vendor values (e.g. 4.0-4.3% Ag and 0.5-0.6% Cu, and within 0.1% of the specified Bi value).

Table 6.1 Vendor Specified Compositions of Solder Alloys (wt%)

Alloy	Sn	Ag	Cu	Bi	Ni	Sb
SAC+3% Bi	92.50	4.00	0.50	3.00	0.00	0.00
SAC+2% Bi	93.50	4.00	0.50	2.00	0.00	0.00
SAC+1% Bi	94.50	4.00	0.50	1.00	0.00	0.00
Sn-3.5Ag	96.50	3.50	0.00	0.00	0.00	0.00

A large test matrix of experiments was studied here for uniaxial tensile testing. Poisson's ratio experimentally. Uniaxial stress-strain tests were performed for each SAC+Bi and Sn-3.5Ag alloy with three strain rates (0.001, 0.0001, and 0.00001 (sec^{-1})),

and five different testing temperatures (T = 25, 50, 75, 100, and 125 ºC) for reflowed (RF) microstructure. Table 6.2 represents the no aging test matrix.

The effects of aging were studied for two if the new SAC+Bi (1%, and 2%) alloys where the fabricated uniaxial specimens were aged (preconditioned) at T = 125 °C for several durations of aging including 0, 1, 5, and 20 days. Stress-strain tests on the aged specimens were then performed at a single strain rate of 0.001 (sec^{-1}), and temperatures of 25, 50, 75, 100, and 125 °C. Table 6.3 represents the isothermal aging test matrix.

Table 6.2 Test Matrix for Uniaxial Tensile Tests (RF, No Aging)

Alloy	Strain Rate (sec^{-1})	Test Temperature (°C)				
		25	50	75	100	125
SAC+1% Bi	10^{-3}	√	√	√	√	√
	10^{-4}	√	√	√	√	√
	10^{-5}	√	√	√	√	√
SAC+2% Bi	10^{-3}	√	√	√	√	√
	10^{-4}	√	√	√	√	√
	10^{-5}	√	√	√	√	√
SAC+3% Bi	10^{-3}	√	√	√	√	√
	10^{-4}	√	√	√	√	√
	10^{-5}	√	√	√	√	√
Sn-3.5Ag	10^{-3}	√	√	√	√	√
	10^{-4}	√	√	√	√	√
	10^{-5}	√	√	√	√	√

Table 6.3 Isothermal Aging Test Matrix

Alloy	Strain Rate (sec^{-1})	Test Temperature (°C)	Aging Condition (Isothermal Aging T= 125 °C)			
			No Aging	1 Day Aging	5 Days Aging	20 Days Aging
SAC+1% Bi	10^{-3}	25	√	√	√	√
		50	√	√	√	√
		75	√	√	√	√
		100	√	√	√	√
		125	√	√	√	√
SAC+2% Bi		25	√	√	√	√
		50	√	√	√	√
		75	√	√	√	√
		100	√	√	√	√
		125	√	√	√	√

6.3 Stress-Strain Response for Various Test Temperatures and Strain Rates

The recorded experimental results from uniaxial tensile tests results for various SAC+Bi (1%, 2%, and 3%) as well as Sn-3.5 solder alloy with different test temperatures, and strain rates are plotted in Figures 6.1-6.4. As mentioned in chapter 3, the curves in the plots are the "average" stress-strain curves found by fitting the raw experimental data with the empirical model in Equation 3.2. In all the plots, a single color curve is the average of 8-10 uniaxial stress-strain tests, whereas, the various colored curves in a particular plot representing the different test temperatures with black = 25 °C, blue = 50 °C, green = 75 °C, orange = 100 °C, and red = 125 °C. Again, in each plot, top curve corresponds to 25 °C and bottom curve represents 125 °C test result.

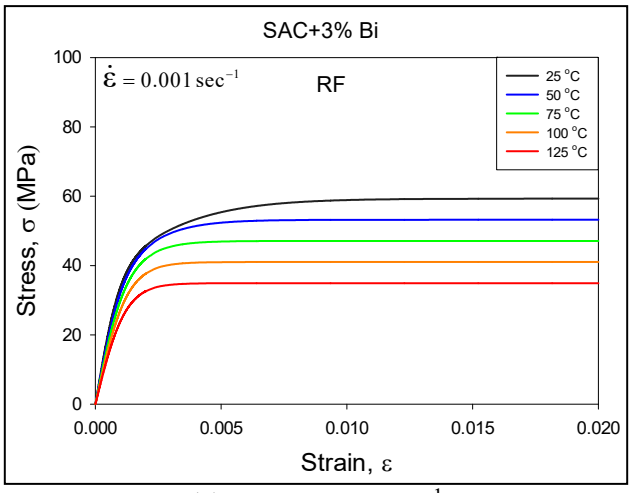

(a) SR = 0.001 sec^{-1}

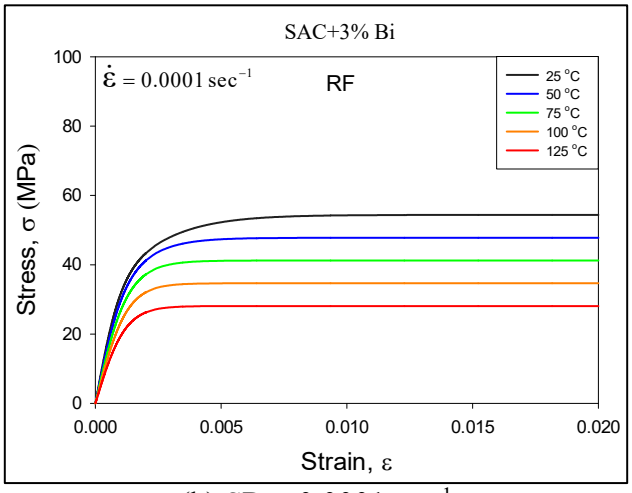

(b) SR = 0.0001 sec^{-1}

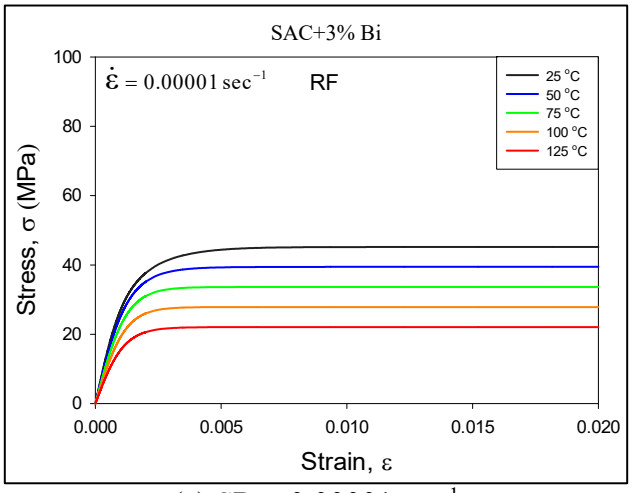

(c) SR = 0.00001 sec^{-1}

Figure 6.1 Stress-Strain Curves for SAC+3% Bi (RF, No Aging)

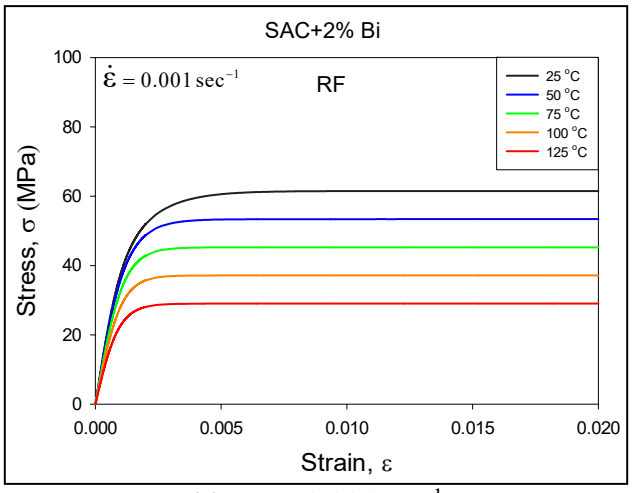

(a) SR = 0.001 sec^{-1}

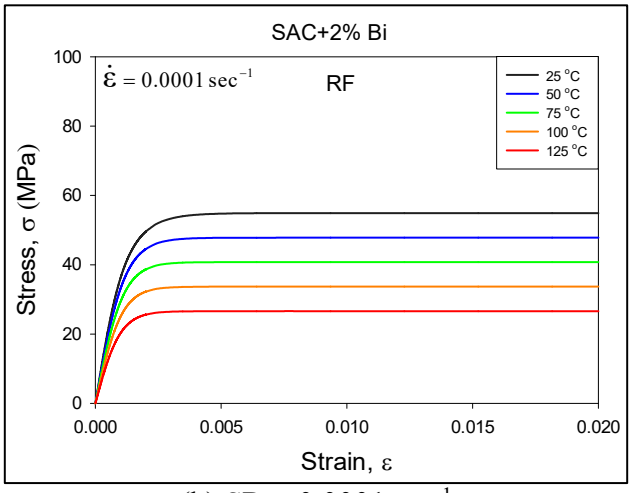

(b) SR = 0.0001 sec^{-1}

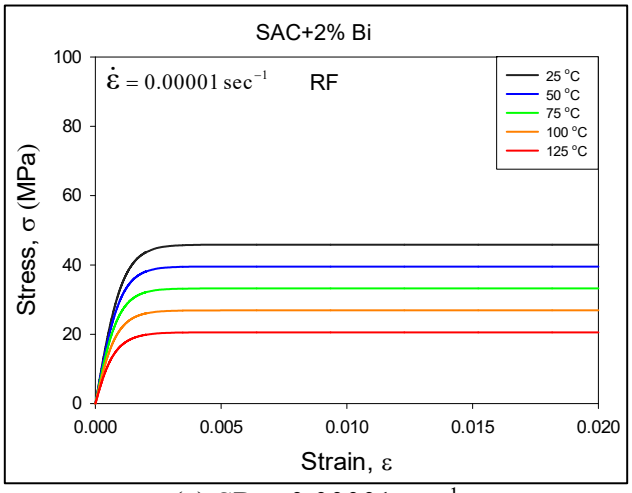

(c) SR = 0.00001 sec^{-1}

Figure 6.2 Stress-Strain Curves for SAC+2% Bi (RF, No Aging)

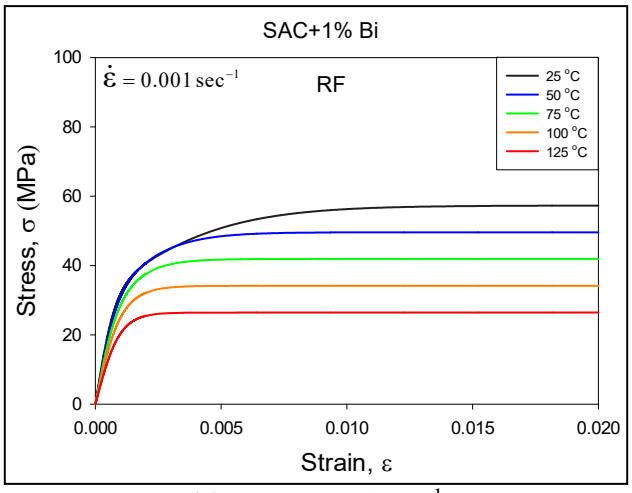

(a) SR = 0.001 sec^{-1}

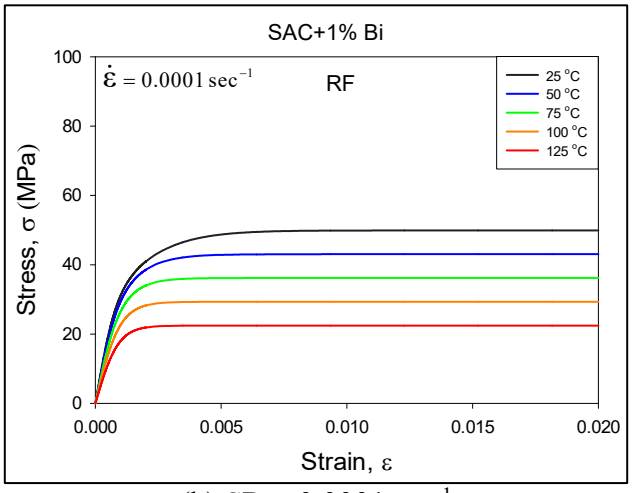

(b) SR = 0.0001 sec^{-1}

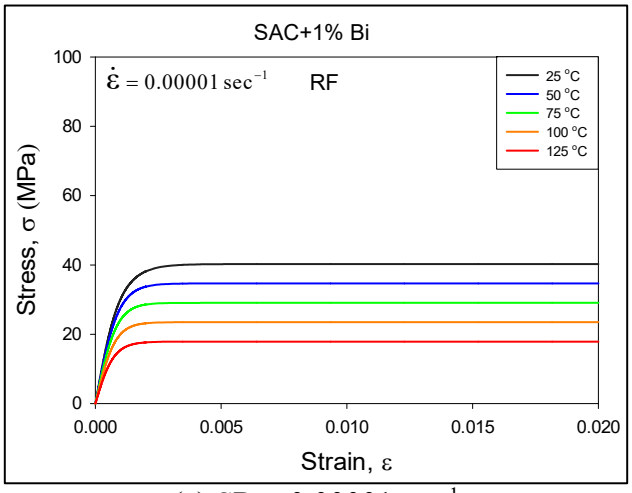

(c) SR = 0.00001 sec^{-1}

Figure 6.3 Stress-Strain Curves for SAC+1% Bi (RF, No Aging)

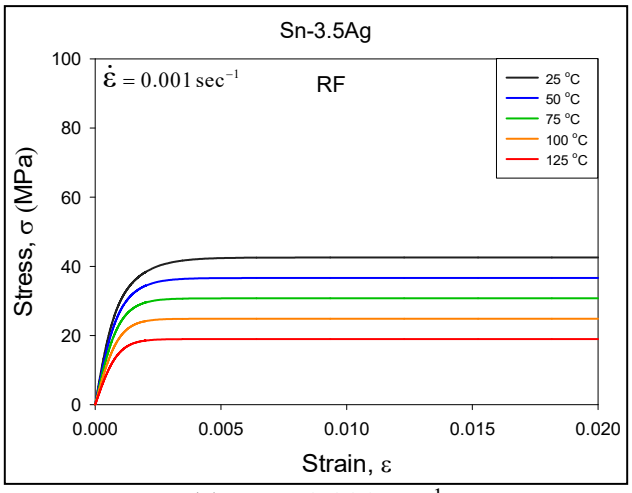

(a) SR = 0.001 sec^{-1}

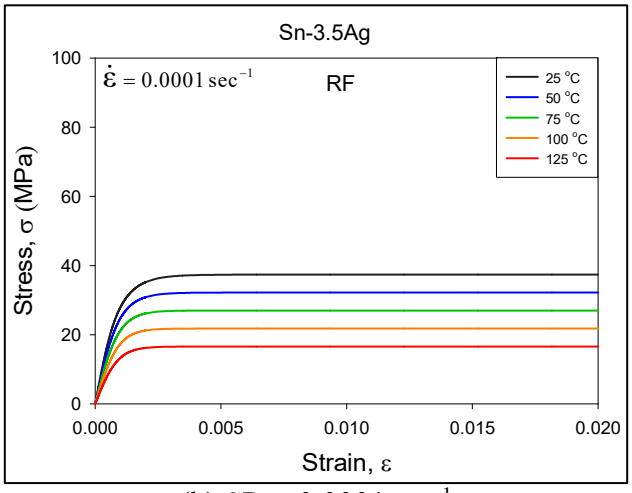

(b) SR = 0.0001 sec^{-1}

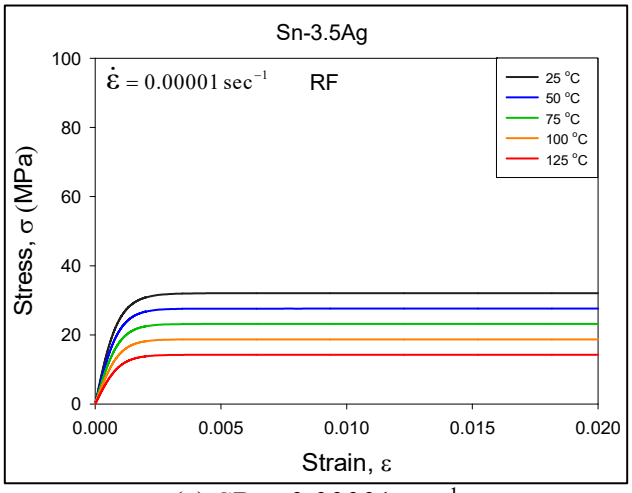

(c) SR = 0.00001 sec^{-1}

Figure 6.4 Stress-Strain Curves for Sn-3.5Ag (RF, No Aging)

6.4 Comparison of Stress-Strain Behavior of Various New SAC+Bi Solder Alloy with Conventional SACN05, SAC_Q and Sn-3.5Ag

A comparison of stress-strain curves for the new SAC+Bi alloys along with the conventional SACN05 (N = 1, 2, 3, 4), Sn-3.5 Ag as well as another popular SAC+3% Bi alloy are shown in Figures 6.5 and 6.6. To distinguish between the two SAC+3% alloys, their commercial names were also added in the plots. SAC+3% Bi tested in this study is commercially known as M758 whereas, another SAC+3% Bi alloy used for comparison purposes is popularly known as SAC_Q. Again, here all plots are the "average" stress-strain curves representing the fit of the empirical 4-parameter hyperbolic tangent model presented in Equation 3.2, and different color represents different alloys, such as, black = SAC+3% Bi (SAC_Q), dark pink = SAC+3% Bi (M758)), blue = SAC+2% Bi, green = SAC+1% Bi, orange = SAC405, pink = SAC305, dark cyan = SAC205, red = SAC105, and dark yellow = Sn-3.5Ag.

Figures 6.5, and 6.6 represents results for T = 25, and 125 ^{o}C respectively. Where comparisons were shown for all three strain rates (0.001, 0.0001, and 0.00001 (sec^{-1})). Results for SACN05 (N = 1, 2, 3, 4), and SAC_Q were collected from old works [200, 201] for comparison purposes.

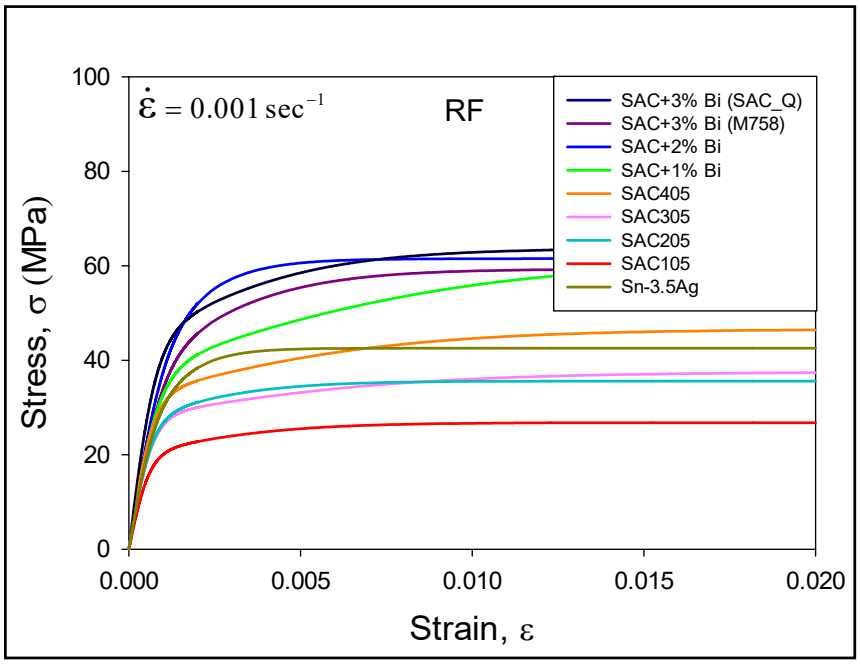

(a) SR = 0.001 sec^{-1}

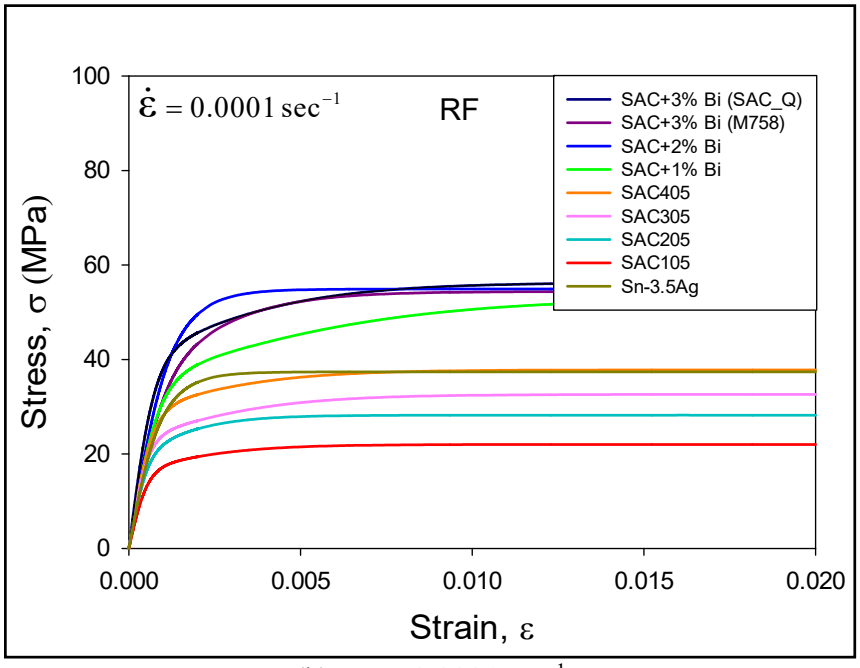

(b) SR = 0.0001 sec^{-1}

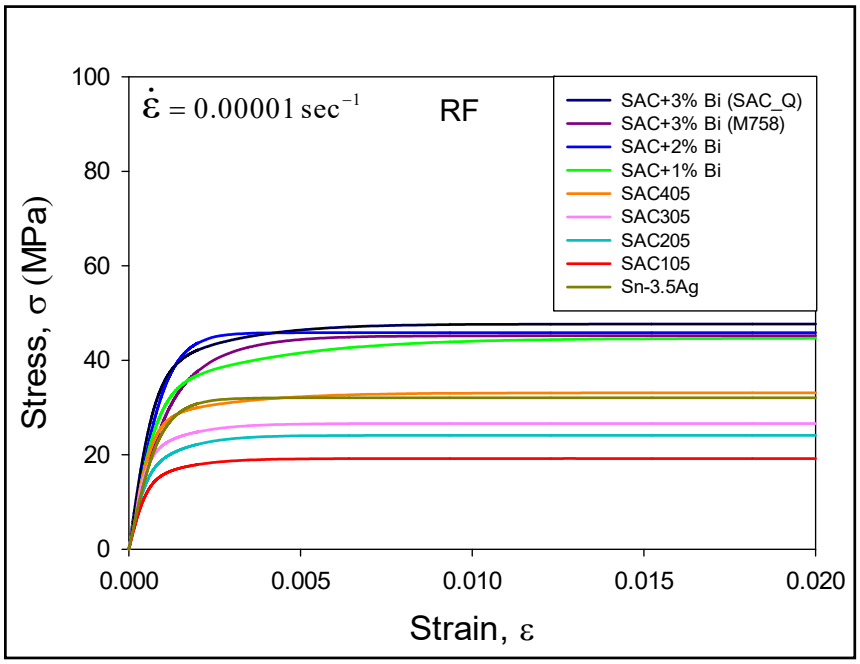

(c) SR = 0.00001 sec^{-1}

Figure 6.5 Stress-Strain Curves for Different SAC and SAC+Bi Alloys (RF, No Aging, Test T = 25 °C)

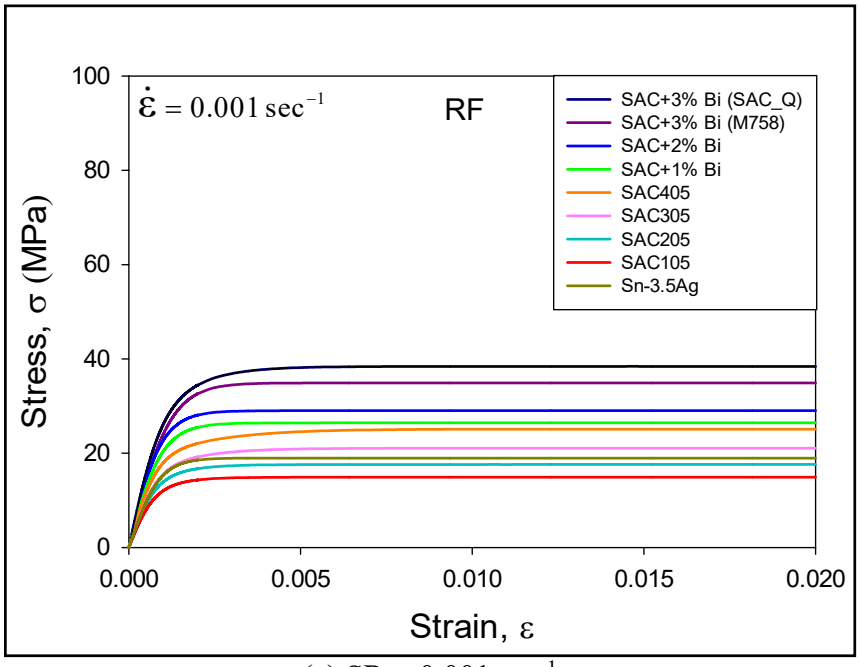

(a) SR = 0.001 sec^{-1}

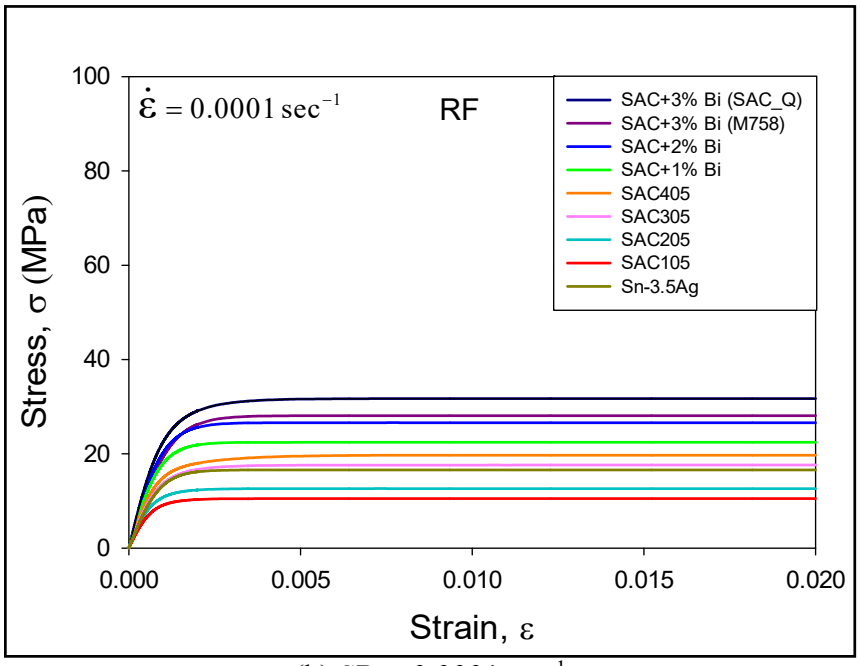

(b) SR = 0.0001 sec^{-1}

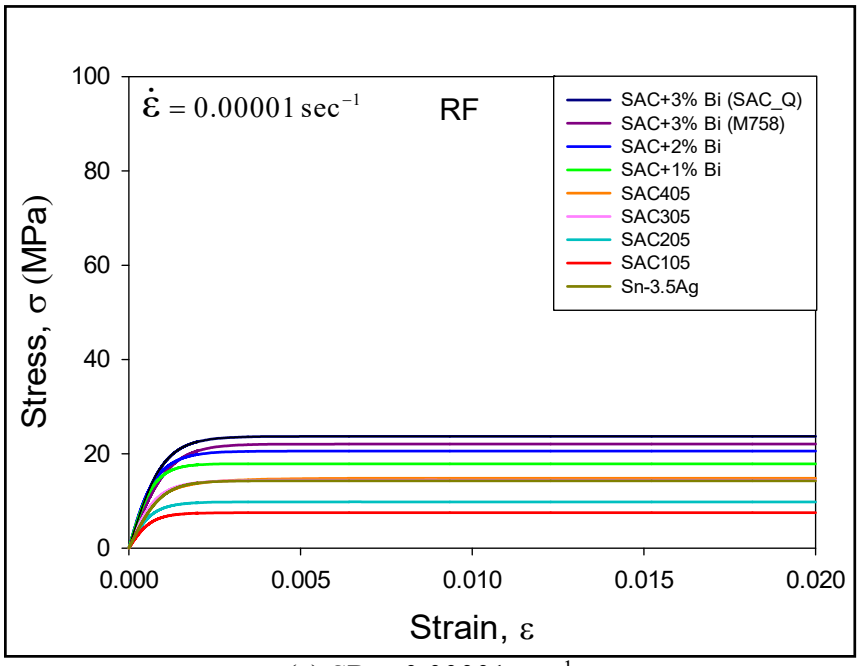

(c) SR = 0.00001 sec^{-1}

Figure 6.6 Stress-Strain Curves for Different SAC and SAC+Bi Alloys (RF, No Aging, Test T = 125 °C)

6.5 Comparison of Mechanical Properties of Various New SAC+Bi Solder Alloy with Conventional SACN05, SAC_Q and Sn-3.5Ag

The mechanical properties, such as, initial effective modulus, ultimate tensile strength, and yield stress of the three new SAC+Bi alloys as well as Sn-3.5 Ag alloy are listed in Tables 6.4-6.6. The mechanical properties have been extracted from the measured stress-strain data presented in Figures 6.1-6.4 in the previous section. These properties, have been plotted in Figures 6.7-6.9 as a function of temperature at each of the three strain rates to show the comparison among the new SAC+Bi alloys along with the conventional SACN05 (N = 1, 2, 3, 4), Sn-3.5 Ag as well as another SAC+3% Bi alloy popularly known as SAC_Q. Results for SACN05 (N = 1, 2, 3, 4), and SAC_Q were collected from old works [200, 201] for comparison purposes.

As expected, the mechanical properties of the alloys decreased significantly with temperature. Approximately 40-60% drop in ultimate strength and modulus occurred during testing for various temperatures and strain rates. The results have shown that all of the SAC+Bi alloys demonstrate superior mechanical properties relative to all of the SACN05 alloys. As the Bi content decreased, the strength of the SAC+Bi alloys also decreased correspondingly. The variations were observed to be nearly linear with temperature at all three strain rates for all of the alloys.

Table 6.4 Effective Modulus (E) of Various SAC+Bi and Sn-3.5Ag

Alloy	Strain Rate (sec^{-1})	Effective Modulus, E (GPa)				
		25 (°C)	50 (°C)	75 (°C)	100 (°C)	125 (°C)
SAC+1% Bi	10^{-3}	45.9	41.6	38.3	34.5	27.3
	10^{-4}	43.5	40.4	37.4	31.3	25.7
	10^{-5}	41.6	39.0	35.4	27.8	24.8
SAC+2% Bi	10^{-3}	46.9	44.6	41.2	36.7	31.1
	10^{-4}	45.0	41.3	37.9	32.3	26.9
	10^{-5}	42.5	39.9	36.3	31.6	25.8
SAC+3% Bi	10^{-3}	41.8	39.4	38.9	36.6	32.0
	10^{-4}	39.4	38.4	36.1	28.9	25.0
	10^{-5}	37.4	36.8	33.8	27.1	21.5
Sn-3.5Ag	10^{-3}	42.7	38.0	31.5	27.7	21.2
	10^{-4}	39.2	33.4	29.2	24.3	18.1
	10^{-5}	34.8	29.8	24.4	19.7	15.1

Table 6.5 Ultimate Strength (UTS) of Various SAC+Bi and Sn-3.5Ag

Alloy	Strain Rate (sec^{-1})	Ultimate Strength, UTS (MPa)				
		25 (°C)	50 (°C)	75 (°C)	100 (°C)	125 (°C)
SAC+1% Bi	10^{-3}	57.3	49.6	41.9	34.2	26.4
	10^{-4}	49.9	43.1	36.2	29.3	22.4
	10^{-5}	40.3	34.7	29.1	23.5	17.9
SAC+2% Bi	10^{-3}	61.5	53.4	45.3	37.2	29.0
	10^{-4}	54.9	47.8	40.8	33.7	26.6
	10^{-5}	45.9	39.5	33.2	26.9	20.6
SAC+3% Bi	10^{-3}	59.3	53.2	47.1	41.0	34.9
	10^{-4}	54.4	47.8	41.2	34.7	28.1
	10^{-5}	45.2	39.4	33.6	27.9	22.1
Sn-3.5Ag	10^{-3}	42.6	36.6	30.8	24.9	19.0
	10^{-4}	37.4	32.2	27.0	21.8	16.6
	10^{-5}	32.1	27.6	23.2	18.7	14.3

Table 6.6 Yield Stress (YS) of Various SAC+Bi and Sn-3.5Ag

Alloy	Strain Rate (sec^{-1})	Yield Stress, YS (MPa)				
		25 (°C)	50 (°C)	75 (°C)	100 (°C)	125 (°C)
SAC+1% Bi	10^{-3}	22.3	19.6	16.4	13.8	10.9
	10^{-4}	19.7	16.5	14.1	12.0	9.4
	10^{-5}	16.1	13.8	11.4	9.3	7.5
SAC+2% Bi	10^{-3}	25.6	22.4	19.4	15.9	12.7
	10^{-4}	22.9	20.5	17.4	14.6	11.6
	10^{-5}	19.6	16.9	14.3	11.5	9.0
SAC+3% Bi	10^{-3}	22.8	20.0	17.8	15.6	13.5
	10^{-4}	20.3	17.6	15.8	13.1	11.0
	10^{-5}	17.2	14.8	12.9	10.8	8.5
Sn-3.5Ag	10^{-3}	19.8	17.2	15.0	12.2	9.5
	10^{-4}	17.5	15.2	13.0	10.8	8.4
	10^{-5}	15.2	13.1	11.0	9.1	7.0

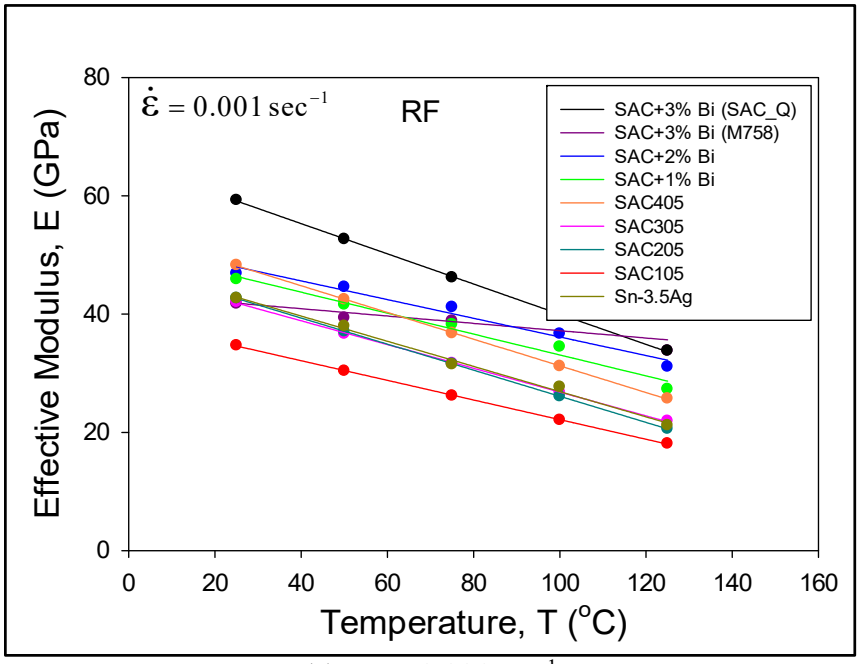

(a) SR = 0.001 sec^{-1}

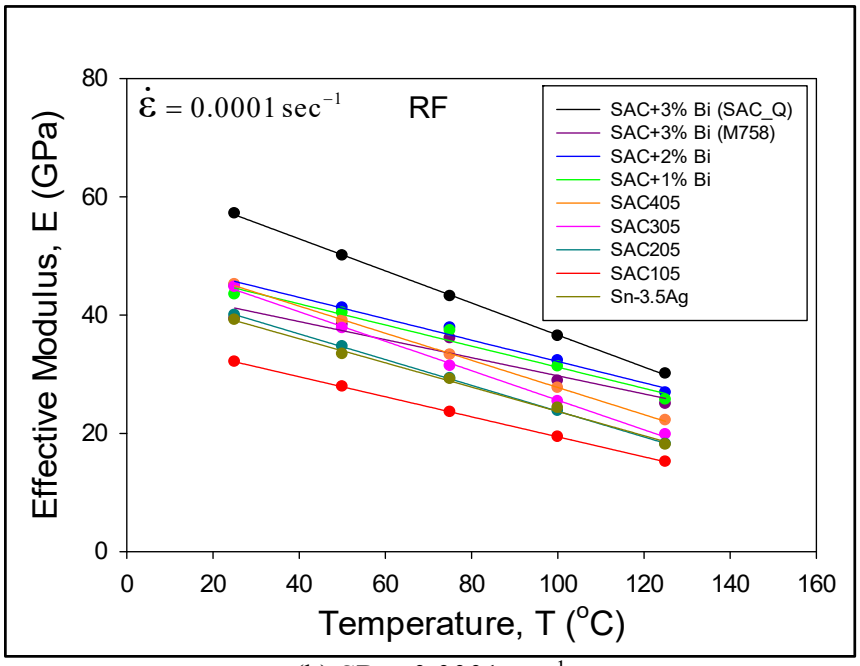

(b) SR = 0.0001 sec^{-1}

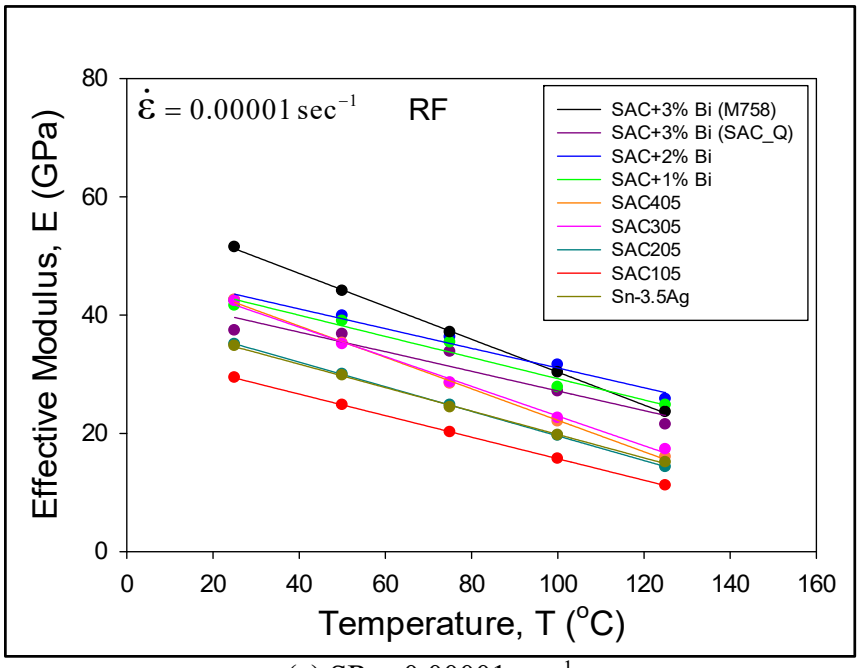

(c) SR = 0.00001 sec^{-1}

Figure 6.7 Variation of Effective Modulus with Temperature for Different SAC and SAC+Bi Alloys (RF, No Aging)

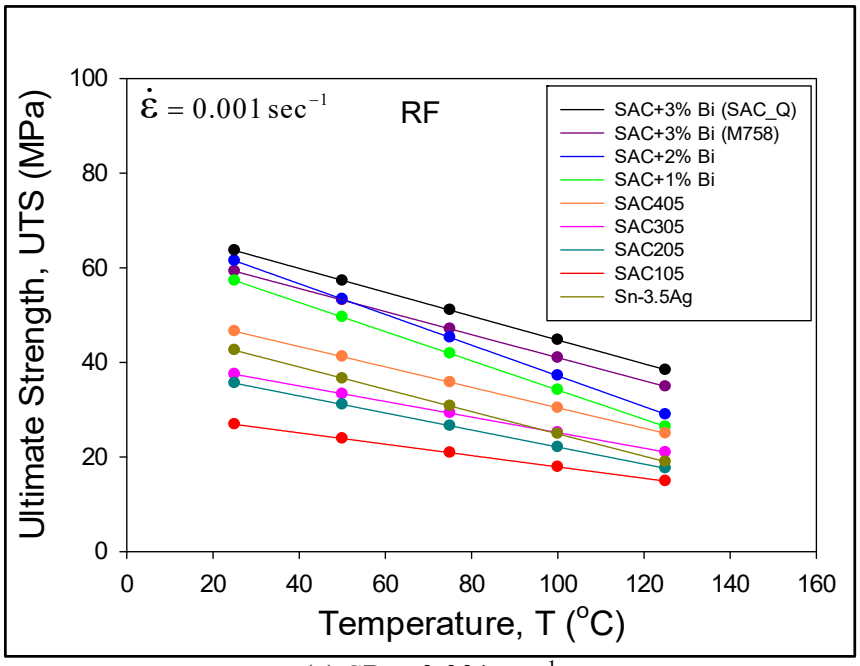

(a) SR = 0.001 sec^{-1}

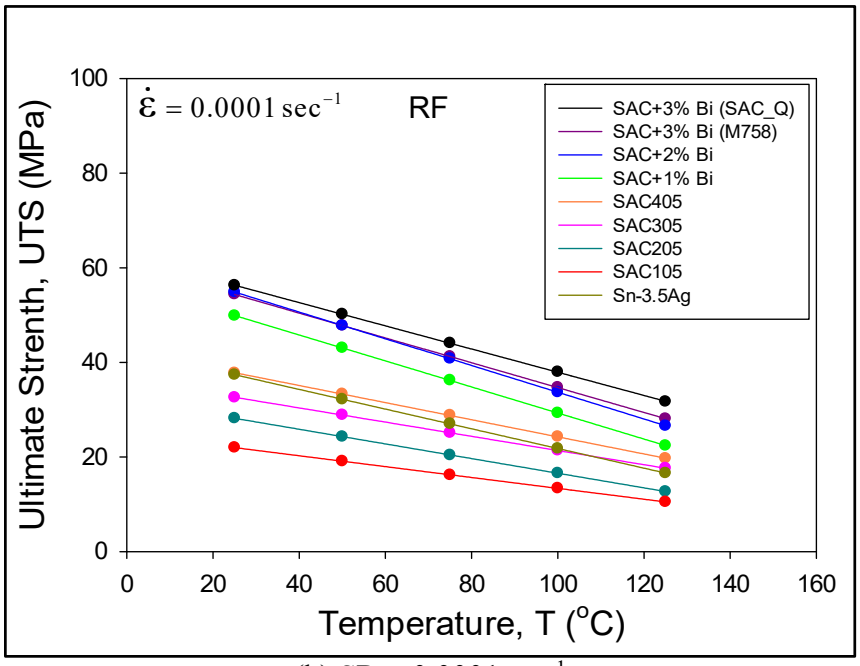

(b) SR = 0.0001 sec^{-1}

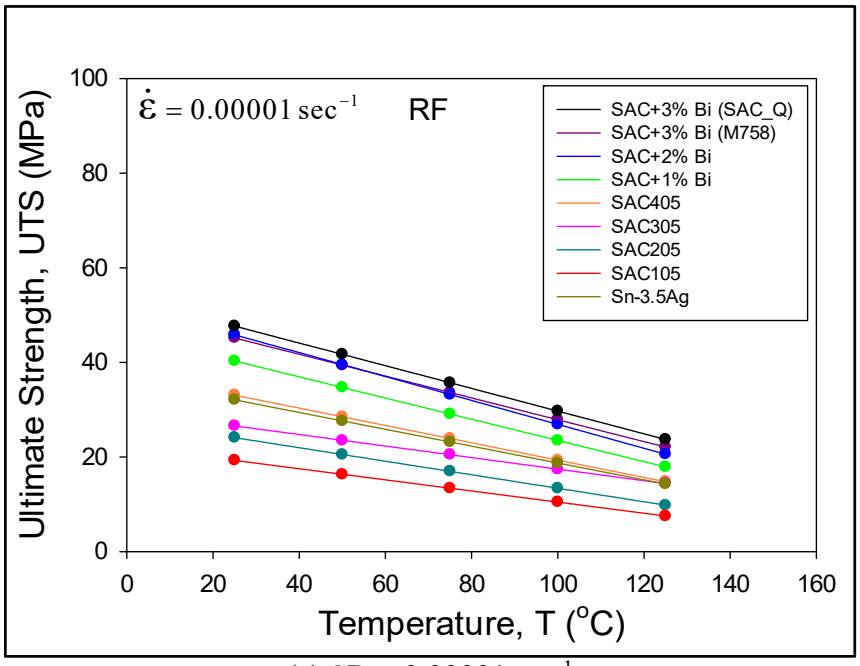

(c) SR = 0.00001 sec^{-1}

Figure 6.8 Variation of Ultimate Strength with Temperature for Different SAC and SAC+Bi Alloys (RF, No Aging)

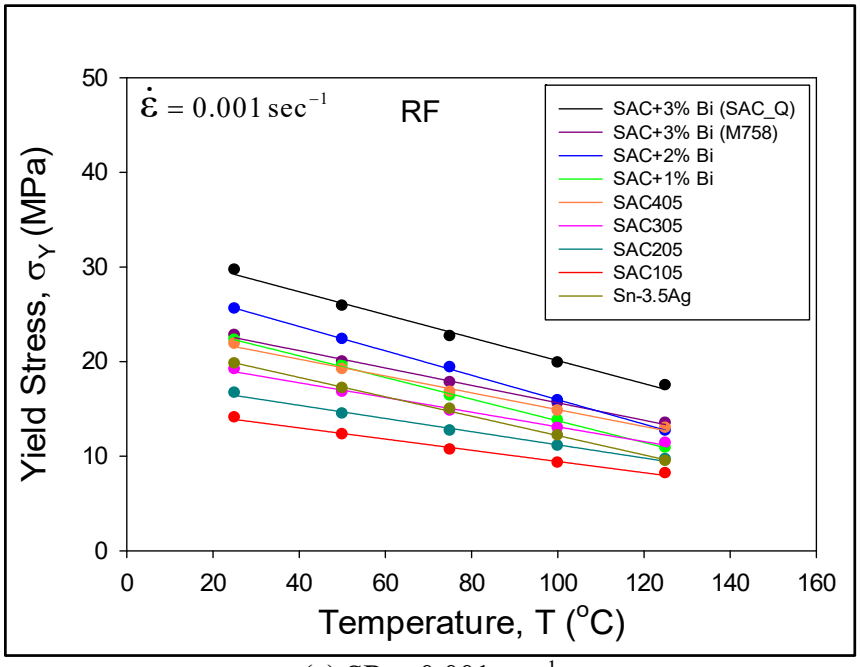

(a) SR = 0.001 sec^{-1}

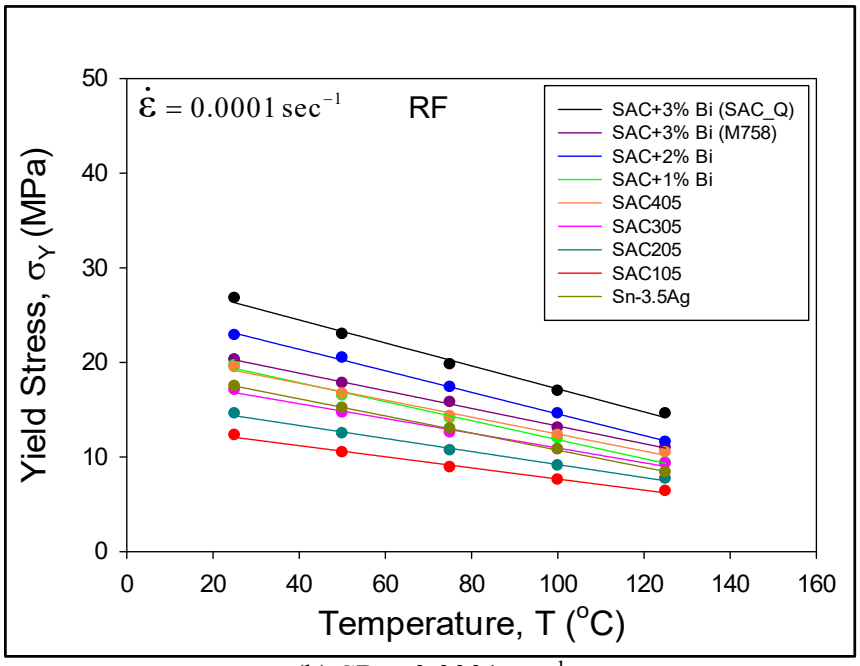

(b) SR = 0.0001 sec^{-1}

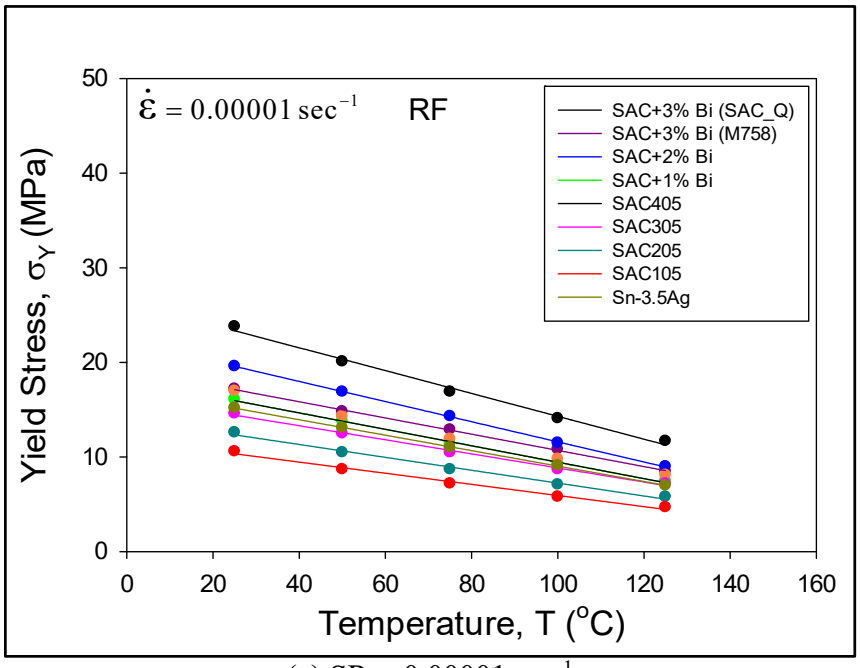

(c) SR = 0.00001 sec^{-1}

Figure 6.9 Variation of Yield Stress with Temperature for Different SAC and SAC+Bi Alloys (RF, No Aging)

6.6 Determination of Anand Model Parameters

Anand model is the most popular constitutive equation for solder alloys built into ANSYS and ABAQUS finite element codes. Therefore, temperature and strain rate dependent stress-strain results obtained from uniaxial tensile tests were utilized to determine the nine parameters (A, ξ, Q/R, m, h_o, a, s_o, $\hat{s}$, and n) of Anand model. The detail steps and equations to determine the Anand model parameters were described in section 3.6. Utilizing the approach high temperature aging dependent Anand model parameters were determined for SAC305 solder alloy and listed in Table 6.7.

Table 6.7 Anand Model Parameters of Various SAC+Bi and Sn-3.5Ag

Constant Number	Anand Constant	Units	Alloy			
			SAC+3% Bi	SAC+2% Bi	SAC+1% Bi	Sn-3.5Ag
1	s_o	MPa	22.50	26.50	21.80	20.70
2	Q/R	1/K	10270	9820	9950	9250
3	A	sec^{-1}	8200	10200	8000	7750
4	ξ	Dimensionless	6.00	6.00	6.00	4.00
5	m	Dimensionless	0.31	0.31	0.30	0.21
6	h_o	MPa	66500	95000	80000	77000
7	$\hat{S}$	MPa	57.00	59.50	53.00	42.00
8	n	Dimensionless	0.0043	0.0044	0.0038	0.0032
9	a	Dimensionless	1.16	1.08	1.02	1.14

6.7 Correlation between Anand Model Predictions and Experimental Results

After determining the set of parameters, they were utilized to predict the stress-strain curves and compare with the experimental results following the method described in section 3.6.4. Figures 6.10-6.13 represents the correlation.

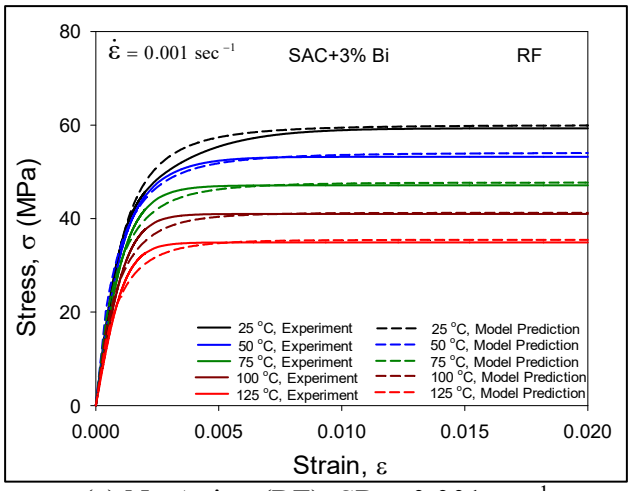

(a) No Aging (RF), SR = 0.001 sec^{-1}

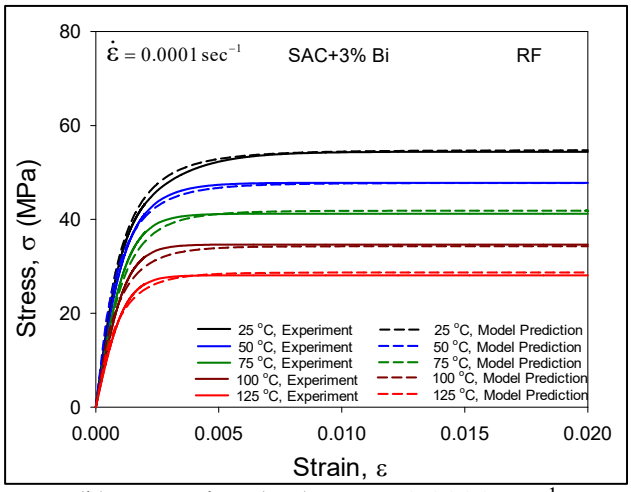

(b) No Aging (RF), SR = 0.0001 sec^{-1}

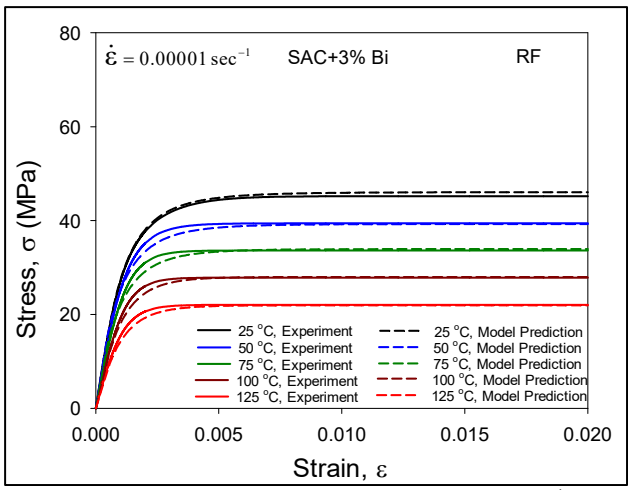

(c) No Aging (RF), SR = 0.00001 sec^{-1}

Figure 6.10 Correlation between Anand Model Predicted and Experimental Results for SAC+3% Bi Alloy

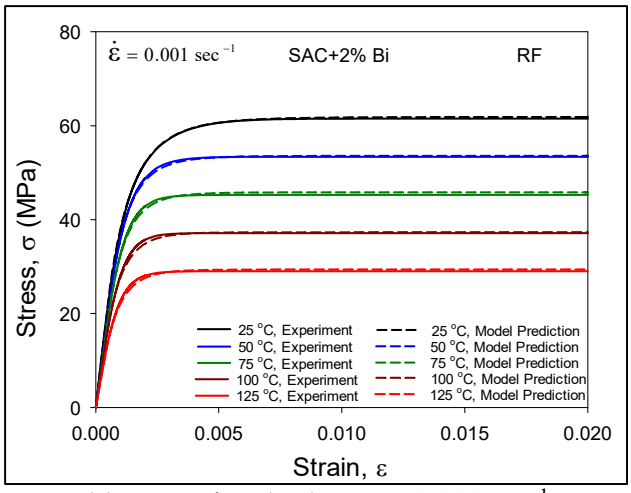

(a) No Aging (RF), SR = 0.001 sec^{-1}

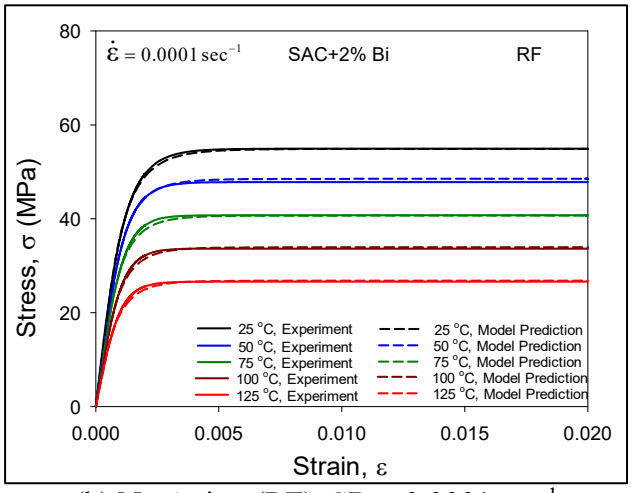

(b) No Aging (RF), SR = 0.0001 sec^{-1}

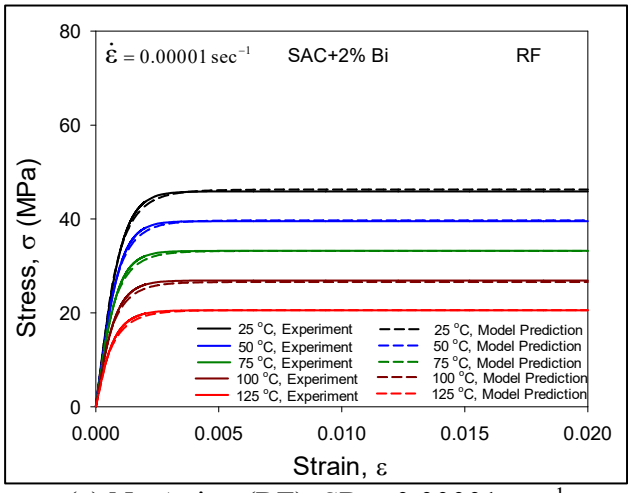

(c) No Aging (RF), SR = 0.00001 sec^{-1}

Figure 6.11 Correlation between Anand Model Predicted and Experimental Results for SAC+2% Bi Alloy

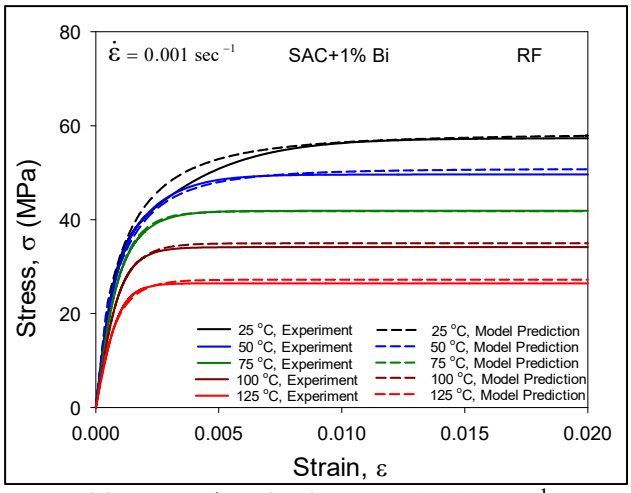

(a) No Aging (RF), SR = 0.001 sec^{-1}

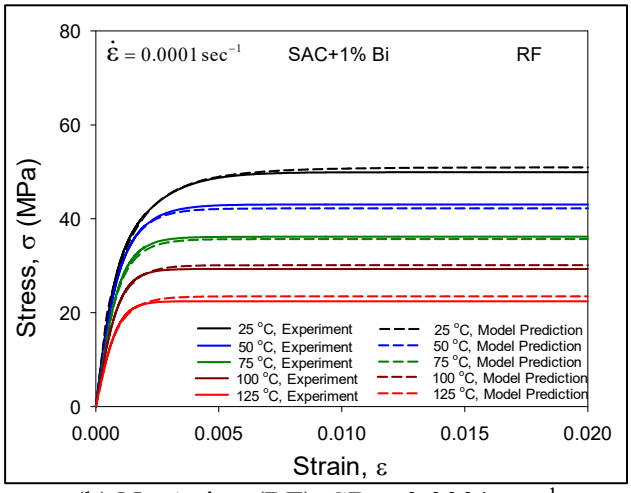

(b) No Aging (RF), SR = 0.0001 sec^{-1}

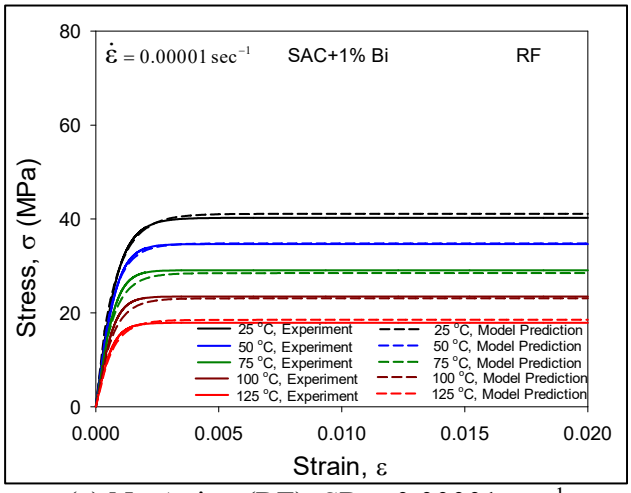

(c) No Aging (RF), SR = 0.00001 sec^{-1}

Figure 6.12 Correlation between Anand Model Predicted and Experimental Results for SAC+1% Bi Alloy

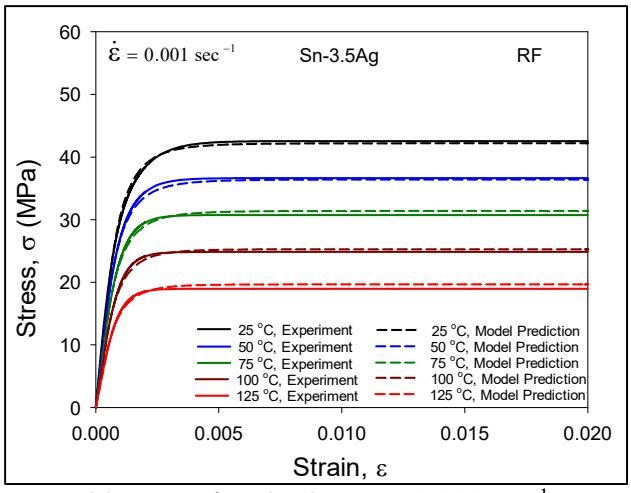

(a) No Aging (RF), SR = 0.001 sec^{-1}

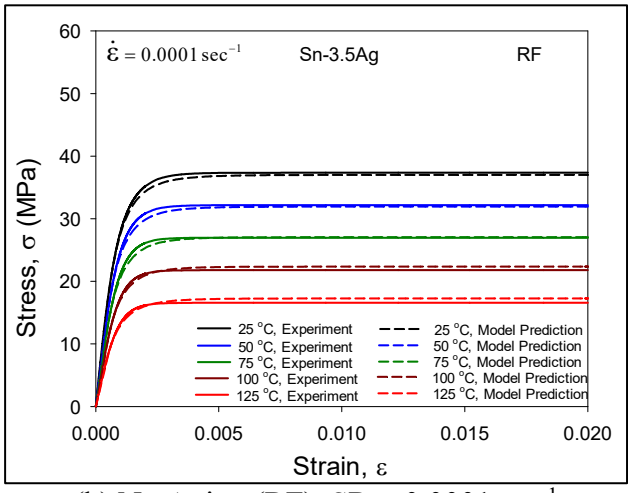

(b) No Aging (RF), SR = 0.0001 sec^{-1}

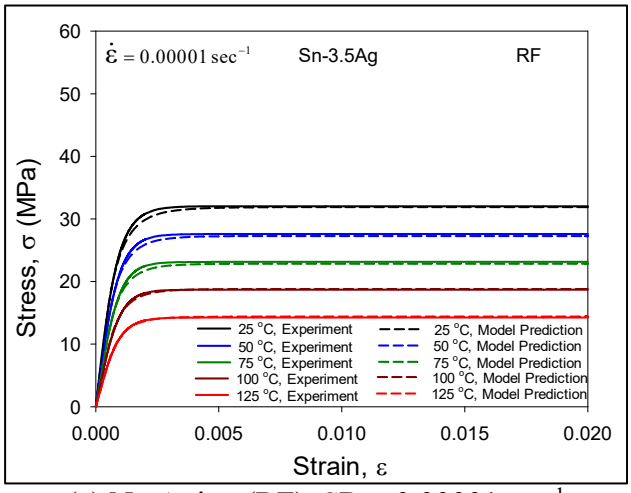

(c) No Aging (RF), SR = 0.00001 sec^{-1}

Figure 6.13 Correlation between Anand Model Predicted and Experimental Results for Sn-3.5Ag Alloy

6.8 Effect of Isothermal Aging on Experimental Results

After exploring the effects of temperature and strain rates on various new SAC+Bi alloy it was observed that Bi helped to improve mechanical response specially at high test temperatures as the mechanical properties of the SAC+Bi alloys were better compared to SACN05 (N= 1, 2, 3, 4), and Sn-3.5Ag. Many previous studies [202-205] were focused to examine the effects of isothermal aging on the mechanical response of the well-known SAC_Q (SAC+3% Bi) alloy. To further investigate the influence of Bi at mitigating aging effects, additional research was conducted on the other two SAC+Bi alloys (1% and 2% Bi) using both mechanical testing and microstructural observations.

6.8.1 Effect of Isothermal Aging on Stress-Strain Response

For the solder mechanical response, the fabricated uniaxial specimens were aged (preconditioned) at T = 125 °C for several durations of aging including 0, 1, 5, and 20 days. Stress-strain tests on the aged specimens were then performed at a single strain rate of 0.001 (sec^{-1}), and temperatures of 25, 50, 75, 100, and 125 °C. Figures 6.14, and 6.15 represents the variation of mechanical properties for individual SAC+Bi alloy, whereas, Figure 6.16 shows the comparison between SAC+2% Bi, and SAC+1% Bi alloy. Here, two different types of line represents two different SAC+Bi alloys, such as, solid line = SAC+2% Bi, dashed line = SAC+1% Bi alloy. Again, one single color curve in any of these plots represent the average results for 8-10 tests, whereas, the various colored curves in a particular plot representing the different test temperatures with black = 25 °C, blue = 50 °C, green = 75 °C, orange = 100 °C, and red = 125 °C. Again, in each plot, top curve corresponds to 25 °C and bottom curve represents 125 °C test result.

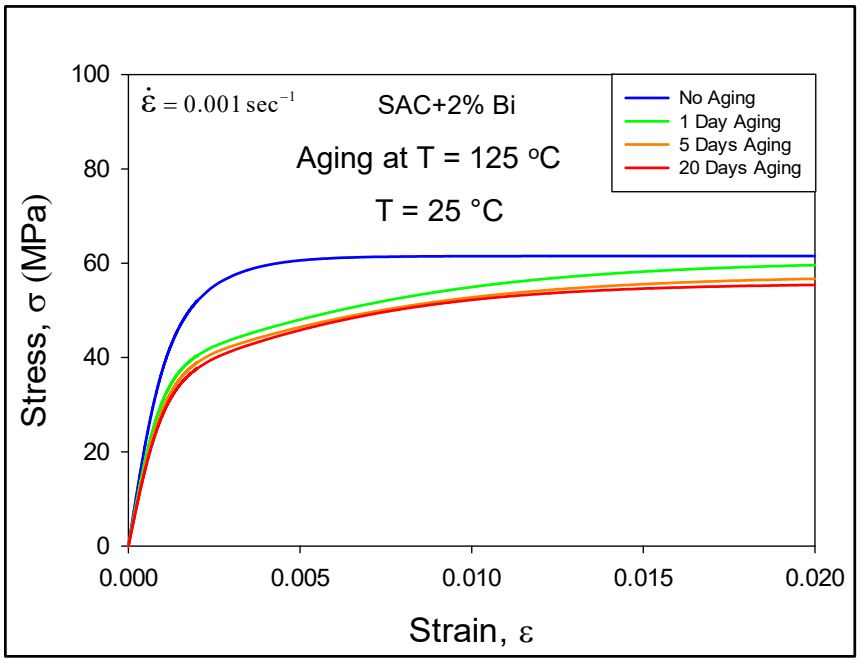
100
80
60
40
20
0
0.000
0.005
0.010
0.015
0.020
Stress, σ (MPa)
Strain, ε
$\dot{\varepsilon} = 0.001\,\mathrm{sec}^{-1}$
SAC+2% Bi
Aging at T = 125 °C
T = 25 °C
No Aging
1 Day Aging
5 Days Aging
20 Days Aging

(a) T = 25 °C

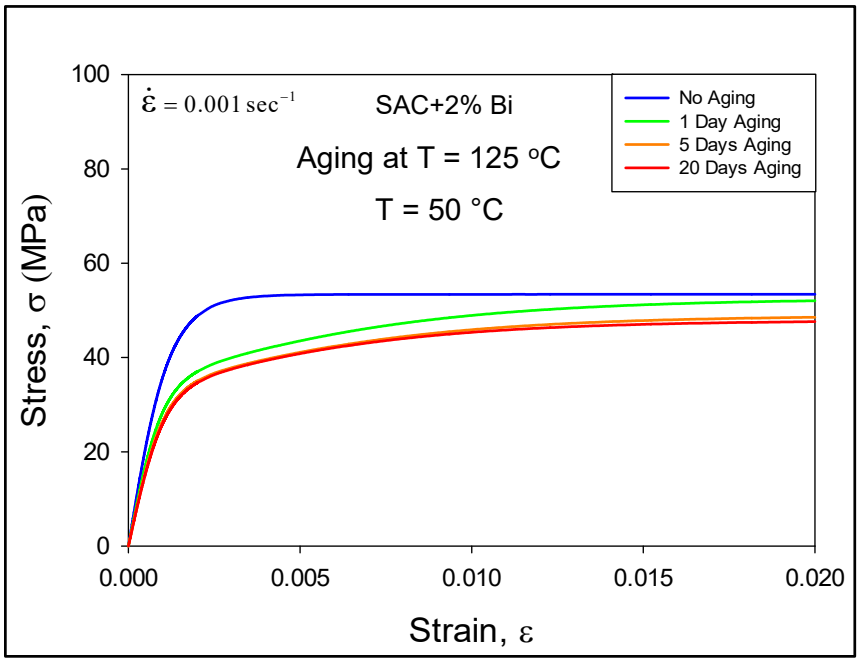
100
80
60
40
20
0
0.000
0.005
0.010
0.015
0.020
Stress, σ (MPa)
Strain, ε
$\dot{\varepsilon} = 0.001\,\mathrm{sec}^{-1}$
SAC+2% Bi
Aging at T = 125 °C
T = 50 °C
No Aging
1 Day Aging
5 Days Aging
20 Days Aging

(b) T = 50 °C

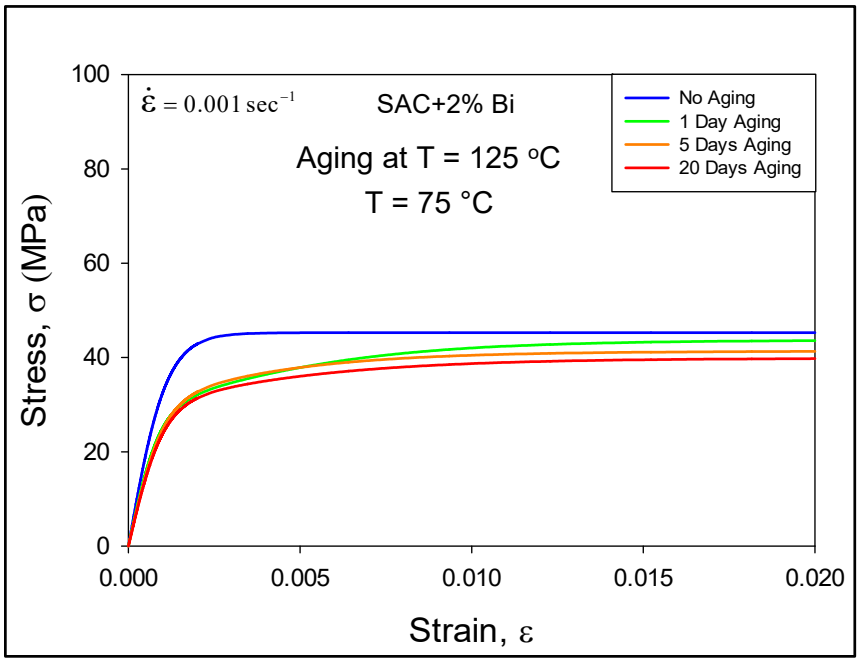

(c) T = 75 °C

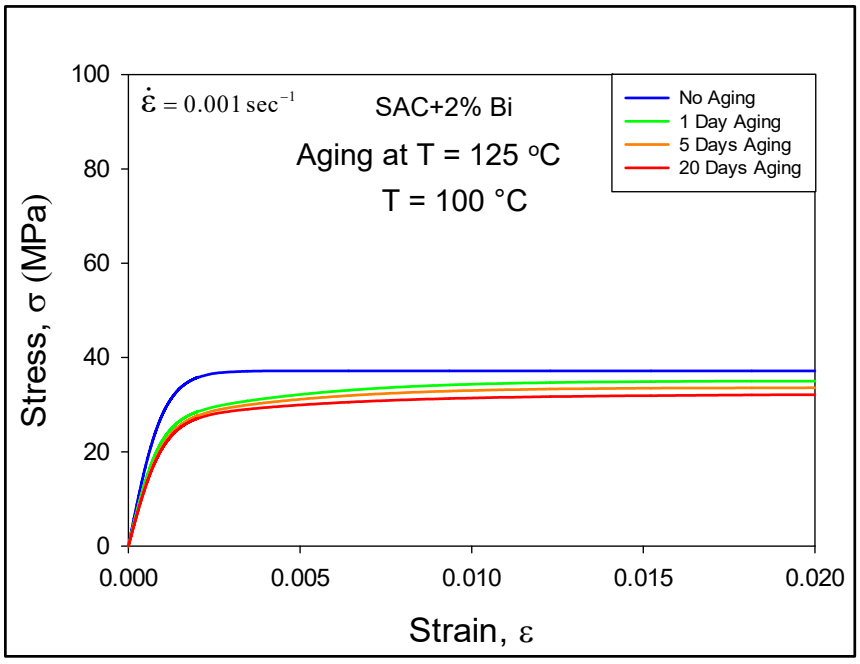

(d) T = 100 °C

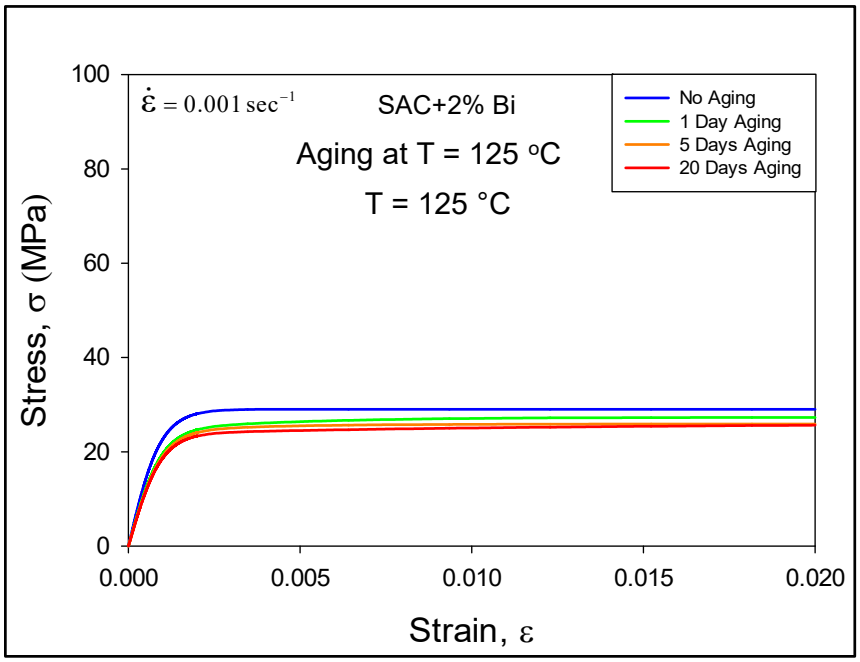

(e) T = 125 °C

Figure 6.14 Comparison of Stress-Strain Curves for SAC+2% Bi Alloy for Various Aging Durations (Aging at T = 125 °C, SR = 0.001 sec^{-1})

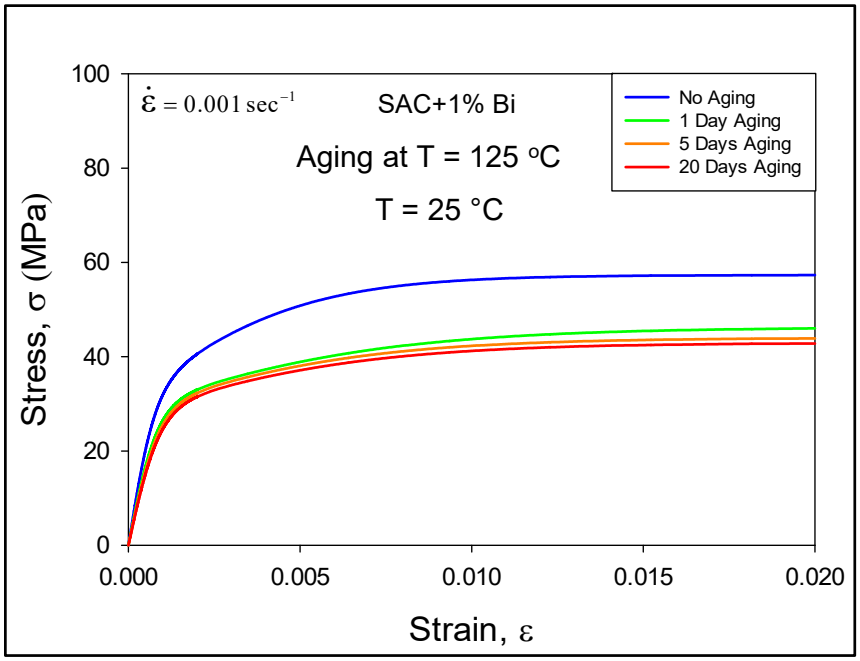

(a) T = 25 °C

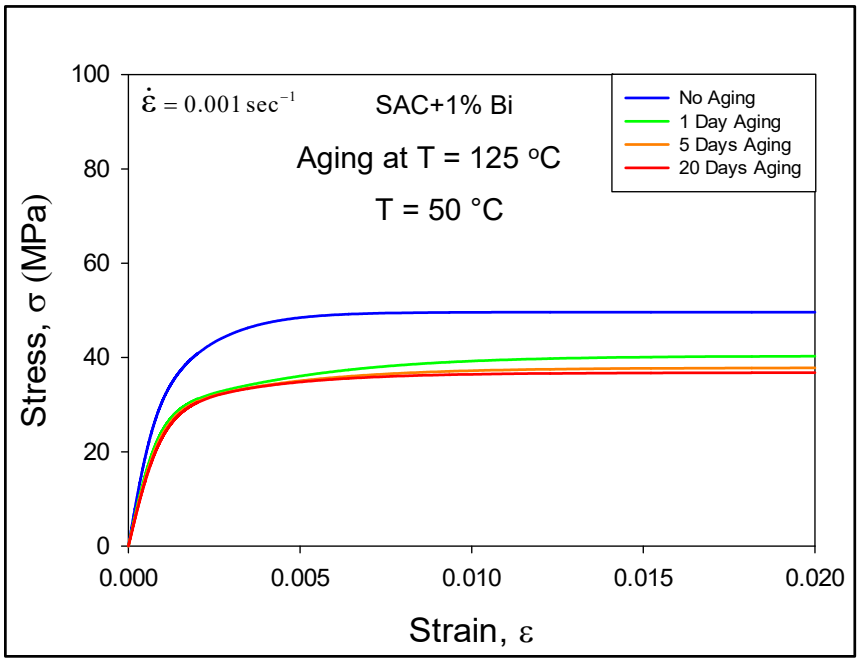
100
80
60
40
20
0
0.000
0.005
0.010
0.015
0.020
Stress, σ (MPa)
Strain, ε
$\dot{\varepsilon} = 0.001\,\mathrm{sec}^{-1}$
SAC+1% Bi
Aging at T = 125 °C
T = 50 °C
No Aging
1 Day Aging
5 Days Aging
20 Days Aging

(b) T = 50 °C

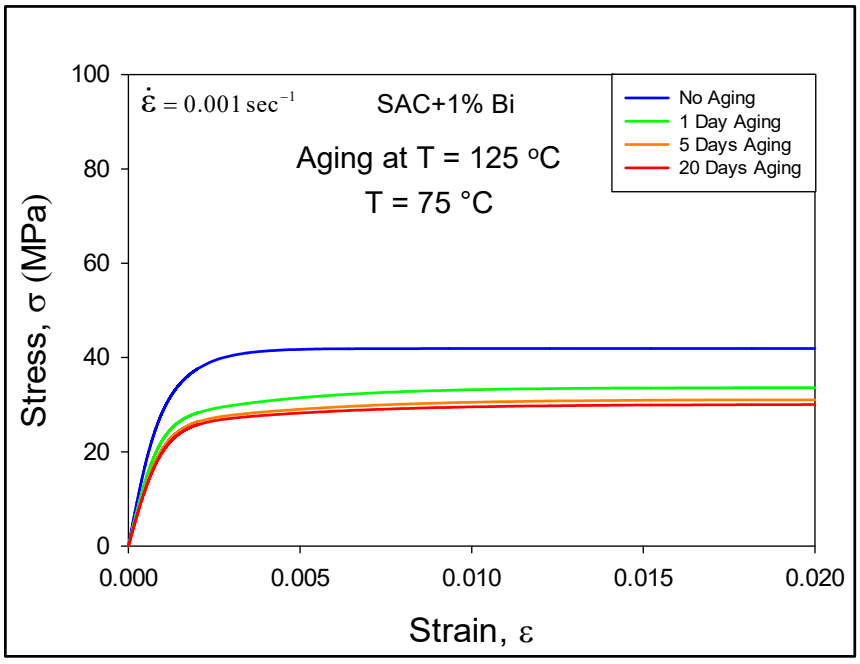
100
80
60
40
20
0
0.000
0.005
0.010
0.015
0.020
Stress, σ (MPa)
Strain, ε
$\dot{\varepsilon} = 0.001\,\mathrm{sec}^{-1}$
SAC+1% Bi
Aging at T = 125 °C
T = 75 °C
No Aging
1 Day Aging
5 Days Aging
20 Days Aging

(c) T = 75 °C

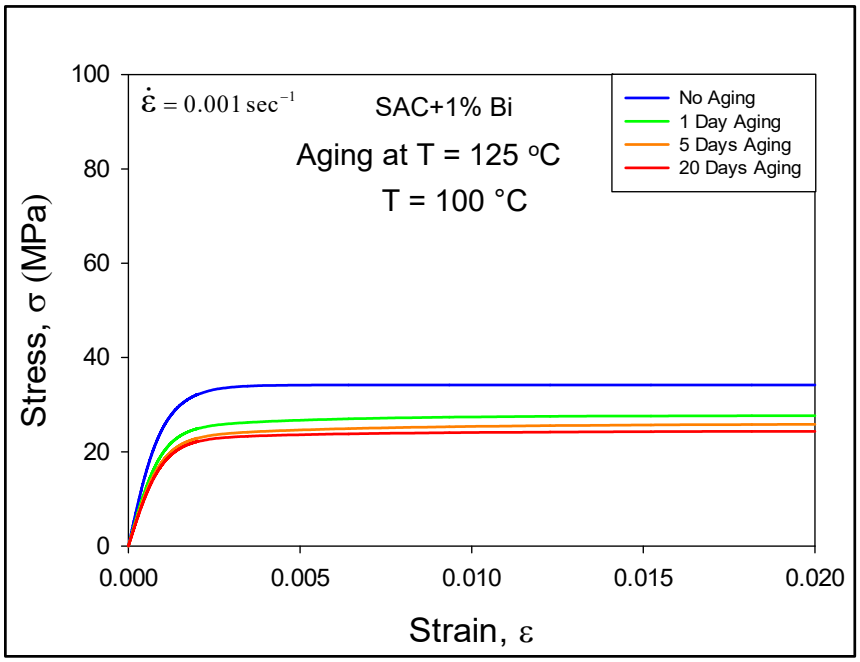

(d) T = 100 °C

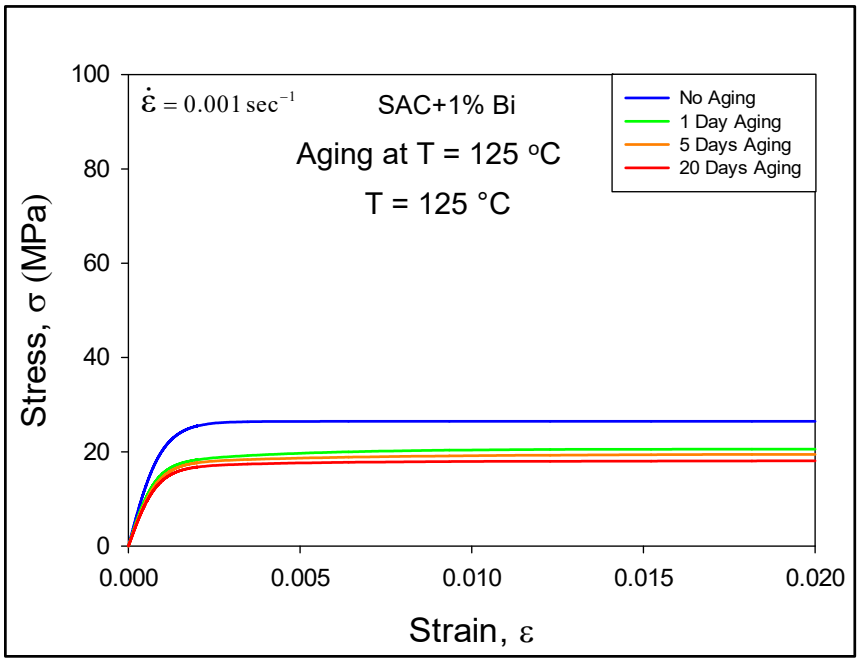

(e) T = 125 °C

Figure 6.15 Comparison of Stress-Strain Curves for SAC+1% Bi Alloy for Various Aging Durations (Aging at T = 125 °C, SR = 0.001 sec^{-1})

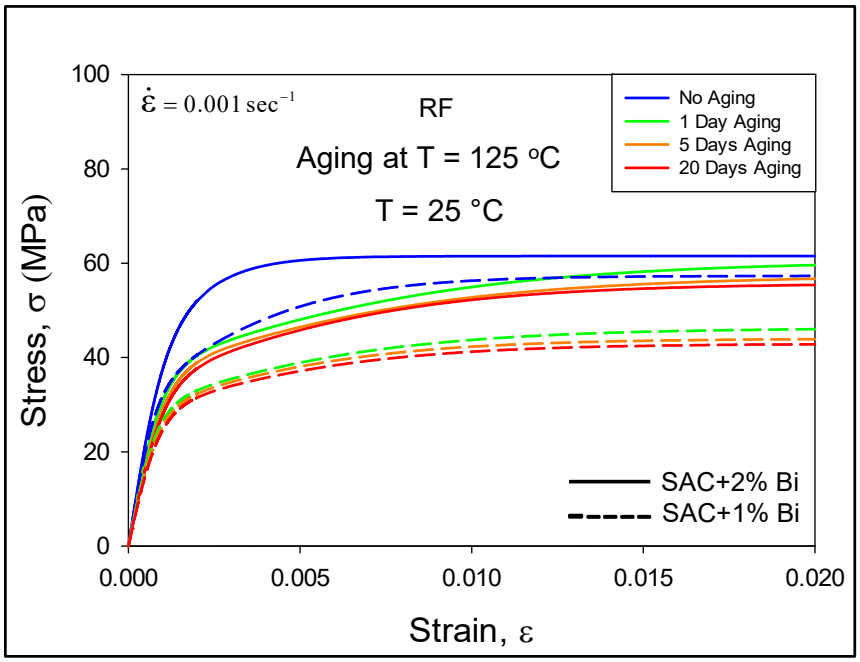
$\dot{\varepsilon} = 0.001\,\mathrm{sec}^{-1}$
RF
Aging at T = 125 °C
T = 25 °C
No Aging
1 Day Aging
5 Days Aging
20 Days Aging
SAC+2% Bi
SAC+1% Bi
Stress, σ (MPa)
Strain, ε
0
20
40
60
80
100
0.000
0.005
0.010
0.015
0.020

(a) T = 25 °C

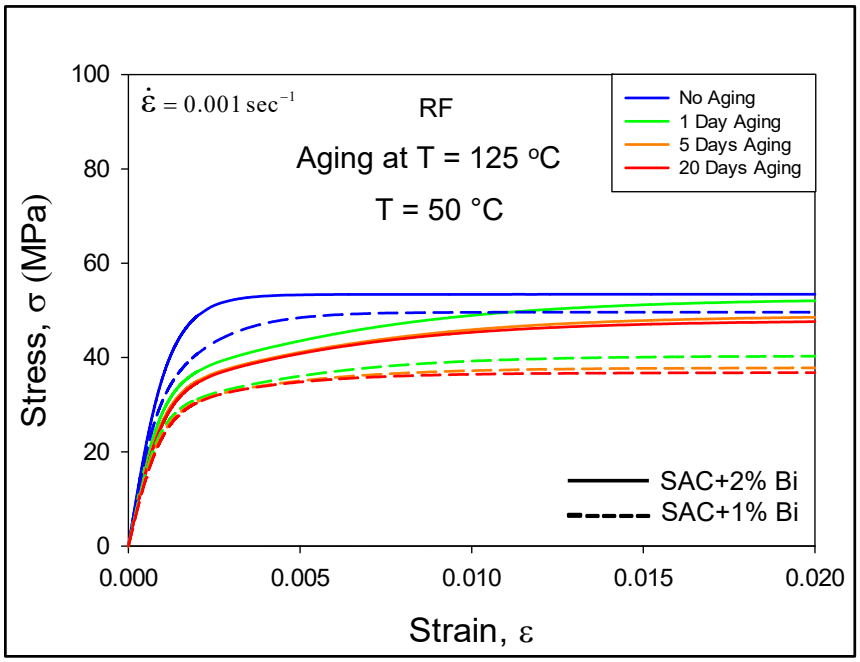
$\dot{\varepsilon} = 0.001\,\mathrm{sec}^{-1}$
RF
Aging at T = 125 °C
T = 50 °C
No Aging
1 Day Aging
5 Days Aging
20 Days Aging
SAC+2% Bi
SAC+1% Bi
Stress, σ (MPa)
Strain, ε
0
20
40
60
80
100
0.000
0.005
0.010
0.015
0.020

(b) T = 50 °C

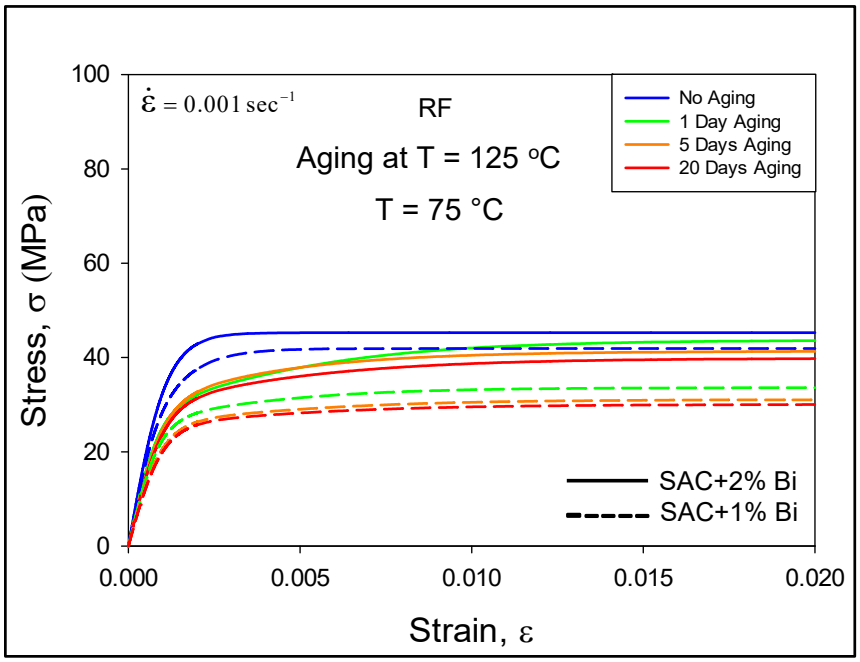

(c) T = 75 °C

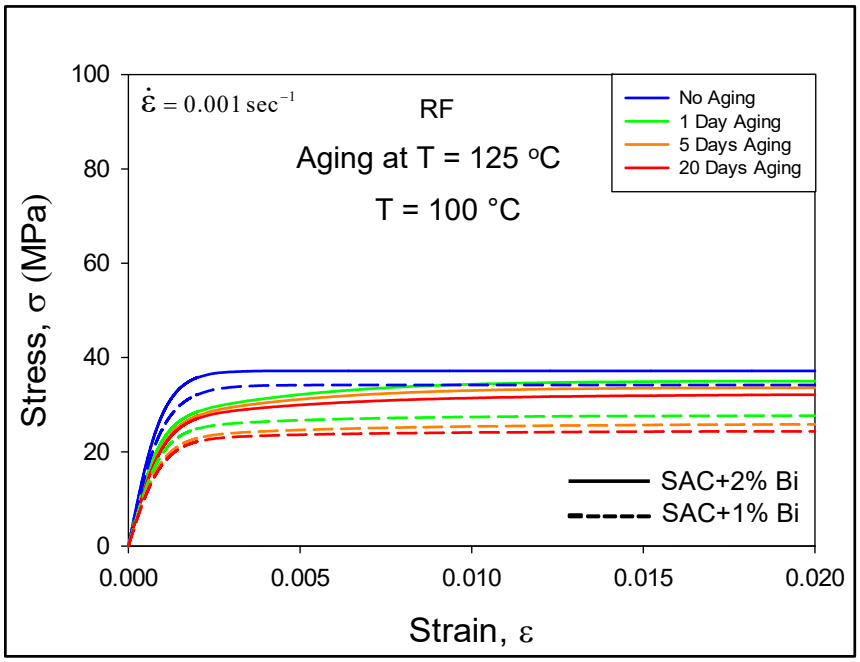

(d) T = 100 °C

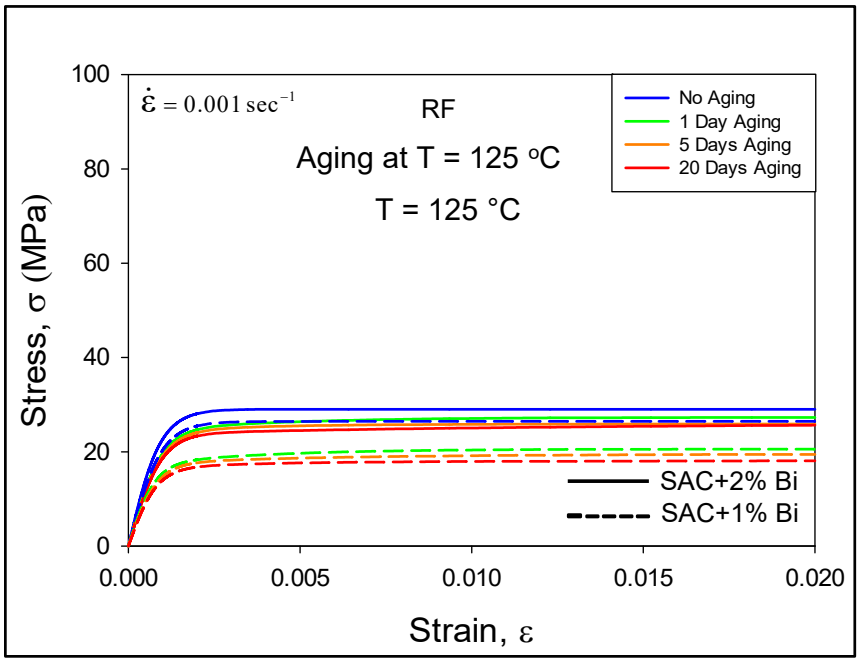

(e) T = 125 °C

Figure 6.16 Comparison of Stress-Strain Curves for SAC+2% Bi and SAC+1% Bi Alloy for Various Aging Durations (Aging at T = 125 °C, SR = 0.001 sec^{-1})

6.8.2 Comparison of Mechanical Properties

The mechanical properties, such as, initial effective modulus, and ultimate tensile strength of the two new SAC+Bi alloys were extracted from the measured stress-strain data and listed in Table 6.8, and 6.9. They are plotted as a function of isothermal aging duration in Figures 6.17-6.19. Figures 6.17, and 6.18 represents the variation of mechanical properties for individual SAC+Bi alloy, whereas, Figure 6.19 shows the comparison between SAC+2% Bi, and SAC+1% Bi alloy. Here, two different types of line represents two different SAC+Bi alloys, such as, solid line = SAC+2% Bi, dashed line = SAC+1% Bi alloy. The aging induced degradations are evident for both the SAC+2% Bi and the SAC+1% Bi alloys. However, the degradations are higher for the SAC+1% Bi alloy relative to those for the SAC+2% Bi. The most significant degradations occurred during the first 5 days of aging.

Table 6.8 Aging Dependent Effective Modulus (E) of SAC+1% Bi and SAC+2% Bi

Alloy	Strain Rate (sec^{-1})	Test Temperature (°C)	Effective Modulus, E (GPa) (Isothermal Aging T= 125 °C)			
			No Aging	1 Day Aging	5 Days Aging	20 Days Aging
SAC+1% Bi	10^{-3}	25	45.9	37.5	34.8	33.2
		50	41.6	33.8	31.6	30.4
		75	38.3	30.9	27.6	26.4
		100	34.5	26.3	24.4	23.1
		125	27.3	22.8	21.0	20.2
SAC+2% Bi		25	46.9	40.6	36.9	35.3
		50	44.6	37.5	34.2	33.2
		75	41.2	34.1	31.9	30.9
		100	36.7	30.7	28.0	27.3
		125	31.1	26.3	25.3	24.9

Table 6.9 Aging Dependent Ultimate Strength (UTS) of SAC+1% Bi and SAC+2% Bi

Alloy	Strain Rate (sec^{-1})	Test Temperature (°C)	Ultimate Strength, UTS (MPa) (Isothermal Aging T= 125 °C)			
			No Aging	1 Day Aging	5 Days Aging	20 Days Aging
SAC+1% Bi	10^{-3}	25	57.3	46.5	44.2	43.1
		50	49.6	40.5	38.0	36.9
		75	41.9	33.8	31.2	30.1
		100	34.2	27.6	25.7	24.5
		125	26.4	20.7	19.2	18.1
SAC+2% Bi		25	61.5	60.4	56.7	54.9
		50	53.4	52.2	48.9	47.8
		75	45.3	43.9	41.4	39.9
		100	37.2	35.3	33.8	31.8
		125	29.0	27.1	25.9	25.0

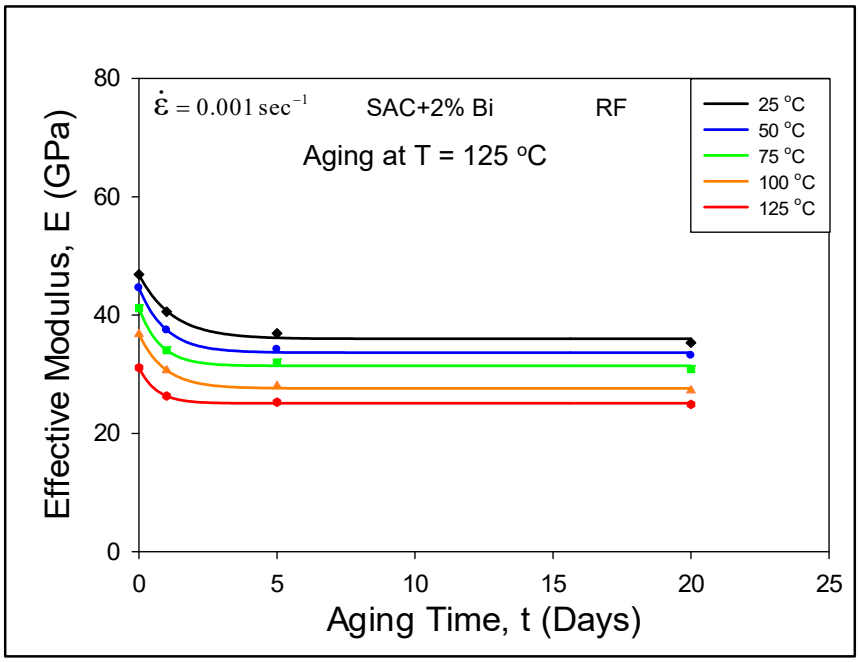

(a) SAC+2% Bi (RF)

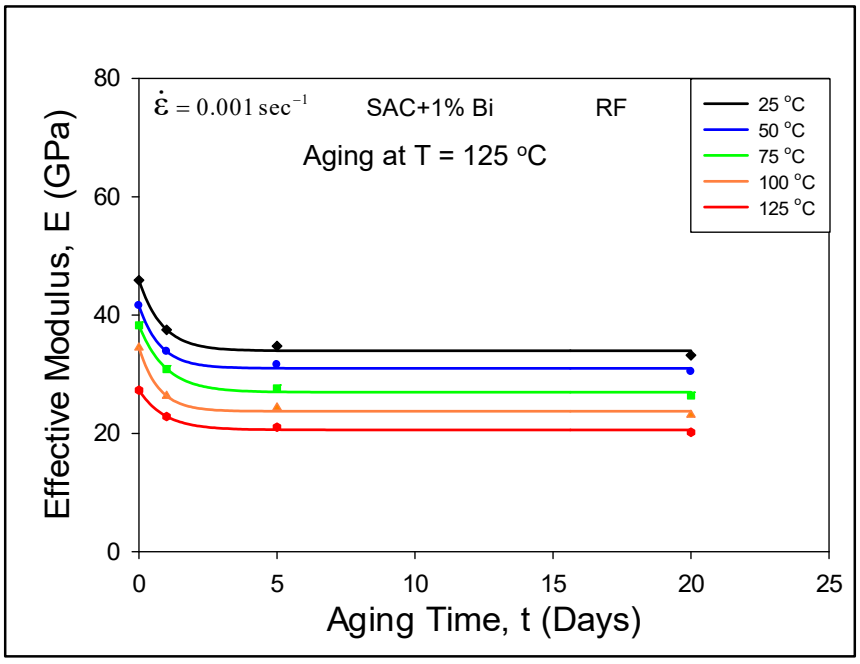

(b) SAC+1% Bi (RF)

Figure 6.17 Variation of Effective Modulus with Aging Time for SAC+Bi Lead Free Solder Alloys (Aging at T = 125 °C, SR = 0.001 sec^{-1})

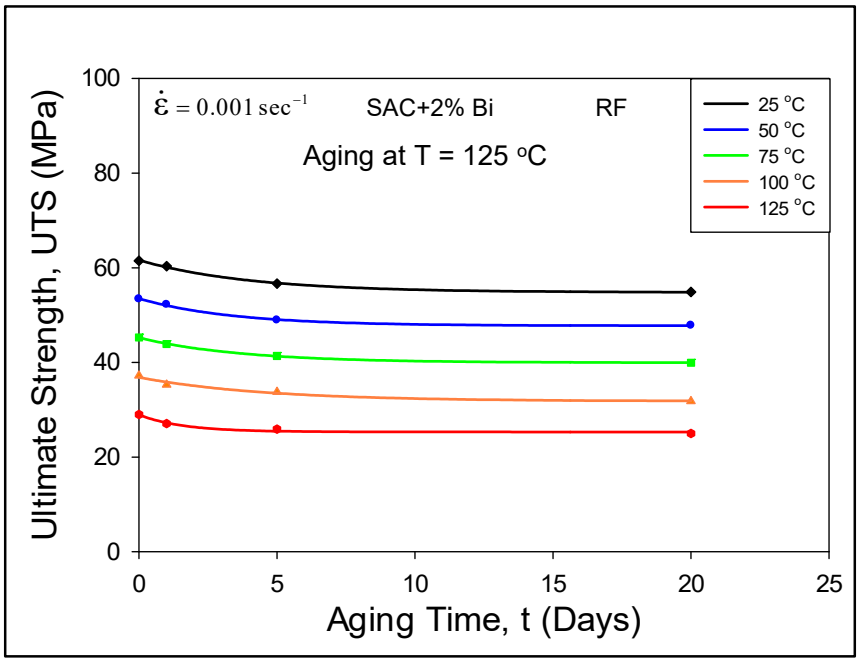

(a) SAC+2% Bi (RF)

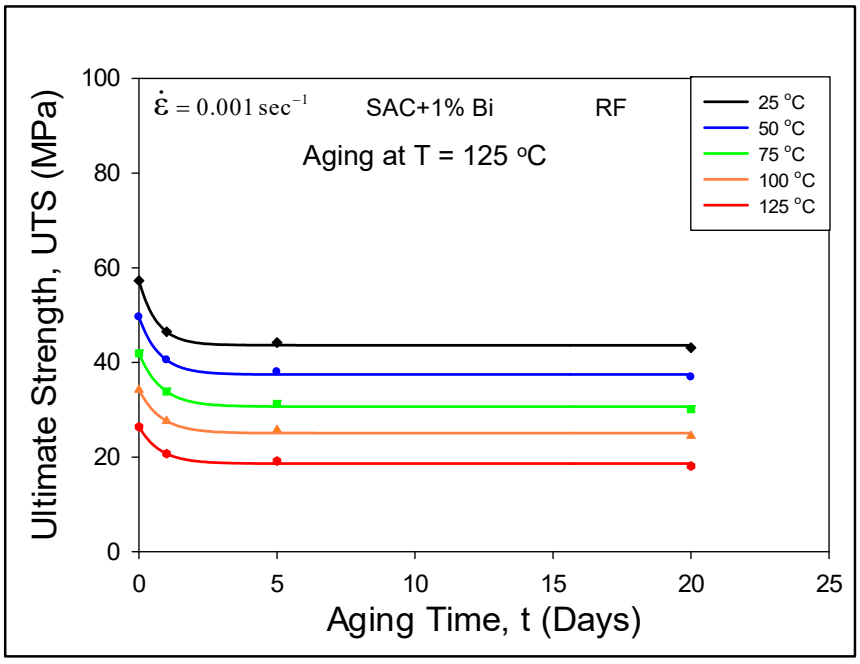

(b) SAC+1% Bi (RF)

Figure 6.18 Variation of Ultimate Strength with Aging Time for SAC+Bi Lead Free Solder Alloys (Aging at T = 125 °C, SR = 0.001 sec^{-1})

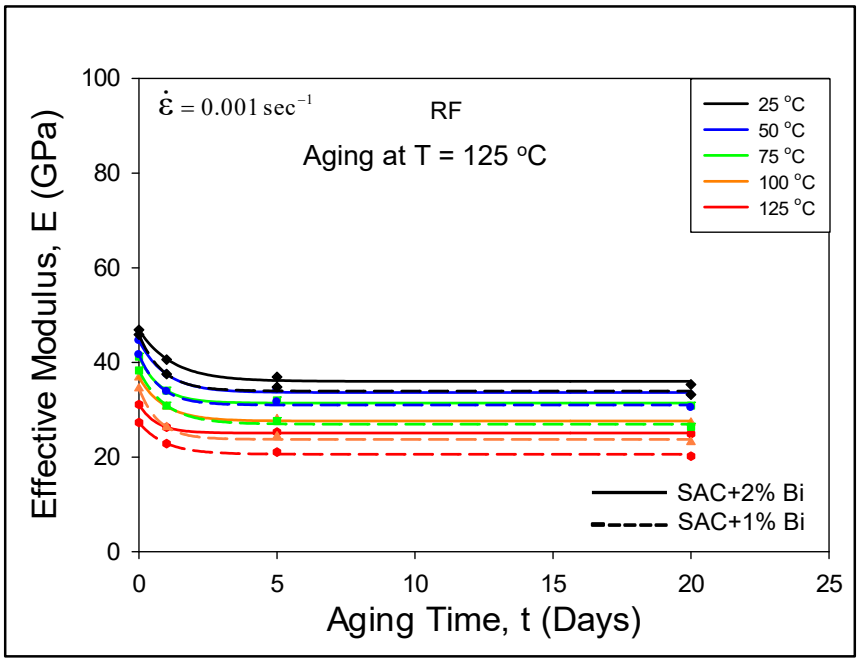

(a) Effective Modulus

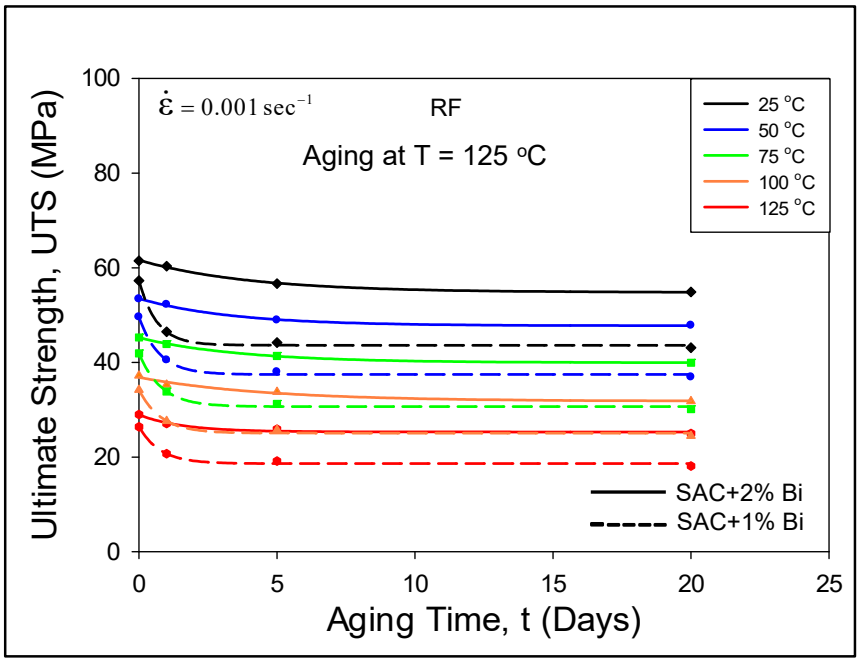

(b) Ultimate Strength

Figure 6.19 Comparison of Mechanical Properties with Aging Time for SAC+Bi Lead Free Solder Alloys (Aging at T = 125 °C, SR = 0.001 sec^{-1})

6.8.3 Microstructural Evolution during Isothermal Aging for SAC+Bi Alloy

In the current work, microstructural evolutions of the two new SAC+Bi (1%, and 2%) solder alloys were also observed for aging at T = 125 °C for the same durations of 0, 1, 5, and 20 days. In particular, aging induced coarsening of the IMCs was studied for each alloy using Scanning Electron Microscopy (SEM), and correlated to corresponding material property evolution. During this process, the topography of the microstructure of a fixed region was captured using the SEM system. This process generated several images of the microstructure as the aging progressed. These images were used to predict the microstructural evolution in SAC+Bi solder alloys exposed to high temperature aging. Image analysis software was utilized to quantify microstructural changes (total area, number and average diameter of IMC particles, inter particle spacing etc.) with respect to aging time.

The details of sample preparation including cross-sectioning, potting, and mechanical grinding was discussed in section 3.7.1, whereas, the image capturing mechanism using Scanning Electron Microscopy (SEM) was discussed in section 3.7.2. Utilizing the method, several images were captured for both SAC+2% Bi, and SAC+1% Bi alloys as shown in Figures 6.20, and 6.21.

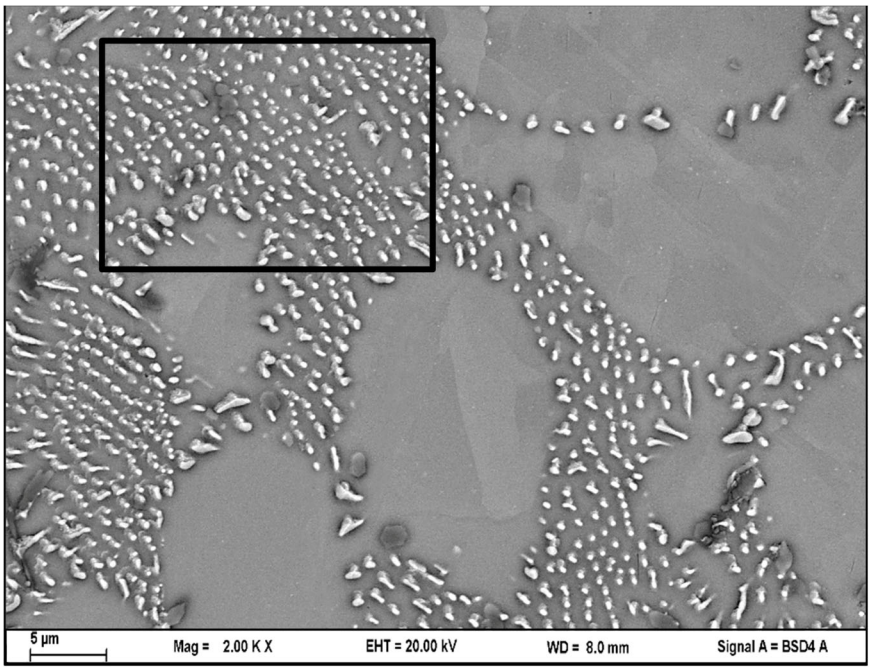

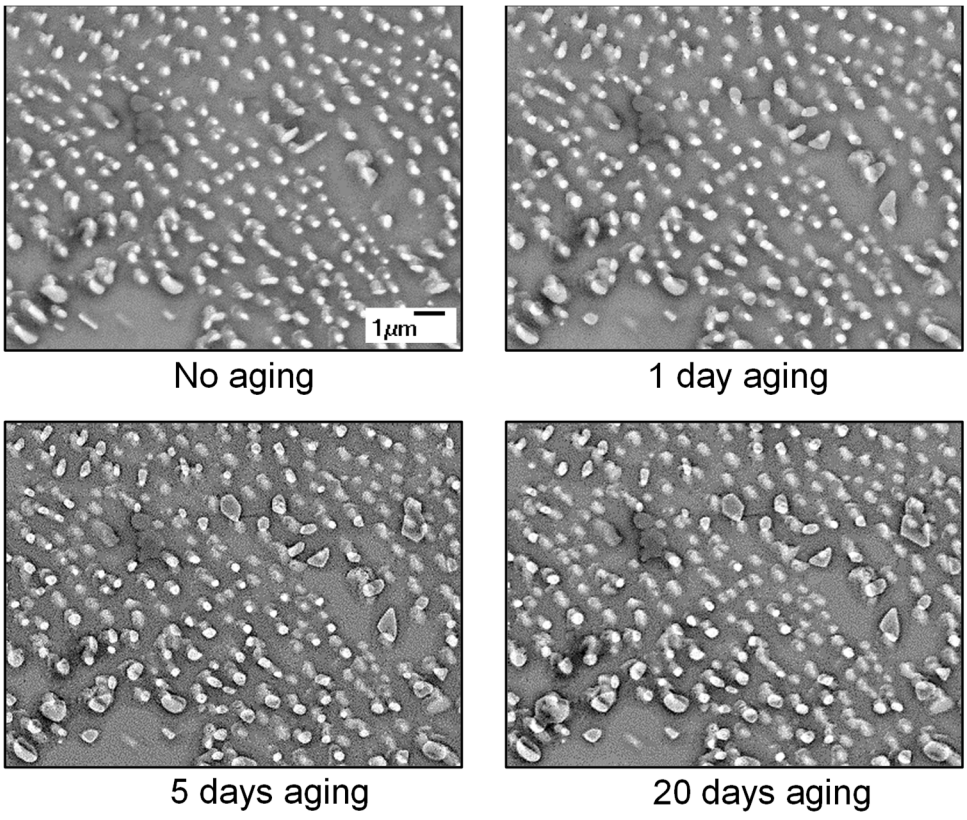

(a) Aging at T = 125 ºC (Region 1)

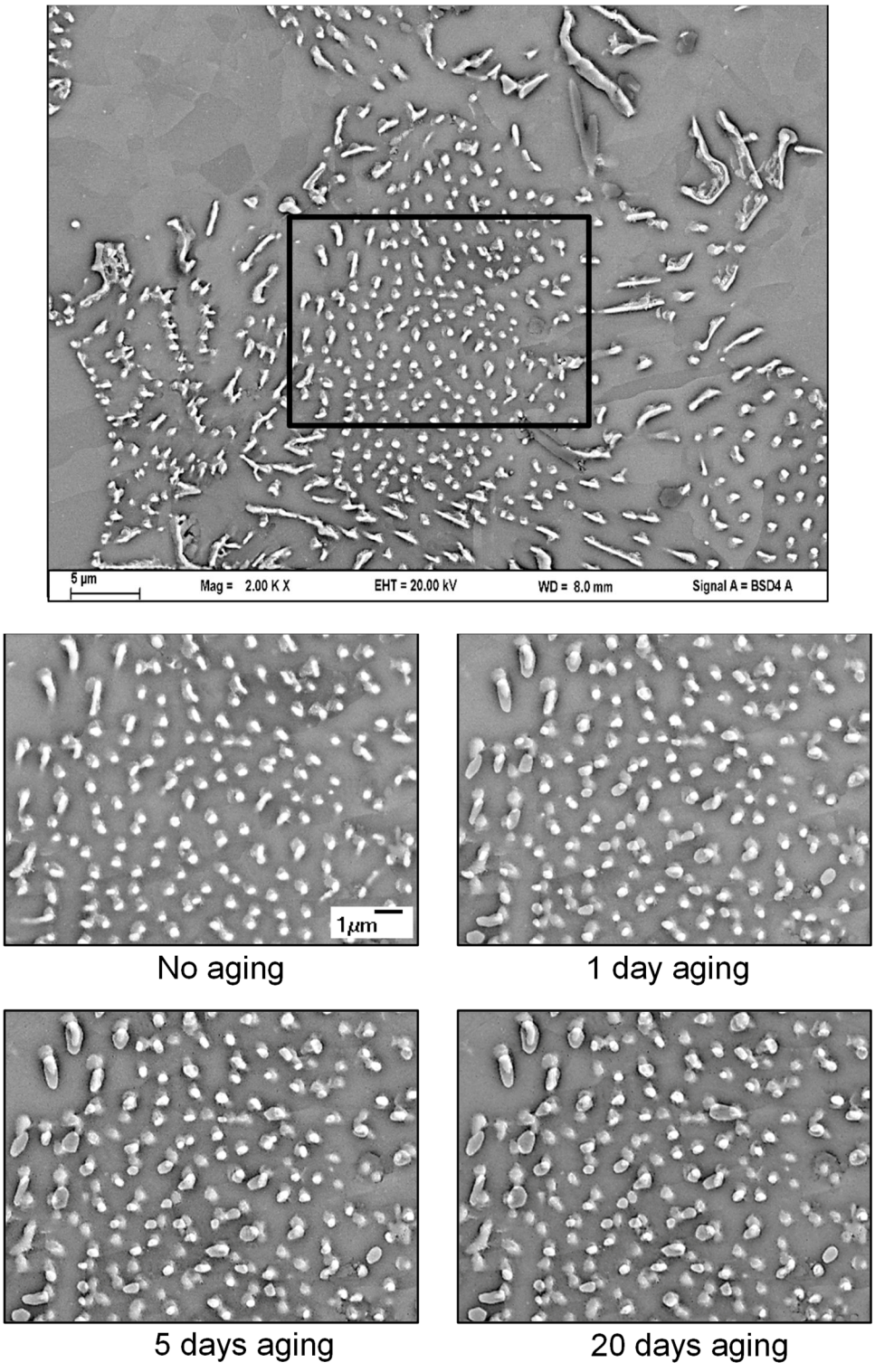

(b) Aging at T = 125 ºC (Region 2)

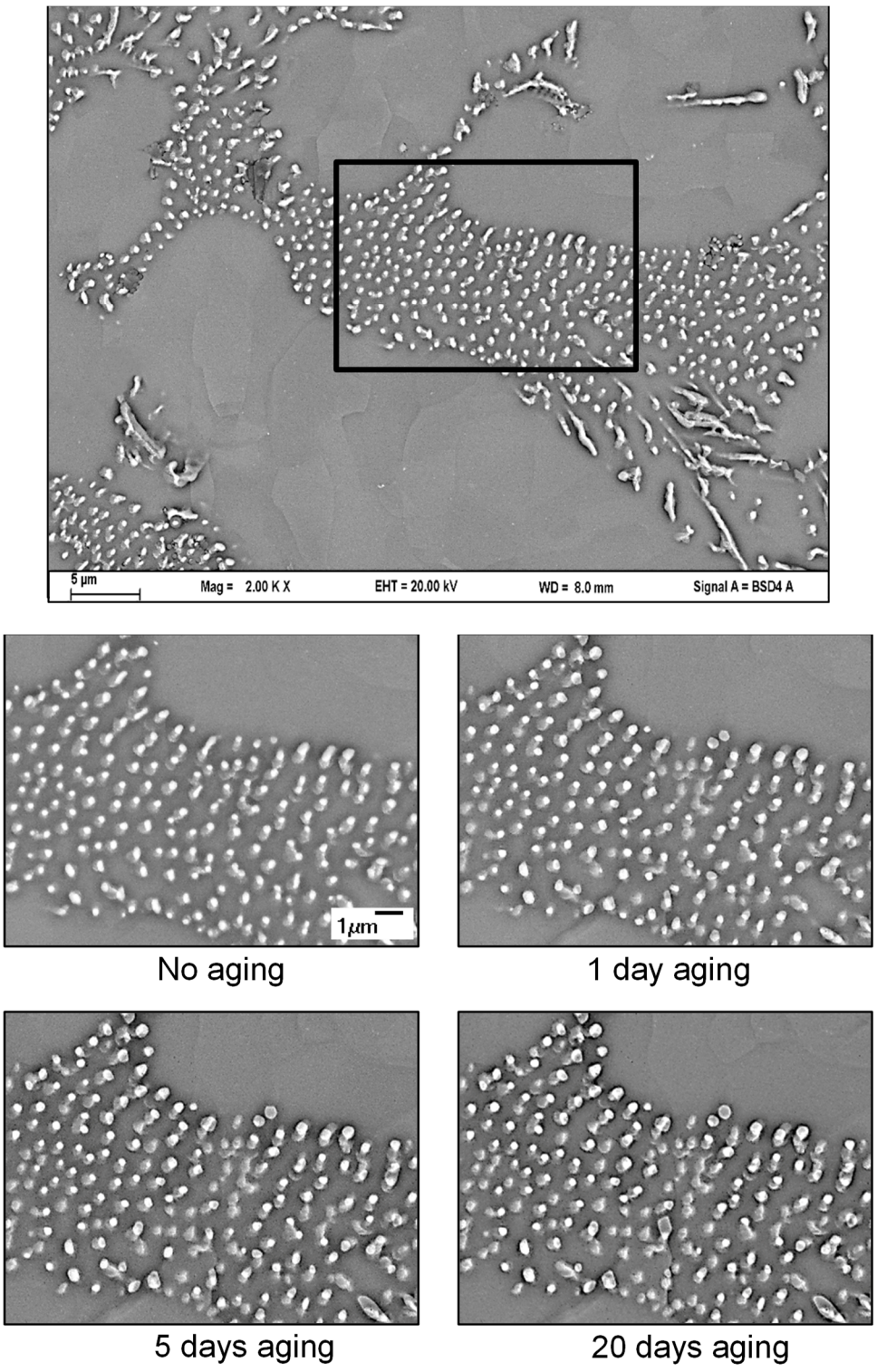

(c) Aging at T = 125 ºC (Region 3)

Figure 6.20 Microstructural Evolution of SAC+2% Bi Subjected to Isothermal Aging

(Aging at T = 125 ºC)

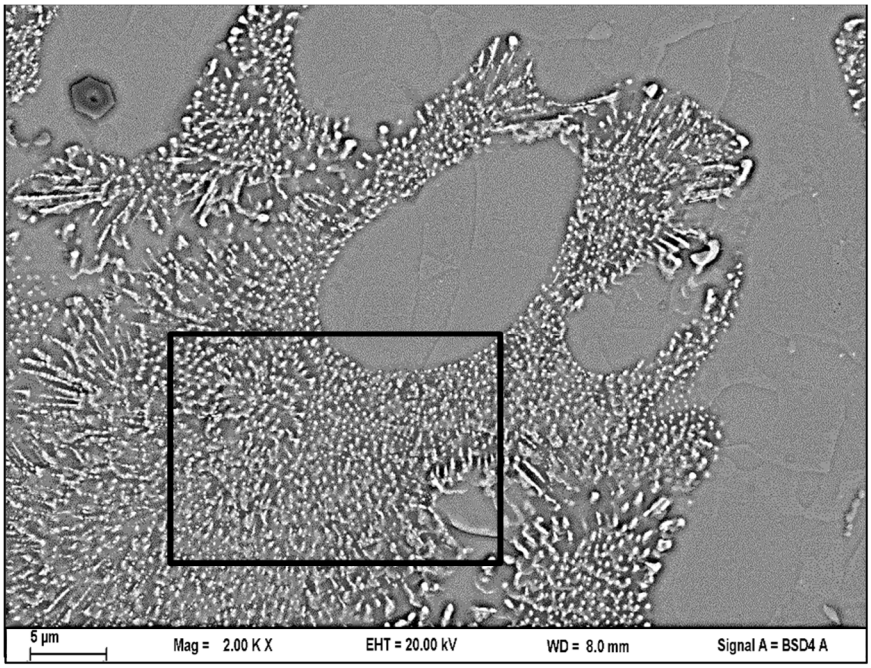

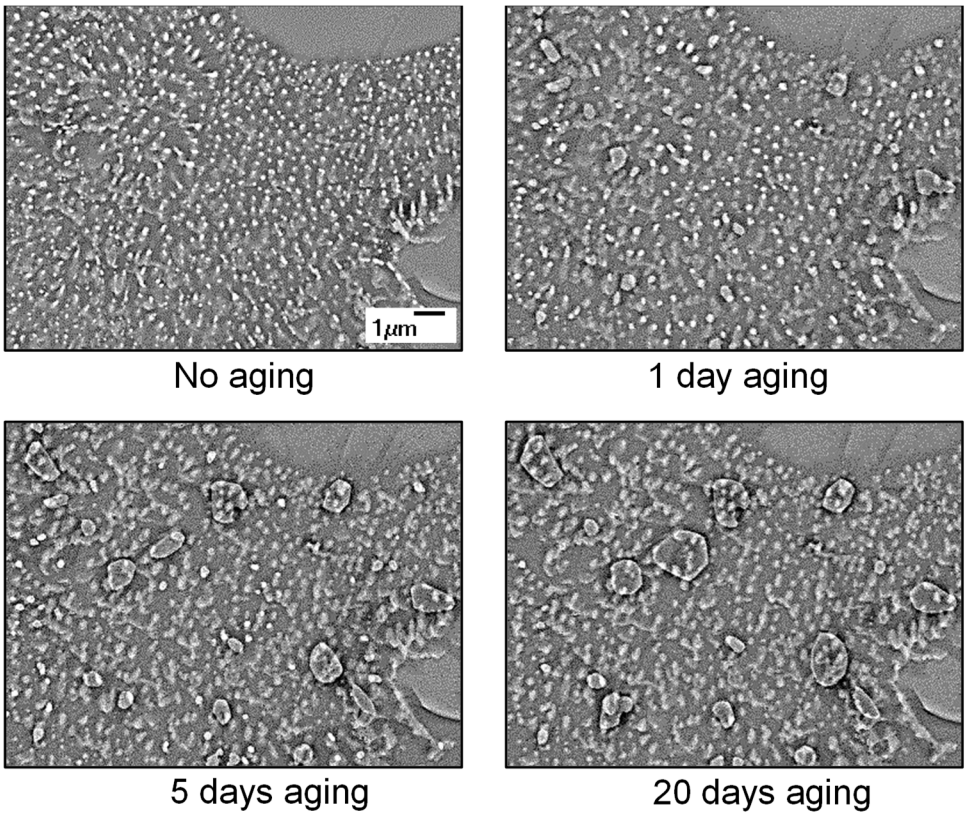

(a) Aging at T = 125 ºC (Region 1)

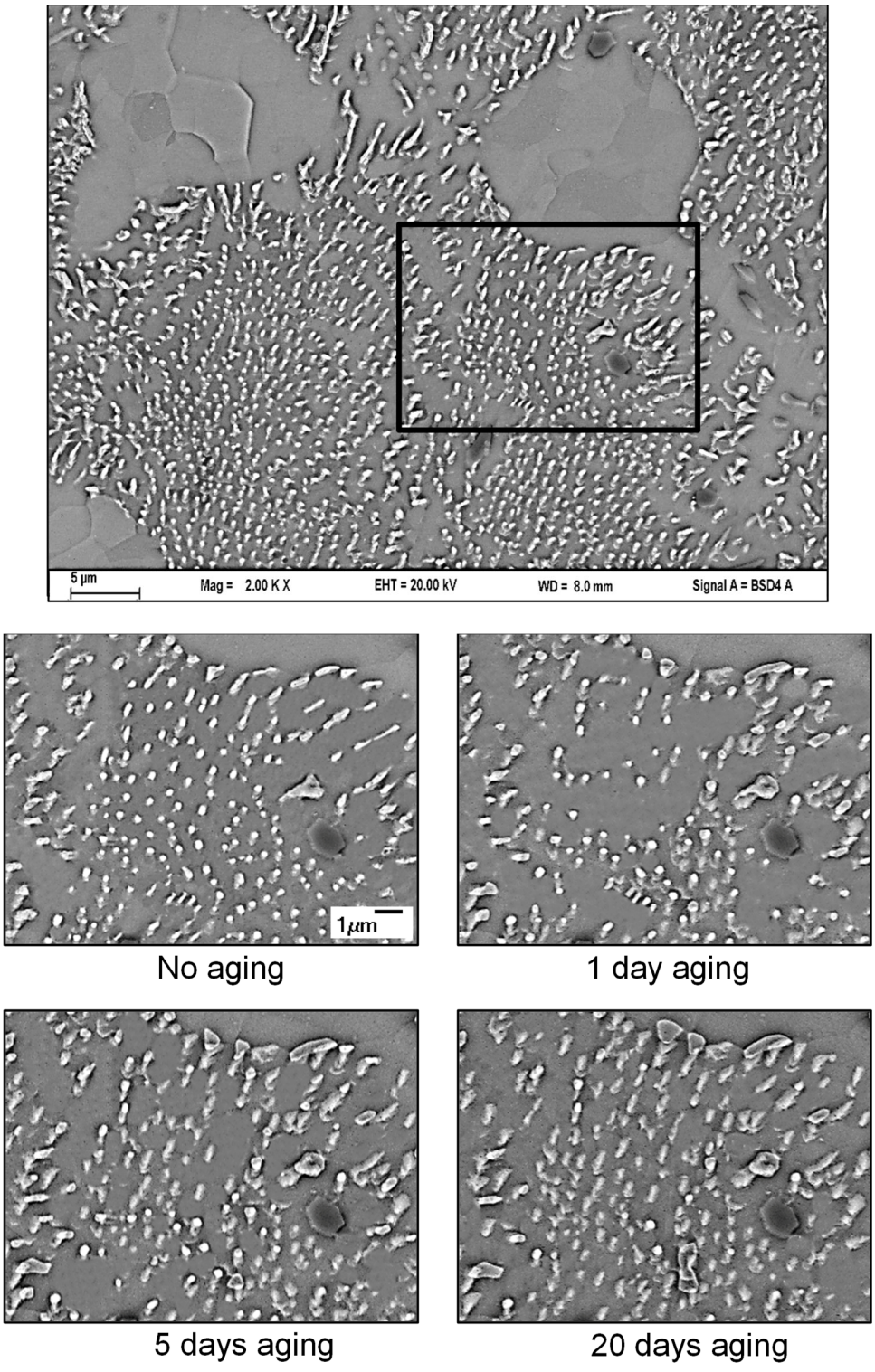

(b) Aging at T = 125 ºC (Region 2)

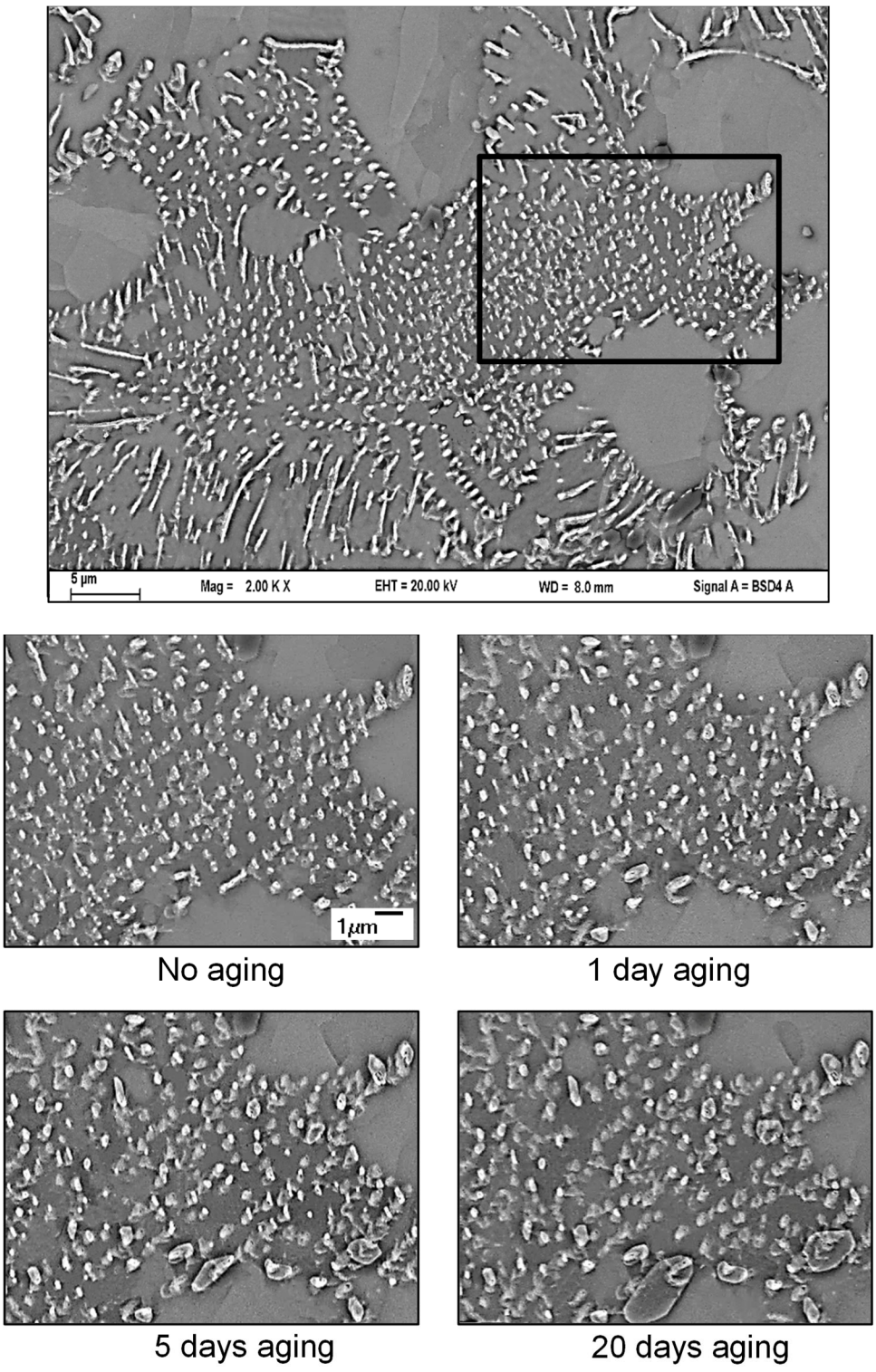

(c) Aging at T = 125 ºC (Region 3)

Figure 6.21 Microstructural Evolution of SAC+1% Bi Subjected to Isothermal Aging

(Aging at T = 125 ºC)

From all the images shown in Figures 6.20, and 6.21, a diffusion based IMC coarsening was observed where larger particles are produced at the expense of smaller particles which is popularly known as Ostwald Ripening [180-183]. Coarsening of intermetallic particles occurred due to aging. Some IMC particles grew in size, some split into several smaller particles, and some decreased in size and disappeared in the end. In other words, the number of IMC particles decreased, the average particle size increased, and the average particle separation distance increased. Also, the particles shifted to more spherical shapes. The shape and size of the dendrites remained nearly unchanged. Again, from visual comparison between images it was observed that the growth of IMC particles during isothermal aging was higher in SAC+1% Bi compared to SAC+2% Bi.

6.8.4 Measurement of IMC Particle Diameter

The images obtained from SEM were further processed to quantify the evolution of IMC particles during isothermal aging. Image processing and analysis steps were outlined before in sections 3.7.3, 3.7.4, and 3.7.5. The quantitative analysis results are summarized in Table 6.10 which represents the variation in average particle diameters with the aging duration. The variations of the average IMC particle diameter with aging time are shown in Figure 6.22. It is evident that the average size of the particles increases with the progression of aging for both of the SAC+Bi alloys but the growth was more for SAC+1% Bi compared to SAC+2% Bi alloy. The data for three regions of each alloy presented in Figures 6.20, and 6.21 were fitted using a two term exponential relation represented by Equation 3.30 in section 3.7.

Table 6.10 IMC Particle Diameter of Different Locations for SAC+Bi Alloys after Different Aging Duration

Alloy	Aging Temperature (°C)	Aging Time (Days)	Avg. Diameter (nm)			
			R- 1	R- 2	R- 3	Avg
SAC+1% Bi	125	0	320	351	358	343
		1	367	389	396	384
		5	502	523	554	526
		20	738	756	788	761
SAC+2% Bi		0	315	366	391	358
		1	356	398	424	393
		5	496	502	555	518
		20	708	762	766	745

This coarsening and coalescing of IMC particles during aging is known to play a critical role in the degradations of solder mechanical properties. IMC particles will pin and block the movement of dislocations. However, aging leads to both a smaller number of larger IMC particles, and increased spacing between the particles. This results in dislocations being able to pass more easily through the material, decreasing both the yield stress and strength. The correlation between the IMC particle evolution and mechanical property degradation is shown in normalized form in the same graph in Figure 6.23 to show a comparison among SAC_Q (SAC+3% Bi), SAC+2% Bi, SAC+1% Bi, and SAC305. Results for SAC_Q and SAC305 were obtained from old works listed in references [205].

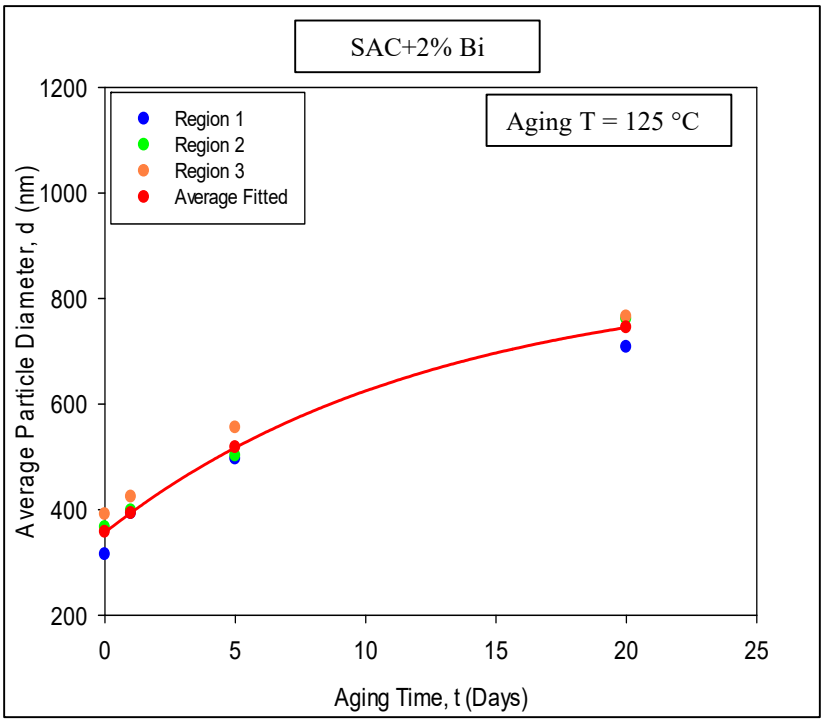

(a) SAC+2% Bi

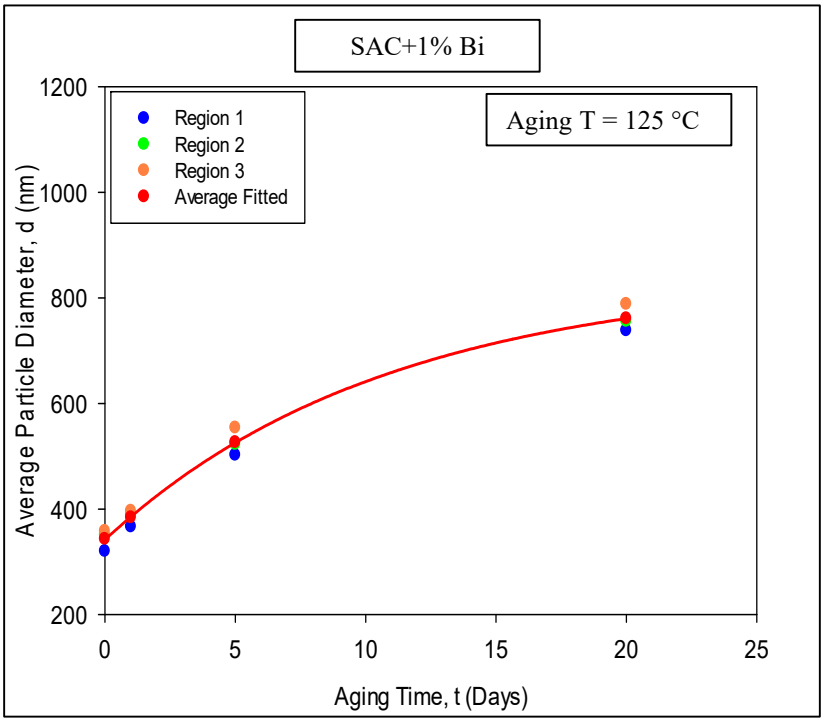

(b) SAC+1% Bi

Figure 6.22 Changes in IMC Particle Diameter with Aging Time for SAC+Bi Alloy (Aging at T = 125 ºC)

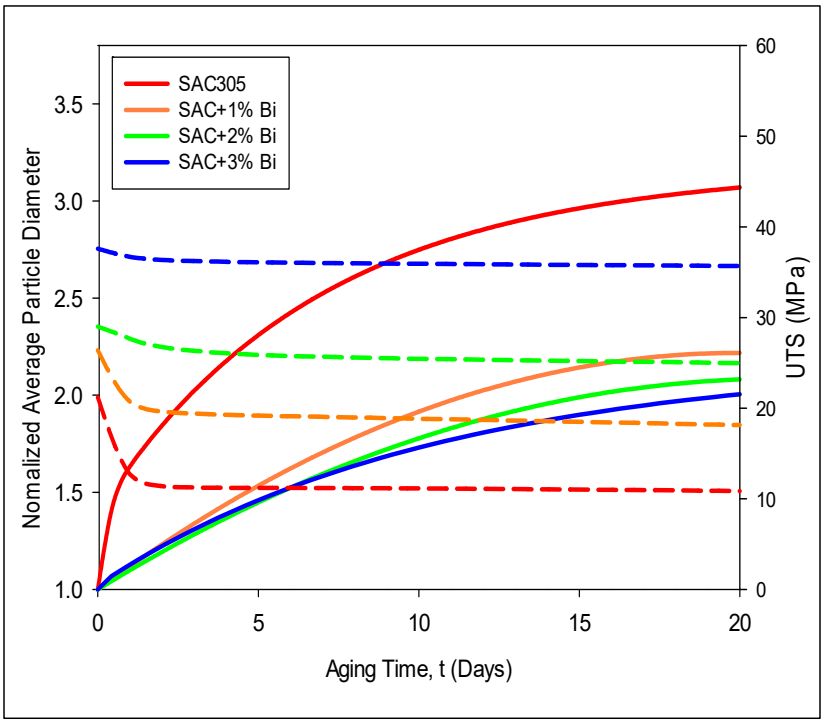

Figure 6.23 Effect of Aging on IMC Particle Diameter and Ultimate Strength for SAC+Bi Alloys and SAC305 (Aging at T = 125 ºC)

6.9 Summary and Discussion

In this chapter, study the mechanical behavior, and reliability of several different SAC+Bi alloys with various levels of Bismuth were studied. The overall goal was to identify optimal SAC+Bi alloy compositions for various applications and usage environments. The alloys considered were based on SAC405, with various levels of Sn replaced by Bi. The percentages of Bi considered include 1.0%, 2.0%, and 3.0%. To examine base mechanical behavior, uniaxial tensile tests were performed using rectangular cross-section samples prepared from vacuum suction method and SMT reflow oven. Tests were performed for each new SAC+Bi alloy with three strain rates (0.001, 0.0001, and 0.00001 (sec^{-1})), and five different testing temperatures (T = 25, 50, 75, 100, and 125 ºC).

Experimental results showed that severe degradations of the mechanical properties (initial modulus, ultimate tensile strength) occur in SAC+Bi doped alloys during high temperature testing. Approximately, 40-50% drop in strength and modulus occurred between T = 25 °C and T = 125 °C testing for various strain rates and test temperatures. Comparing with the conventional SACN05 (N = 1, 2, 3, 4) lead free alloys, experimental results showed that solder alloys with Bi content showed better mechanical properties both at room temperature, T = 25 °C (SAC+3% Bi showed approximately 70% better strength than SAC305, whereas, SAC+1% Bi showed around 53% better property than SAC305), and at high temperature, T = 125 °C (SAC+3% Bi showed approximately 83% better strength than SAC305, and, SAC+1% Bi showed around 26% better property than SAC305). As the Bi content decreased their strength also decreased correspondingly.

The Anand parameters were calculated for each SAC+Bi alloy from the stress-strain data, and then the parameters were used to predict the stress-strain curves. For all cases, only very minor differences were seen between the model predictions and the experimental results. Due to these good correlations, the applicability of the Anand model for a wide range of temperatures and strain rates was confirmed.

To investigate the effect of isothermal aging, the specimens were aged (preconditioned) at T = 125 °C for several durations of aging including 0, 1, 5, and 20 days. From the results of mechanical testing and microstructural analysis, it was found that the SAC+Bi alloys demonstrated superior resistance to aging effects relative to SAC305. The coarsening of the IMC particles is much larger in the SAC305 alloy relative to all three SAC+Bi alloys. In addition, the growth rate is reduced as the percentage of Bi in the alloy is increased. For the SAC-Bi alloy, the additional Bi content doesn't form any IMC with

Sn. Therefore, the only IMCs that should present in microstructure of SAC_Q and Innolot are Ag_3Sn and Cu_6Sn_5. However, Bi remains as a separate phase in the microstructure enhance the strength of the SAC-Bi alloys. Also, from the Sn-Bi phase diagram shown in Figure 6.24, it is observed that Bi has a good (~1.8%) solid solubility in Sn at room temperature. Hence Bi contributes more enhancement in strength of the SAC-Bi alloy before aging by the solid solution strengthening mechanism.

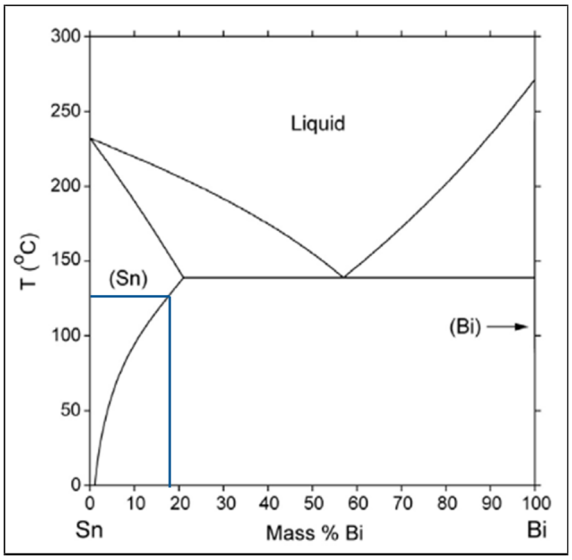

Figure 6.24 Sn-Bi Phase Diagram (http://www.metallurgy.nist.gov/)

Many researchers, such as,, Cai and coworkers [51] have demonstrated that additional Bi will go into solution in the β-Sn matrix during the aging of SAC-Bi alloys. As seen in Figure 6.24, the solid solution solubility of Bi increases from 1.8% at T = 25 °C, to about 17% at 125 °C. Thus, the Bi present in the as solidified microstructure of SAC-Bi alloys as a separate Bi phase will have the tendency to go into the solution with the β-Sn matrix during aging. This will lead to additional solid solution strengthening of the SAC-Bi alloy. Therefore, alloys with more Bi content showed better resistance to aging by showing better mechanical properties and limiting the growth of IMC particles during isothermal aging.

CHAPTER 7

ISOTHERMAL AGING DEPENDENT MECHANICAL RESPONSE AND ANAND MODEL PARAMETERS OF SAC305 SOLDER AT EXTREME HIGH TEMPERATURES

7.1 Introduction

The mechanical properties as well as the reliability of a solder, which is the primary interconnect of electronic assemblies are strongly influenced by its microstructure, which is controlled by its thermal history including its solidification rate and thermal exposures after solidification. Solder joint reliability in harsh environment applications are big concerns in the electronic packaging industry. The reliabilities of electronic packages used in various products depend on the environmental conditions experienced during field use. Consumer electronics are typically designed using maximum operating temperatures of 100 °C or less. However, there are several important harsh environment uses of electronic packaging, where electronics can be exposed to temperatures up to 200 °C. This leads to reduced values of the solder mechanical properties due to the normal temperature dependencies exhibited by metals. It is important to make accurate predictions of solder joint reliability at extreme high Temperatures. The nine parameter Anand viscoplastic constitutive model is a popular commercial finite element code built in to many commercial FEA packages like ANSYS and ABAQUS, which is widely used in the electronic packaging industry to predict reliability. Reliability prediction results are often highly

sensitive to the specified Anand parameters, and there are great variations in the available literature values for common solder alloys. Previous investigations on the nine parameters have mainly emphasized mechanical testing and fitting at temperatures up to 125 °C. In real life, electronic devices frequently experience harsh environment applications where solders are exposed to very high temperatures from 125-200 °C. Mechanical properties as well as Anand model parameters of lead free solders at elevated temperatures are not available in previous literatures.

In this chapter, a detail study was conducted to investigate the changes in mechanical properties and nine parameters of the Anand viscoplastic constitutive model for SAC305 (96.5Sn-3.0Ag-0.5Cu) lead free solder considering the isothermal aging effect. The pre aging was done at 125 ºC. Uniaxial tensile stress-strain tests were carried out on SAC305 specimens using a micro tension/torsion testing machine with three strain rates (0.001, 0.0001 and 0.00001 (1/sec)), four extreme high testing temperatures (T = 125, 150, 175, and 200 ºC), and four different pre-aging conditions (0, 1, 5, and 20 days at 125 ºC). The details of tensile testing was discussed in chapter 3. More specifically, sample preparation was discussed in section 3.2, whereas, micro tension-torsion system and raw data processing were discussed in details in sections 3.4, and 3.5 respectively. Utilizing the method the experimental results are discussed now.

7.2 Isothermal Aging and Test Matrix

Table 7.1 represents the isothermal aging and extreme high temperature test matrix. In short, SAC305 reflowed samples were pre-aged at a temperature of 125 ºC for several durations including 0, 1, 5, and 20 days. Then uniaxial tensile tests were carried out at four

extreme high test temperatures (T = 125, 150, 175, and 200 ºC) and three different strain rates (0.001, 0.0001 and 0.00001 (1/sec)) to extract different mechanical properties like effective modulus, yield stress, and ultimate strength.

Table 7.1 Aging Dependent High Temperature Test Matrix

Alloy	Strain Rate (sec^{-1})	Test Temperature (°C)	Isothermal Aging at T = 125 °C			
			No Aging	1 Day Aging	5 Days Aging	20 Days Aging
SAC305	10^{-3}	125	√	√	√	√
		150	√	√	√	√
		175	√	√	√	√
		200	√	√	√	√
	10^{-4}	125	√	√	√	√
		150	√	√	√	√
		175	√	√	√	√
		200	√	√	√	√
	10^{-5}	125	√	√	√	√
		150	√	√	√	√
		175	√	√	√	√
		200	√	√	√	√

7.3 Stress-Strain Data for Various Test Temperatures, Strain Rates and Aging Conditions

The recorded experimental tensile test results for SAC305 solder alloy with different test temperatures, strain rate, and aging durations (Aging T = 125 °C) are plotted in Figures 7.1-7.4. Graphs in each plot shows the temperature dependent uniaxial stress-strain behavior of SAC305 solder alloy at a particular aging duration (0, 1, 5, or 20 days.), with the various colored curves representing the different test temperature with blue = 125 °C, green = 150 °C, orange = 175 °C, and red = 200 °C. Again, in each plot, top curve corresponds to 125 °C and bottom curve represents 200 °C test result.

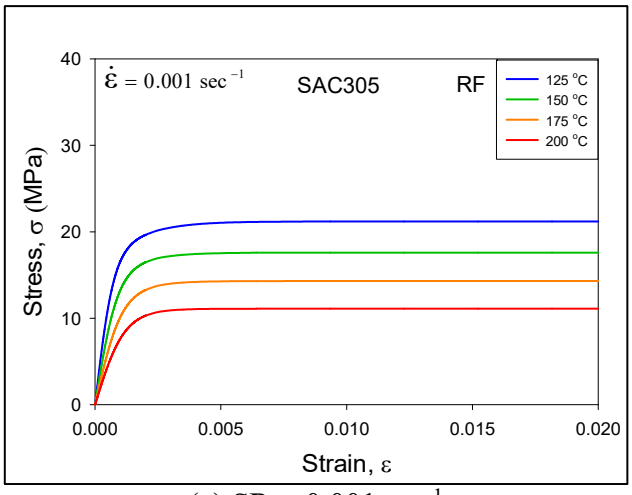

(a) SR = 0.001 sec^{-1}

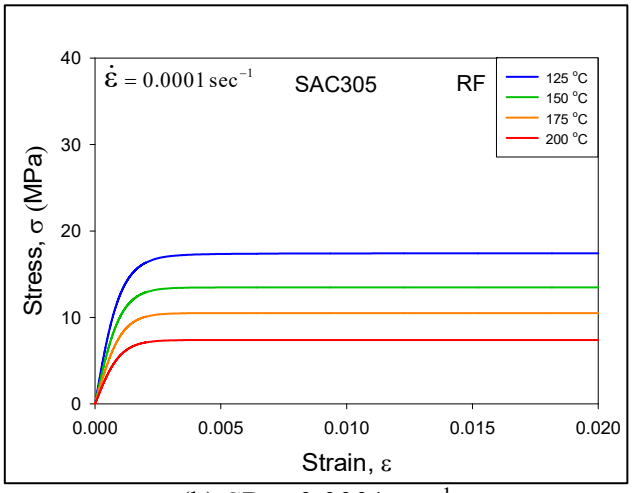

(b) SR = 0.0001 sec^{-1}

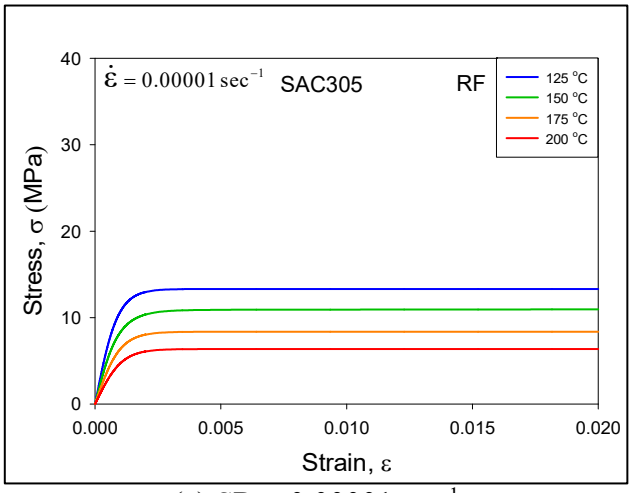

(c) SR = 0.00001 sec^{-1}

Figure 7.1 Stress-Strain Curves for SAC305 (RF, No Aging)

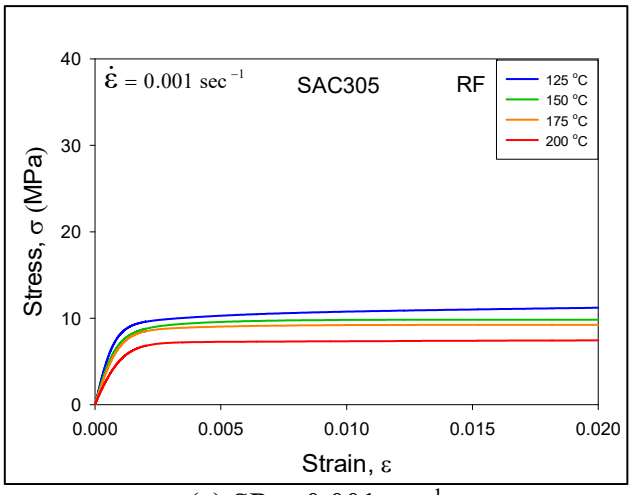

(a) SR = 0.001 sec^{-1}

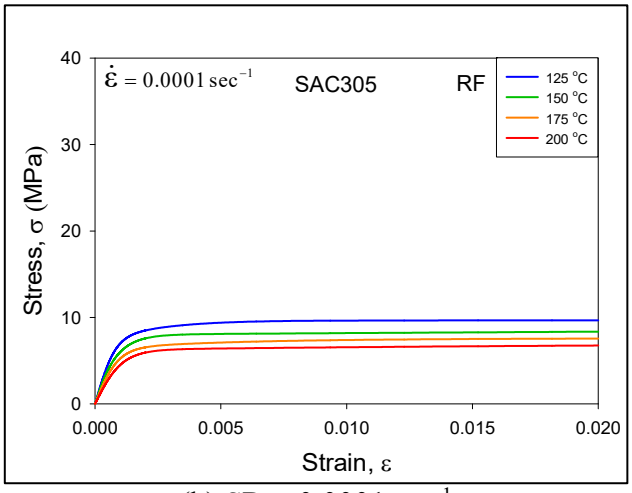

(b) SR = 0.0001 sec^{-1}

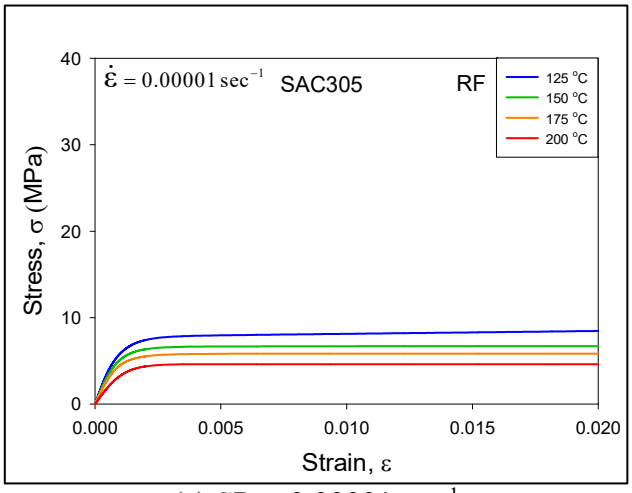

(c) SR = 0.00001 sec^{-1}

Figure 7.2 Stress-Strain Curves for SAC305 (RF, 1 Day Aging at T = 125 °C)

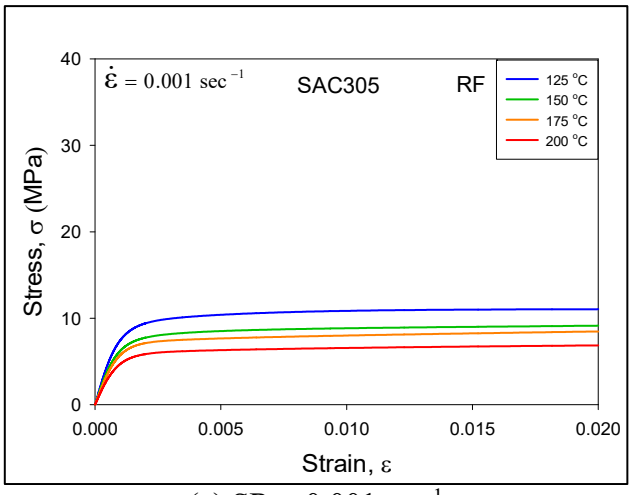

(a) SR = 0.001 sec^{-1}

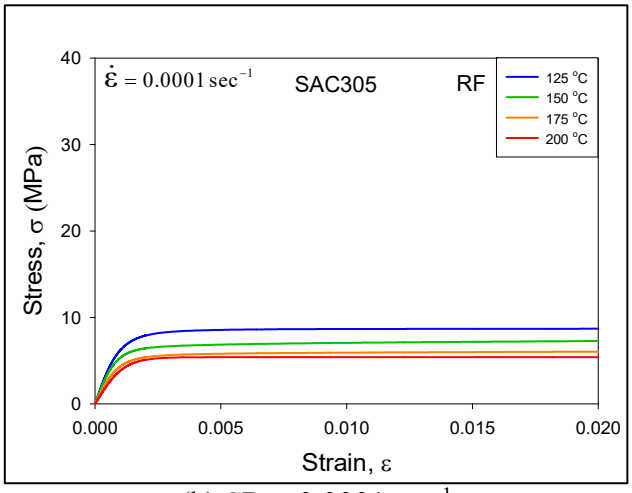

(b) SR = 0.0001 sec^{-1}

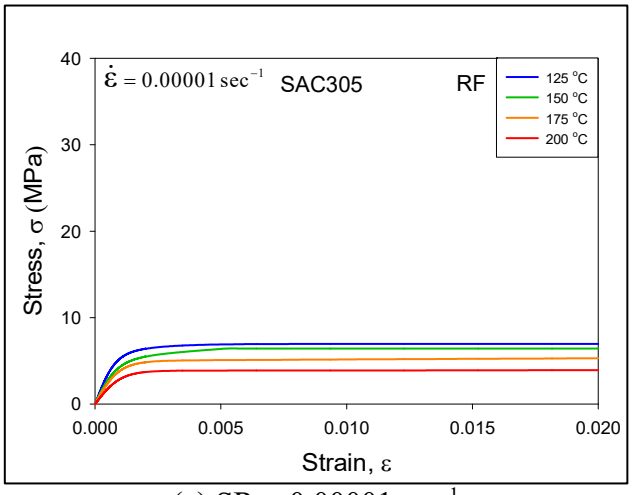

(c) SR = 0.00001 sec^{-1}

Figure 7.3 Stress-Strain Curves for SAC305 (RF, 5 Days Aging at T = 125 °C)

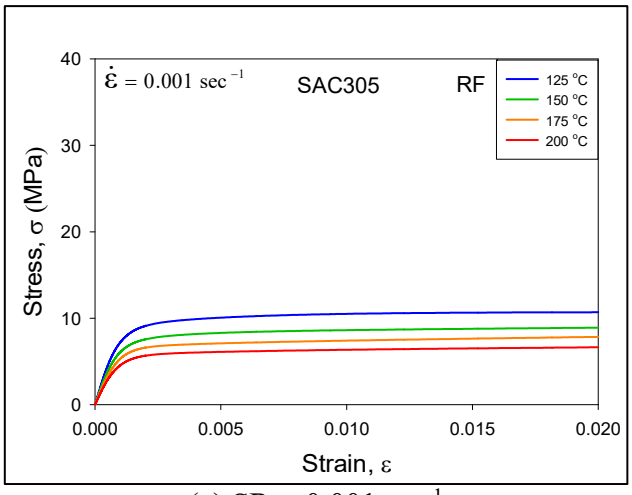

(a) SR = 0.001 sec^{-1}

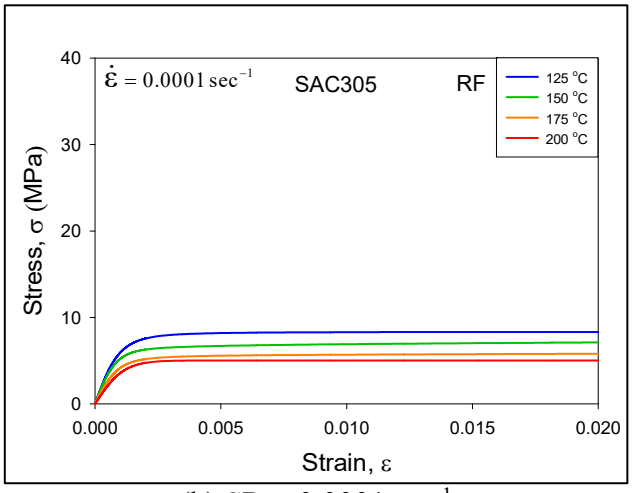

(b) SR = 0.0001 sec^{-1}

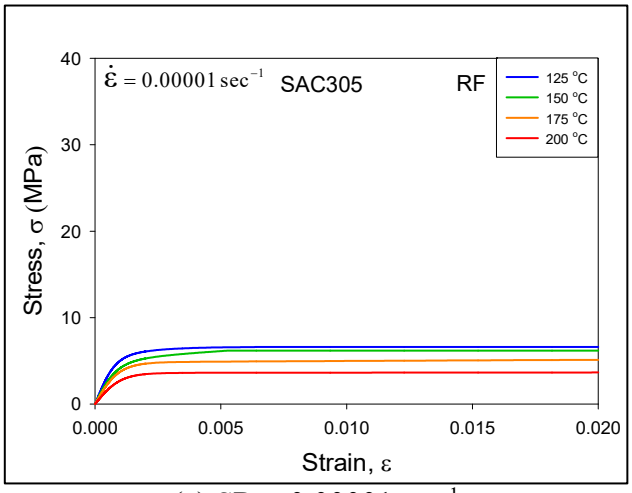

(c) SR = 0.00001 sec^{-1}

Figure 7.4 Stress-Strain Curves for SAC305 (RF, 20 Days Aging at T = 125 °C)

7.4 Comparison of Stress-Strain Behavior of SAC305 Solder Alloy at Various Temperature, Strain Rates and Aging Conditions

Comparisons of the uniaxial tensile test results for SAC305 solder alloy at different test temperature, strain rates, and isothermal aging (Aging at T = 125 °C) are shown in Figures 7.5-7.7. Figure 7.5 represents comparison at 0.001 sec^{-1} strain rate. Figures 7.6 and 7.7 correspond to the comparison of similar results obtained at 0.0001 and 0.00001 sec^{-1} strain rate respectively. Each of the graphs shows a comparative analysis of the uniaxial stress-strain behavior of SAC305 solder alloy at a particular test temperature, with the various colored curves representing the different aging durations with blue= no aging, green= 1 day aging, orange= 5 days aging, and red= 20 days aging at T = 125 °C.

As mentioned before, the curves in the plots are the "average" stress-strain curves found by fitting the raw experimental data with the empirical model in Equation 3.2. Here a single color curve is the average of 8-10 uniaxial stress-strain tests. For each of the graphs, the top (blue) curve represents the average stress-strain curve for no aging condition, and the bottom (red) curve shows the average stress-strain curve at 20 days of isothermal aging at T = 125 125 °C.

From all the plots, it was very clear that at each test temperature, the SAC305 solder alloy demonstrated large aging induced degradations with significant drop in mechanical properties after only 1 day of high temperature aging. The gap between the blue and green curve represents the significant drop of stress-strain response as well as mechanical behavior. After that, still the degradation continued but in a much slower rate as the orange and red curved were almost close to each other in all figures.

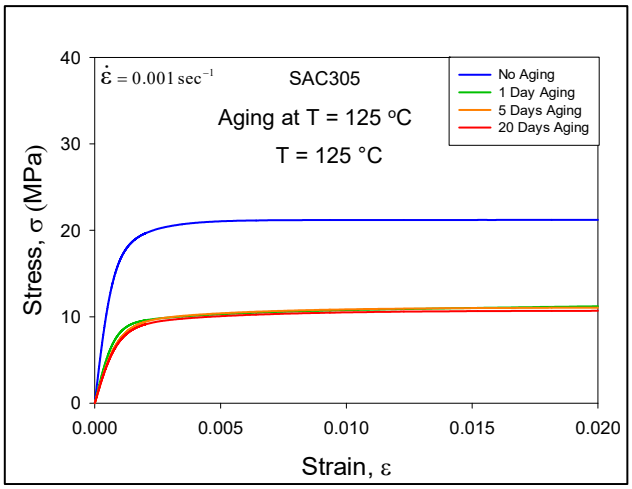

(a) T = 125 °C

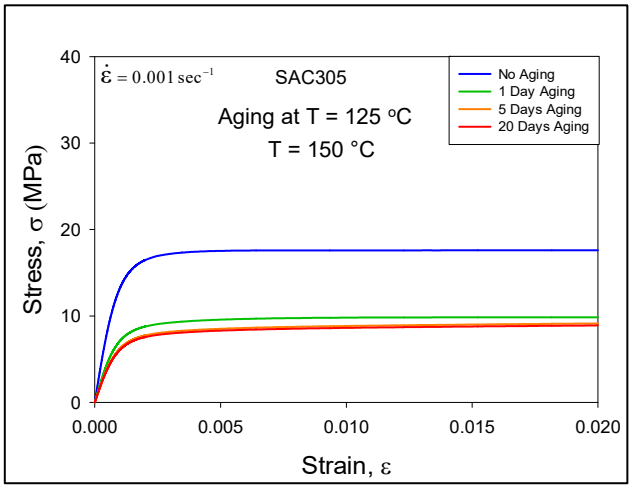

(b) T = 150 °C

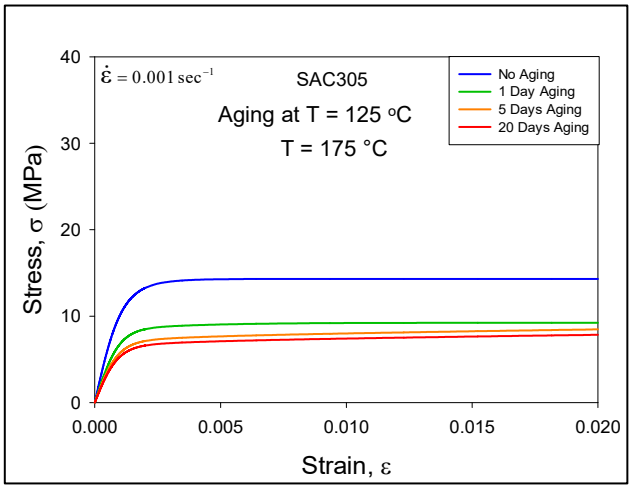

(c) T = 175 °C

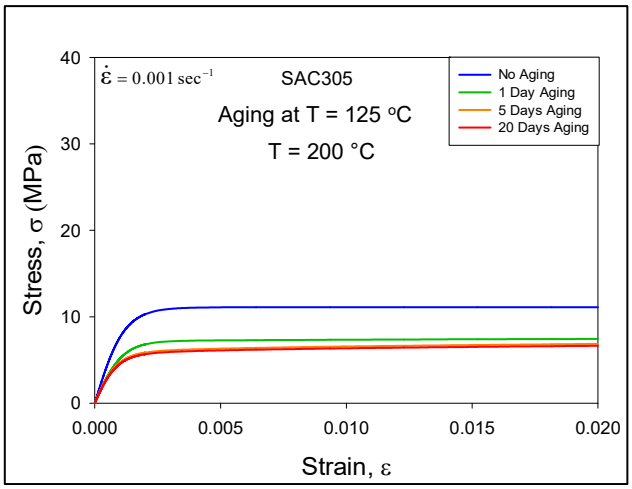

(d) T = 200 °C

Figure 7.5 Comparison of Stress-Strain Curves for SAC305 (RF, Aging at T = 125 °C, SR = 0.001 sec^{-1})

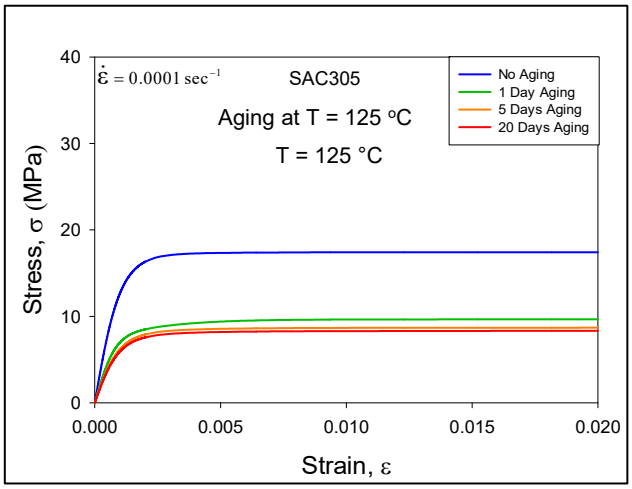

(a) T = 125 °C

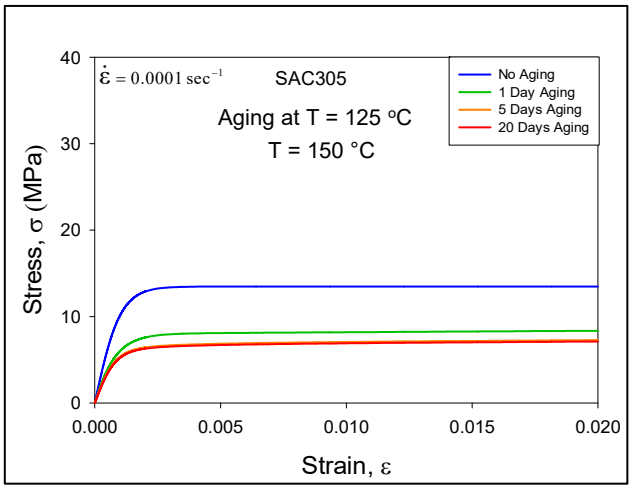

(b) T = 150 °C

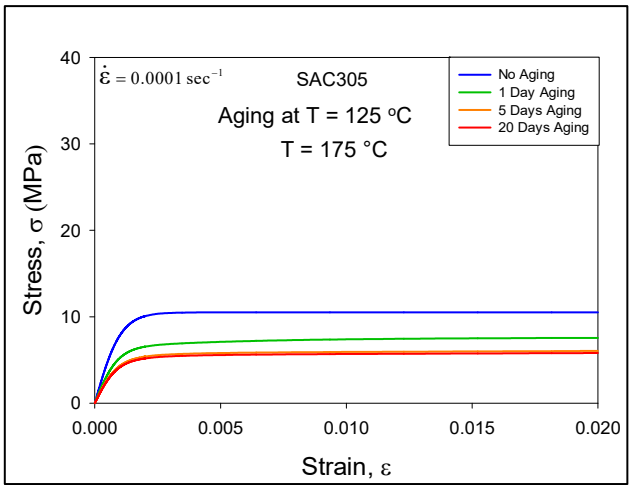

(c) T = 175 °C

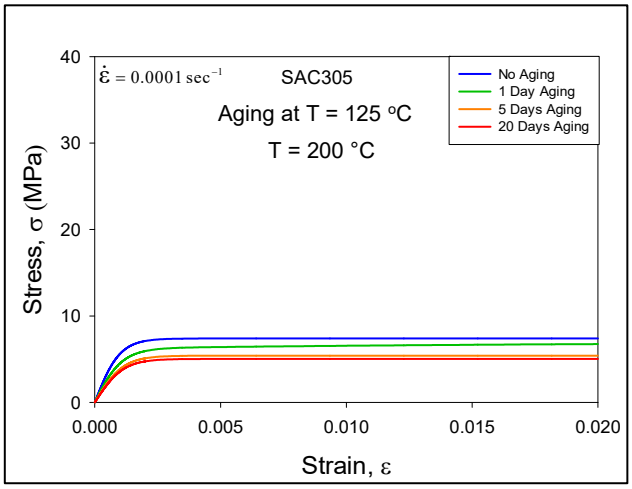

(d) T = 200 °C

Figure 7.6 Comparison of Stress-Strain Curves for SAC305 (RF, Aging at T = 125 °C, SR = 0.0001 sec^{-1})

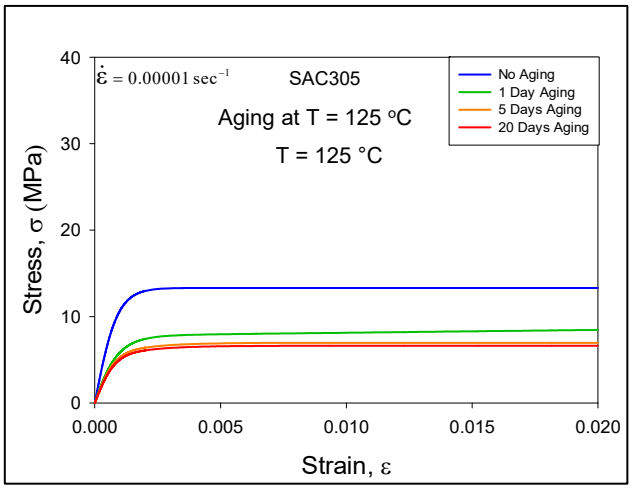

(a) T = 125 °C

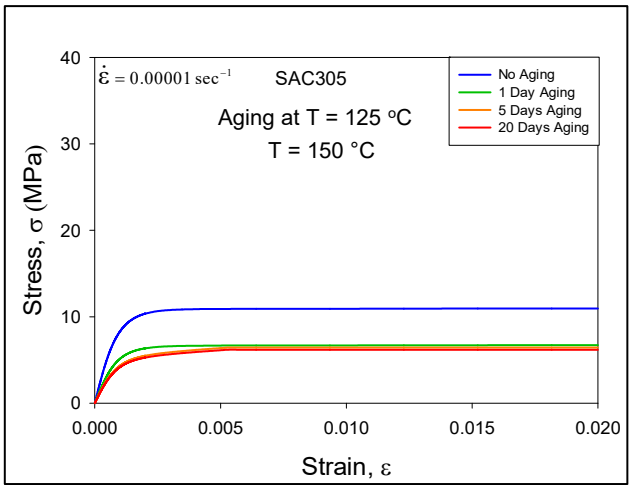

(b) T = 150 °C

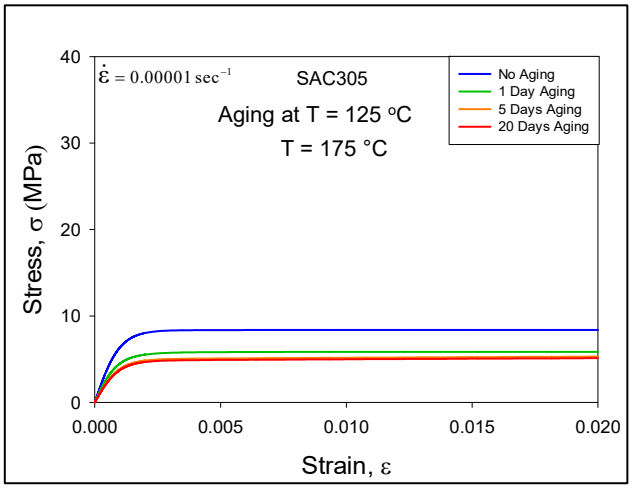

(c) T = 175 °C

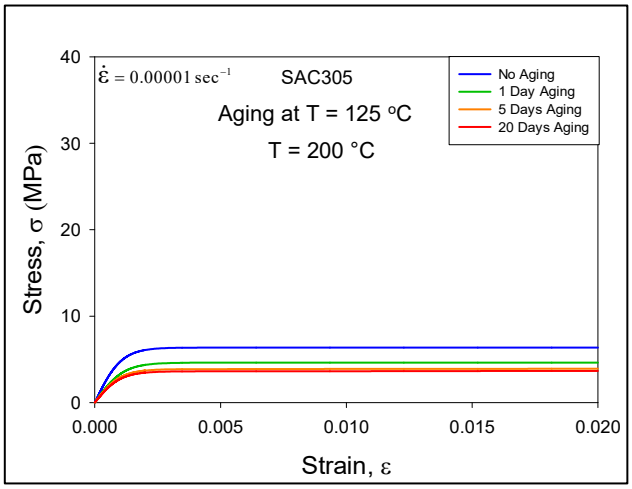

(d) T = 200 °C

Figure 7.7 Comparison of Stress-Strain Curves for SAC305 (RF, Aging at T = 125 °C, SR = 0.00001 sec^{-1})

7.5 Comparison of Mechanical Properties of SAC305 Solder Alloy at Various Temperature, Strain Rates and Aging Conditions

Table 7.2, 7.3, and 7.4 show the aging dependent mechanical properties of SAC 305 solder alloys for aging at 125 °C for several durations including 0, 1, 5, and 20 days. The mechanical properties have been extracted from the measured stress-strain data presented in Figures 7.1-7.4 in the previous section. These properties, such as, initial effective modulus, ultimate tensile strength, and yield stress have been plotted in Figures 7.8-7.10 as a function of temperature at each of the three strain rates. Again, these properties are plotted as a function of aging duration in Figures 7.11-7.13.

Large reductions in the properties were observed to occur between test temperatures of T = 125 °C and T = 200 °C. For example, 40-60% drop in ultimate strength and modulus occurred during testing for various temperatures, strain rates and aging durations. Most severe changes occurred for non-aged to 1 day aging, after that the rate became slower.

Table 7.2 Aging Dependent Effective Modulus (E) of SAC305

Alloy	Strain Rate (sec^{-1})	Test Temperature (°C)	Effective Modulus, E (GPa) (Isothermal Aging at T = 125 °C)			
			No Aging	1 Day Aging	5 Days Aging	20 Days Aging
SAC305	10^{-3}	125	19.9	12.2	10.3	9.9
		150	15.5	10.3	8.8	8.6
		175	11.8	9.1	7.9	7.3
		200	9.2	7.6	6.6	6.4
	10^{-4}	125	18.9	10.1	8.5	8.2
		150	13.0	8.9	7.8	7.7
		175	9.7	7.2	6.1	5.8
		200	6.6	5.8	4.8	4.5
	10^{-5}	125	16.6	8.4	7.7	7.3
		150	12.1	7.3	6.1	5.9
		175	8.2	6.4	5.3	5.1
		200	5.5	4.1	3.8	3.6

Table 7.3 Aging Dependent Ultimate Strength (UTS) of SAC305

Alloy	Strain Rate (sec^{-1})	Test Temperature (°C)	Ultimate Strength, UTS (MPa) (Isothermal Aging at T = 125 °C)			
			No Aging	1 Day Aging	5 Days Aging	20 Days Aging
SAC305	10^{-3}	125	21.2	12.7	11.2	10.8
		150	17.9	10.0	9.0	8.8
		175	14.3	9.3	7.8	7.2
		200	10.9	7.4	6.4	6.2
	10^{-4}	125	16.5	10.0	9.1	8.7
		150	13.2	8.6	7.5	7.3
		175	10.7	7.5	6.2	5.9
		200	7.5	6.5	5.5	5.1
	10^{-5}	125	14.5	8.4	7.7	7.3
		150	10.9	7.2	6.4	6.1
		175	8.4	6.3	5.3	5.1
		200	6.4	4.7	4.4	4.1

Table 7.4 Aging Dependent Yield Stress (YS) of SAC305

Alloy	Strain Rate (sec^{-1})	Test Temperature (°C)	Yield Stress, YS (MPa) (Isothermal Aging at T = 125 °C)			
			No Aging	1 Day Aging	5 Days Aging	20 Days Aging
SAC305	10^{-3}	125	10.5	6.3	5.7	5.6
		150	9.3	5.2	4.8	4.7
		175	8.3	5.1	4.7	4.5
		200	7.4	5.0	4.5	4.4
	10^{-4}	125	9.0	5.3	5.2	5.1
		150	7.8	5.1	4.9	4.8
		175	6.8	4.8	4.6	4.5
		200	5.9	4.6	4.4	4.2
	10^{-5}	125	7.5	4.4	4.2	4.1
		150	6.3	4.2	4.0	3.9
		175	5.3	3.9	3.9	3.7
		200	4.4	3.2	3.1	2.9

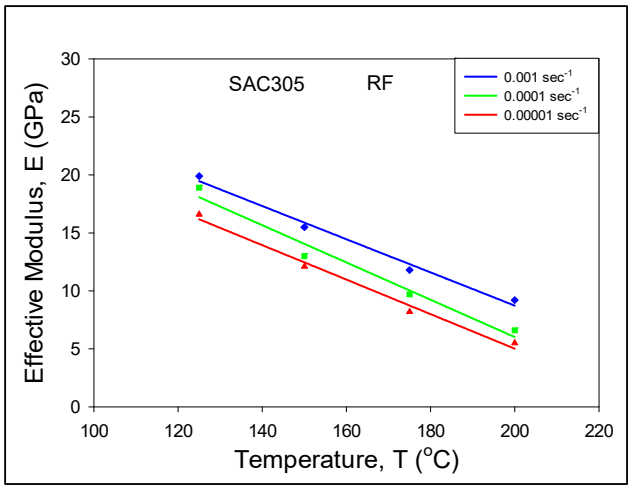

(a) No Aging

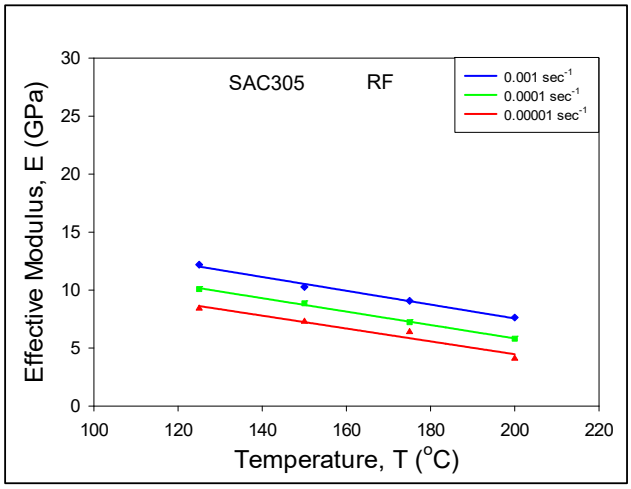

(b) 1 Day Aging at T = 125 °C

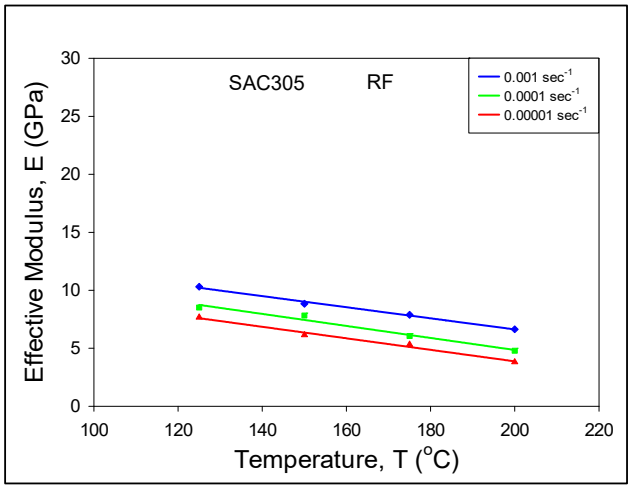

(c) 5 Days Aging at T = 125 °C

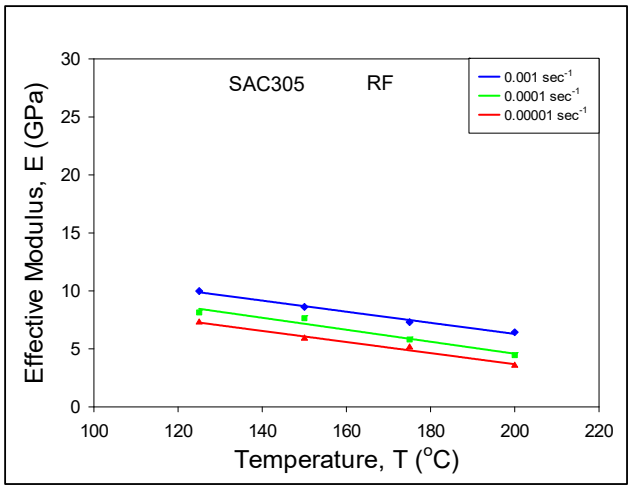

(d) 20 Days Aging at T = 125 °C

Figure 7.8 Variation of Effective Modulus of SAC305 with Temperature for Different Aging Time

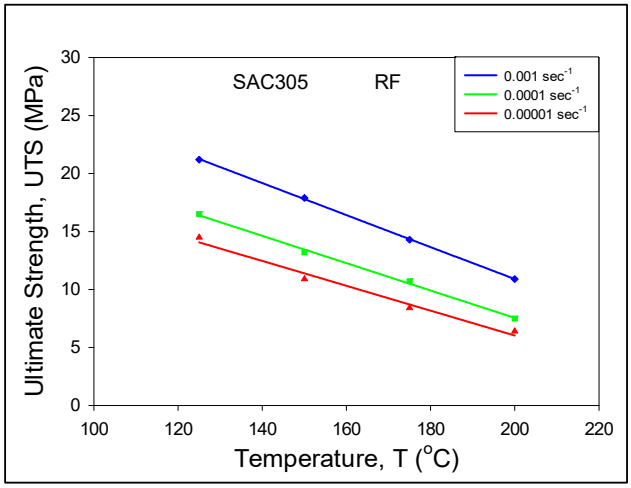

(a) No Aging

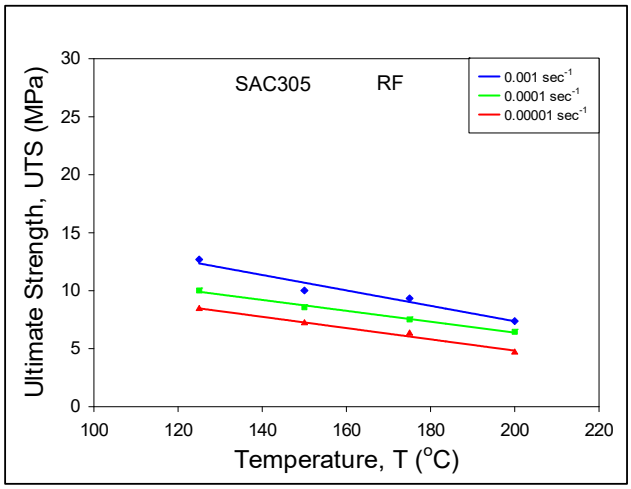

(b) 1 Day Aging at T = 125 °C

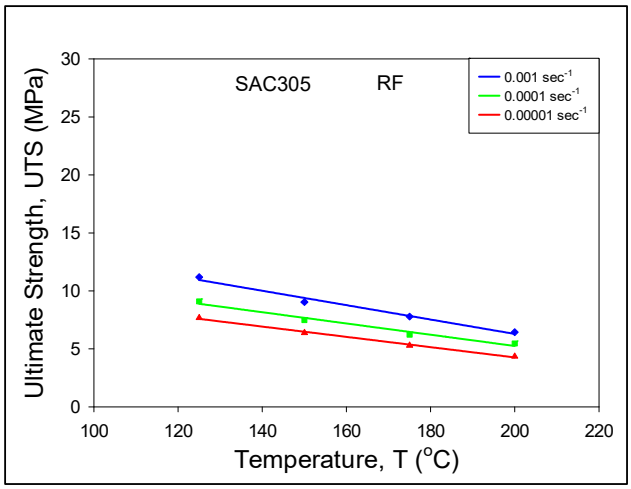

(c) 5 Days Aging at T = 125 °C

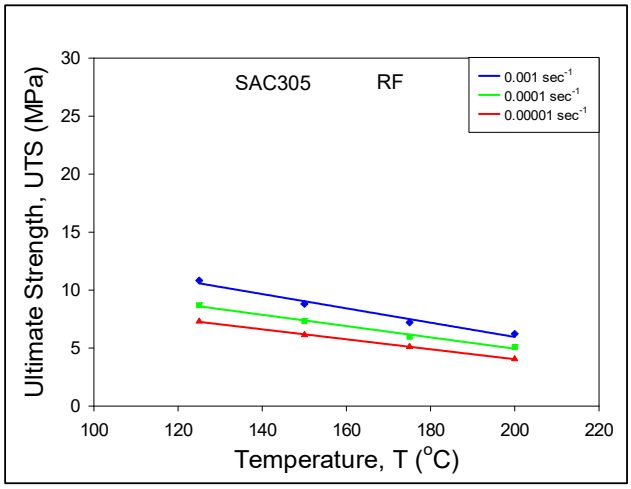

(d) 20 Days Aging at T = 125 °C

Figure 7.9 Variation of Ultimate Strength of SAC305 with Temperature for Different Aging Time

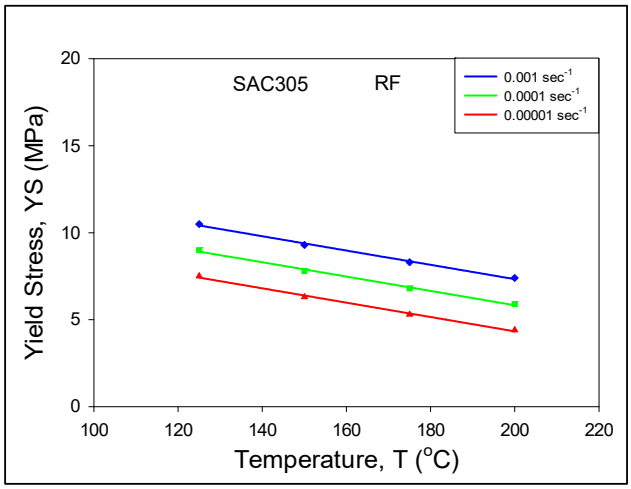

(a) No Aging

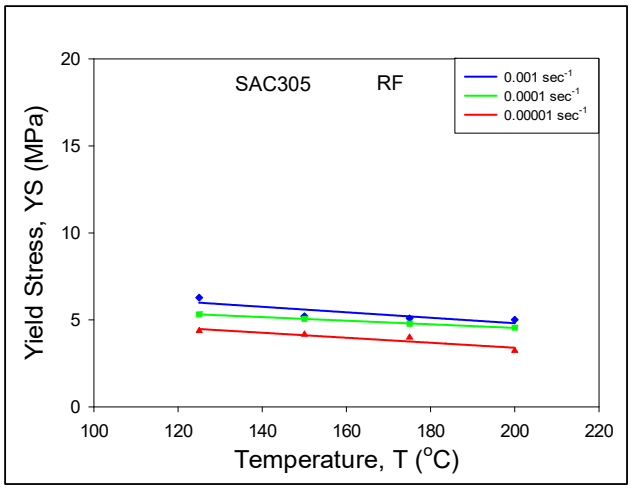

(b) 1 Day Aging at T = 125 °C

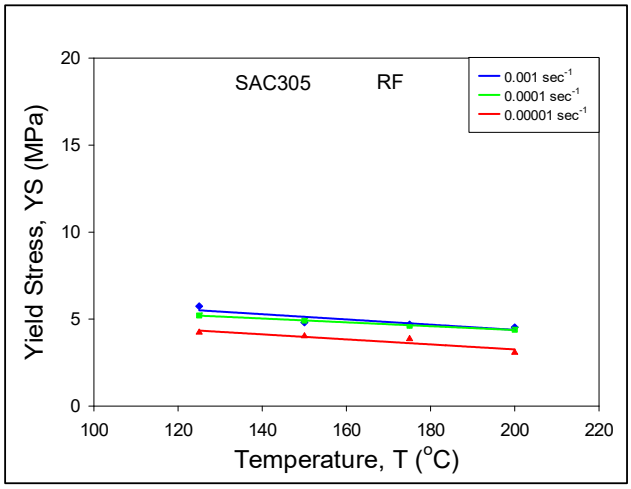

(c) 5 Days Aging at T = 125 °C

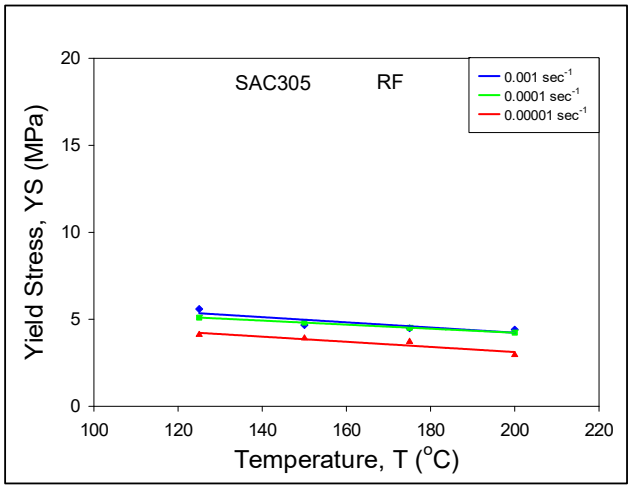

(d) 20 Days Aging at T = 125 °C

Figure 7.10 Variation of Yield Stress of SAC305 with Temperature for Different Aging Time

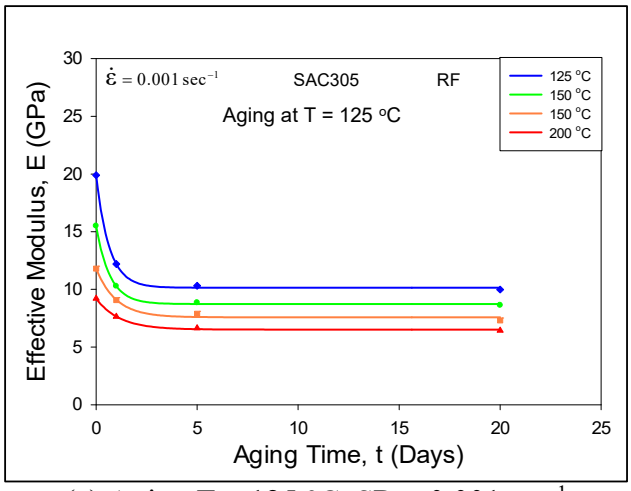

(a) Aging T = 125 °C, SR = 0.001 sec^{-1}

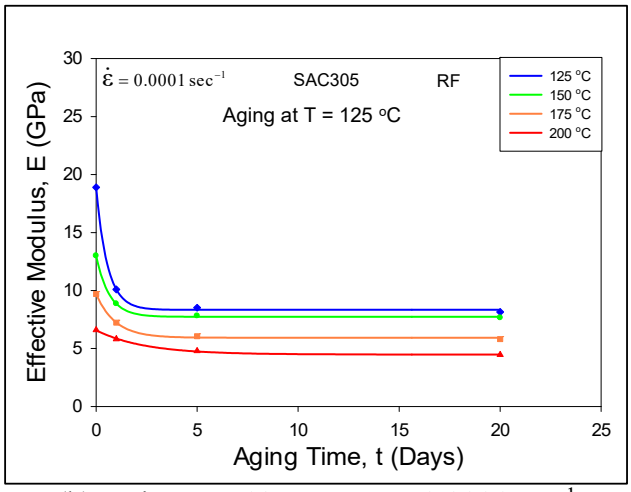

(b) Aging T = 125 °C, SR = 0.0001 sec^{-1}

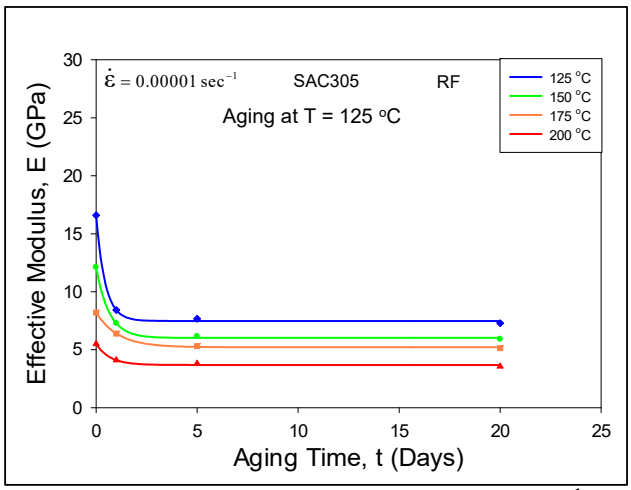

(c) Aging T = 125 °C, SR = 0.00001 sec^{-1}

Figure 7.11 Variation of Effective Modulus of SAC305 with Aging Time for Different Strain Rates

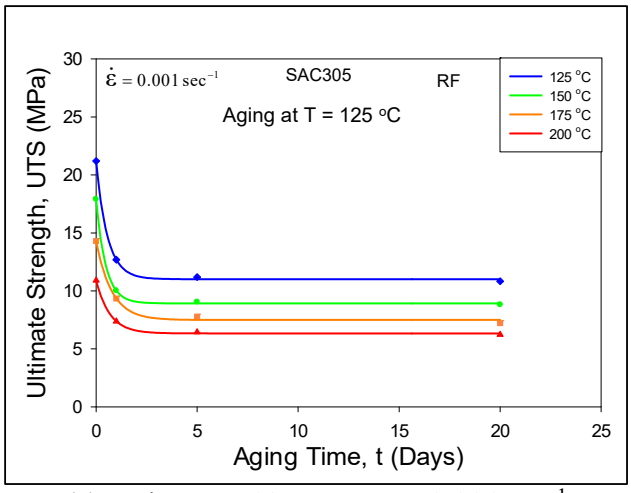

(a) Aging T = 125 °C, SR = 0.001 sec^{-1}

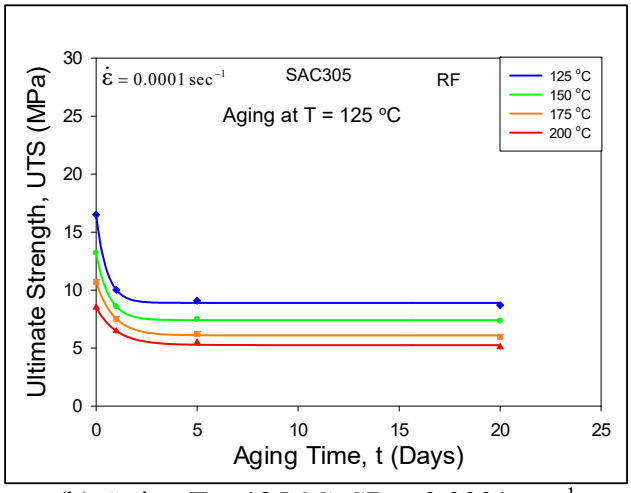

(b) Aging T = 125 °C, SR = 0.0001 sec^{-1}

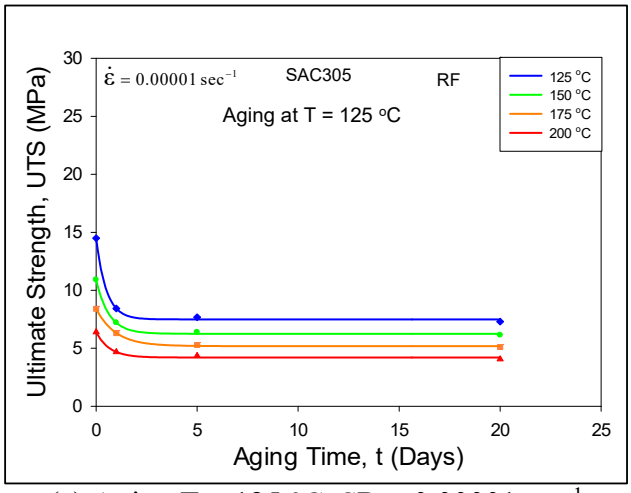

(c) Aging T = 125 °C, SR = 0.00001 sec^{-1}

Figure 7.12 Variation of Ultimate Strength of SAC305 with Aging Time for Different Strain Rates

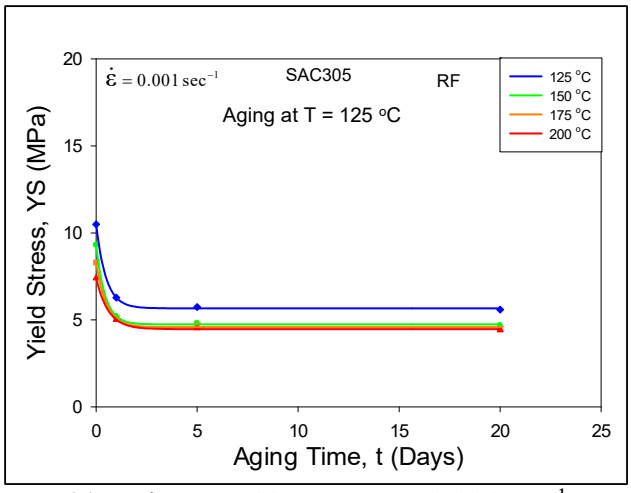

(a) Aging T = 125 °C, SR = 0.001 sec^{-1}

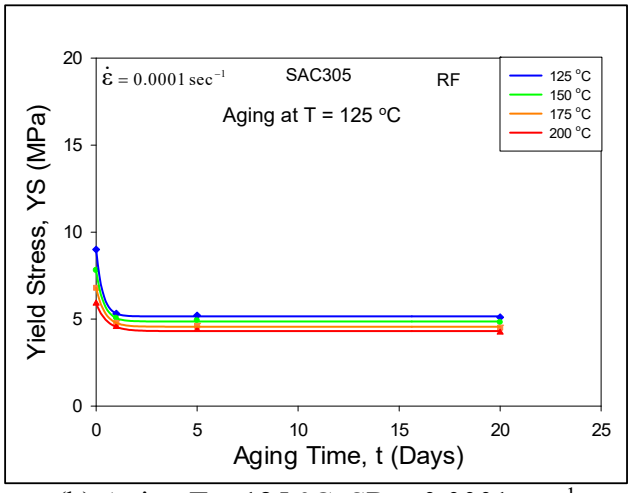

(b) Aging T = 125 °C, SR = 0.0001 sec^{-1}

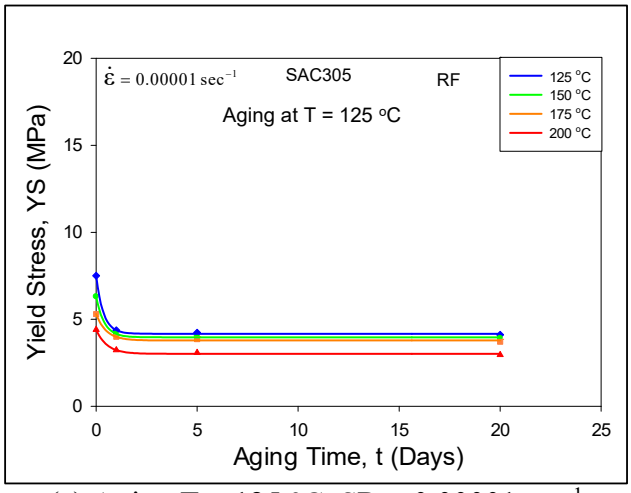

(c) Aging T = 125 °C, SR = 0.00001 sec^{-1}

Figure 7.13 Variation of Yield Stress of SAC305 with Aging Time for Different Strain Rates

7.6 Determination of Anand Model Parameters

The temperature and strain rate dependent stress-strain results obtained from uniaxial tensile tests were utilized to determine the nine parameters (A, ξ, Q/R, m, h_o, a, s_o, $\hat{s}$, and n) of Anand model by simultaneous solution of three sets of equations known as stress, flow and evolution equation. The detail steps and equations to determine the Anand model parameters were described in section 3.6. Utilizing the approach Anand model parameters for three new SAC+Bi alloys as well as for Sn-3.5Ag alloy were determined for no aging condition. The parameters are listed in Table 7.5.

Table 7.5 Aging Dependent Anand Model Parameters of SAC305

Constant Number	Anand Constant	Units	SAC305 (RF) (Isothermal Aging at T = 125 °C)			
			No Aging	1 Day Aging	5 Days Aging	20 Days Aging
1	s_o	MPa	5.50	4.65	4.20	4.00
2	Q/R	1/K	11900	11260	11200	11200
3	A	sec^{-1}	4000	4500	4500	4500
4	ξ	Dimensionless	4.00	4.00	4.00	4.00
5	m	Dimensionless	0.4700	0.0661	0.0782	0.0851
6	h_o	MPa	30000	50000	50000	50000
7	$\hat{S}$	MPa	5.00	15.70	13.26	12.30
8	n	Dimensionless	0.059	0.05	0.05	0.05
9	a	Dimensionless	1.60	1.45	1.60	1.70

7.7 Correlation between Anand Model Predictions and Experimental Results

After determining the set of parameters, they were utilized to predict the stress-strain curves and compare with the experimental results following the method described in section 3.6.4. Figures 7.14-7.17 represents the correlation.

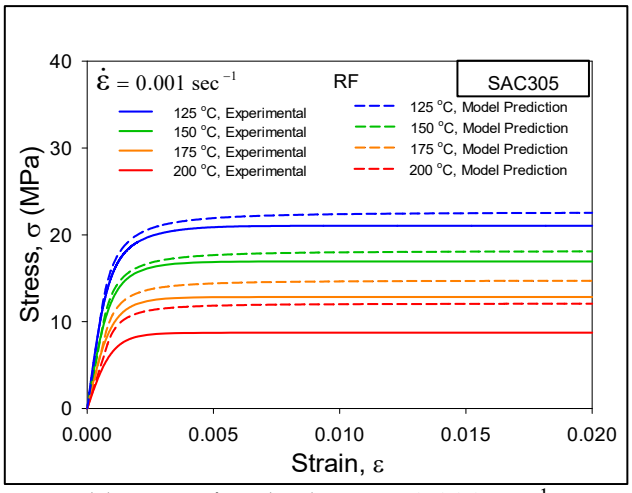

(a) No Aging (RF), SR = 0.001 sec^{-1}

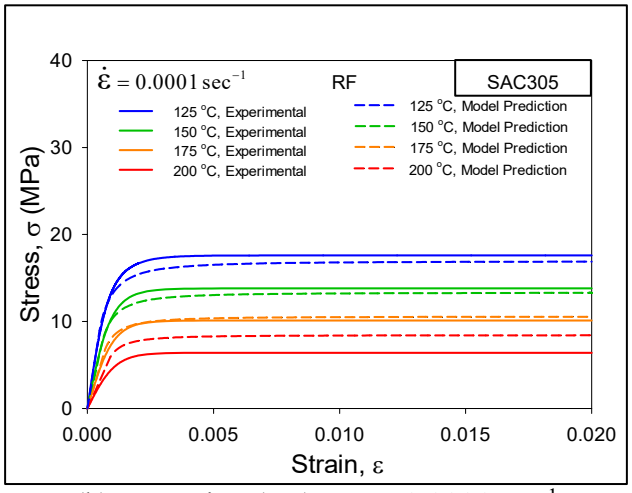

(b) No Aging (RF), SR = 0.0001 sec^{-1}

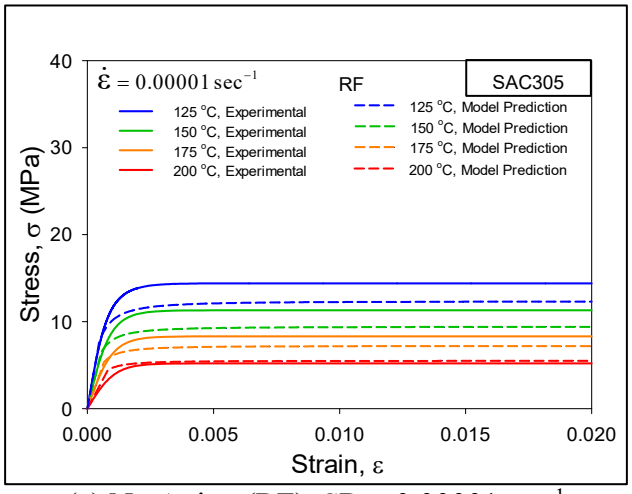

(c) No Aging (RF), SR = 0.00001 sec^{-1}

Figure 7.14 Correlation between Anand Model Predicted and Experimental Results for Non-aged Condition

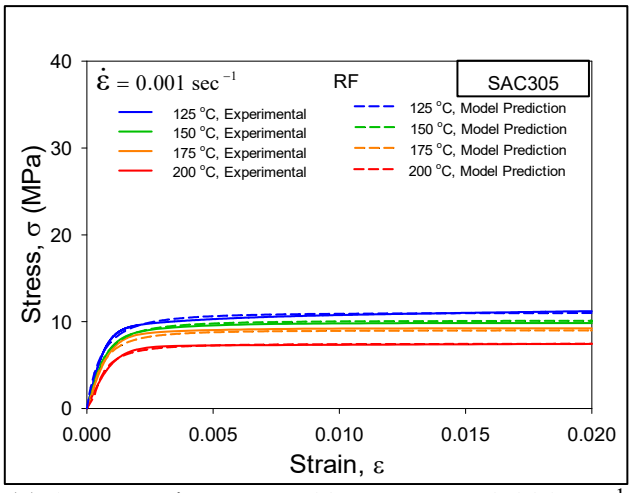

(a) 1 Day Aging at T = 125 °C, SR = 0.001 sec^{-1}

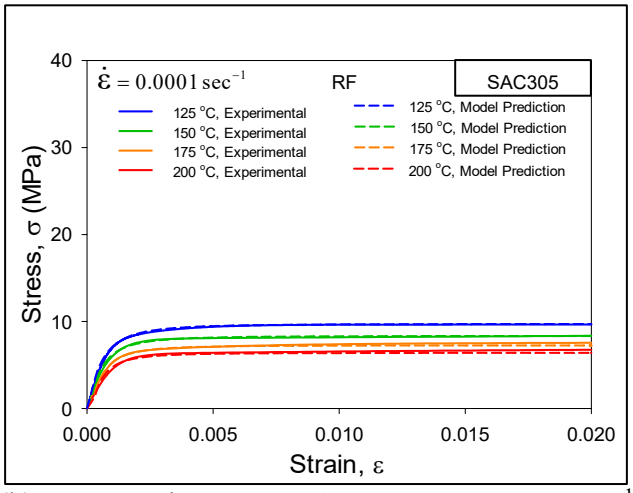

(b) 1 Day Aging at T = 125 °C, SR = 0.0001 sec^{-1}

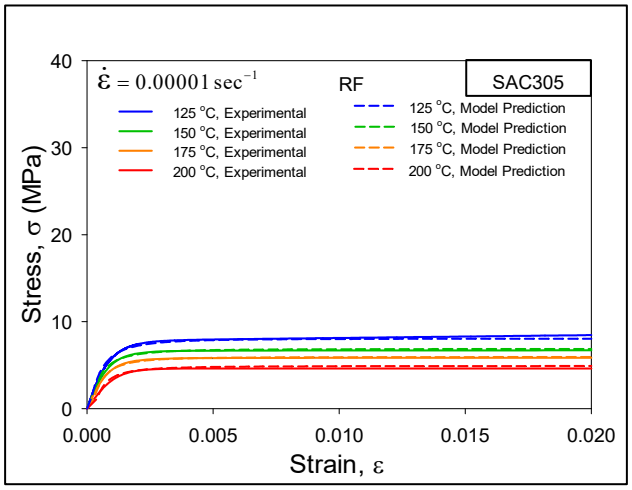

(c) 1 Day Aging at T = 125 °C, SR = 0.00001 sec^{-1}

Figure 7.15 Correlation between Anand Model Predicted and Experimental Results for 1 Day Aging at T = 125 °C

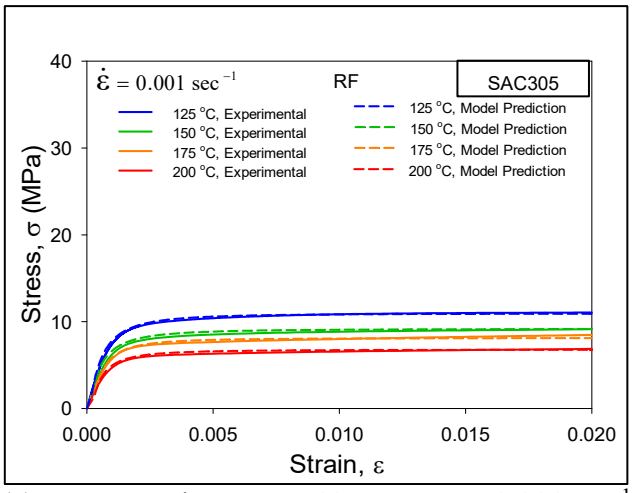

(a) 5 Days Aging at T = 125 °C, SR = 0.001 sec^{-1}

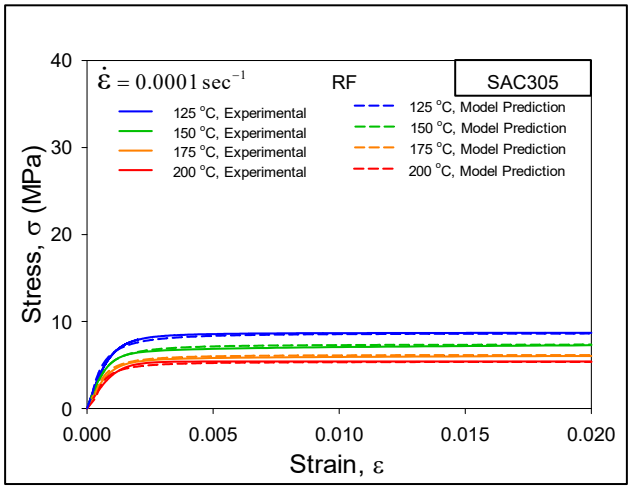

(b) 5 Days Aging at T = 125 °C, SR = 0.0001 sec^{-1}

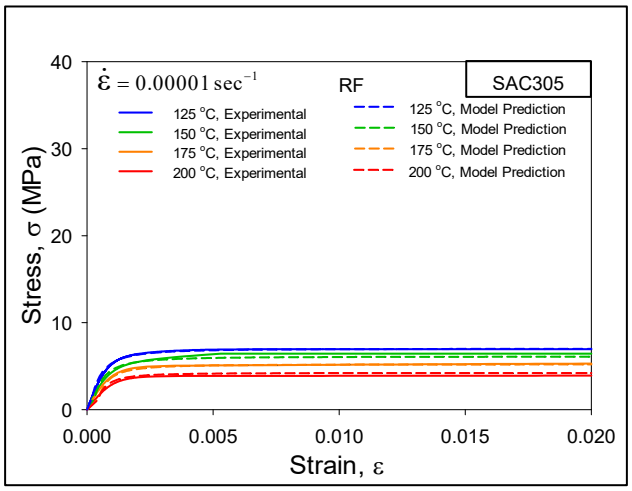

(c) 5 Days Aging at T = 125 °C, SR = 0.00001 sec^{-1}

Figure 7.16 Correlation between Anand Model Predicted and Experimental Results for 5 Days Aging at T = 125 °C

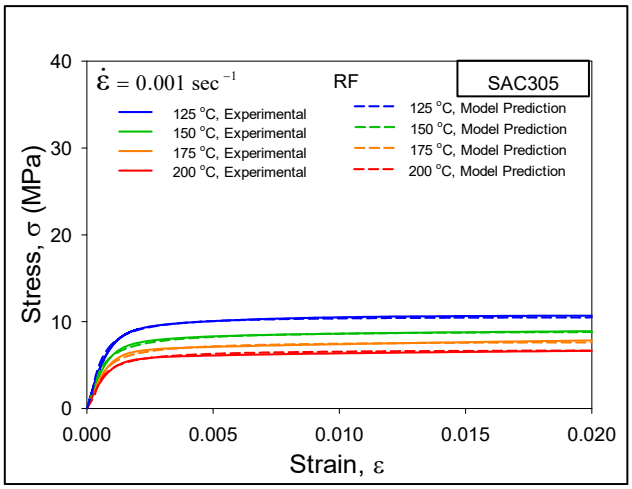

(a) 20 Days Aging at T = 125 °C, SR = 0.001 sec^{-1}

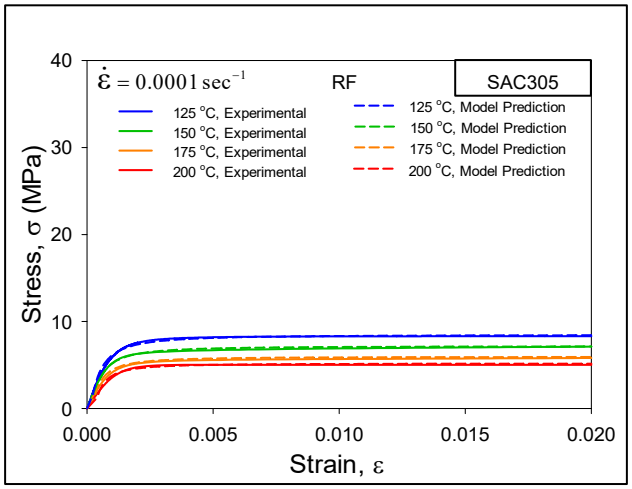

(b) 20 Days Aging at T = 125 °C, SR = 0.0001 sec^{-1}

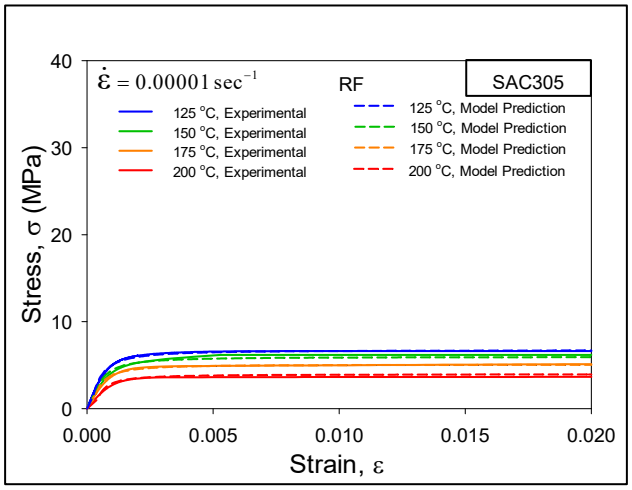

(c) 20 Days Aging at T = 125 °C, SR = 0.00001 sec^{-1}

Figure 7.17 Correlation between Anand Model Predicted and Experimental Results for 20 Days Aging at T = 125 °C

7.8 Summary and Discussion

In this work, a detailed study of the aging dependent mechanical behavior of SAC305 lead free solder alloy at extreme high temperatures (T= 125, 150, 175, and 200 °C) were investigated at three different strain rates (0.001, 0.0001 and 0.00001 sec^{-1}). Before testing, the solder uniaxial specimens were aged (preconditioned) at the extreme high temperature of T = 125 °C ,and several different durations of aging were considered (no aging, and 1 day, 5 days, and 20 days of aging). Uniaxial tests were then performed on the samples and average stress-strain curves were generated using 8 to 10 tests for each condition. Utilizing the recorded data mechanical properties like effective modulus, yield stress, and ultimate strength were determined to show the evolution of mechanical properties as a function of aging time and temperature for various strain rates.

Experimental measurements showed severe degradations in the mechanical properties (effective modulus, yield stress, and ultimate tensile strength) of SAC305 during extreme high temperature aging and testing. Approximately, 40-60% drop in strength and modulus occurred between T = 125 °C and T = 200 °C testing for various strain rates and aging duration. Most severe changes occurred for non-aged to 1 day aging, after that the rate became slower. Linear variations in the properties with temperature were observed. By comparing the analogous results for the same temperature and alloy, but different strain rates, it has also been observed that as the strain rate decreases, the effective elastic modulus, ultimate tensile strength, and yield stress also decrease.

Results from the uniaxial tensile test, performed at three different strain rates (0.001, 0.0001 and 0.00001 sec^{-1}) and four different test temperatures (125, 150, 175, and 200 °C), and different durations of aging were used to determine the Anand parameters for

all the conditions mentioned before. From the numerical values, significant changes (approximately 30-40%) were found in some of the Anand parameters like m, h_o, s_o, and $\hat{s}$. These parameters were used to predict the stress-strain behavior of the corresponding solder alloy. The experimental results and the model predicted results were compared. A good correlation was found between Anand model predicted and experimentally obtained results. The correlation of experimental results with Anand model prediction shows a very small difference (< 10% in most conditions), thus, confirming the applicability of the model for a wide range of temperatures and strain rates.

CHAPTER 8

VISUALIZATION AND MODELING OF MICROSTRUCTURAL EVOLUTION IN SAC305 BGA JOINTS DURING EXTREME HIGH TEMPERATURE AGING

8.1 Introduction

The microstructure of SAC lead frees older is inherently unstable and it evolves continuously with the exposure to environmental condition. The mechanical properties as well as the reliability of solder joint interconnects are strongly influenced by its microstructure, which is controlled by its thermal history including its solidification rate and thermal exposures after solidification. The microstructure of Sn-Ag-Cu (SAC) solder consists of β-Sn dendrites surrounded by eutectic regions, which are mixtures of Ag_3Sn, Cu_6Sn_5, and β-Sn phases. The IMCs (Ag_3Sn, Cu_6Sn_5) in the eutectic regions help to improve strength of the solder alloy by restricting dislocation motion. The degradation of mechanical properties of solder alloys are result of the microstructural evolution occurring during isothermal aging and high temperature testing. The most well-known and widely observed changes are coarsening of the Ag_3Sn and Cu_6Sn_5 intermetallic compounds (IMCs) present in the eutectic regions between β-Sn dendrites. In addition to this, other changes (e.g. size/shape of β-Sn dendrites, migration of intermetallic particles etc.) have also been observed in solder microstructure but due to lack of in depth study they are not well understood. Many researchers have also suggested empirical representations to

quantify the growth of IMC particles or solder-Cu pad layers as a function of aging temperature and aging time. Most prior studies conducted on the effect of isothermal aging on microstructural evolution failed to show direct comparison between aged and non-aged conditions of a single sample. Instead, observations and measurements were done on two different solder joints (one aged and one non-aged). Comparisons made in this manner are totally qualitative in nature, since the microstructures are from two different samples and cannot be directly compared.

In this work, the microstructural evolution of SAC305 (96.5Sn-3.0Ag-0.5Cu) BGA joints were investigated for different aging conditions utilizing Scanning Electron Microscopy (SEM). In particular, efforts have been taken to monitor aging induced microstructural changes occurring within fixed regions in selected lead free solder joints, and to create time-lapse imagery of the microstructure evolution. Aging was performed at T = 125, and 150 °C for several durations including 0, 1, 5, 10, and 20up to 20 days, and the topography of the microstructure of a fixed region was captured using the SEM system. This process generated several images of the microstructure as the aging progressed. The overall objective was to visualize the diffusion of silver and copper in the beta-tin matrix during aging. In addition, the growth of the copper-tin layer at the solder joint and copper pad interface at the PCB side has been visualized, and then measured as a function of aging time and temperature. Finally, the images were used to quantify the microstructural evolution of SAC305 BGA joints exposed to high temperature aging. Image analysis software was utilized to quantify microstructural changes, such as, total area, number and average diameter of IMC particles, inter-particle spacing etc. The details of sample preparation including cross-sectioning, potting, and mechanical grinding was discussed in

section 3.7.1, whereas, the image capturing mechanism using Scanning Electron Microscopy (SEM) was discussed in section 3.7.2. Utilizing the method, several images were captured, and the results are discussed now.

8.2 Microstructure of SAC305 BGA Joint

In this study, the microstructure of SAC305 BGA joints were observed in different location with different durations of high temperature aging. In particular aging was done at two high temperature at T = 125, and 150 ºC. Figure 8.1 illustrates a typical SEM image (secondary electrons, SEI) of one of the cross-sectioned solder joints in the non-aged condition. After recording the non-aged images in different regions interest, the joints were then aged at T= 125, and 150 ºC, and additional SEM images of the same regions were recorded after 1, 5, 10, and 20 days of aging.

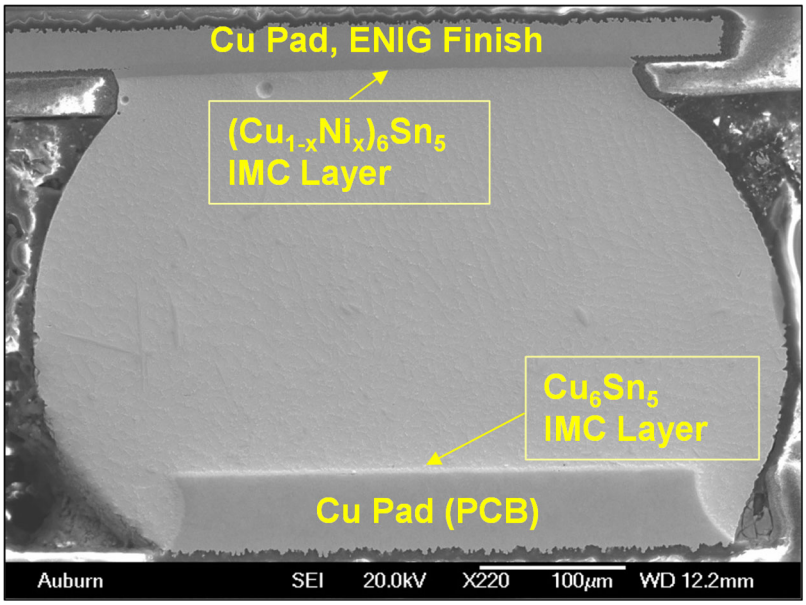

Figure 8.1 SEM Image of BGA Joint Cross-section (Non-aged)

8.3 Visualization of Diffusion of Copper

First of all, investigation was carried out on visual basis to observe the diffusion of copper in β-Sn matrix. Figures 8.2, and shows two example BGA joints that were used for two different aging temperatures (T= 125, and 150 ºC).

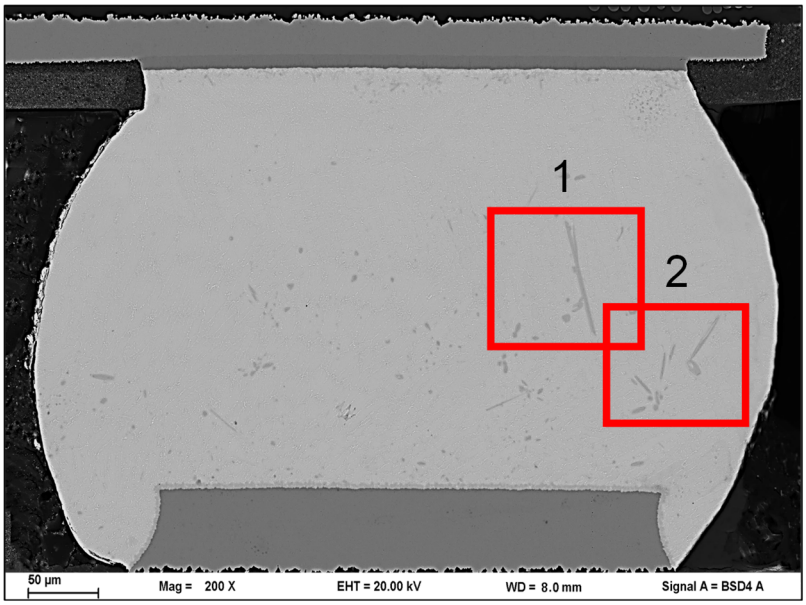

(a) BGA Joint for 125 ºC Aging Study

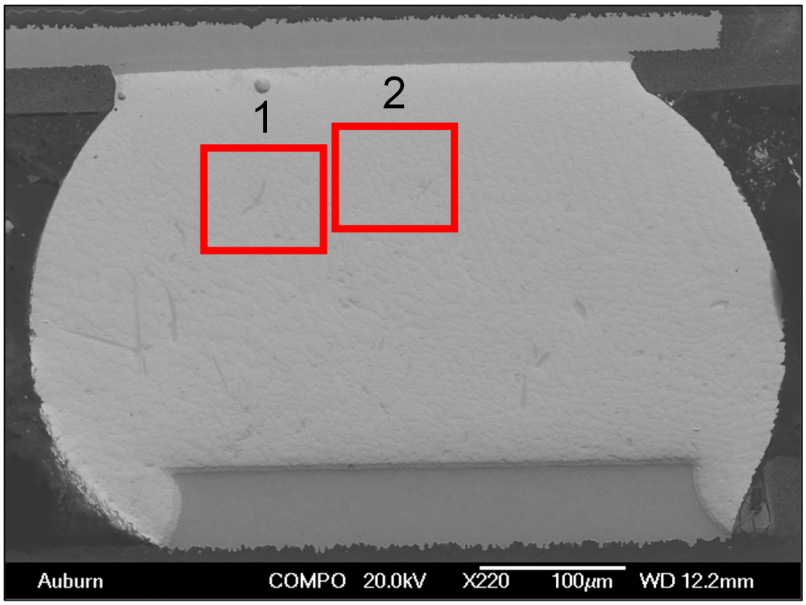

(b) BGA Joint for 150 ºC Aging Study

Figure 8.2 SEM Image (Back Scattered) of Example Region of Interest (Non-aged, Region 1 and 2)

In each of the joints, two example regions of interest were outlined with red rectangular boxes that each include a large number of β-Sn dendrites that are surrounded by interdendritic eutectic regions incorporating a fine dispersion of Ag_3Sn and Cu_6Sn_5 intermetallic particles. Figures 8.3, and 8.4 show magnified views of these regions to illustrate the diffusion process for several different aging intervals. Figure 8.3 represents the diffusion corresponding to aging at T= 125 ºC, whereas, Figure 8.4 represents aging at T= 150 ºC. Similar images have been recorded for several different joints and zones of interest.

The composition of the larger dark IMC particles in the backscattered electron (BSE) SEM images in Figures 8.3, and 8.4 were found to be $(Cu_{1-x}Ni_x)_6Sn_5$ using Energy Dispersive X-ray Spectroscopy (EDS) within the SEM. One example EDS mapping for region 1 in Figure 8.3 with the progression of isothermal aging at T = 125 ºC is shown in Figure 8.5, and various composition of elements for different aging durations are listed in Table 8.1. A rapid diffusion of Cu to these larger particles were observed during the first 20 days of aging. Again, diffusion was observed to be more for higher aging temperature at 150 ºC compared to 125 ºC.

Table 8.1 Aging Dependent Composition from EDS Analysis of SAC305 (wt%)

Element	Composition (wt%) (Isothermal Aging at T = 125 °C)				
	No Aging	1 Day Aging	5 Days Aging	10 Days Aging	20 Days Aging
Sn	94.3	93.7	93.3	92.8	92.4
Ag	3.1	3.4	3.7	4.1	4.2
Cu	2.6	2.9	3.0	3.1	3.4

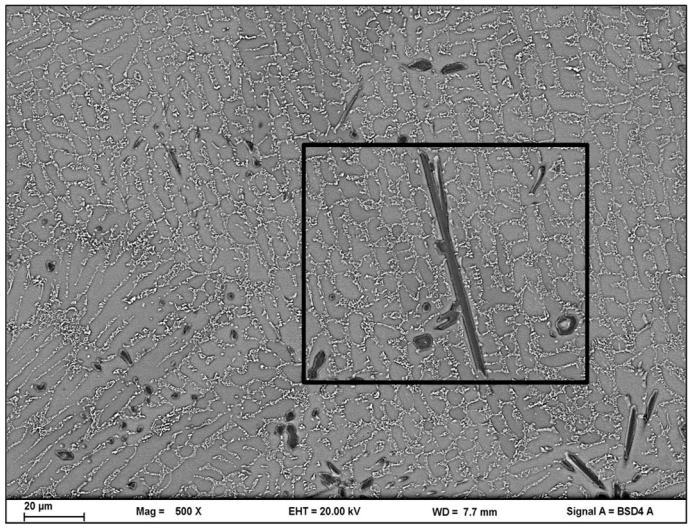

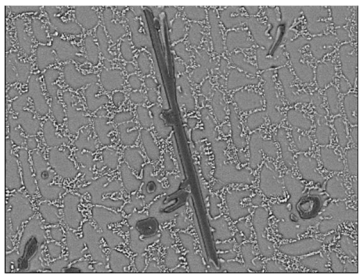

No aging

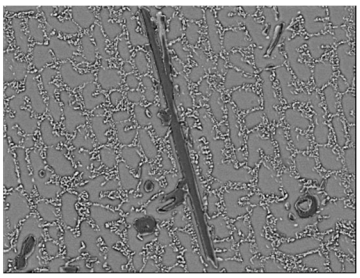

1 day aging

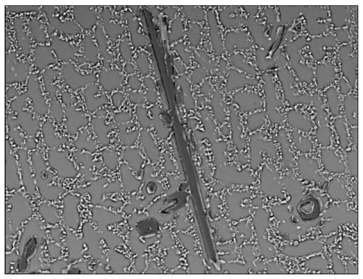

5 days aging

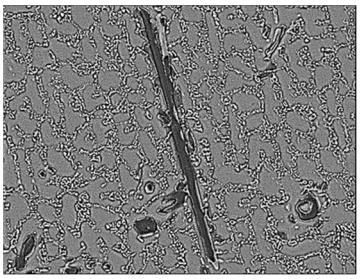

10 days aging

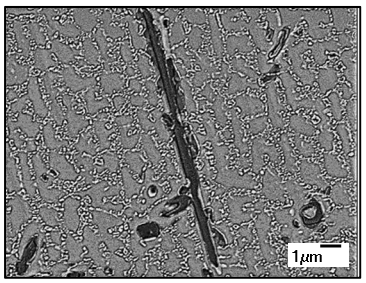

20 days aging

(a) Aging at T = 125 °C (Region 1)

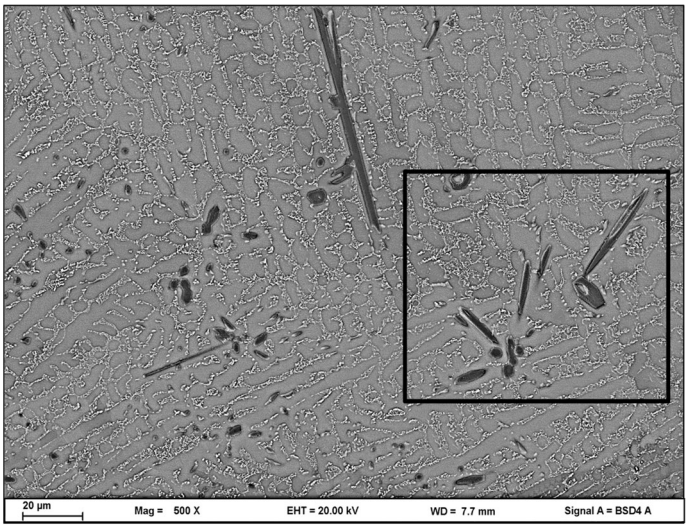

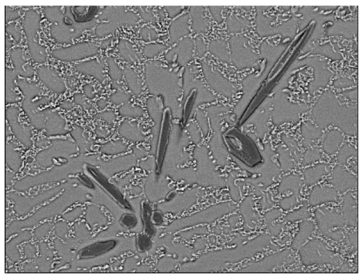

No aging

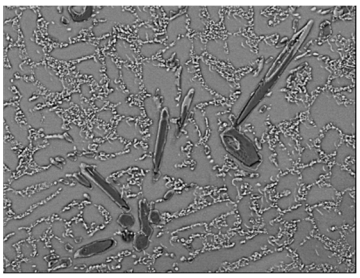

1 day aging

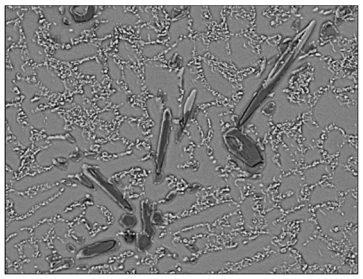

5 days aging

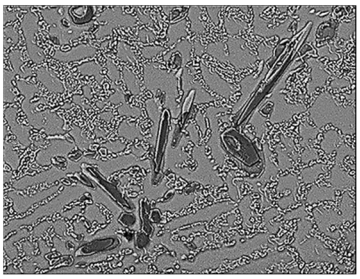

10 days aging

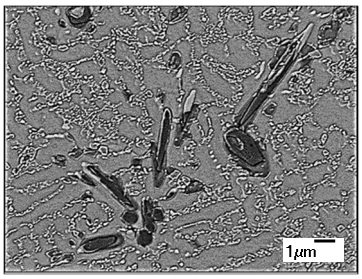

20 days aging

(a) Aging at T = 125 °C (Region 2)

Figure 8.3 Diffusion of Copper in SAC305 BGA Joint during 20 Days of Aging at T = 125 °C

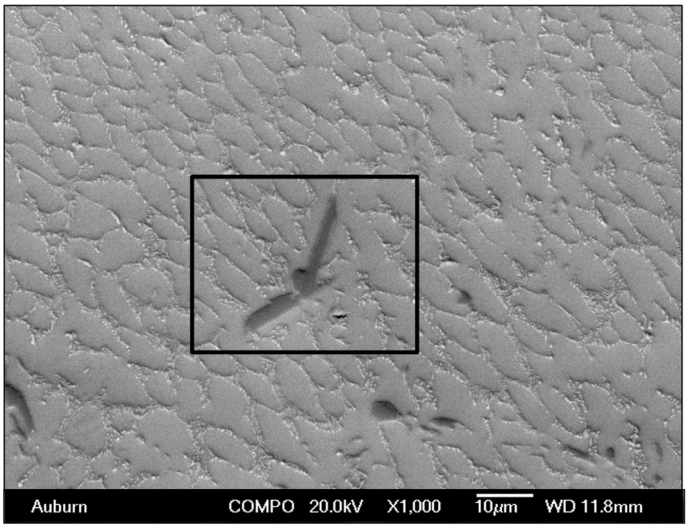

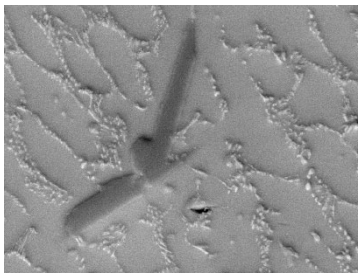

No aging

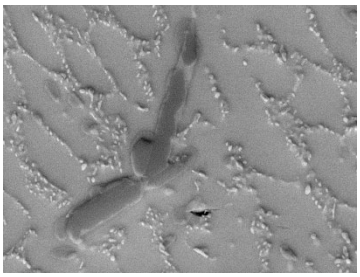

1 day aging

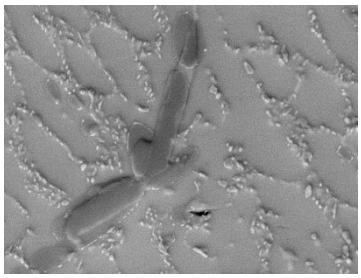

5 days aging

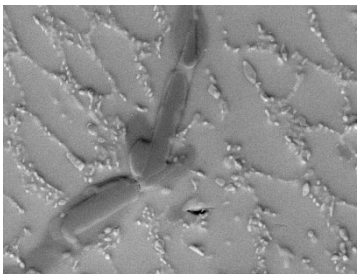

10 days aging

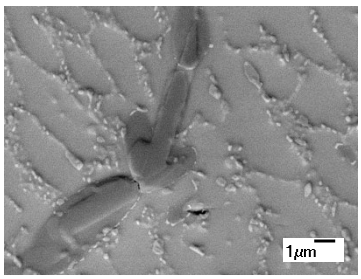

20 days aging

(a) Aging at T = 150 °C (Region 1)

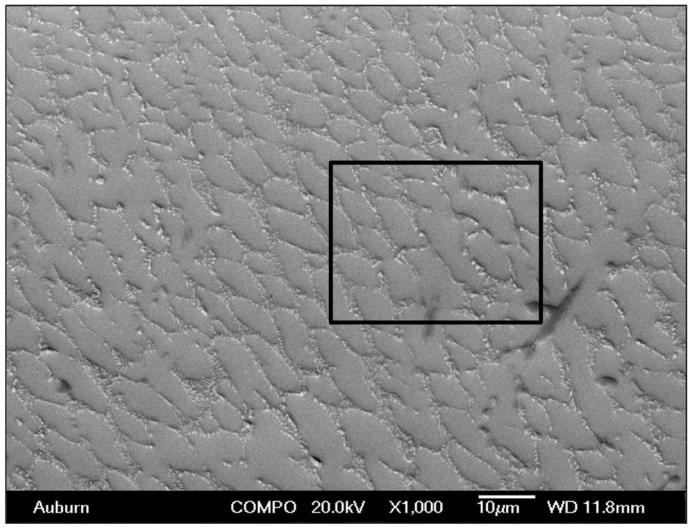

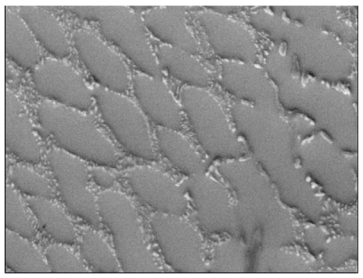

No aging

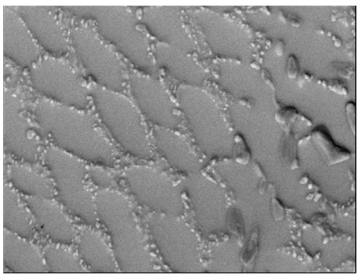

1 day aging

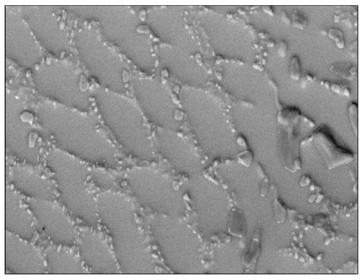

5 days aging

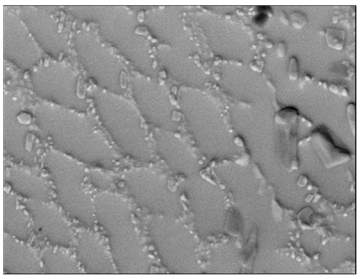

10 days aging

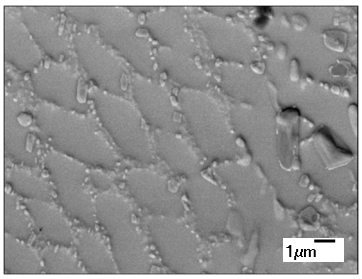

20 days aging

(a) Aging at T = 150 °C (Region 2)

Figure 8.4 Diffusion of Copper in SAC305 BGA Joint during 20 Days of Aging at T = 150 °C

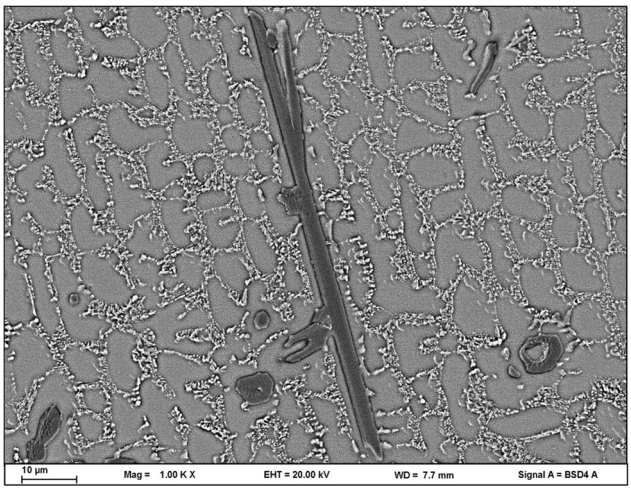

(a) Region 1, BSE, No Aging

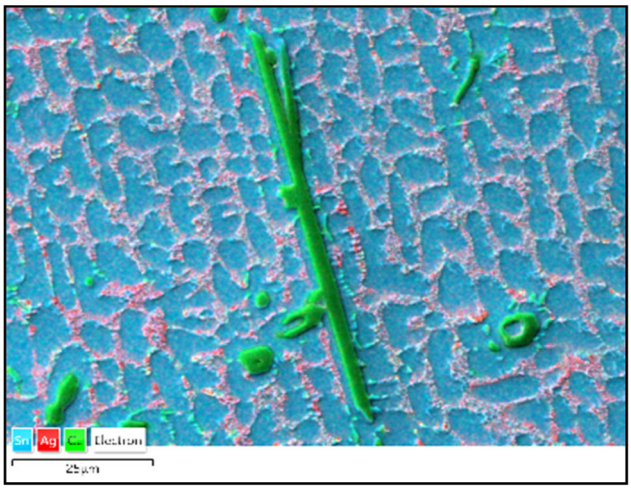

(b) Region 1, EDS Mapping, No Aging

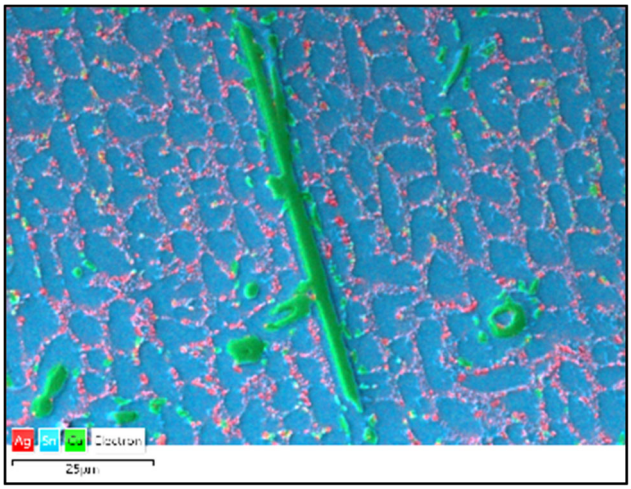

(c) Region 1, EDS Mapping, 1 Day Aging

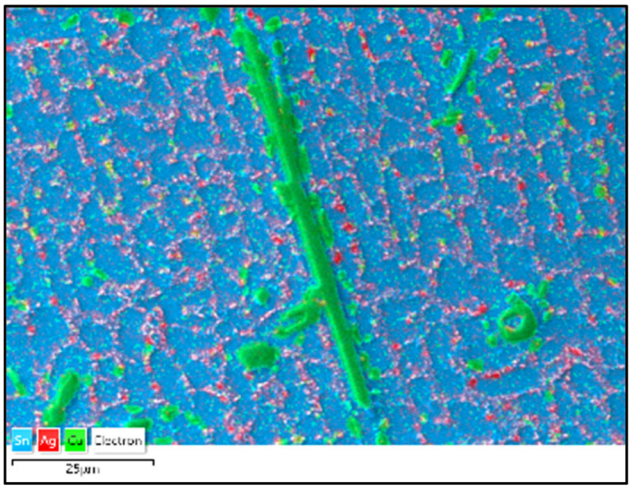

(d) Region 1, EDS Mapping, 5 Days Aging

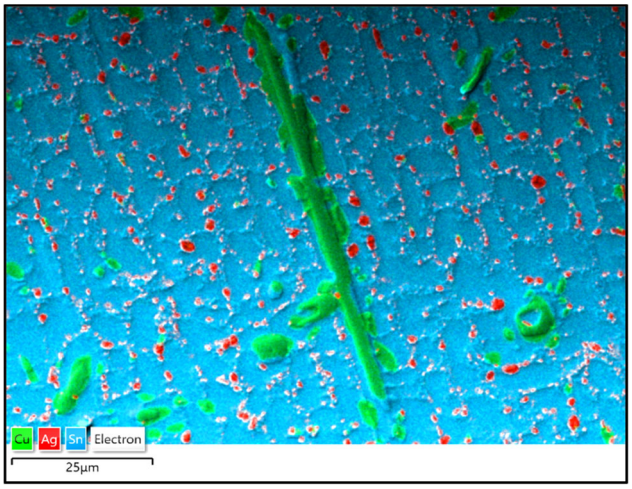

(e) Region 1, EDS Mapping, 10 Days Aging

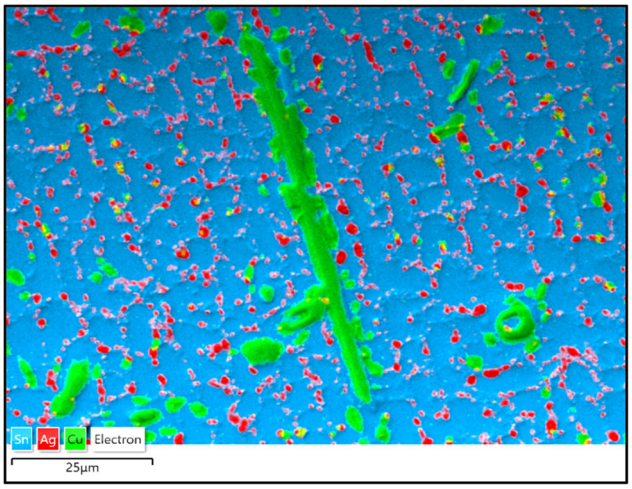

(f) Region 1, EDS Mapping, 20 Days Aging

Figure 8.5 EDS Mapping of a Selected Region in SAC305 BGA Joint with Various Durations of Aging at T = 125 °C

8.4 Visualization and Measurement of Growth of IMC Layer

The growth of Cu_6Sn_5 layer at solder joint and copper pad interface on the PCB side was also monitored as a function of aging time for two different aging temperature at T = 125, and 150 ºC. Figure 8.6 shows a magnified view of the bottom side of the joint shown in Figure 8.2 (b).

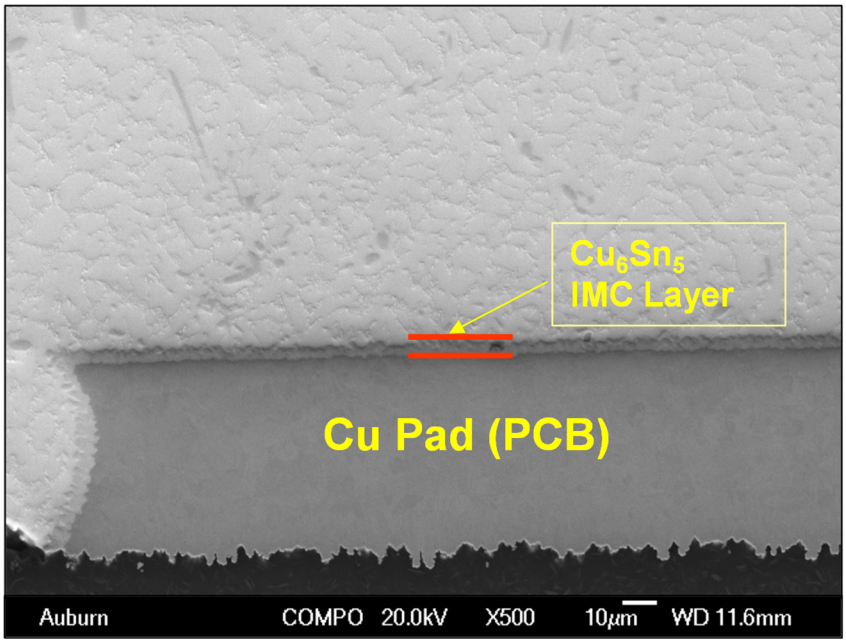

Figure 8.6 Cu_6Sn_5 IMC Layer at the PCB Cu Pad (Non-aged)

Close-up photos of the IMC layer growth in two example BGA joints used for two different temperature aging studies are shown in Figures 8.7, and 8.8, and Figure 8.9 illustrates the EDS mapping of the same region shown in Figure 8.7.

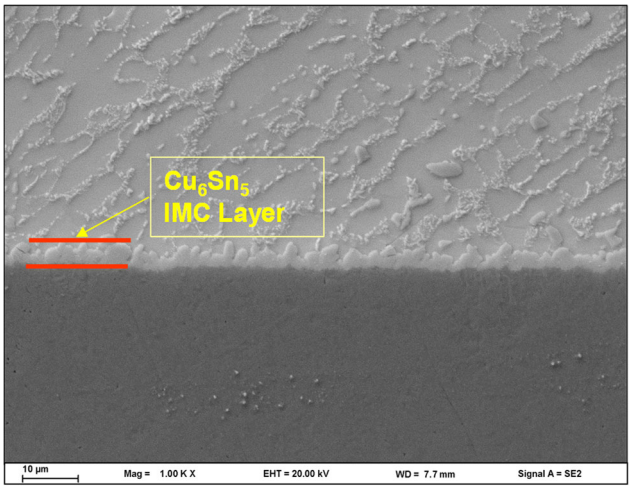

(a) Region 1, SE, No Aging

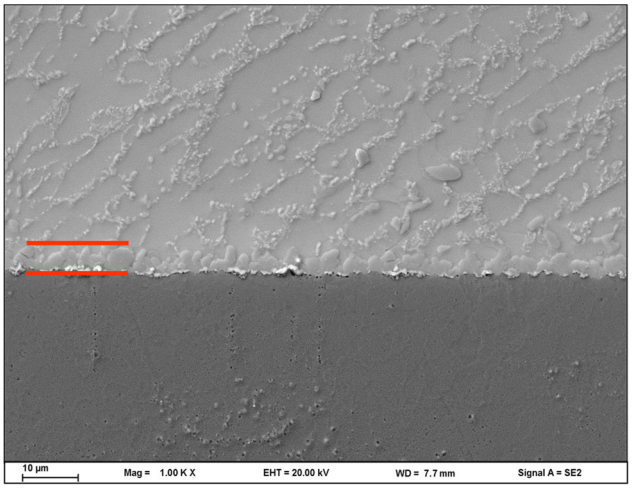

(b) Region 1, SE, 1 Day Aging

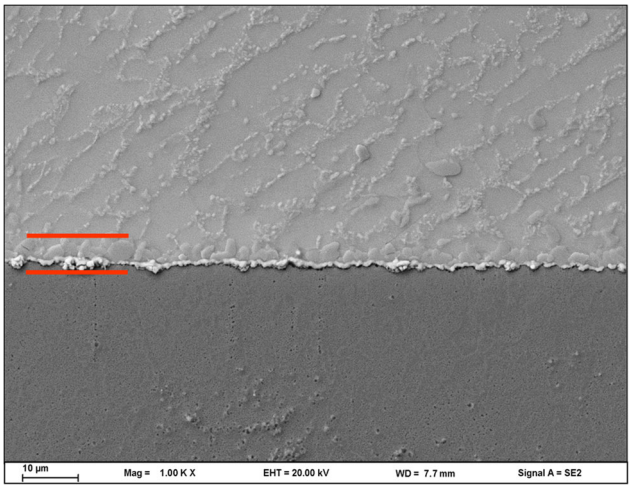

(c) Region 1, SE, 5 Days Aging

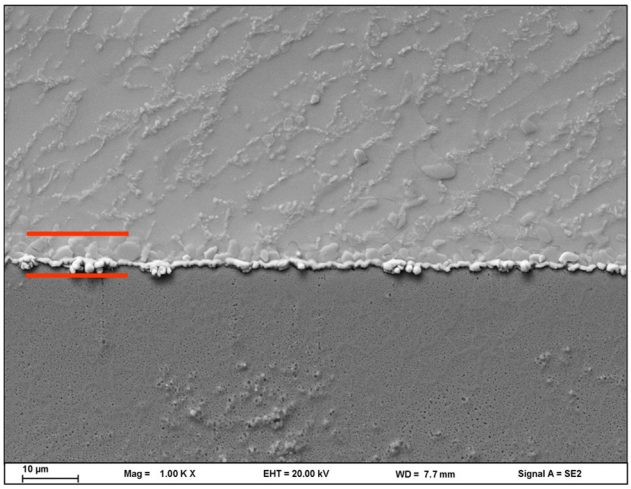

(d) Region 1, SE, 10 Days Aging

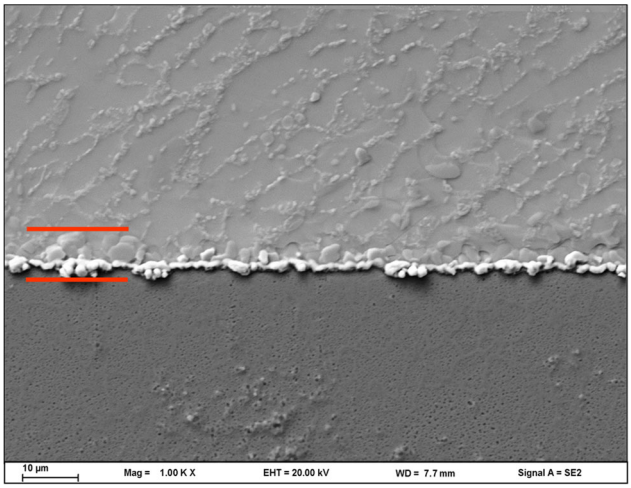

(e) Region 1, SE, 20 Days Aging

Figure 8.7 Growth of Cu_6Sn_5 IMC Layer in SAC305 BGA Joint during 20 Days of Aging at T = 125 °C

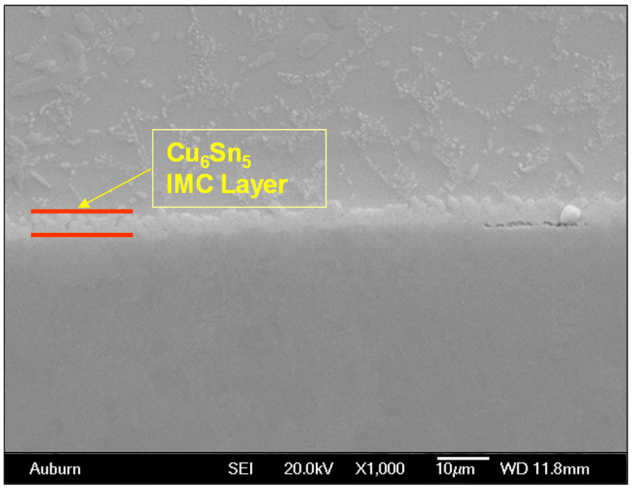

(a) Region 1, SE, No Aging

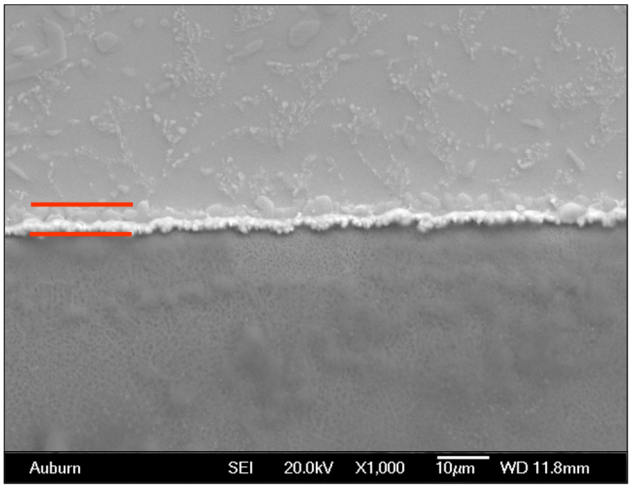

(b) Region 1, SE, 1 Day Aging

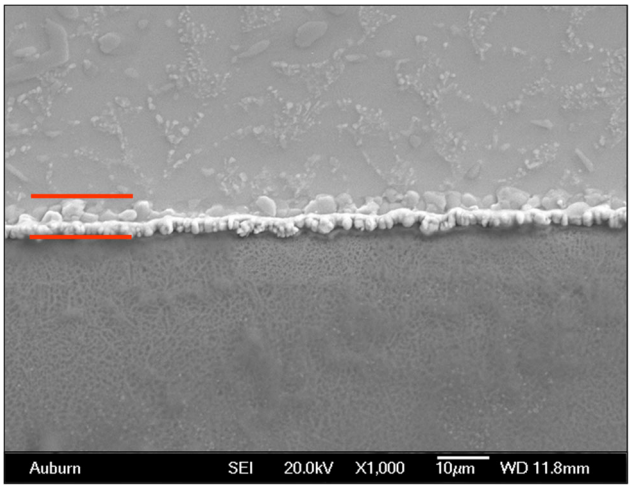

(c) Region 1, SE, 5 Days Aging

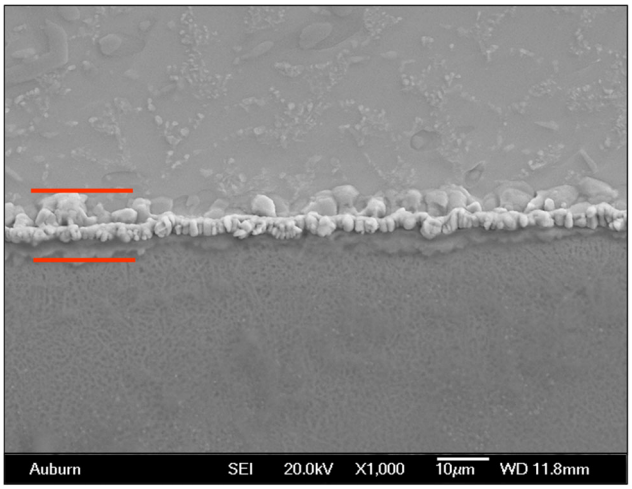

(d) Region 1, SE, 10 Days Aging

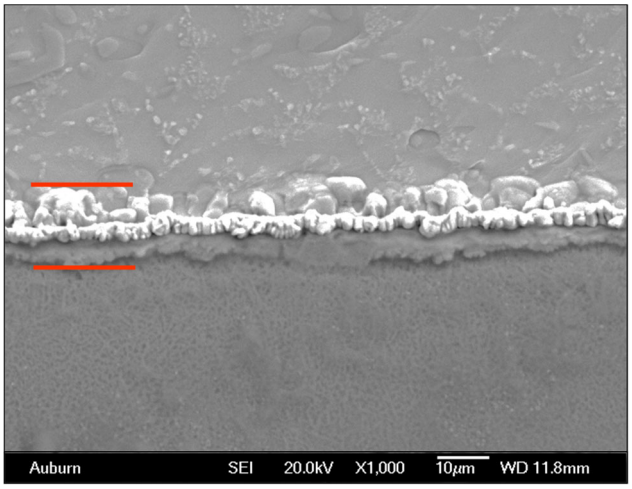

(e) Region 1, SE, 20 Days Aging

Figure 8.8 Growth of Cu_6Sn_5 IMC Layer in SAC305 BGA Joint during 20 Days of Aging at T = 150 °C

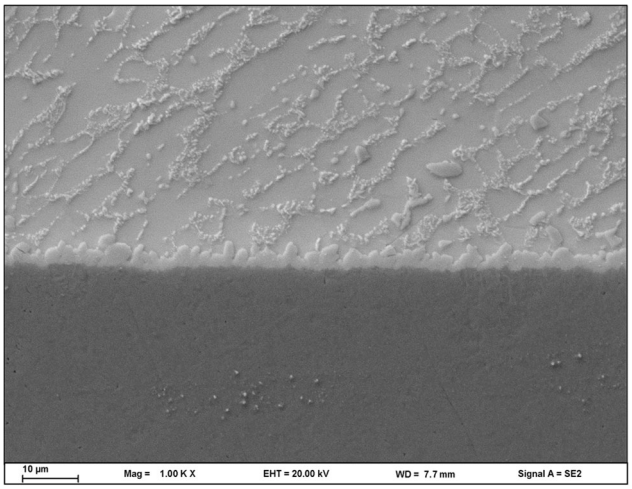

(a) Region 1, SE, No Aging

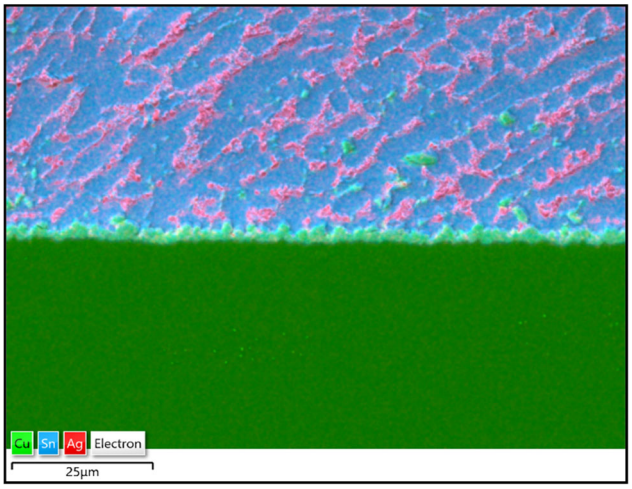

(b) Region 1, EDS Mapping, No Aging

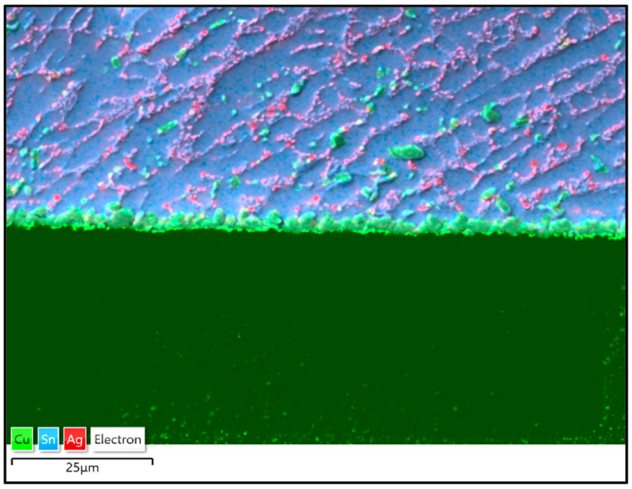

(c) Region 1, EDS Mapping, 1 Day Aging

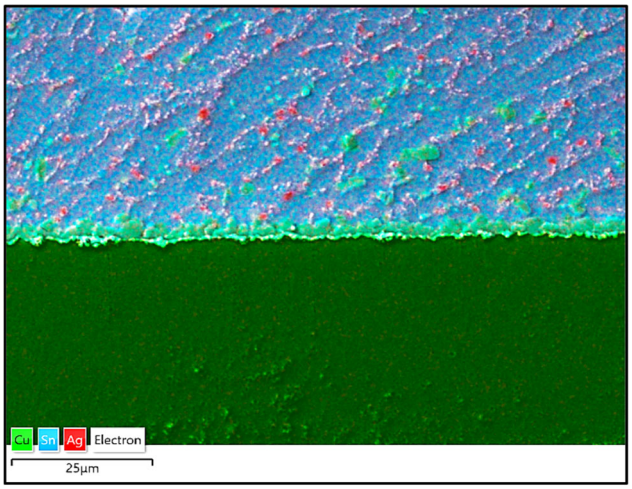

(d) Region 1, EDS Mapping, 5 Days Aging

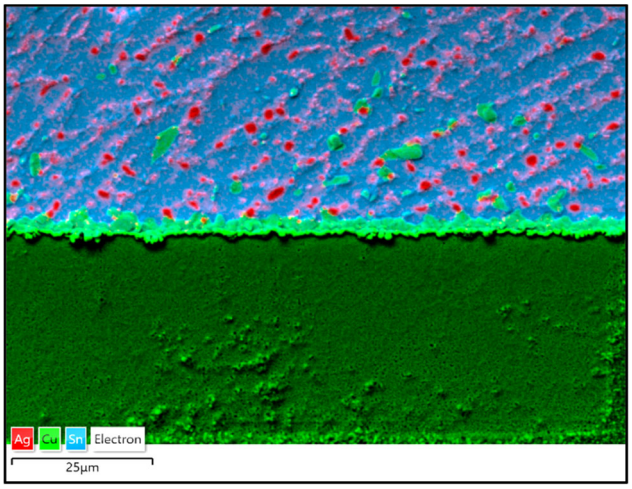

(e) Region 1, EDS Mapping, 10 Days Aging

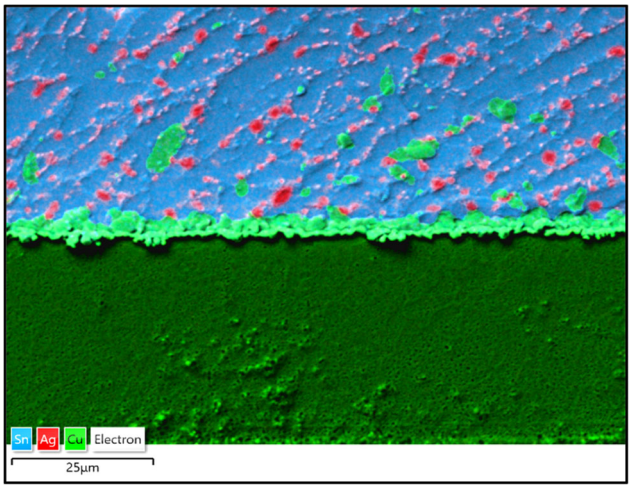

(f) Region 1, EDS Mapping, 20 Days Aging

Figure 8.9 EDS Mapping of a Selected Region near Cu_6Sn_5 IMC Layer in SAC305 BGA Joint with Various Durations of Aging at T = 125 °C

To measure the growth of the layer, three regions were selected at each aging temperature as shown in Figures 8.10, and 8.11, and the growth of the measured average layer thickness as a function of aging time are listed in Table 8.2, and plotted in Figures 8.12, and 8.13. The data were well fit with the traditional parabolic growth model [206]:

$$w = k\sqrt{t} + w_0 \tag{8.1}$$

where w is the IMC layer thickness, t is the aging time, k is IMC growth rate constant, and w_0 is the initial thickness of the IMC layer. As expected from the measurement, a significant amount of growth Cu_6Sn_5 IMC layer in the solder joint and copper pad interface were observed, and with the incremental aging temperature from 125 to 150 °C, more growth were observed.

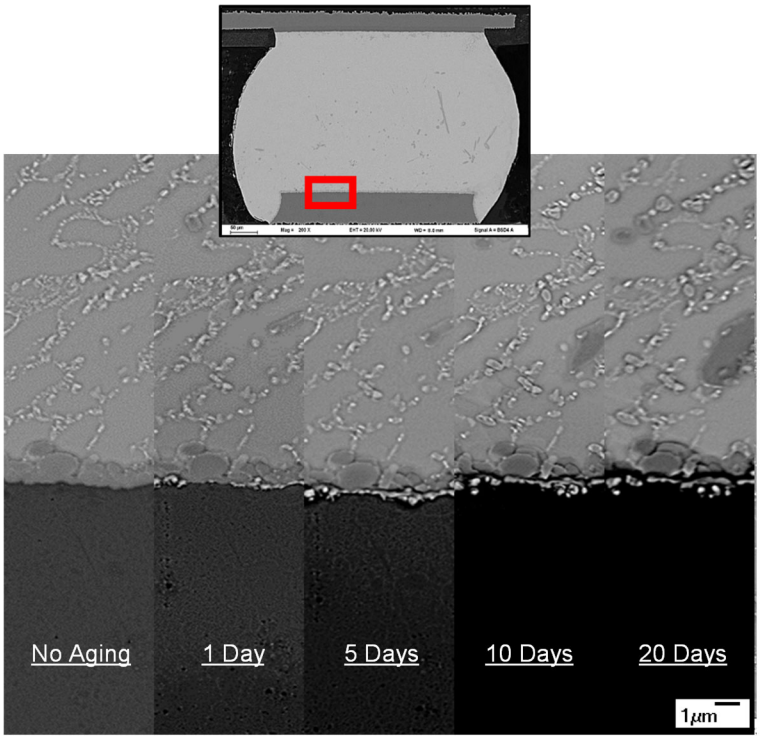

(a) Region 1, BSE

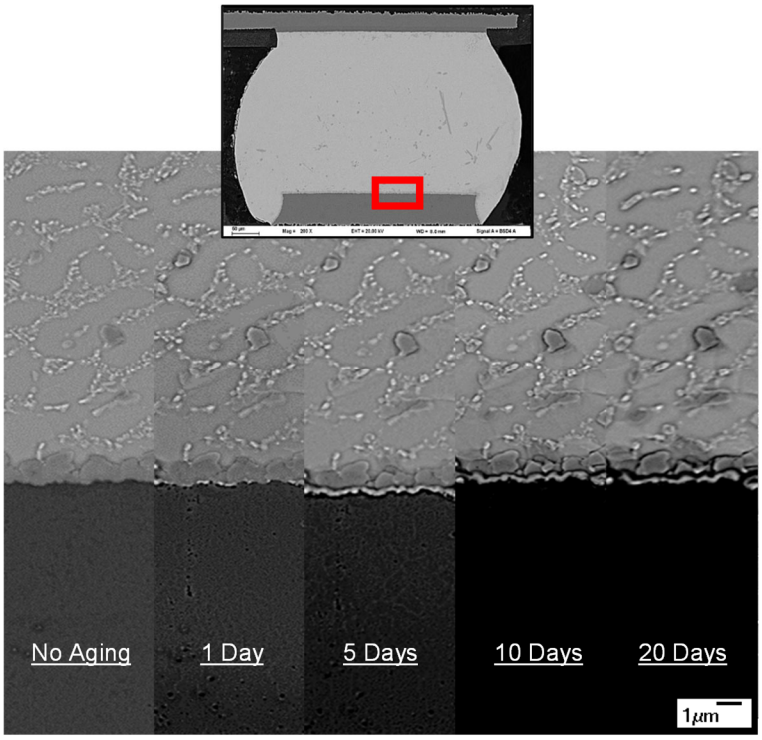

(b) Region 2, BSE

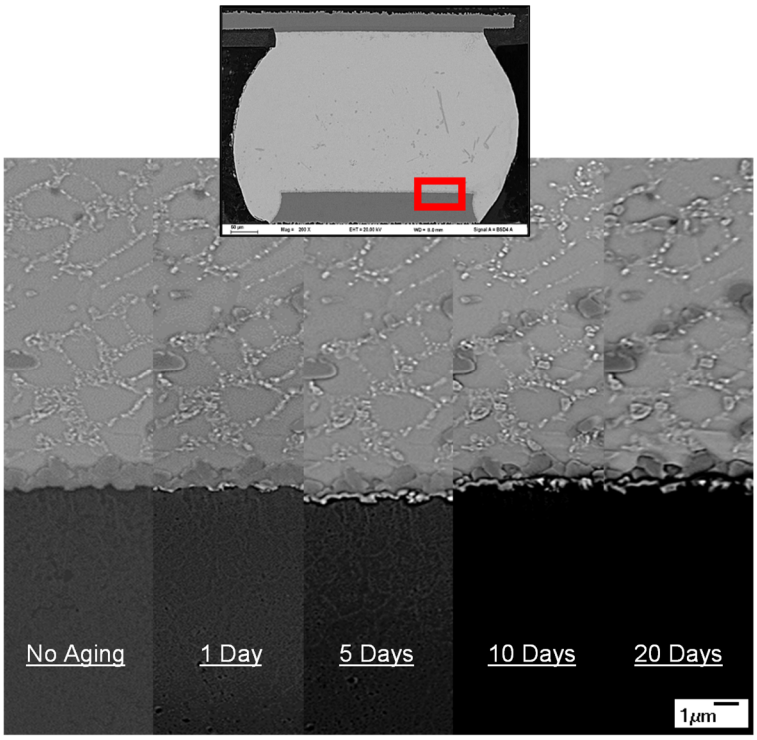

(c) Region 3, BSE

Figure 8.10 Growth of Cu_6Sn_5 IMC Layer during 20 Days of Aging at T = 125 °C

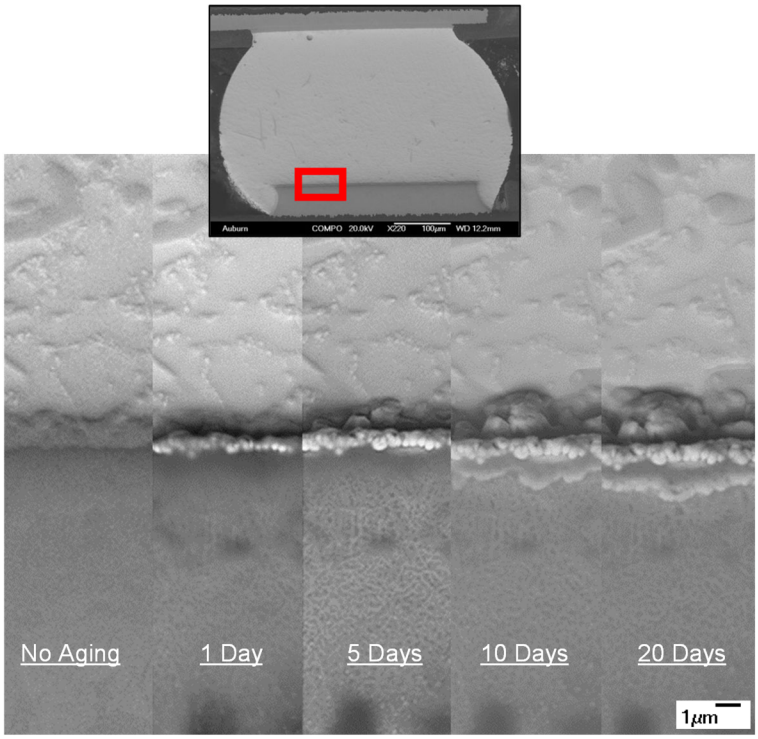

(a) Region 1, BSE

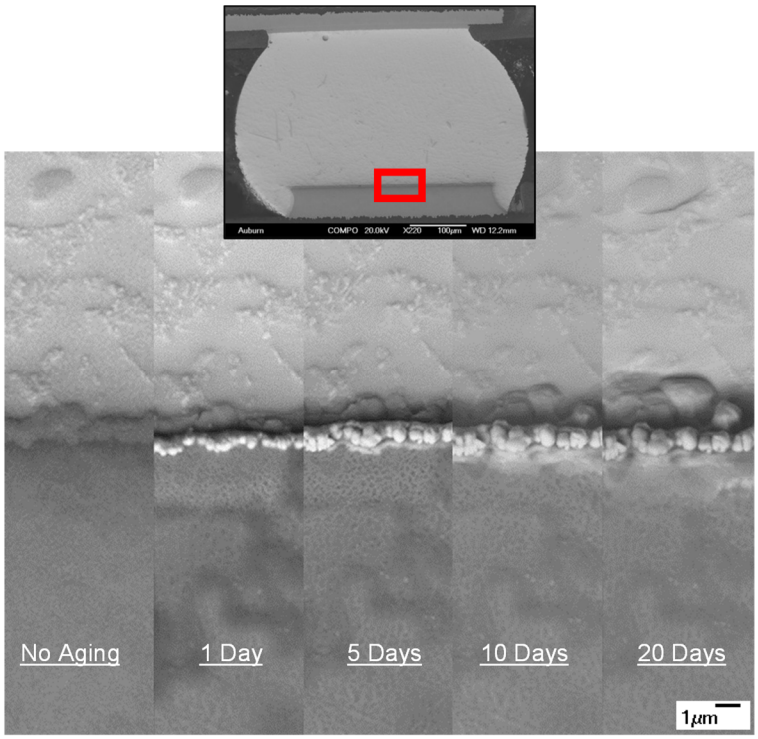

(b) Region 2, BSE

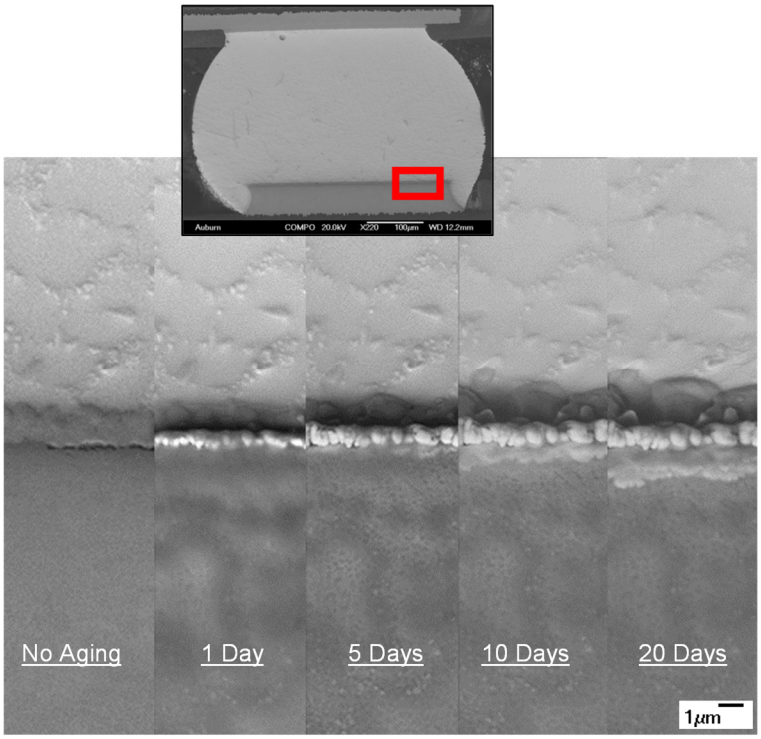

(c) Region 3, BSE

Figure 8.11 Growth of Cu_6Sn_5 IMC Layer during 20 Days of Aging at T = 150 °C

Table 8.2 Aging Dependent Growth of Cu_6Sn_5 IMC Layer

Aging Temperature (°C)	Aging Time (Days)	IMC Layer Thickness, w (μm)			
		R- 1	R- 2	R- 3	Avg
125	0	5.27	3.74	3.52	4.17
	1	5.45	4.33	4.78	4.85
	5	5.66	4.55	4.99	5.07
	10	6.56	5.11	5.33	5.67
	20	7.56	5.33	5.56	6.15
150	0	2.80	2.43	4.11	3.12
	1	4.02	3.18	4.67	3.96
	5	4.95	5.33	5.70	5.33
	10	9.53	8.78	7.57	8.63
	20	10.56	11.68	9.91	10.72

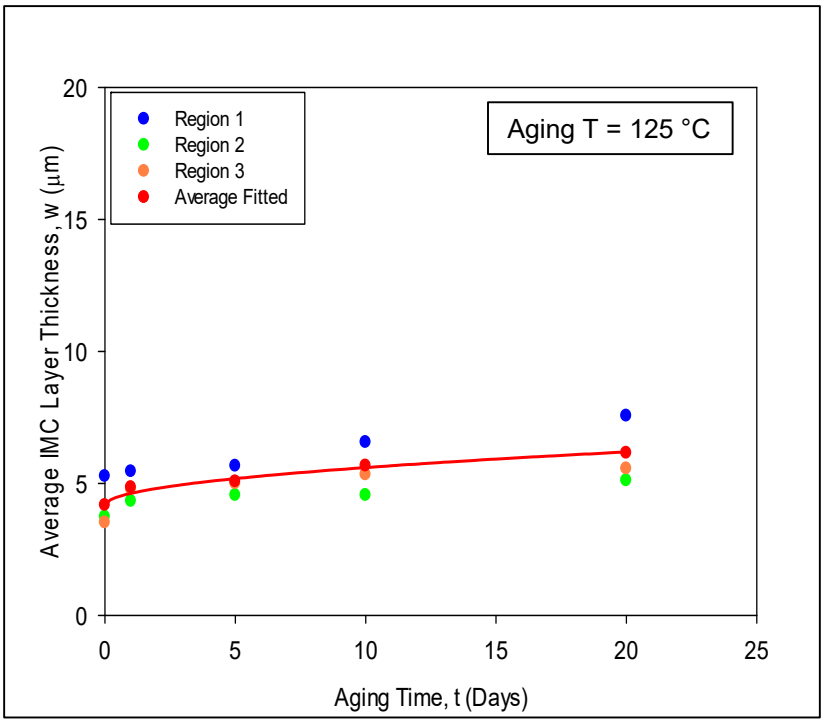

(a) Aging T = 125 °C

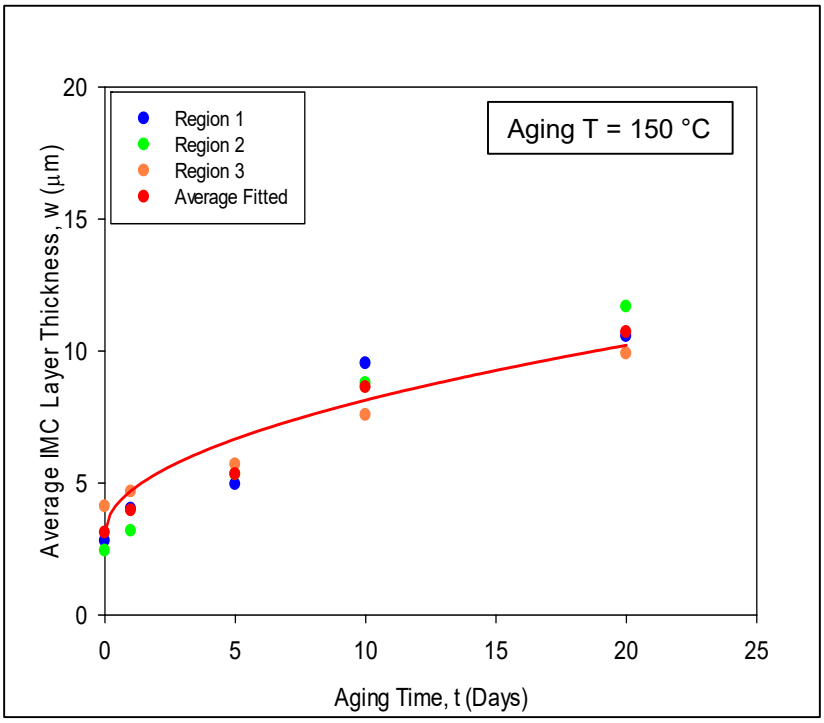

(b) Aging T = 150 °C

Figure 8.12 Measured Growth of Cu_6Sn_5 IMC Layer during Aging

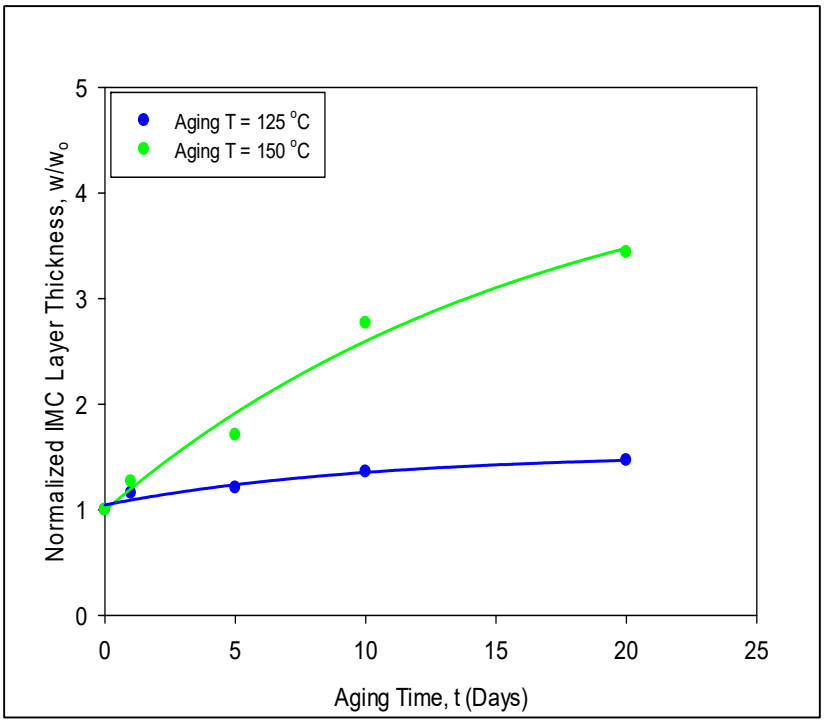

Figure 8.13 Normalized Measured Growth of Cu_6Sn_5 IMC Layer during Aging

8.5 Quantitative Analysis of Microstructural Evolution during Isothermal Aging for SAC305 BGA Joint

Final investigation of this chapter is to visualize and quantify the microstructural evolutions of SAC305 BGA joints during two high temperature aging at T = 125, and 150 °C for several durations including 0, 1, 5, 10, and 20 days. In particular, aging induced coarsening of the IMCs was studied for each alloy using Scanning Electron Microscopy (SEM). During this process, the topography of the microstructure of a fixed region was captured using the SEM system. This process generated several images of the microstructure as the aging progressed. These images were used to predict the microstructural evolution in SAC305 BGA joints exposed to high temperature aging. Image analysis software was utilized to quantify microstructural changes (total area,

number and average diameter of IMC particles, inter particle spacing etc.) with respect to aging time.

The details of sample preparation including cross-sectioning, potting, and mechanical grinding was discussed in section 3.7.1, whereas, the image capturing mechanism using Scanning Electron Microscopy (SEM) was discussed in section 3.7.2. Utilizing the method, several images were captured for both of the aging temperatures as shown in Figures 8.14, and 8.15. Figure 8.14 shows the microstructural evolution for aging at T = 125 °C, whereas, Figure 8.15 corresponds to aging at 150 °C.

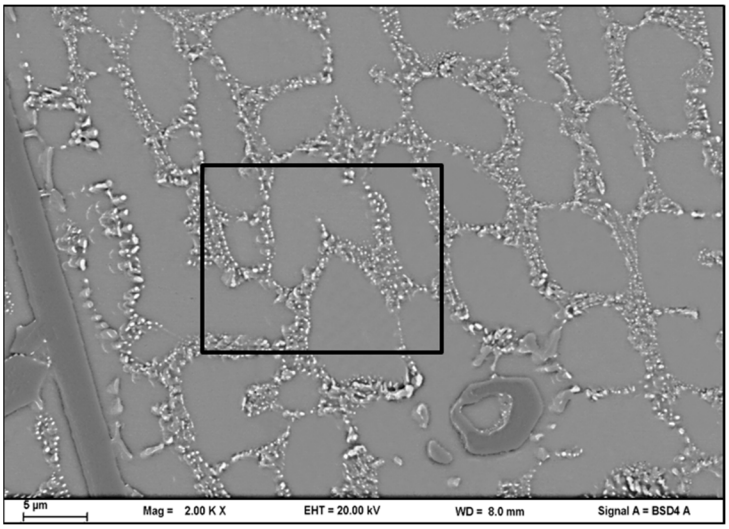

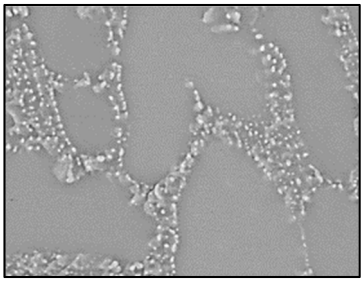

No aging

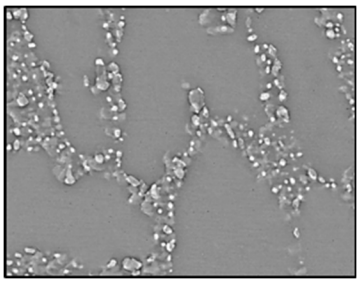

1 day aging

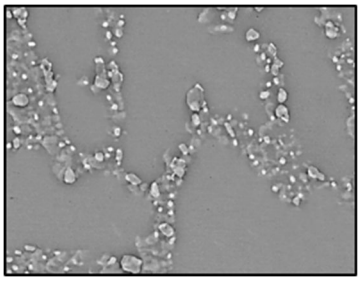

5 days aging

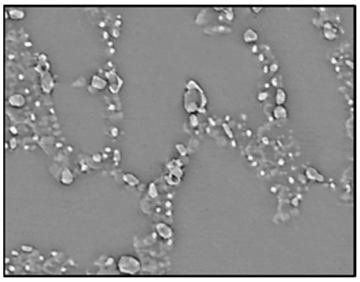

10 days aging

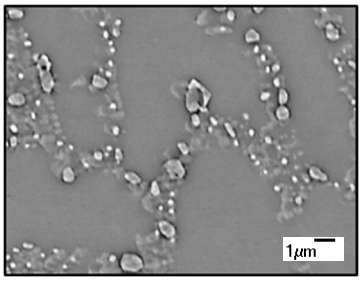

20 days aging

(a) Aging at T = 125 °C (Region 1)

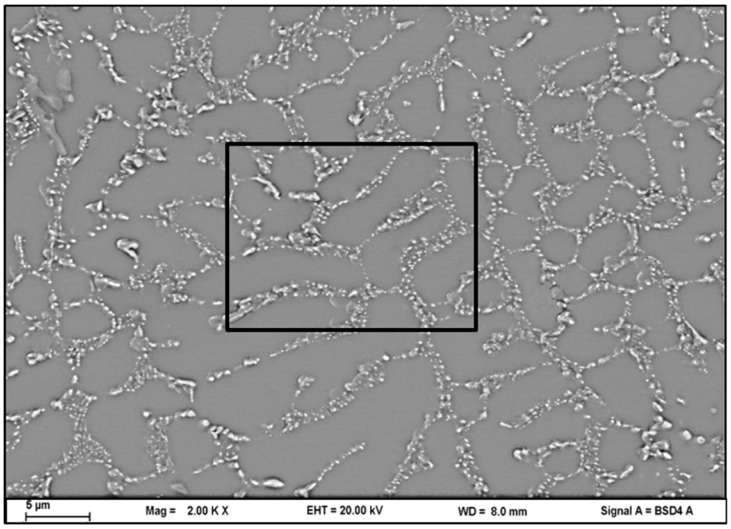

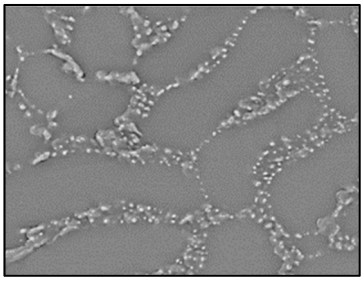

No aging

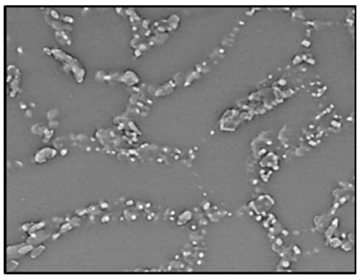

1 day aging

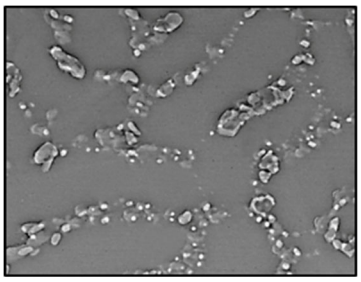

5 days aging

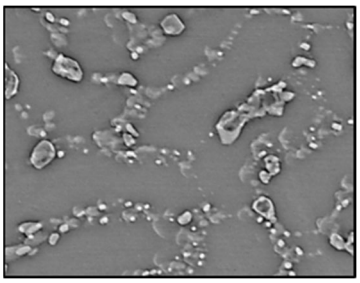

10 days aging

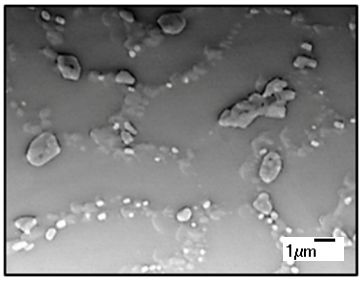

20 days aging

(b) Aging at T = 125 °C (Region 2)

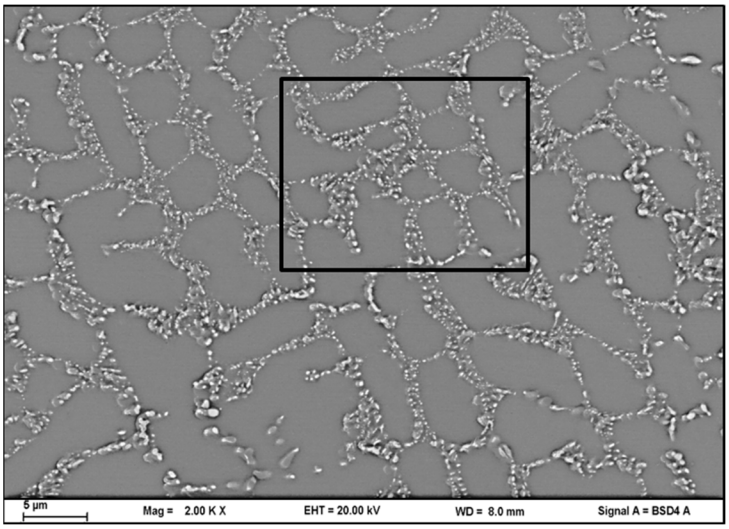

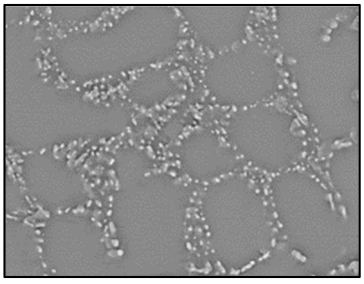

No aging

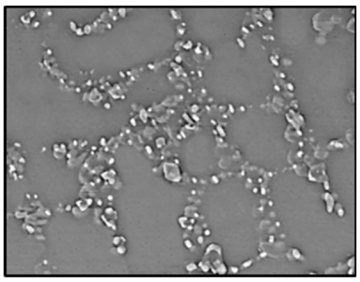

1 day aging

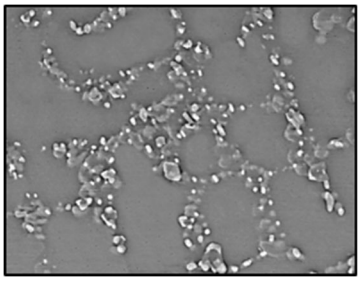

5 days aging

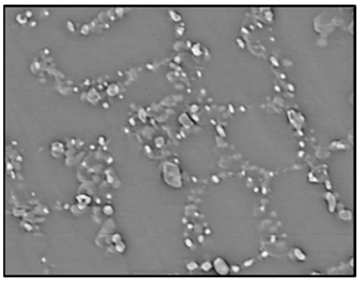

10 days aging

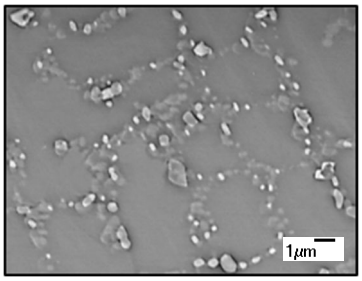

20 days aging

(c) Aging at T = 125 °C (Region 3)

Figure 8.14 Microstructural Evolution of SAC305 BGA Joints Subjected to Isothermal Aging (Aging at T = 125 ºC)

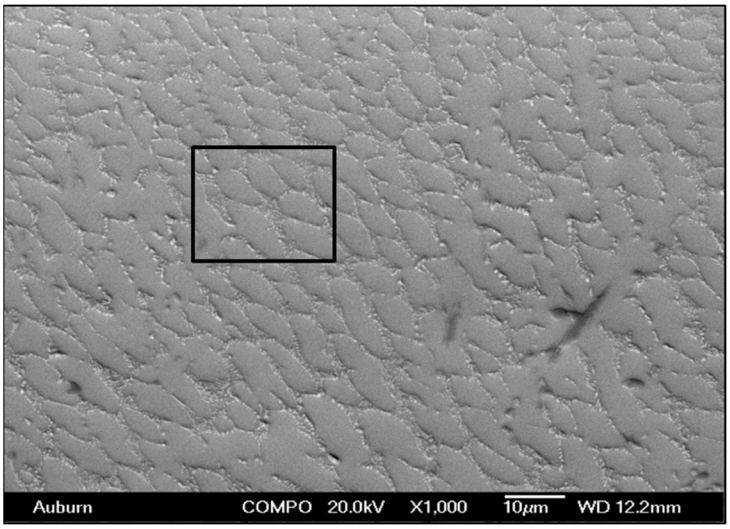

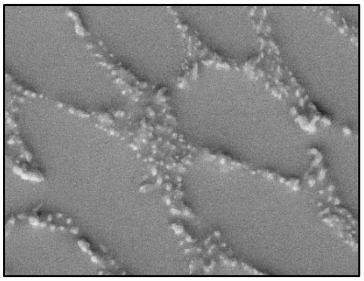

No aging

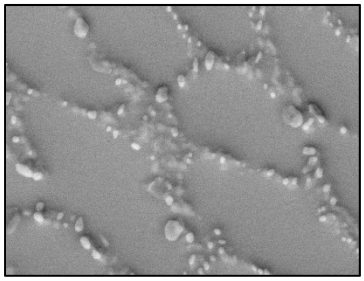

1 day aging

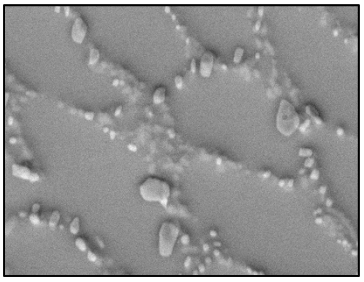

5 days aging

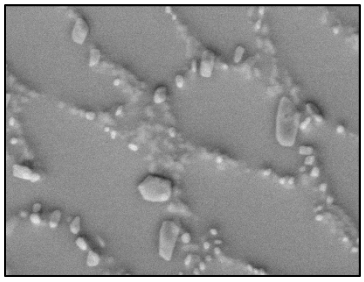

10 days aging

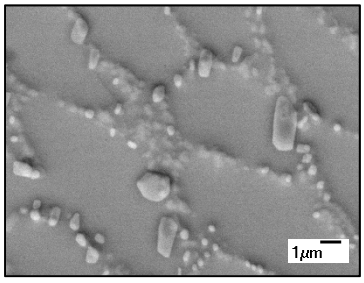

20 days aging

(a) Aging at T = 150 °C (Region 1)

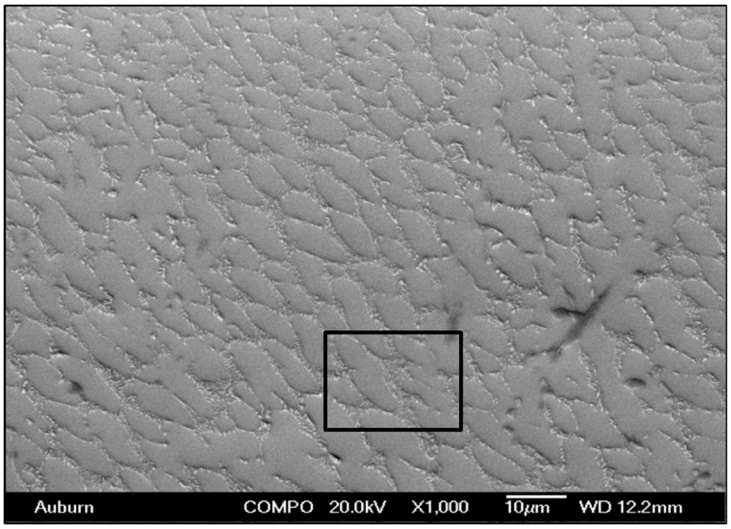

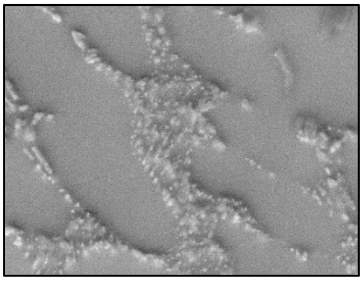

No aging

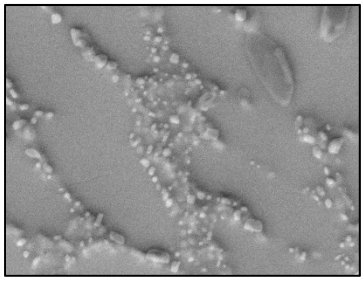

1 day aging

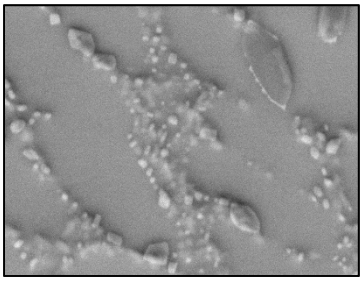

5 days aging

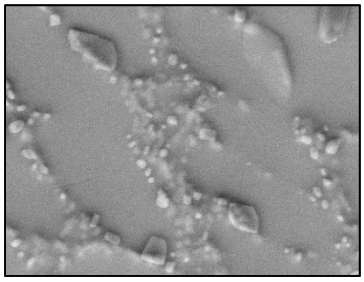

10 days aging

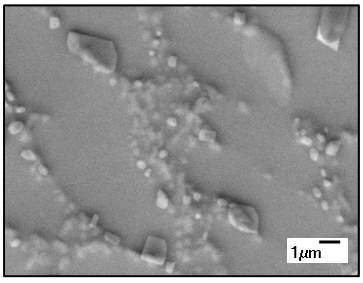

20 days aging

(b) Aging at T = 150 °C (Region 2)

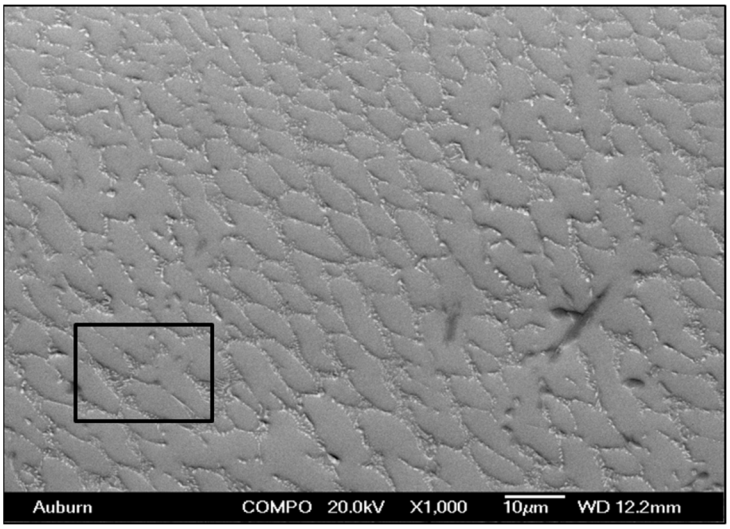

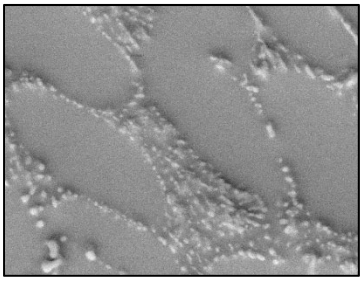

No aging

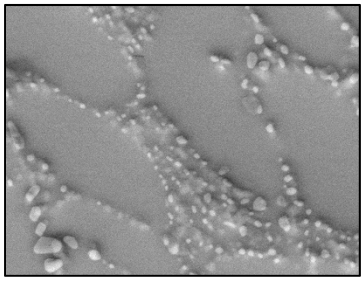

1 day aging

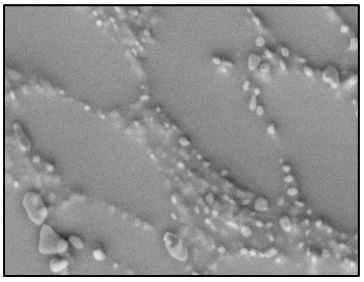

5 days aging

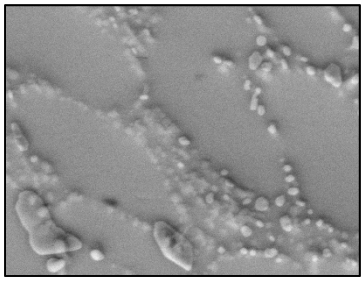

10 days aging

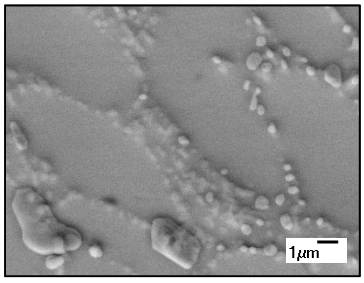

20 days aging

(c) Aging at T = 150 °C (Region 3)

Figure 8.15 Microstructural Evolution of SAC305 BGA Joints Subjected to Isothermal Aging (Aging at T = 150 ºC)

From all the images shown in Figures 8.14, and 8.15, a diffusion based IMC coarsening was observed where larger particles are produced at the expense of smaller particles which is popularly known as Ostwald Ripening [180-183]. Coarsening of intermetallic particles occurred due to aging. Some IMC particles grew in size, some split into several smaller particles, and some decreased in size and disappeared in the end. In other words, the number of IMC particles decreased, the average particle size increased, and the average particle separation distance increased. Also, the particles shifted to more spherical shapes. The shape and size of the dendrites remained nearly unchanged. Again, from visual comparison between images it was observed that the growth of IMC particles during isothermal aging was higher for aging at T = 150 °C compared to T = 125°C.

8.5.1 Measurement of IMC Particle Diameter and Number of IMC

The images obtained from SEM were further processed to quantify the evolution of IMC particles during isothermal aging. Image processing and analysis steps were outlined before in sections 3.7.3, 3.7.4, and 3.7.5. The quantitative analysis results are summarized in Table 8.3 which represents the variation in average particle diameters and number of IMC particles with the aging temperature and duration. The evolution of the IMC particles with aging time are shown in Figure 8.16, and 8.17. It is evident that the average size of the particles increases, while the number of particle decreases with the progression of aging. The data for three regions at each aging temperature and durations were fitted using a two term exponential relation represented by Equation 3.30 in section 3.7, and plotted in Figures 8.16, and 8.17.

Table 8.3 Evolution of IMC Particles of SAC305 for Different Aging Temperature and Duration

Aging Temperature (°C)	Aging Time (Days)	No. of Particles				Avg. Diameter (nm)			
		R- 1	R- 2	R- 3	Avg	R- 1	R- 2	R- 3	Avg
125	0	165	182	187	178	248	265	276	263
	1	102	108	132	114	398	417	433	416
	5	83	88	108	93	492	500	538	510
	10	73	90	95	86	547	585	602	578
	20	66	79	86	77	594	665	676	645
150	0	174	199	186	187	268	273	299	280
	1	89	100	99	96	470	480	488	479
	5	71	73	80	75	639	637	621	632
	10	63	60	65	63	740	754	799	764
	20	55	52	58	55	841	831	893	855

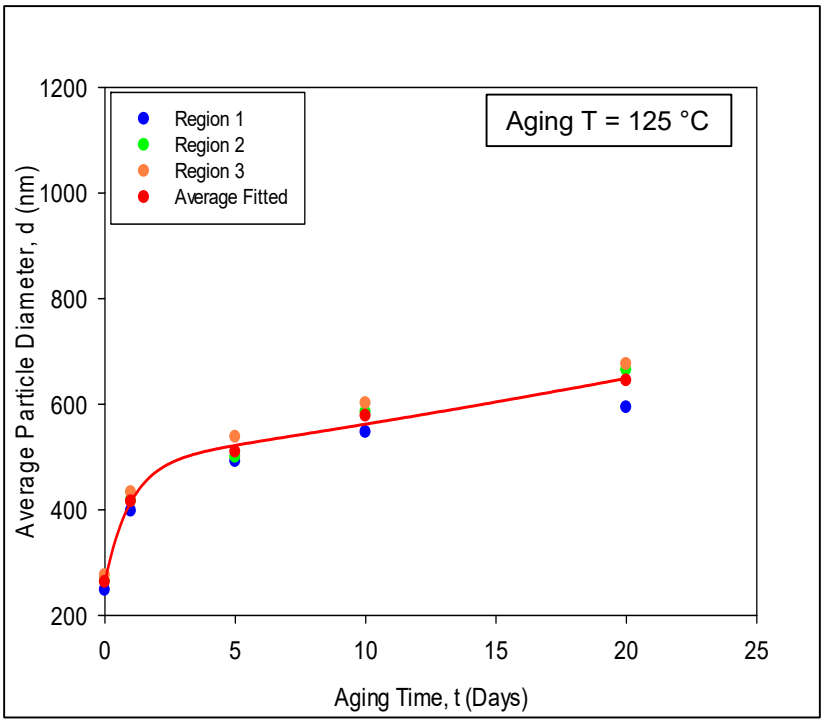

(a)

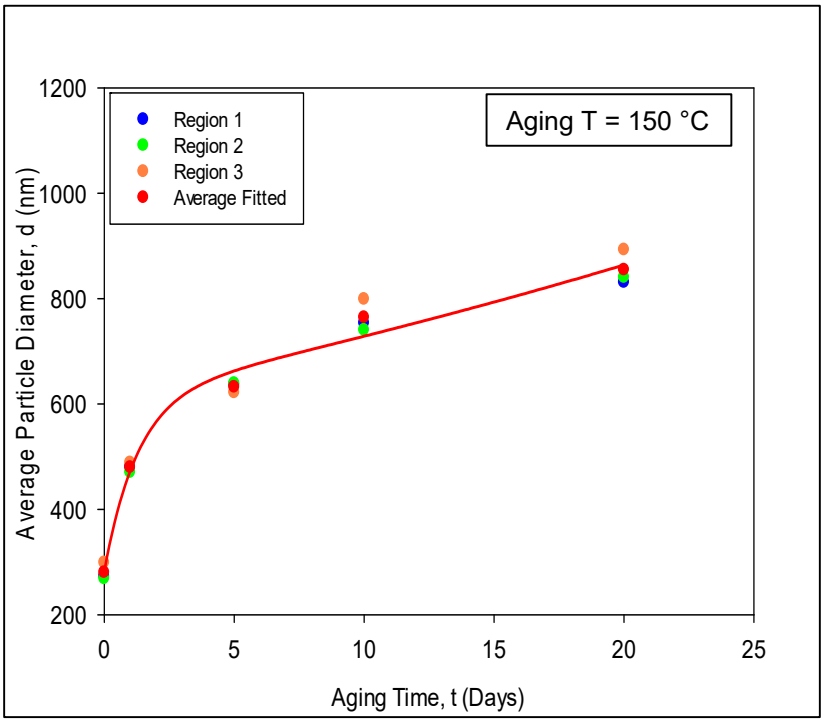

(b)

Figure 8.16 Changes in IMC Particle Diameter with Aging Time for SAC305 BGA Joint

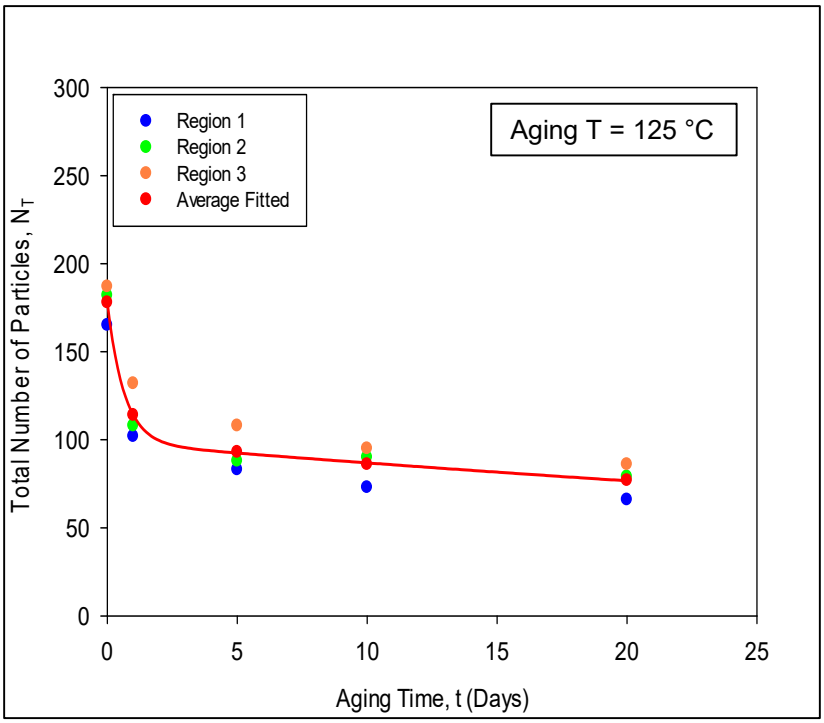

(a)

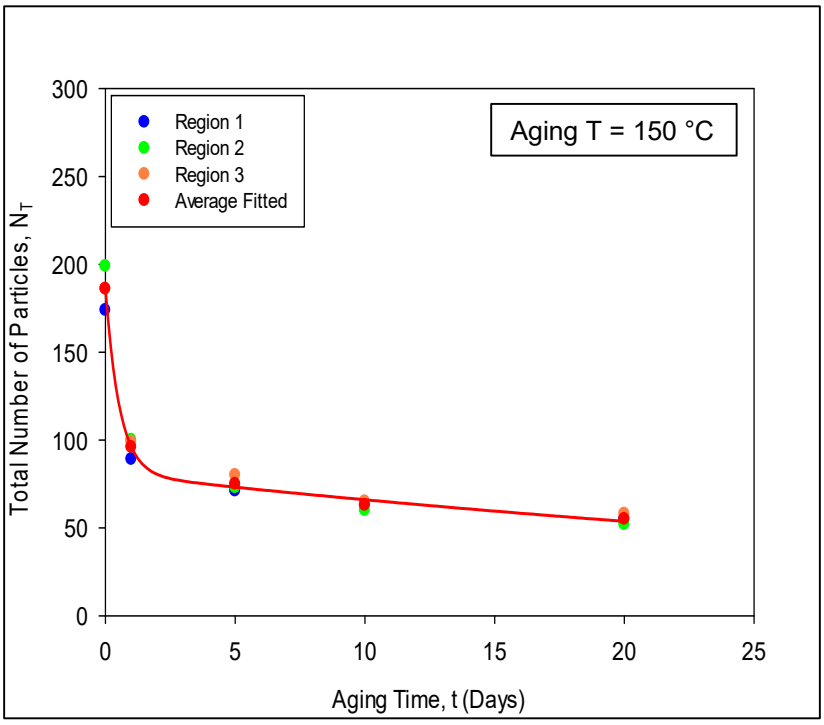

(b)

Figure 8.17 Changes in IMC Particle Number with Aging Time for SAC305 BGA Joint

The average fitted curves for particle size and particle numbers for different aging temperatures are plotted in the same graph for comparison in Figure 8.18. The colors of the data points and associated fitting curves indicate the aging temperature.

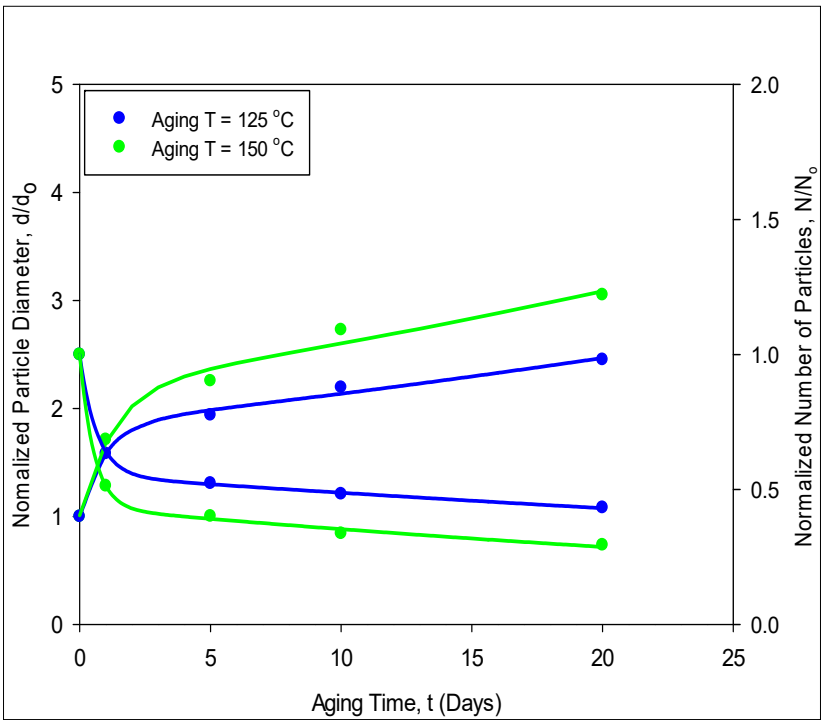

Figure 8.18 Variation in Total IMC Particle Area with Aging Time for SAC305 BGA Joint

8.6 Discussion on Evolution of IMC Particles during Aging

Typically, IMC particles tend to become more round (spherical) with aging. Atoms on the surface of a particle have higher energy than the atoms inside a particle due to unsatisfied bonds in the surface atoms. A cylindrical or elongated particle has a higher fraction of surface atoms (or higher surface to volume ratio) compared to a spherical (round) particle with the same volume. As a result, the free energy per atom of an elongated particle or several small particle is higher than a big round particle with equal volume. This free energy difference is the driving force that causes the transition of IMC particles from smaller to a bigger size as seen in Figures 8.14, and 8.15.

This IMC coarsening phenomenon is also known as Ostwald Ripening. According to the Gibbs-Thompson effect [181, 182], an increase in particle size is accompanied by a decrease of the solute concentration in the matrix surrounding the particle. This leads to a concentration gradient, and solute atoms near smaller particles will diffuse towards the larger particles where the reductions in solute concentration has occurred. In addition, atoms from the smaller particles will go back into solution. The overall effects are shrinkage of smaller particles, and growth of larger particles. A schematic of the variation of solute concentration around a small and a large particles is shown in Figure 8.19. Since Ostwald Ripening is a diffusion-based process, use of higher aging temperatures will increase the rate of coarsening significantly.

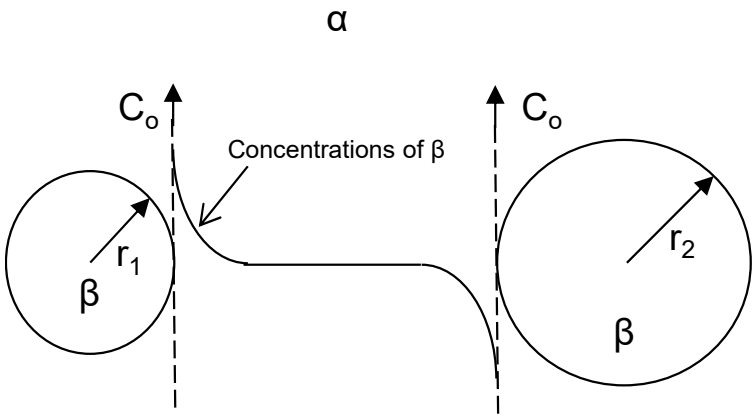

Figure 8.19 Schematic of Solute Concentration in Front of Particle [181].

The coarsening and coalescing of IMC particles during aging is known to play a critical role in the degradations of solder mechanical properties. IMC particles will pin and block the movement of dislocations. However, aging leads to both a smaller number of larger IMC particles and increased spacing between the IMC particles. The interparticle spacing λ can be calculated from the following equation:

$$\lambda = \frac{4(1-f)r}{3f} \tag{8.2}$$

where f is the volume fraction of the particles and r is the particle radius. Hence for a fixed volume fraction of the IMC particles, spacing between the particles increases with increasing particle diameter. Orowan proposed a mechanism that when a dislocation crosses incoherent precipitate particles (like the IMC particles in present case), it will bow and leave a loop of stress field around the particle [181, 182, 184]. A schematic of the interaction between a dislocation and IMC particles is shown in Figure 8.20.

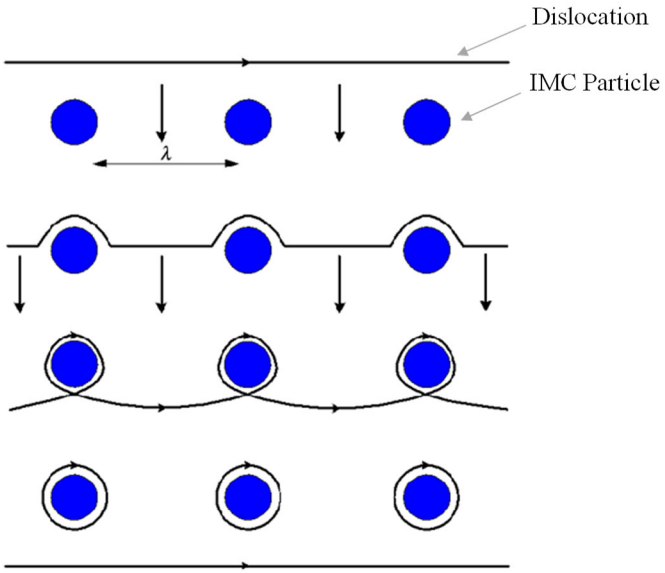

Figure 8.20 Schematic of a Dislocation Passing IMCs (Orowan Looping)

The yield stress and strength of a material depends on the shear stress (also known as the Orowan stress) that is required for a dislocation to pass through the particles. This shear stress will decrease as the inter-particle spacing increases during aging as shown in Equation 8.3 [180-182].

$$\tau_o = \frac{Gb}{\lambda} \tag{8.3}$$

where τ_o is the shear stress required for a dislocation to pass through the particles, G is the shear modulus, and b is the magnitude of the burgers vector. Therefore, aging leads to the coarsening of the IMC particles which causes to increase the interparticle spacing (Equation 8.2). The yield stress and strength of a material decrease after aging due to the increased interparticle spacing.

8.7 Summary and Discussion

In this study, the microstructural evolution of SAC305 BGA joints was investigated for different aging conditions. In particular, aging was performed at T = 125, and 150 °C for 0, 1, 5, 10, and 20 days. The primary reason behind the degradation of mechanical behavior of different solder alloys during prolonged storage at elevated temperature is microstructural evolution. As found from prior studies, the microstructure of SAC305 is primarily composed of a β-Sn matrix and Ag3Sn and Cu6Sn5 intermetallic compounds (IMC). The degradations of mechanical properties like modulus and strength occur mainly due to coarsening of the Ag3Sn and Cu6Sn5 IMC particles, which reduces their ability to block dislocation movements.

From the experimental time lapsed micrographs, a significant amount of copper diffusion in the β-Sn matrix have been visualized. In addition, growth of the Cu6Sn5 IMC layer was visualized and measured as a function of aging time at the solder joint to PCB copper pad interface. Quantitative analysis of the measured microstructures has shown that the number of Ag3Sn IMC particles decreased during aging, while the average diameter of the particles increased significantly. In particular, around 2.5 X increase in the

average particle diameter, and approximately a 2.3 X reduction in the total number of IMC particles during isothermal aging for 20 days at T = 125 °C were observed. However, the effects were more severe for aging at T = 150 °C where around 3.1X increase in average particle diameter, and approximately 3.5X reduction in the total number of IMC particles were observed over the aging duration of 20 days.

.

CHAPTER 9

EFFECT OF EXTREME HIGH TEMPERATURE ON THE MECHANICAL BEHAVIOR OF SAC305 BGA JOINTS USING NANOINDENTATION

9.1 Introduction

In this chapter, a high temperature stage and test protocols were used within the Hysitron TI950 nanoindentation system shown in Figure 3.24 to explore the mechanical behavior, and aging effects of SAC305 (96.5Sn-3.0Ag-0.5Cu) solder joints at several extreme high testing temperatures (T = 125, 150, 175, and 200 °C). The testing temperature within the high temperature stage was carefully controlled to make the measurements insensitive to thermal drift problems. Figure 3.20 in chapter 3 showed the BGA joints which were extracted from 14 x 14 mm PBGA assemblies (0.8 mm ball pitch, 0.46 mm ball diameter) that were built as part of the iNEMI Characterization of Pb-Free Alloy Alternatives Project. Since the properties of SAC BGA joints are highly dependent on crystal orientation, polarized light microscopy (Figure 3.23) was utilized to determine the orientation of the tested joints. For all of the experiments, only single grain solder joints were used to avoid introducing any unintentional variation from changes in the crystal orientation across the joint cross-section. To study the aging effects, solder joints were preconditioned for 0, 1, 5, 10, and 30 days at T = 125 °C in a box oven. Nanoindentation testing was then performed on the aged specimens at four different extreme high test temperatures (T = 125, 150, 175, and 200 °C) to extract the mechanical properties of the

aged material. Throughout this study, a constant force of 10 mN was applied for 900 seconds.

As expected, mechanical properties including effective modulus, and hardness were highly dependent on the test temperature and degrade significantly as the temperature increases. In addition, the effects of aging on mechanical response for SAC305 BGA joints become much more significant as the aging time and test temperature increases.

9.2 Sample Preparation for High Temperature Nanoindentation

The details of the sample cross sectioning using IsoMet 1000 Precision Cutter (Figure 3.21) and special polishing procedure (Figure 3.22) due to limited space inside the high temperature stage were outlined in section 3.8.1 in chapter 3. Since the mechanical behavior of solder alloys depends on crystal orientation, the orientation of the SAC305 BGA joints were initially determined using polarized light microscopy (Figure 3.23). Only single-grain solder joints were identified and used in this study to avoid any variation in properties associated with different crystal orientation. Figures 9.1 shows polarized light images of multi-grain and single grain solder joint samples.

Five different SAC305 BGA joints with single grain orientation and uniform IMC distributions were chosen used for the high temperature nanoindentation study. Of them, one joint was utilized for temperature study and remaining four joints were utilized for aging study.

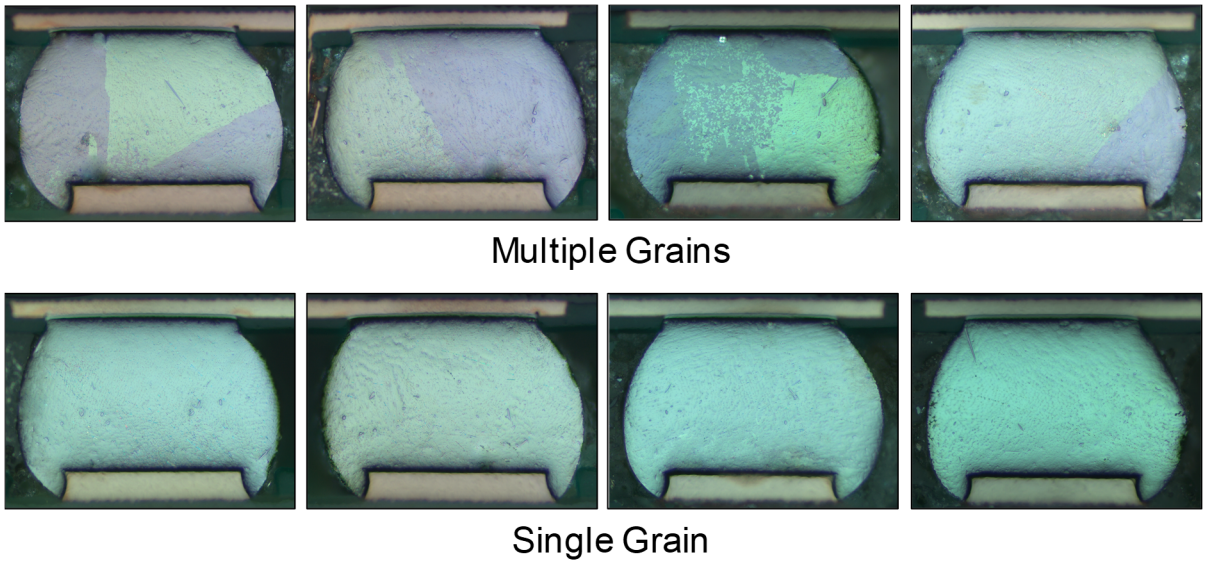

Figure 9.1 Multi-Grain and Single Grain SAC305 BGA Joint

9.3 High Temperature Nanoindentation System and Test Procedures

Section 3.8 showed the details of the nanoindentation testing and data processing system. In brief, Hysitron TI 950 nanoindentation system (Figure 3.240 with a Berkovich indenter tip has been used to perform the nanoindentation creep tests. A specially designed high temperature stage (xSOL 400) was used to perform indentation at extreme high test temperatures (T = 125, 150, 175, and 200 °C). Figure 9.2 shows the high temperature stage within the nanoindentation system, while Figure 9.3 shows images of a test sample in the high temperature stage. During each indentation experiment, load versus indentation displacement response of the solder material in the direction normal to the cross-sectional surface was measured.

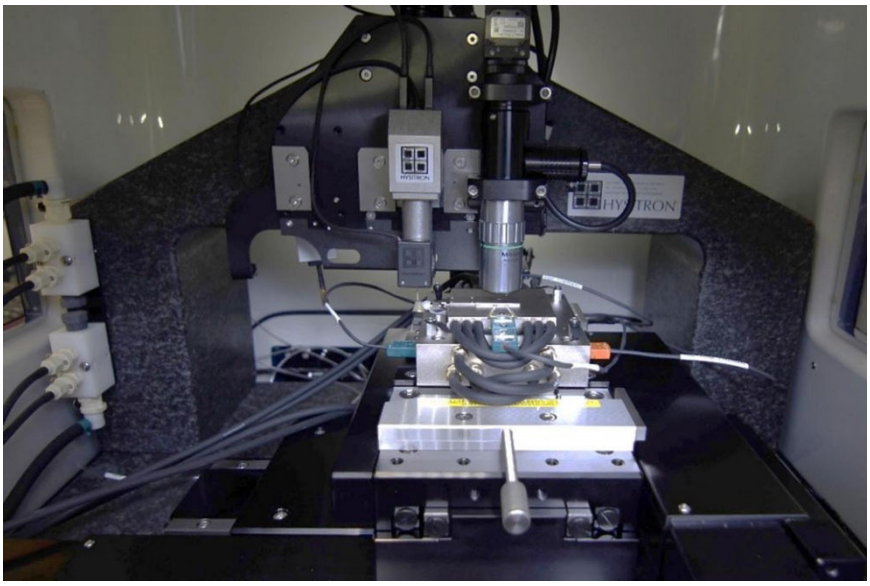

Figure 9.2 High Temperature Nanoindentation System

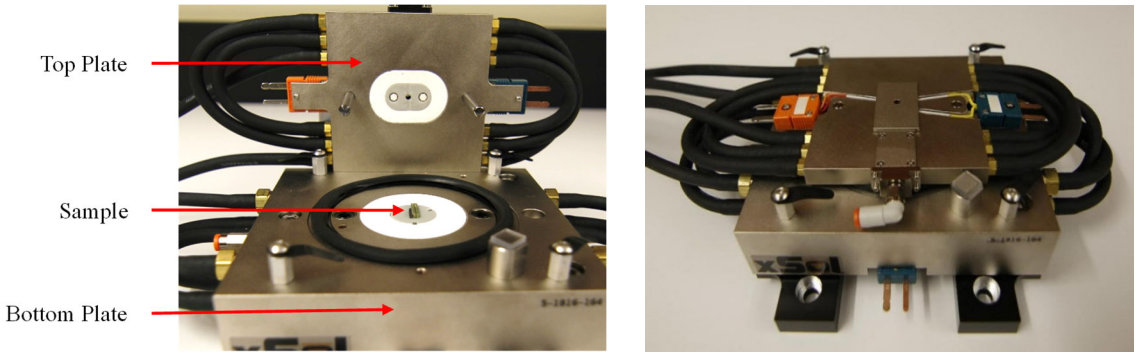

Figure 9.3 Solder Joint Sample in the High Temperature Stage

Figure 9.4 shows a Scanning Electron Microscopy (SEM) image of a typical permanent indentation mark after a nanoindentation experiment. About 5-8 indentations were performed at a particular test condition (e.g. temperature and prior aging), and the average results of all the indents were considered for comparison between different test conditions. The indents were made in 50-80 μm apart to avoid locations that were deformed plastically by the previous indents. As mentioned before, all tests in this work were performed on single grain (Sn crystal) solder joints, so that there were no orientation

effects caused by an indentation array covering two or more grain boundaries of grains with different crystal orientations.

Again, the indentation marks were ensured to cover all the available phases of the material as shown in Figure 7.4. Thus, the nanoindentation tests represents the global properties of the solder joints, instead of the localized mechanical properties of the phases (β-Sn dendrites or Ag_3Sn and Cu_6Sn_5 IMC particles). Calibration of the indenter tip shape was performed on a standard fused quartz sample.

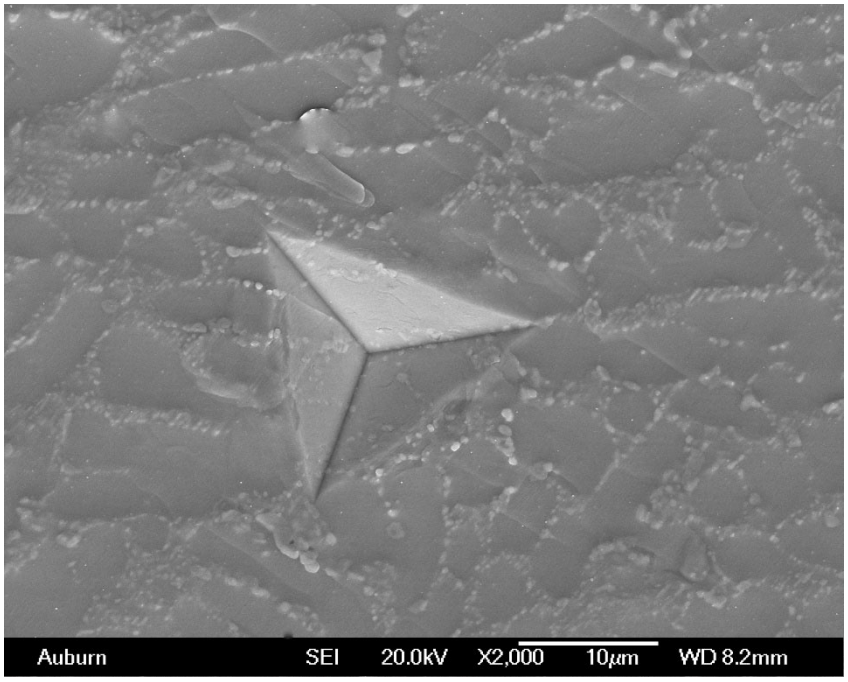

Figure 9.4 Permanent Indentation Mark after Testing

The maximum load of 10 mN was chosen for all the creep tests. Once the peak load reaches to 10 mN, the load was held constant for 900 sec. A load versus time graph for a single indentation test performed in this work is shown in Figure 9.5. As shown, a small sinusoidal load was introduced with the static load of 10 mN during the start of the dwell period.

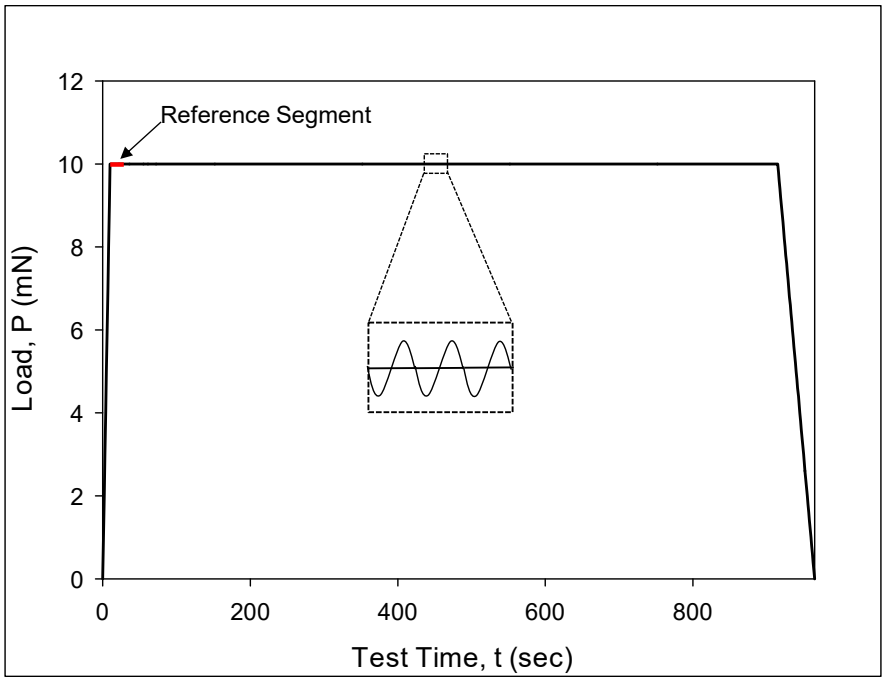

Figure 9.5 Loading Profile Used for Nanoindentation Creep Tests

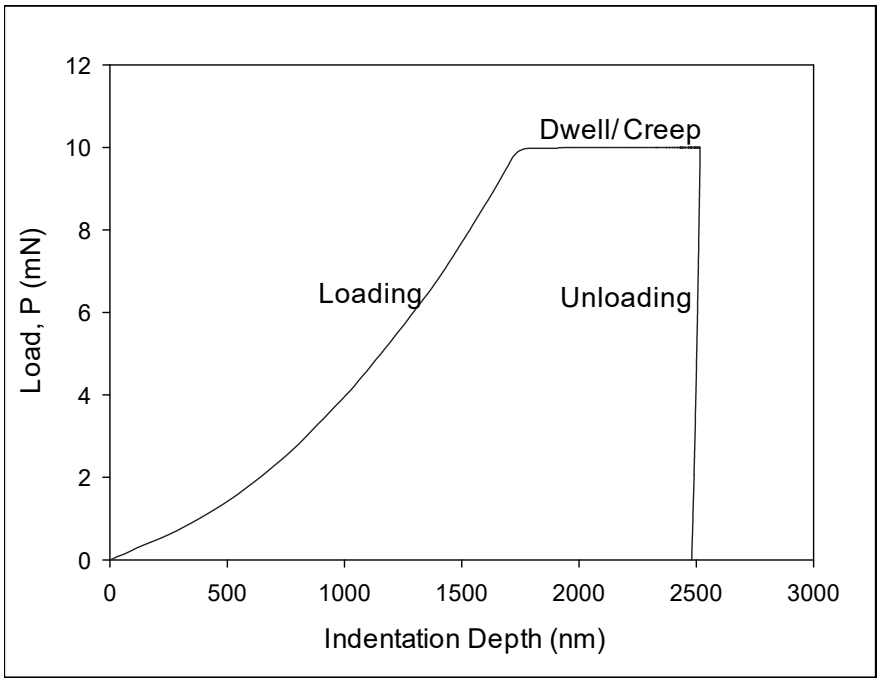

Figure 9.6 Load-Displacement Curve Obtained from a Nanoindentation Creep Test

Thermal drift has negligible effects in the beginning at constant load during dwell time. Therefore, a "reference segment" of 5 sec duration was introduced at the beginning of the creep deformations. During this reference segment, modulus of the material was

calculated from the indentation displacements, which was utilized later to calculate the total area of indent, making the tests quite unaffected by thermal drift problems. Thus, the reference segment makes the experiments relatively insensitive to thermal drift problems. An example of a load vs. indent displacement graph obtained after a nanoindentation creep test is shown in Figure 9.6.

9.4 Pile-up Correction for High Temperature Nanoindentation Tests

Theoretically, pile-up is defined as the accumulation of material near the edges of an indent during indentation test. Figure 9.7 shows a pile-up effect that was observed in the high-temperature tests from the 3D SPM image of a single indent on SAC305 BGA joint.

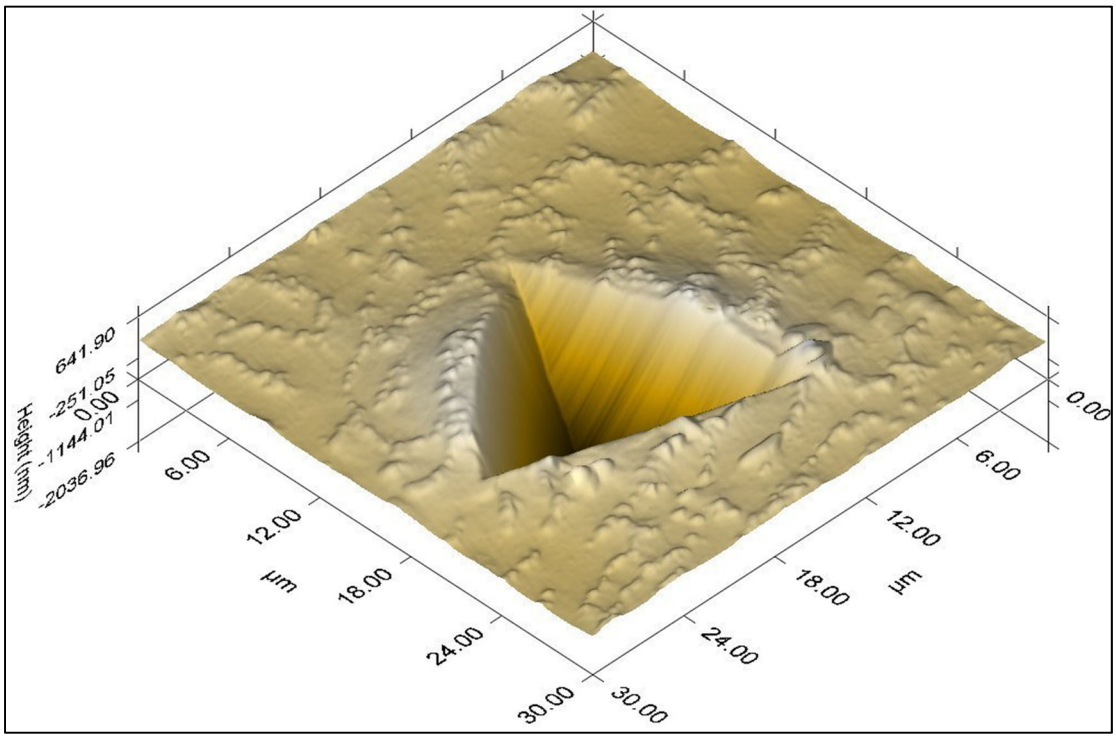

Figure 9.7 3D SPM Image of a Single Indent

The semi-ellipse method for pile-up correction proposed by Kese, et al. [150] was used here to adjust our nanoindentation creep data. According to this method, the corrected contact area A is given by:

$$A = A_{OP} + A_{PU} = A_{OP} + 5.915 h_c \sum_{i=1}^{3} a_i \tag{9.1}$$

where A_{OP} is the contact area obtained from the normal calculations based on the tip shape, A_{PU} is the additional pile-up area, h_c is contact depth, and a_i (i = 1, 2, 3) are the height of pile-ups mid-way along the three edges. In this investigation, A_{OP} and h_c were obtained from the normal indentation results reported by the system. In order to determine a_i, the profile of each indent was scanned using SPM imaging. A sample of the topographic SPM image obtained for one typical indent and the location of a_i is shown in Figure 9.8. The surface profile was measured along three different sections as shown in Figure 9.9 to determine the value of a_i along each edges.

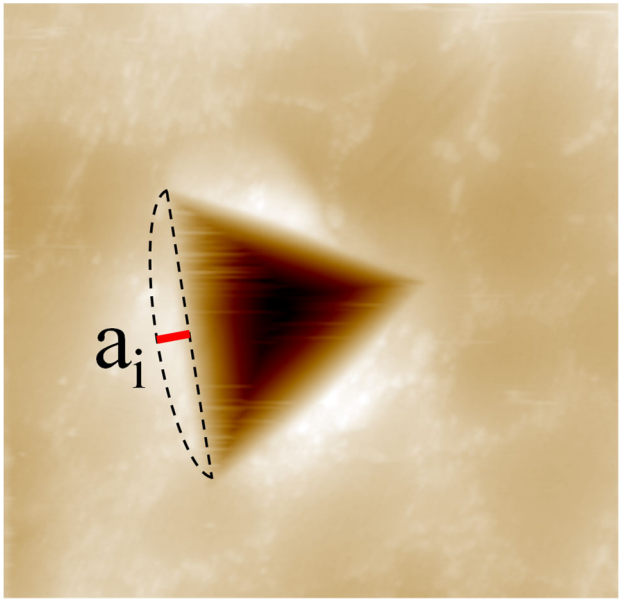

Figure 9.8 2D SPM Topography Data for a Single Indent

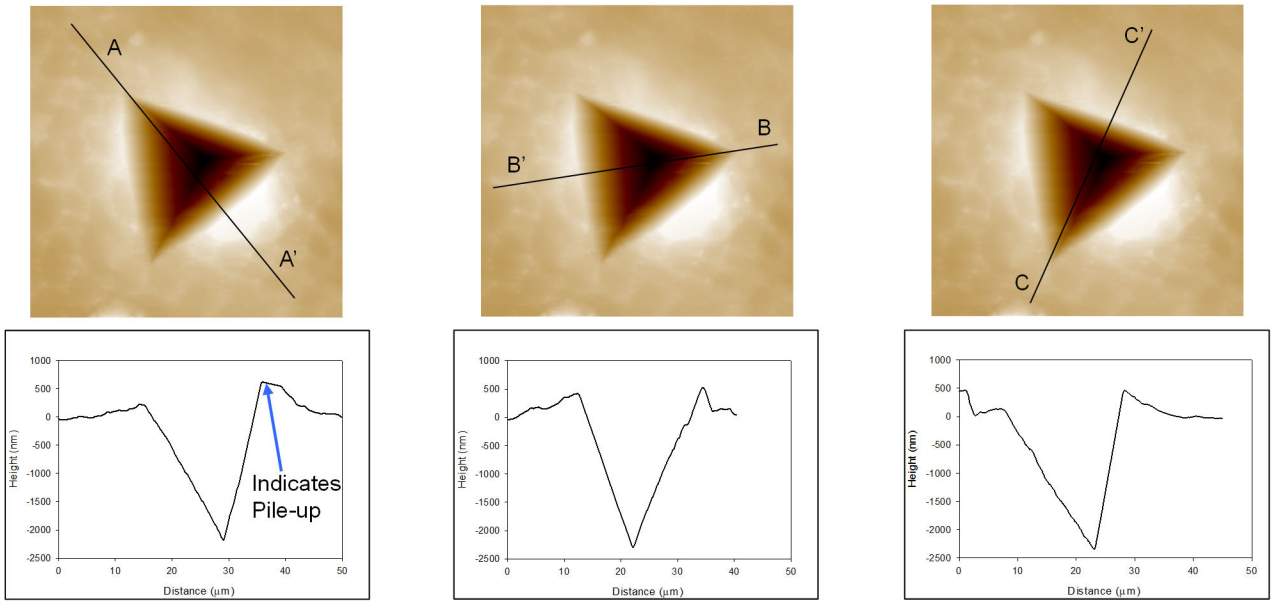

Figure 9.9 SPM Topography Data for a Single Indent and Pile-up Measurement

9.5 High Temperature Nanoindentation Test Matrix

In this study, high temperature tests were performed by placing cross-sectioned and polished single grain solder joint samples into the heating chamber mounted within the nanoindentation system. The test sample set consisted of five single crystal SAC305 BGA joints. One joint was used to study only the effect of test temperatures while the rest 4 joints were used to study the combined effect of aging time and test temperatures on the creep properties. The first study involved investigation of the effect of test temperature on the mechanical properties of SAC305 solders. Four different test temperatures (T = 125, 150, 175, and 200 °C) were explored on a single grain joint. For each aging condition and temperature, 6-7 indentations were performed. In the second study, the effect of high temperature aging was explored. For each tested joint and temperature, five unique sets of aging conditions are being explored: no aging; and 1, 5, 10, and 30 days of prior aging at T = 125 °C. Before prior aging, a series of indents were made on 4 single grain SAC305

solder joints at 4 different test temperatures. In this case, test temperature for each joint was kept constant and indents were made at different aging time. After having the initial series of indents in no aging condition, all the joints were kept inside an oven at 125 °C for 1 day. After removing the samples from the aging oven, another series of indents (1 day aging) were made on each joint and then kept them back for the next aging cycle.

9.5.1 Effects of Test Temperature on Mechanical Response

Using the nanoindentation test methods described in the above sections 9.2-9.4, the effect of test temperatures on the indentation size, indentation load vs. indentation size depth, and mechanical properties, such as, effective modulus, and hardness of SAC305 BGA joints were explored using the nanoindentation system. At a particular test temperature, a series of 6-7 indents were made with a maximum load of 10 mN for 900 seconds as shown in Figure 9.10. In this figure, different rows of indents represents different test temperature, with top row representing 125 °C test temperature and bottom row representing 200 °C test temperature. As seen from Figure 9.10, the size of indent increases with increase in test temperature inside the high temperature stage of the indentation system.

Figure 9.11 shows the applied load vs. indentation depth curves obtained at different test temperatures from indentations shown in Figure 9.10. In this figure, the various colored curves representing the different extreme high test temperatures with blue = 125 °C, green = 150 °C, orange = 175 °C, and red = 200 °C. As expected, the indentation depth increased significantly as test temperature increases for a constant load of 10 mN.

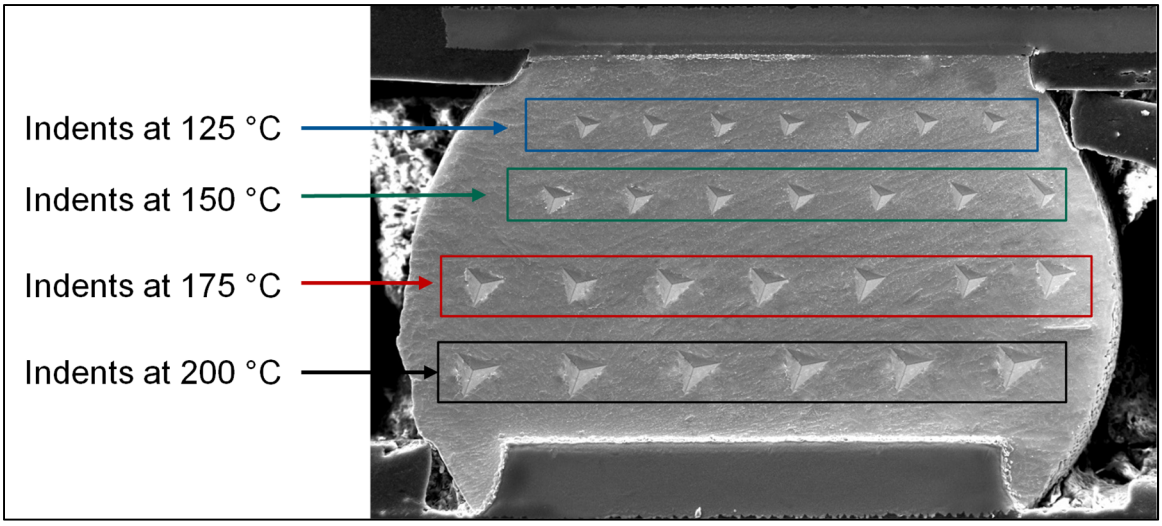

Figure 9.10 SAC305 BGA Joint after Nanoindentation Test at Different Temperatures

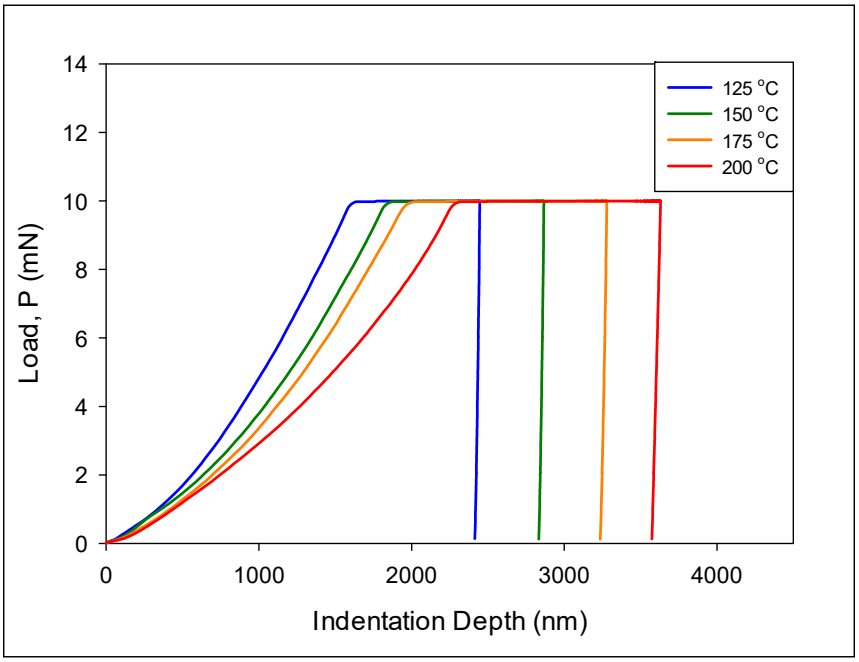

Figure 9.11 Variation of Nanoindentation Load vs. Indentation Depth at Various High Test Temperatures

Utilizing the methods discussed in section 3.8.3 the temperature dependent mechanical properties, such as, effective modulus, and hardness of SAC305 BGA joints were extracted from the extreme high temperature nanoindentation test and the numerical values are listed in Table 9.1.

Table 9.1 Variation of Properties of SAC305 BGA Joint with Testing Temperature

Test Temperature (°C)	Hardness (MPa)	Effective Modulus (GPa)
125	65.5	41.1
150	52.8	27.8
175	41.5	18.8
200	35.5	12.6

The properties (effective modulus, and hardness) were plotted as a function of test temperature as shown in Figures 9.12, and 9.13. As expected, both the mechanical properties of SAC305 BGA joint decreased significantly with temperature. Approximately 69% drop in effective modulus, and 46% drop in hardness occurred during testing for various temperatures between 125 to 200 °C.

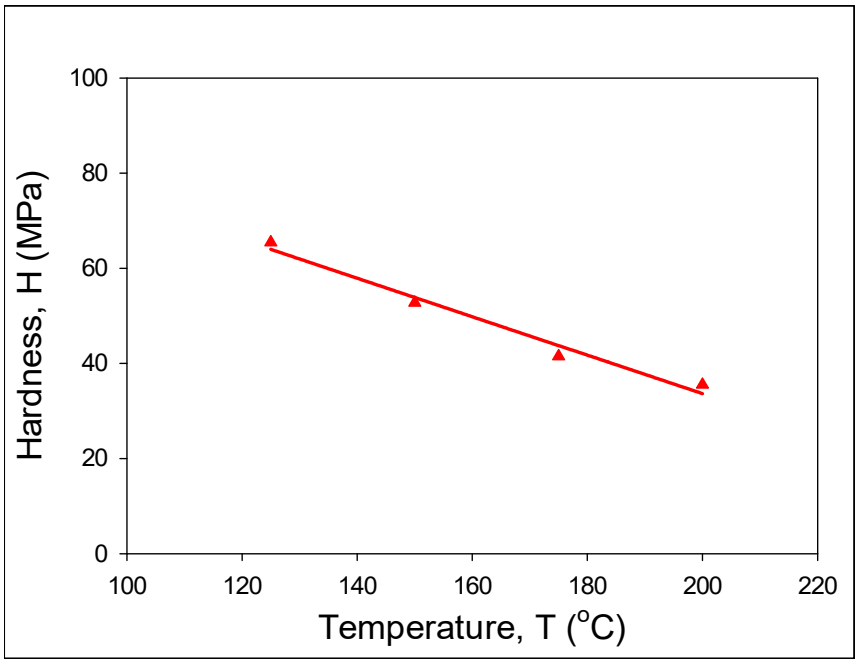

Figure 9.12 Variation of Hardness with Temperature (No Aging)

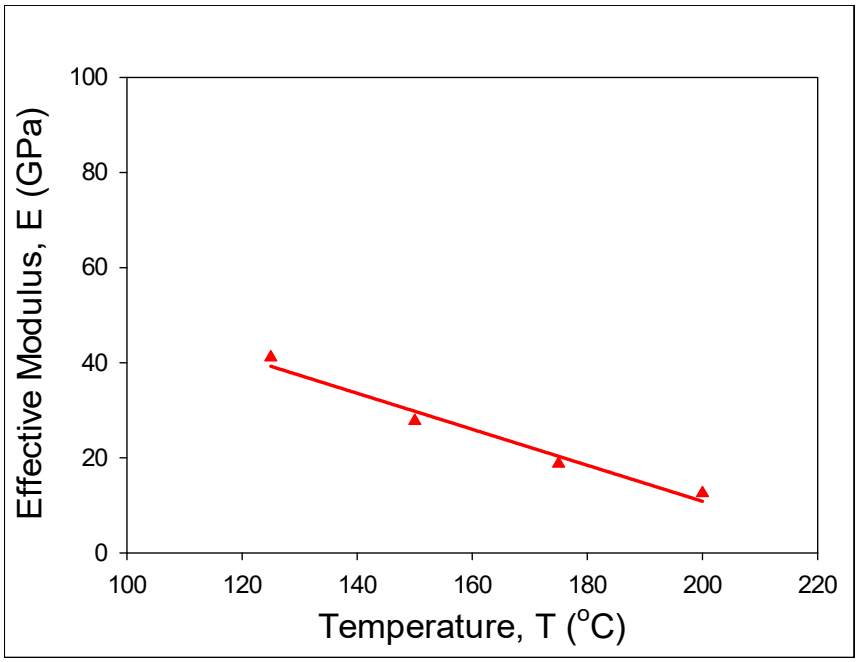

Figure 9.13 Variation of Effective Modulus with Temperature (No Aging)

9.5.2 Effects of Isothermal Aging on Mechanical Response

In this study, four different single grain SAC305 BGA joints were used to explore the isothermal aging effects in mechanical response. In particular, aging was done at 125 °C for different durations including 0, 1, 5, 10, and 30 days and four different test temperatures (T = 125, 150, 175, and 200 °C). Images of the four single grain solder joints after performing indentation experiments at four different test temperature and five different aging conditions are presented in Figure 9.14. The row of indents on the top of each joint were obtained in no aging condition while the row of indents at the bottom of each joint were obtained after 30 days of aging at 125 °C.

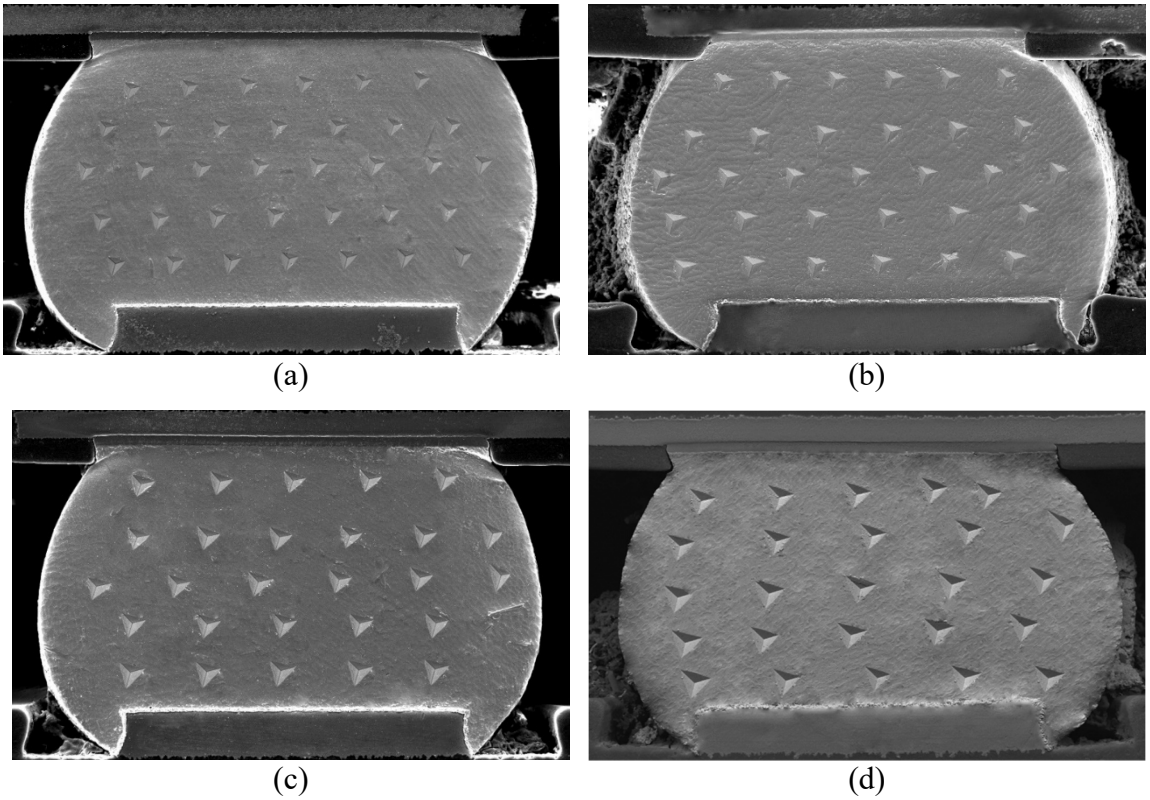

Figure 9.14 Indents on SAC305 BGA Joints at Different Aging Conditions Obtained at (a) 125 °C, (b) 150 °C, (c) 175 °C, and (d) 200 °C

Temperature and aging dependent applied load vs. indentation depth of SAC305 BGA joints are shown in Figure 9.15. In these Figures, each of the four plots for different test temperatures illustrates the response at different aging condition by the various colored curves, such as, no aging = blue, 1 day aging = 5 days aging, 10 days aging = red, and 30 days aging = dark red of isothermal aging at T = 125 °C.

As expected, the indentation depth increased significantly as test temperature increases for a constant load of 10 mN. Again, it was observed that the indentation depth increased with the progression of aging from no aging to 30 days of aging at T = 125 °C.

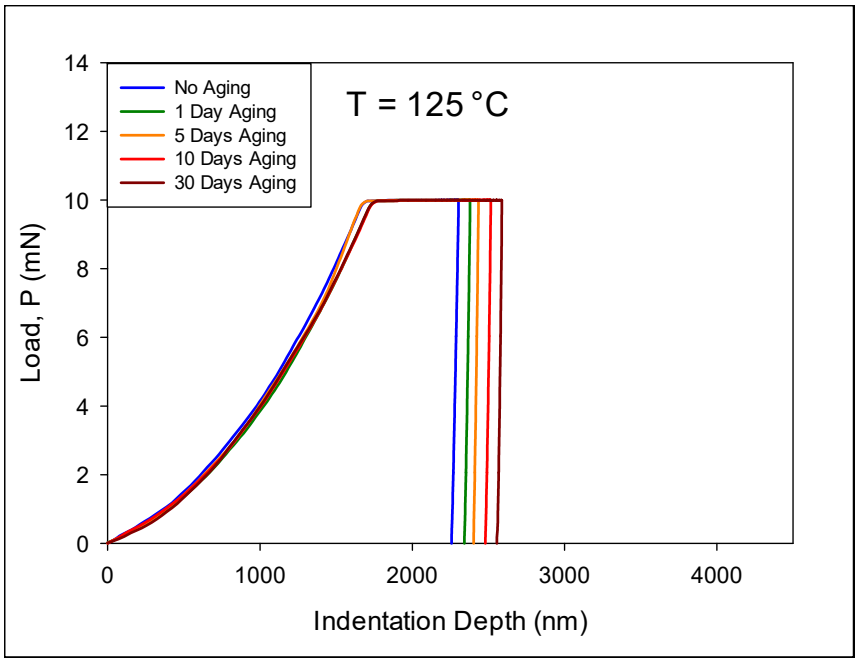
No Aging
1 Day Aging
5 Days Aging
10 Days Aging
30 Days Aging
T = 125 °C
Load, P (mN)
Indentation Depth (nm)
0
2
4
6
8
10
12
14
0
1000
2000
3000
4000

(a)

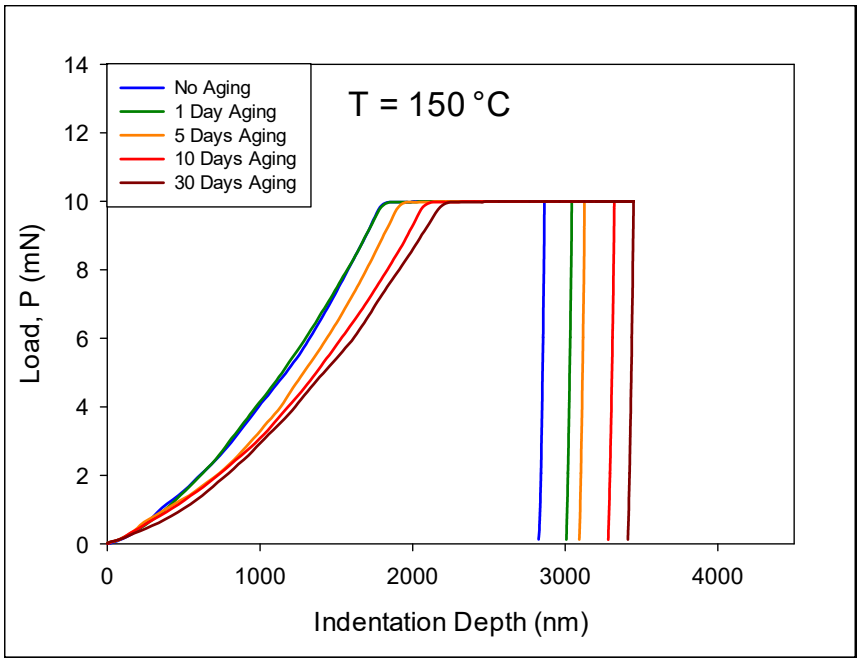
No Aging
1 Day Aging
5 Days Aging
10 Days Aging
30 Days Aging
T = 150 °C
Load, P (mN)
Indentation Depth (nm)
0
2
4
6
8
10
12
14
0
1000
2000
3000
4000

(b)

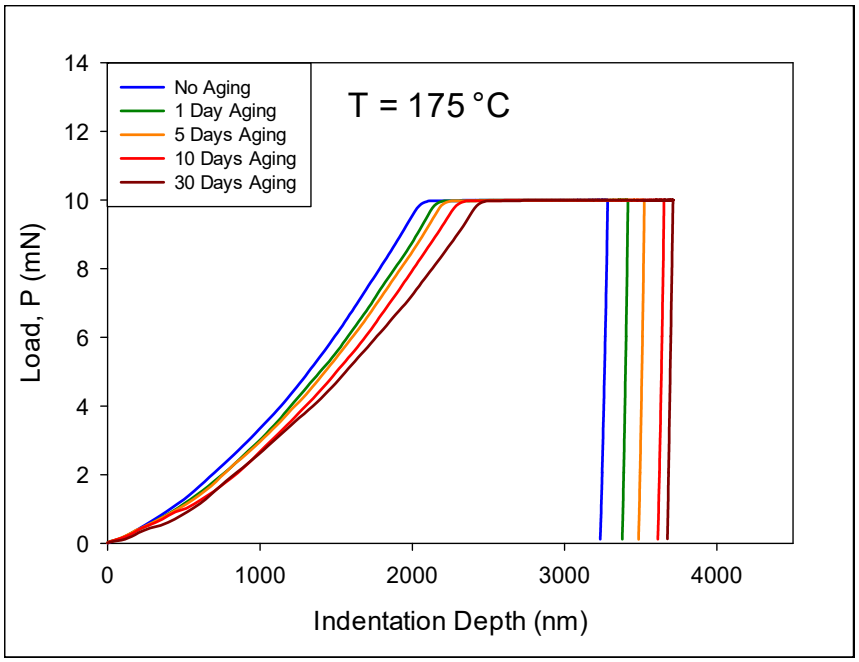

(c)

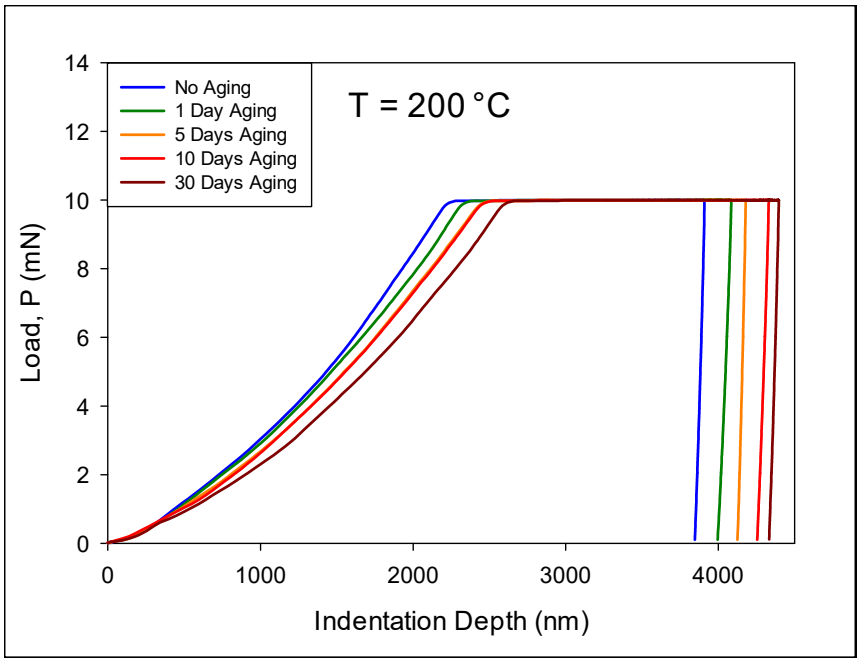

(d)

Figure 9.15 Applied Load vs. Indentation Depth Curves at Different Aging Time

Again, by utilizing the methods discussed in section 3.8.3 the temperature and aging dependent mechanical properties, such as, effective modulus, and hardness of SAC305

BGA joints were extracted from the extreme high temperature nanoindentation test and the numerical values are listed in Table 9.2, and plotted in Figures 9.16, and 9.17.

Table 9.2 Variation of Properties of SAC305 BGA Joint with Aging Time

Test Temperature (°C)	Aging Time (Days)	Hardness (MPa)	Effective Modulus (GPa)
125	0	78.1	41.6
	1	63.4	35.7
	5	61.9	33.1
	10	59.9	31.9
	30	58.2	29.1
150	0	47.8	28.7
	1	45.8	27.2
	5	44.4	26.4
	10	42.8	24.6
	30	40.9	23.8
175	0	36.6	20.2
	1	34.8	18.8
	5	33.3	18.3
	10	32.6	17.1
	30	32.1	16.0
200	0	27.3	11.4
	1	25.7	9.9
	5	24.9	9.6
	10	23.9	8.4
	30	22.6	8.3

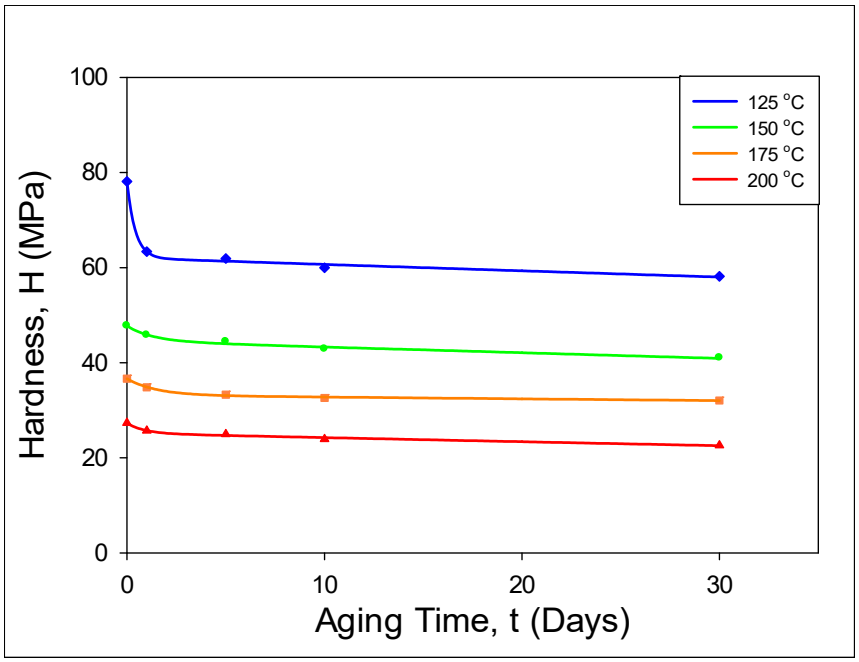

Figure 9.16 Variation of Hardness with Aging Time (Aging at T = 125 °C)

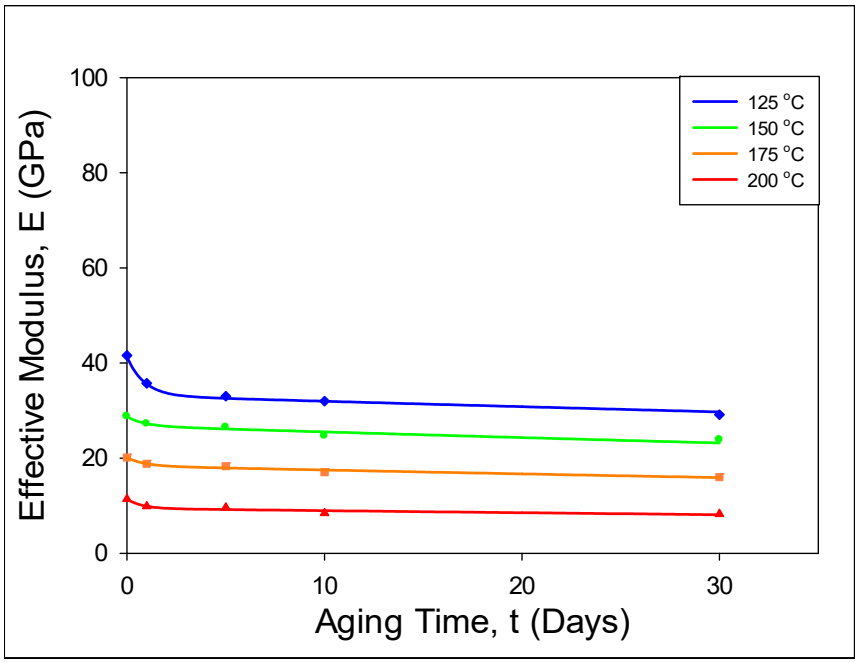

Figure 9.17 Variation of Effective Modulus with Aging Time (Aging at T = 125 °C)

9.6 Correlation of IMC Particle Evolution and Mechanical Property Degradation

The growth of IMC particle size with the progression of isothermal aging were discussed in section 8.5.1 in chapter 8 for two different aging temperature at T= T = 125, and T = 150 °C. This coarsening and coalescing of IMC particles during aging is known to play a critical role in the degradations of solder mechanical properties. IMC particles will pin and block the movement of dislocations. However, aging leads to both a smaller number of larger IMC particles, and increased spacing between the particles. This results in dislocations being able to pass more easily through the material, decreasing both the yield stress and strength. The Correlations between the reductions in effective modulus and the increase in IMC particle diameter are shown in the same graph in Figure 9.18.

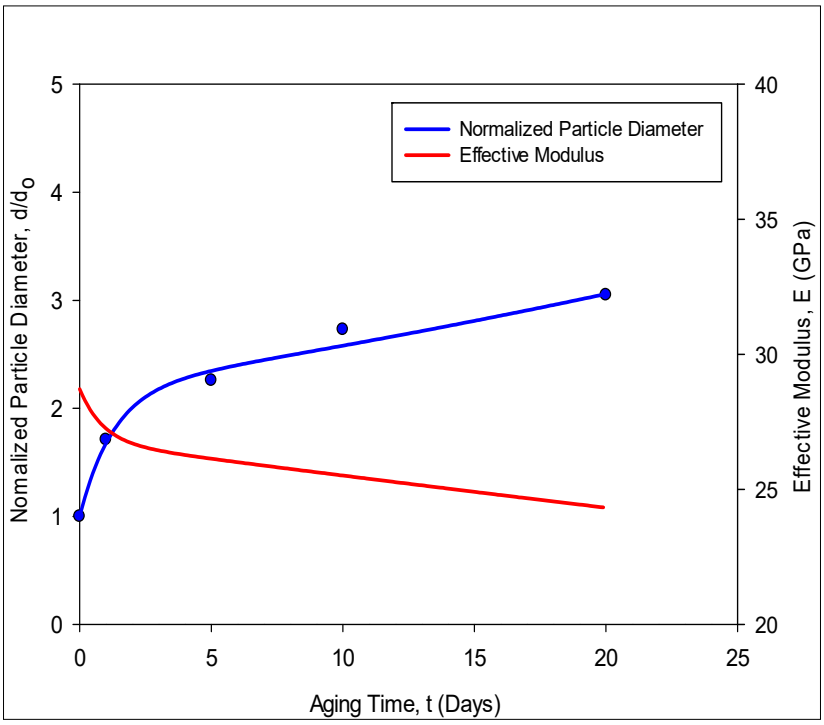

Figure 9.18 Effect of Aging on IMC Particle Diameter and effective Modulus for SAC305 BGA Joints

Here, effective modulus was used as an example of mechanical property degradation with the progression of aging. Values of aging dependent (aging at T = 125 °C) effective modulus at 125, and 150 °C test temperatures were used for comparison. It is clear that the degradation of the mechanical property (effective modulus) of the solder alloy is closely linked to variation in the IMC particle diameter.

9.7 Summary and Discussion

In this chapter, nanoindentation technique was used to explore the effect of test temperature and isothermal aging on the mechanical response of SAC305 BGA joints. The overall objective was to study the aging dependent mechanical behavior of SAC305 BGA joints at extreme high temperatures (T= 125, 150, 175, and 200 °C) and correlate with the IMC particle evolution presented in chapter 8. Nanoindentation creep tests were performed on SAC305 BGA joints at different test temperatures, and temperature dependent mechanical properties, such as effective modulus, and hardness were recorded. In addition, Effect of high temperature aging on these properties have been explored. Before testing, four different solder joints were aged (preconditioned) at the high temperature (aging at T = 125 °C), and several different durations of aging were considered (no aging, and 1 day, 5 days, 10 days, and 30 days of aging). Nanoindentation tests were then performed on these aged specimens, and aging induced degradation of mechanical properties were recorded. A special high temperature test system was used to control the test temperature, and avoid any thermal drift occur during the high temperature tests. To avoid any variation in the mechanical properties due to grain orientation variation, SAC305 BGA joints with single grain crystal structure were chosen for this study.

Experimental measurements showed that the mechanical response of SAC305 BGA joints are highly sensitive to test temperature. Mechanical properties, such as, elastic modulus, and hardness degraded significantly with the increase in temperatures. This degradations were more severe when specimens were preconditioned with aging at T = 125 °C for different durations. At a fixed temperature, the effective modulus and hardness decreases with increasing aging time. Most significant degradation occurred from no aging to 1 days of aging at T = 125 °C. After that, still the degradation continued but with a much slower rate. Finally, the time dependent evolution of the microstructure was compared to the degradation in the modulus during aging, and good correlation was observed.

CHAPTER 10

CONCLUSIONS

10.1 Literature Review

With the emergence of the modern electronic packaging technology over the last few decades, solder alloys have been the primary interconnect material used in electronic packaging. The mechanical properties of a solder are strongly influenced by its microstructure, which is controlled by its thermal history including its solidification rate and thermal exposures after solidification. Aging of lead free solders leads to degradations in their constitutive and failure behaviors. For example, research in the literature has shown that aging leads to large reductions in solder material properties including shear strength, effective modulus, nanoindentation joint modulus and hardness, high strain rate mechanical behavior, creep response, and Anand model parameters. Other studies have shown that aging causes severe degradations in uniaxial cyclic stress-strain curves and fatigue life, shear cyclic stress-strain curves and fatigue life, fracture behavior, drop reliability, and thermal cycling reliability.

Finite element reliability prediction models were found to be highly sensitive of choosing appropriate mechanical properties. Finite element results such as plastic work per cycle (delta W) were found to be very sensitive of different input parameters. Therefore, proper reliability prediction largely depends on the use of correct input parameters during modeling different failure criteria.

Adding small amount of dopants have been found to strongly influence the properties and behaviors of lead free solders. For Example, Bi can improve the wetting ability and reduce melting temperature of lead free solder alloys. Not only that but also, it can increase strength by means of precipitation hardening, reducing IMC (Intermetallic Compound) layer thickness, and therefore, it can reduce the aging induced degradation of mechanical properties in lead free solder materials. Ni helps to improve thermal fatigue life and drop test performance by refining Sn grain size and reducing the IMC layer formation near the Cu pad. The effects of rear earth (RE) elements and nanoparticle addition on the properties of lead free solder was also discussed in this chapter.

One of the recent techniques, known as nanoindentation has shown a great potential for characterizing solder materials and aging effects at the joint scale. Nanoindentation is mainly used to extract elastic modulus and hardness of solder joints. Some of the prior works have also used nanoindentation technique to characterize the creep properties although most of the nanoindentation experiments, on solder joints, were conducted at room temperature.

The changes in solder mechanical behavior are a result of the evolution of the SAC solder microstructure that occurs during aging. The most well-known and widely observed changes are coarsening of the Ag_3Sn and Cu_6Sn_5 intermetallic compounds (IMCs) present in the eutectic regions between beta-Sn dendrites. Several researchers have proposed empirical models to describe the growth of these secondary phase particles as a function of aging temperature and aging time, and related this growth to mechanical property changes.

10.2 Experimental Procedure, data Processing and Constitutive Modeling

All the experimental procedures, raw data processing, and constitutive modeling used to fit the experimental results were presented in chapter 3. Micro-scale uniaxial tensile specimens

were prepared in a rectangular shaped hollow glass tube using a unique technique known as vacuum suction method followed by an industry standard SMT reflow process. Typical dimension of the uniaxial tensile specimens were 80 (length) x 3 (width) x 0.5 (height) mm. Uniaxial tensile tests were performed using a micro tension torsion testing system. Nanoindentation experiments and a part of microstructural study were conducted on actual SAC305 BGA joints extracted from 14 x 14 mm PBGA assemblies (0.8 mm ball pitch, 0.46 mm ball diameter). Nanoindentation experiments were performed using Hysitron TI950 Triboindenter and Zeiss crossbeam 550 scanning electron microscopy (SEM) was used for microstructural study to explain the physics behind mechanical property evolution.

10.3 Finite Element Prediction of the Influence of Poisson's Ratio on the Reliability of SAC Lead free Solder Joints

In the current work, it has been extended the previous research on the effects of aging on lead free solder material behavior to explore the effects of prior aging on solder joint (board level) reliability in actual assemblies. The overall objective was to develop new reliability prediction procedures counting the influence of solder joint Poisson's ratio in finite element modeling to investigate its effect on reliability. The developed reliability modeling procedure has been applied to a family of assembled PBGA components. In the simulations, the packages were subjected to thermal cycling between -40 to +125 ^{o}C.

From the finite element results presented in chapter 4, the value of the input Poisson's ratio specified in the FEA simulation affected the results for both the plastic work per cycle and the cycles to crack initiation considerably. The variations in the plastic work per cycle for different Poisson's ratio values were ~22% for the 15 mm BGA, ~23% for the 10 mm BGA, and ~27% for

the 5 mm BGA. The effect was more significant in terms of the reliability. For the predicted cycles to crack initiation, the variations for different Poisson's ratio values were ~33% for the 15 mm BGA, ~34% for the 10 mm BGA, and ~38% for the 5 mm BGA. In summary, the finite element simulation results have demonstrated that for specified values of $0.15 < \nu < 0.40$, the solder plastic work varied over 25% and the predicted reliability varied approximately 40% when using a Morrow-Darveaux energy-based fatigue model. Thus, the FEA results are highly sensitive to the specified value of the solder Poisson's ratio, so that it is important to carefully characterize the Poisson's effect in lead free solders.

10.4 Experimental Characterization of the dependence of Poisson's ratio of Lead Free Solder on Temperature, Strain Rate, Solidification Profile and Isothermal Aging

In this work, experimental investigations were conducted to characterize the Poisson's ratio of several SAC and SAC+X lead free solders. Uniaxial tensile stress-strain tests were carried out on SAC305 (96.5Sn3.0Ag0.5Cu), SAC405 (95.5Sn4.0Ag0.5Cu), Innolot (SAC+3% Bi), and SAC_Q (SAC+3% Bi) specimens using a micro tension/torsion testing machine with two strain rates (0.0001, and 0.00001 (sec^{-1})) and four testing temperatures (T = 25, 50, 75, 100 ^{o}C). Deformations and strains in the axial and transverse directions were measured using miniature strain gages with automatic data acquisition from LabVIEW software. The recorded transverse strain vs. axial strain data for each test were then fit with a linear regression analysis to determine the Poisson's ratio value.

A large test matrix of experiments was developed to study the effects of temperature, strain rate, alloy composition, solidification cooling profile, and isothermal aging exposure on the value of solder Poisson's ratio; and to create a material property database for finite element simulations.

The Poisson's ratio was found to increase significantly (15-25%) with increasing temperature. It was also found to decrease with increasing strain rate, alloy silver content, and cooling rate after solidification. Finally, the microstructural coarsening that occurs during isothermal aging led to an increase in the Poisson's ratio (up to 15% increase with one day of aging). Considering all of the possible branches of the test matrix (temperatures, strain rates, prior aging conditions, and microstructure), the value of the Poisson's ratio of SAC305 ranged from $0.31 < \nu < 0.44$. Similarly, the Poisson's ratio of SAC405 ranged from $0.28 < \nu < 0.42$, and the Poisson's ratio of Innolot and SAC_Q ranged from $0.27 < \nu < 0.38$, and $0.26 < \nu < 0.37$ respectively. Overall, the SAC_Q alloy had the lowest PR values for all temperatures, strain rates, solidification profiles, and durations of aging.

10.5 Mechanical Behavior and Reliability of SAC+Bi Lead Free Solders with Various Levels of Bismuth

In this chapter, study the mechanical behavior, and reliability of several different SAC+Bi alloys with various levels of Bismuth were studied. The overall goal was to identify optimal SAC+Bi alloy compositions for various applications and usage environments. The alloys considered were based on SAC405, with various levels of Sn replaced by Bi. The percentages of Bi considered include 1.0%, 2.0%, and 3.0%. To examine base mechanical behavior, uniaxial tensile tests were performed using rectangular cross-section samples prepared from vacuum suction method and SMT reflow oven. Tests were performed for each new SAC+Bi alloy with three strain rates (0.001, 0.0001, and 0.00001 (sec^{-1})), and five different testing temperatures (T = 25, 50, 75, 100, and 125 ^{o}C).

Experimental results showed that severe degradations of the mechanical properties (initial modulus, ultimate tensile strength) occur in SAC+Bi doped alloys during high temperature testing. Approximately, 40-50% drop in strength and modulus occurred between T = 25 °C and T = 125 °C testing for various strain rates and test temperatures. Comparing with the conventional SACN05 (N = 1, 2, 3, 4) lead free alloys, experimental results showed that solder alloys with Bi content showed better mechanical properties both at room temperature, T = 25 °C (SAC+3% Bi showed approximately 70% better strength than SAC305, whereas, SAC+1% Bi showed around 53% better property than SAC305), and at high temperature, T = 125 °C (SAC+3% Bi showed approximately 83% better strength than SAC305, and, SAC+1% Bi showed around 26% better property than SAC305). As the Bi content decreased their strength also decreased correspondingly.

The Anand parameters were calculated for each SAC+Bi alloy from the stress-strain data, and then the parameters were used to predict the stress-strain curves. For all cases, only very minor differences were seen between the model predictions and the experimental results. Due to these good correlations, the applicability of the Anand model for a wide range of temperatures and strain rates was confirmed.

To investigate the effect of isothermal aging, the specimens were aged (preconditioned) at T = 125 °C for several durations of aging including 0, 1, 5, and 20 days. From the results of mechanical testing and microstructural analysis, it was found that the SAC+Bi alloys demonstrated superior resistance to aging effects relative to SAC305. The coarsening of the IMC particles is much larger in the SAC305 alloy relative to all three SAC+Bi alloys. In addition, the growth rate is reduced as the percentage of Bi in the alloy is increased. Bi contributes to enhancement in strength of the SAC+Bi doped alloys by the solid solution strengthening mechanism. In addition,

the Bi in solution has been shown to reduce the diffusion rate during Ostwald ripening of the IMC particles.

10.6 Isothermal Aging Dependent Mechanical Response and Anand Model Parameters of SAC305 Solder at Extreme High temperatures

In this work, a detailed study of the aging dependent mechanical behavior of SAC305 lead free solder alloy at extreme high temperatures (T= 125, 150, 175, and 200 °C) were investigated at three different strain rates (0.001, 0.0001 and 0.00001 sec^{-1}). Before testing, the solder uniaxial specimens were aged (preconditioned) at the extreme high temperature of T = 125 °C ,and several different durations of aging were considered (no aging, and 1 day, 5 days, and 20 days of aging). Uniaxial tests were then performed on the samples and average stress-strain curves were generated using 8 to 10 tests for each condition. Utilizing the recorded data mechanical properties like effective modulus, yield stress, and ultimate strength were determined to show the evolution of mechanical properties as a function of aging time and temperature for various strain rates.

Experimental measurements showed severe degradations in the mechanical properties (effective modulus, yield stress, and ultimate tensile strength) of SAC305 during extreme high temperature aging and testing. Approximately, 40-60% drop in strength and modulus occurred between T = 125 °C and T = 200 °C testing for various strain rates and aging duration. Most severe changes occurred for non-aged to 1 day aging, after that the rate became slower. Linear variations in the properties with temperature were observed. By comparing the analogous results for the same temperature and alloy, but different strain rates, it has also been observed that as the strain rate decreases, the effective elastic modulus, ultimate tensile strength, and yield stress also decrease.

Results from the uniaxial tensile tests were used to determine the Anand parameters for all the conditions mentioned before. From the numerical values, significant changes (approximately 30-40%) were found in some of the Anand parameters like m, h_o, s_o, and $\hat{s}$. These parameters were used to predict the stress-strain behavior of the corresponding solder alloy. The experimental results and the model predicted results were compared. A good correlation was found between Anand model predicted and experimentally obtained results. The correlation of experimental results with Anand model prediction shows a very small difference (< 10% in most conditions), thus, confirming the applicability of the model for a wide range of temperatures and strain rates.

10.7 Visualization and Modeling of Microstructural Evolution in SAC305 BGA Joints during Extreme High Temperature Aging

In this study, the microstructural evolution of SAC305 BGA joints was investigated for different aging conditions. In particular, aging was performed at T = 125, and 150 °C for 0, 1, 5, 10, and 20 days. The primary reason behind the degradation of mechanical behavior of different solder alloys during prolonged storage at elevated temperature is microstructural evolution. As found from prior studies, the microstructure of SAC305 is primarily composed of a β-Sn matrix and Ag3Sn and Cu6Sn5 intermetallic compounds (IMC). The degradations of mechanical properties like modulus and strength occur mainly due to coarsening of the Ag3Sn and Cu6Sn5 IMC particles, which reduces their ability to block dislocation movements.

From the experimental time lapsed micrographs, a significant amount of copper diffusion in the β-Sn matrix have been visualized. In addition, growth of the Cu6Sn5 IMC layer was visualized and measured as a function of aging time at the solder joint to PCB copper pad interface. Quantitative analysis of the measured microstructures has shown that the number of Ag3Sn IMC

particles decreased during aging, while the average diameter of the particles increased significantly. In particular, around 2.5 X increase in the average particle diameter, and approximately a 2.3 X reduction in the total number of IMC particles during isothermal aging for 20 days at T = 125 °C were observed. However, the effects were more severe for aging at T = 150 °C where around 3.1X increase in average particle diameter, and approximately 3.5X reduction in the total number of IMC particles were observed over the aging duration of 20 days.

10.8 Effect of Extreme High Temperature on the Mechanical Behavior of SAC305 BGA Joints Using Nanoindentation

In this chapter, nanoindentation technique was used to explore the effect of test temperature and isothermal aging on the mechanical response of SAC305 BGA joints. The overall objective was to study the aging dependent mechanical behavior of SAC305 BGA joints at extreme high temperatures (T= 125, 150, 175, and 200 °C) and correlate with the IMC particle evolution presented in chapter 8. Nanoindentation creep tests were performed on SAC305 BGA joints at different test temperatures, and temperature dependent mechanical properties, such as effective modulus, and hardness were recorded. In addition, Effect of high temperature aging on these properties have been explored. Before testing, four different solder joints were aged (preconditioned) at the high temperature (aging at T = 125 °C), and several different durations of aging were considered (no aging, and 1 day, 5 days, 10 days, and 30 days of aging). Nanoindentation tests were then performed on these aged specimens, and aging induced degradation of mechanical properties were recorded. A special high temperature test system was used to control the test temperature, and avoid any thermal drift occur during the high temperature

tests. To avoid any variation in the mechanical properties due to grain orientation variation, SAC305 BGA joints with single grain crystal structure were chosen for this study.

Experimental measurements showed that the mechanical response of SAC305 BGA joints are highly sensitive to test temperature. Mechanical properties, such as, elastic modulus, and hardness degraded significantly with the increase in temperatures. This degradations were more severe when specimens were preconditioned with aging at T = 125 °C for different durations. At a fixed temperature, the effective modulus and hardness decreases with increasing aging time. Most significant degradation occurred from no aging to 1 days of aging at T = 125 °C. After that, still the degradation continued but with a much slower rate. Finally, the time dependent evolution of the microstructure was compared to the degradation in the modulus during aging, and good correlation was observed.

10.9 Summary

In this dissertation, with a combination of numerical and experimental investigation several popular SAC and relatively new SAC+Bi lead free solder alloys with various bismuth percent (1%, 2%, and 3%) have been studied for making database of their different mechanical properties for better reliability predictions in harsh environment applications. These alloys were subjected to a wide range of temperatures including room temperature (25 °C) to very high testing temperature up to 200 °C and mechanical properties, such as elastic modulus, ultimate tensile strength, and yield stress were recorded. It was found that mechanical properties of lead free solder alloys degrade significantly at higher temperature. About 40-50% decrease in strength has been observed between testing temperatures of T = 25 and T = 125 °C for all the Alloys. The degradation was observed much higher in extreme high temperature testing between T= 125 and T = 200 °C. In

addition, the temperature dependent tensile properties of the SACN05 (N =1, 2, 3, and 4) were compared with the new SAC+Bi (1%, 2%, and 3%), and two other popular alloys known as SAC_Q (SAC+3% Bi), and Sn-3.5Ag. Comparison of the results for different solders has shown that the addition of dopants (e.g. Bi, Ni, and Sb) in the traditional SAC alloys improved their high temperature properties significantly. Also, this study considered aging effects in lead free solder aged at extreme high temperatures to determine the mechanical properties.

The Anand viscoplastic constitutive model is often used to represent the material behavior of the solder in finite element simulations, and the reliability prediction results are often highly sensitive to the Anand parameters. The nine Anand parameters were determined for each unique solder alloy from a set of uniaxial tensile tests performed at several strain rates and extreme high temperatures (125 to 200 °C). Previous studies on solder aging has considered aging temperatures in the range of T = 25-125 °C. This work is the first study of extreme high temperature aging effects.

The effects of aging were studied for the various SAC+Bi alloys using both mechanical testing and microstructure observations. The results have shown that all of the SAC+Bi alloys demonstrate superior resistance to aging effects relative to SAC305. During aging, the bismuth was observed to go into solution within the beta-Sn dendrites and in the intermetallic rich regions between dendrites. It was observed that the coarsening of the intermetallic compounds was greatly mitigated in the SAC+Bi alloys relative to that observed in SAC305. The resistance to aging and increases in mechanical properties were found to be directly proportional to the amount of Bi present in the SAC+X alloy. The material properties of the SAC+Bi alloy will exceed those for SAC305 for all aging times if the level of Bi is at least 1%. Below 1% Bi composition, superior performance relative to SAC105 can be obtained.

Another interesting investigation was the finite element prediction to study the influence of solder joint Poisson's ratio on the reliability of SASC lead free solders. Due to difficulties in measurements, Poisson's ratio of lead free solder was assumed to be 0.3 for finite element modeling in the previous studies. But results from finite element simulation established the fact that specified value of Poisson's ratio greatly influence the finite element results which in term affects the reliability prediction. Therefore, an extensive efforts were taken to experimentally characterize the value of solder Poisson's ratio for various temperatures, strain rates, solidification profile, and isothermal aging conditions. Considering all of the possible branches of the test matrix, the value of the Poisson's ratio of SAC305 ranged from $0.31 < \nu < 0.44$. Similarly, the Poisson's ratio of SAC405 ranged from $0.28 < \nu < 0.42$, and the Poisson's ratio of Innolot and SAC_Q ranged from $0.27 < \nu < 0.38$, and $0.26 < \nu < 0.37$ respectively.

To understand the effect of aging on the actual solder joint at elevated temperatures, both mechanical testing by developing a special test procedure to perform high temperature creep experiments using nanoindentation tool, and microstructural study including measurements and quantitative analysis were carried out at extreme high aging (T= 125, and 150 °C) and test (T = 125, 150, 175, and 200 °C) temperatures. Finally, the time dependent evolution of the microstructure was compared to the degradation in the modulus during aging, and good correlation was observed.

Future Work

Following future work can be performed to extend the findings of this dissertation:

- Isothermal aging dependent studies for the new SAC+Bi alloys can be extended for different aging temperatures, such as, 150, 175, and 200 °C for various strain rates, such as, 10^{-4} and 10^{-5} sec^{-1}.
- High temperature creep behavior of various SAC and SAC+X alloys subjected to aging at very high temperature (such as, up to 200 °C) can be investigated.
- Anand parameters for several lead free solder alloys were included in this dissertation. This work can be extended to explore the effect of extreme high temperature aging on Anand parameters for various SAC+Bi doped alloys.
- The effects of test temperatures and aging conditions on the creep properties of SAC305 solder joints were investigated from 125-200 °C temperature range using nanoindentation system. This project can be continued for other SAC and SAC+Bi lead free solder alloys.
- The microstructure evolution study presented in this dissertation can be extended to a higher aging time. Based on the short and long term aging induced IMC coarsening data, a mathematical model can be developed to predict solder joint reliability as a function of aging time and temperature.
- The evolution of the microstructure of SAC305 BGA joints can be continued for other SAC+Bi BGA joints to investigate the effect of dopant, such as, bismuth in mitigating the aging effect in commercial solder joints.

REFERENCES

[1] M. Abtew and G. Selvaduray, "Lead-Free Solders in Microelectronics," *Materials Science and Engineering: R: Reports,* vol. 27, no. 5, pp. 95-141, 2000.

[2] P. T. Vianco, "Development of Alternatives to Lead-Bearing Solders," *Proceedings of the Technical Program on Surface Mount Technical Association International Conference,* 1993.

[3] J. S. Hwang, *Implementing Lead-Free Electronics*. McGraw-Hill, New York, 2005.

[4] Q. Zhang, A. Dasgupta, and P. Haswell, "Creep and High-Temperature Isothermal Fatigue of Pb-Free Solders," *Proceedings of ASME InterPACK,* no. 36908a, pp. 955-960, 2003.

[5] NCMS, "Lead-Free Solder Project Final Report," *NCMS Report 0401RE96,* 1997.

[6] N. C. Lee, "Getting Ready for Lead-Free Solders," *Soldering & Surface Mount Technology,* vol. 9, no. 2, pp. 65-69, 1997.

[7] K. S. Kim, S. H. Huh, and K. Suganuma, "Effects of Intermetallic Compounds on Properties of Sn–Ag–Cu Lead-Free Soldered Joints," *Journal of Alloys and Compounds,* vol. 352, no. 1, pp. 226-236, 2003.

[8] J.-W. Yoon, S.-W. Kim, and S.-B. Jung, "IMC Morphology, Interfacial Reaction and Joint Reliability of Pb-Free Sn–Ag–Cu Solder on Electrolytic Ni BGA Substrate," *Journal of Alloys and Compounds,* vol. 392, no. 1, pp. 247-252, 2005.

[9] D. Q. Yu and L. Wang, "The Growth and Roughness Evolution of Intermetallic Compounds of Sn–Ag–Cu/Cu Interface During Soldering Reaction," *Journal of Alloys and Compounds,* vol. 458, no. 1, pp. 542-547, 2008.

[10] C. M. L. Wu, D. Q. Yu, C. M. T. Law, and L. Wang, "Properties of Lead-Free Solder Alloys with Rare Earth Element Additions," *Materials Science and Engineering: R: Reports,* vol. 44, no. 1, pp. 1-44, 2004.

[11] Y. C. Chan and D. Yang, "Failure Mechanisms of Solder Interconnects under Current Stressing in Advanced Electronic Packages," *Progress in Materials Science,* vol. 55, no. 5, pp. 428-475, 2010.

[12] C.-h. Wang and S.-w. Chen, "Sn–0.7wt.%Cu/Ni Interfacial Reactions at 250°C," *Acta Materialia,* vol. 54, no. 1, pp. 247-253, 2006.

[13] G. Zeng, S. D. McDonald, Q. F. Gu, K. Sweatman, and K. Nogita, "Effects of Element Addition on the β→α Transformation in Tin," *Philosophical Magazine Letters,* vol. 94, no. 2, pp. 53-62, 2014.

[14] W. J. Plumbridge, "Tin Pest Issues in Lead-Free Electronic Solders," in *Lead-Free Electronic Solders: A Special Issue of the Journal of Materials Science: Materials in Electronics*, pp. 307-318, 2007.

[15] S. Cheng, C.-M. Huang, and M. Pecht, "A Review of Lead-Free Solders for Electronics Applications," *Microelectronics Reliability,* vol. 75, pp. 77-95, 2017.

[16] M. Hasnine, B. Tolla, and M. Karasawa, "Effect of Ge Addition on Wettability, Copper Dissolution, Microstructural and Mechanical Behavior of SnCu–Ge Solder Alloy," *Journal of Materials Science: Materials in Electronics,* vol. 28, no. 21, pp. 16106-16119, 2017.

[17] Q. B. Tao, L. Benabou, L. Vivet, V. N. Le, and F. B. Ouezdou, "Effect of Ni and Sb Additions and Testing Conditions on the Mechanical Properties and Microstructures of Lead-Free Solder Joints," *Materials Science and Engineering: A,* vol. 669, pp. 403-416, 2016.

[18] J. Glazer, "Metallurgy of Low Temperature Pb-Free Solders for Electronic Assembly," *International Materials Reviews,* vol. 40, no. 2, pp. 65-93, 1995.
[19] M. McCormack, S. Jin, G. W. Kammlott, and H. S. Chen, "New Pb-Free Solder Alloy with Superior Mechanical Properties," *Applied Physics Letters,* vol. 63, no. 1, pp. 15-17 1993.
[20] K. Nogita, "Stabilisation of Cu_6Sn_5 by Ni in Sn-0.7 Cu-0.05 Ni Lead-Free Solder Alloys," *Intermetallics,* vol. 18, no. 1, pp. 145-149, 2010.
[21] F. X. Che, J. E. Luan, and X. Baraton, "Effect of Silver Content and Nickel Dopant on Mechanical Properties of Sn-Ag-Based Solders," *Proceedings of the 58th IEEE Electronic Components and Technology Conference,* pp. 485-490, 2008.
[22] F. Guo, J. Lee, S. Choi, J. P. Lucas, T. R. Bieler, and K. N. Subramanian, "Processing and Aging Characteristics of Eutectic Sn-3.5 Ag Solder Reinforced with Mechanically Incorporated Ni Particles," *Journal of Electronic Materials,* vol. 30, no. 9, pp. 1073-1082, 2001.
[23] Z. G. Chen, Y. W. Shi, Z. D. Xia, and Y. F. Yan, "Study on the Microstructure of a Novel Lead-Free Solder Alloy SnAgCu-Re and Its Soldered Joints," *Journal of Electronic Materials,* vol. 31, no. 10, pp. 1122-1128, 2002.
[24] F. Gao, S. Mukherjee, Q. Cui, and Z. Gu, "Synthesis, Characterization, and Thermal Properties of Nanoscale Lead-Free Solders on Multisegmented Metal Nanowires," *Journal of Physical Chemistry C,* vol. 113, no. 22, pp. 9546-9552, 2009.
[25] C. M. T. Law and C. M. L. Wu, "Microstructure Evolution and Shear Strength of Sn-3.5 Ag-Re Lead-Free BGA Solder Balls," *Proceedings of the 6th IEEE CPMT Conference on High Density Microsystem Design and Packaging and Component Failure Analysis,* pp. 60-65, 2004.
[26] N.-C. Lee, "Lead-Free Soldering-Where the World Is Going," *Advancing Microelectronics,* vol. 26, no. 5, pp. 29-35, 1999.
[27] A. Pirondi, "Mechanical Failure in Microelectronic Packaging," 2008.
[28] S. Wiese, A. Schubert, H. Walter, R. Dukek, F. Feustel, E. Meusel, and B. Michel, "Constitutive Behaviour of Lead-Free Solders vs. Lead-Containing Solders-Experiments on Bulk Specimens and Flip-Chip Joints," *Proceedings of the 51st IEEE Electronic Components and Technology Conference,* pp. 890-902, 2001.
[29] R. J. McCabe and M. E. Fine, "Athermal and Thermally Activated Plastic Flow in Low Melting Temperature Solders at Small Stresses," *Scripta Materialia,* vol. 39, no. 2, pp. 189-195, 1998.
[30] J. H. Lau, "Solder Joint Reliability of Flip Chip and Plastic Ball Grid Array Assemblies under Thermal, Mechanical, and Vibrational Conditions," *IEEE Transactions on Components, Packaging, and Manufacturing Technology, Part B,* vol. 19, no. 4, pp. 728-735, 1996.
[31] K. M. Ralls, Courtney, T. H., Wulff, J, *Introduction to Materials Science and Engineering*. Wiley & Sons, 1976.
[32] R. W. Hertzberg, R. P. Vinci, and J. L. Hertzberg, *Deformation and Fracture Mechanics of Engineering Materials*. Wiley New York, 1996.
[33] H. Ma and J. C. Suhling, "A Review of Mechanical Properties of Lead-Free Solders for Electronic Packaging," *Journal of Materials Science,* vol. 44, no. 5, pp. 1141-1158, 2009.
[34] J. H. Lau and Y.-H. Pao, *Solder Joint Reliability of* BGA*, CSP, Flip Chip, and Fine Pitch SMT Assemblies*, McGraw-Hill New York, 1997.
[35] R. W. Evans and B. Wilshire, "Creep of Metals and Alloys," 1985.

[36] M. F. Ashby, "A First Report on Deformation-Mechanism Maps," *Acta Metallurgica,* vol. 20, no. 7, pp. 887-897, 1972.
[37] J. Weertman, "Steady-State Creep through Dislocation Climb," *Journal of Applied Physics,* vol. 28, p. 362, 1957.
[38] R. L. Coble, "A Model for Boundary Diffusion Controlled Creep in Polycrystalline Materials," *Journal of Applied Physics,* vol. 34, p. 1679, 1963.
[39] C. Herring, "Diffusional Viscosity of a Polycrystalline Solid," *Journal of Applied Physics,* vol. 21, pp. 437-445, 1950.
[40] A. C. Fischer-Cripps, *Nanoindentation*, Third ed. Springer, 2011.
[41] P. McCluskey, R. Grzybowski, and T. Podlesak, "High Temperature Electronics," CRC Press, 1997.
[42] S. Ganesan and M. Pecht, *Lead-Free Electronics*. John Wiley and Sons, 2006.
[43] R. W. Johnson, J. L. Evans, P. Jacobsen, J. R. Thompson, and M. Christopher, "The Changing Automotive Environment: High-Temperature Electronics," *IEEE Transactions on Electronics Packaging Manufacturing,* vol. 27, no. 3, pp. 164-176, 2004.
[44] M. Hattori, "Needs and Applications of High-Temperature Lsis for Automotive Electronic Systems," *Proceedings of the International Conference on High Temperature Electronics,* pp. 37-43, 1999.
[45] B. Parmentier, O. Vermesan, and L. Beneteau, "Design of High Temperature Electronics for Well Logging Applications," *Proceedings of the International Conference on High Temperature Electronics,* 2003.
[46] H. Ma, J. C. Suhling, P. Lall, and M. J. Bozack, "Reliability of the Aging Lead Free Solder Joint," *Proceeding of the 56th IEEE Electronic Components and Technology Conference,* pp. 849-864, 2006.
[47] H. Ma, J. C. Suhling, Y. Zhang, P. Lall, and M. J. Bozack, "The Influence of Elevated Temperature Aging on Reliability of Lead Free Solder Joints," *Proceeding of the 57th IEEE Electronic Components and Technology Conference,* pp. 653-668, 2007.
[48] Y. Zhang, Z. Cai, J. C. Suhling, P. Lall, and M. J. Bozack, "The Effects of Aging Temperature on SAC Solder Joint Material Behavior and Reliability," *Proceedings of the 58th IEEE Electronic Components and Technology Conference,* pp. 99-112, 2008.
[49] I. E. Anderson and J. L. Harringa, "Elevated Temperature Aging of Solder Joints Based on Sn-Ag-Cu: Effects on Joint Microstructure and Shear Strength," *Journal of Electronic Materials,* vol. 33, no. 12, pp. 1485-1496, 2004.
[50] I. E. Anderson, J. W. Walleser, J. L. Harringa, F. Laabs, and A. Kracher, "Nucleation Control and Thermal Aging Resistanceof near-Eutectic Sn-Ag-Cu-X Solder Jointsby Alloy Design," *Journal of Electronic Materials,* vol. 38, no. 12, pp. 2770-2779, 2009.
[51] Z. Cai, Y. Zhang, J. C. Suhling, P. Lall, R. W. Johnson, and M. J. Bozack, "Reduction of Lead Free Solder Aging Effects Using Doped SAC Alloys," *Proceedings of the 60th IEEE Electronic Components and Technology Conference,* pp. 1493-1511, 2010.
[52] S. Choi, T. R. Bieler, J. P. Lucas, and K. N. Subramanian, "Characterization of the Growth of Intermetallic Interfacial Layers of Sn-Ag and Sn-Pb Eutectic Solders and Their Composite Solders on Cu Substrate During Isothermal Long-Term Aging," *Journal of Electronic Materials,* vol. 28, no. 11, pp. 1209-1215, 1999.
[53] C. M. Chuang, T. S. Lui, and L. H. Chen, "Effect of Aluminum Addition on Tensile Properties of Naturally Aged Sn-9Zn Eutectic Solder," *Journal of Materials Science,* vol. 37, no. 1, pp. 191-195, 2002.

[54] R. Darveaux, "Shear Deformation of Lead Free Solder Joints," *Proceedings of the 55th IEEE Electronic Components and Technology Conference,* pp. 882-893, 2005.
[55] R. Darveaux and K. Banerji, "Fatigue Analysis of Flip Chip Assemblies Using Thermal Stress Simulations and a Coffin-Manson Relation," *Proceedings of the 41st IEEE Electronic Components & Technology Conference,* pp. 797-805, 1991.
[56] Y. Ding, C. Wang, Y. Tian, and M. Li, "Influence of Aging Treatment on Deformation Behavior of 96.5Sn3.5Ag Lead-Free Solder Alloy During in Situ Tensile Tests," *Journal of Alloys and Compounds,* vol. 428, no. 1, pp. 274-285, 2007.
[57] I. Dutta, D. Pan, R. A. Marks, and S. G. Jadhav, "Effect of Thermo-Mechanically Induced Microstructural Coarsening on the Evolution of Creep Response of SnAg-Based Microelectronic Solders," *Materials Science and Engineering: A,* vol. 410-411, pp. 48-52, 2005.
[58] T.-C. Hsuan and K.-L. Lin, "Effects of Aging Treatment on Mechanical Properties and Microstructure of Sn–8.5Zn–0.5Ag–0.01Al–0.1Ga Solder," *Materials Science and Engineering: A,* vol. 456, no. 1, pp. 202-209, 2007.
[59] K.-S. Kim, C.-H. Yu, and J.-M. Yang, "Aging Treatment Characteristics of Solder Bump Joint for High Reliability Optical Module," *Thin Solid Films,* vol. 462-463, pp. 402-407, 2004.
[60] B. Lampe, "Room Temperature Aging Properties of Some Solder Alloys," *Welding Journal,* vol. 55, no. 10, pp. 330-340, 1976.
[61] X. Luhua, J. H. L. Pang, K. H. Prakash, and T. H. Low, "Isothermal and Thermal Cycling Aging on IMC Growth Rate in Lead-Free and Lead-Based Solder Interface," *IEEE Transactions on Components and Packaging Technologies,* vol. 28, no. 3, pp. 408-414, 2005.
[62] A. S. Medvedev, "Aging of Tin-Lead Solders and Joints Soldered by Them," *Metallovedenie I Obrabotka Metallov,* vol. 7, pp. 16-23, 1956.
[63] K. Mysore, D. Chan, D. Bhate, G. Subbarayan, I. Dutta, V. Gupta, J. Zhao, and D. Edwards, "Aging-Informed Behavior of Sn3.8Ag0.7Cu Solder Alloys," *Proceedings of IEEE ITherm,* pp. 870-875, 2008.
[64] J. H. L. Pang, T. H. Low, B. S. Xiong, X. Luhua, and C. C. Neo, "Thermal Cycling Aging Effects on Sn–Ag–Cu Solder Joint Microstructure, IMC and Strength," *Thin Solid Films,* vol. 462-463, pp. 370-375, 2004.
[65] S. Wiese and K. J. Wolter, "Creep of Thermally Aged SnAgCu-Solder Joints," *Microelectronics Reliability,* vol. 47, no. 2, pp. 223-232, 2007.
[66] Q. Xiao, H. J. Bailey, and W. D. Armstrong, "Aging Effects on Microstructure and Tensile Property of Sn3.9Ag0.6Cu Solder Alloy," *Journal of Electronic Packaging,* vol. 126, no. 2, pp. 208-212, 2004.
[67] J.-W. Yoon, C.-B. Lee, and S.-B. Jung, "Growth of an Intermetallic Compound Layer with Sn-3.5Ag-5Bi on Cu and Ni-P/Cu During Aging Treatment," *Journal of Electronic Materials,* vol. 32, no. 11, pp. 1195-1202, 2003.
[68] Y. Zhang, "The Effects of Aging on the Mechanical Behavior of Lead Free and Mixed Formulation Solder Alloys," PhD, Mechanical Engineering, Auburn University, Auburn, AL, 2010.
[69] Y. Zhang, Z. Cai, J. C. Suhling, P. Lall, and M. J. Bozack, "The Effects of SAC Alloy Composition on Aging Resistance and Reliability," *Proceedings of the 59th IEEE Electronic Components and Technology Conference* pp. 370-389, 2009.

[70] S. L. Allen, M. R. Notis, R. R. Chromik, and R. P. Vinci, "Microstructural Evolution in Lead-Free Solder Alloys: Part I. Cast Sn–Ag–Cu Eutectic," *Journal of Materials Research,* vol. 19, no. 5, pp. 1417-1424, 2004.

[71] A. Bansal, T. Lee, K. Liu, and J. Xue, "Effects of Isothermal Aging and in-Situ Current Stress on the Reliability of Lead-Free Solder Joints," *Proceedings of 60th IEEE Electronic Components and Technology Conference,* pp. 1529-1535, 2010.

[72] S. Chavali, Y. Singh, P. Kumar, G. Subbarayan, I. Dutta, and D. R. Edwards, "Aging Aware Constitutive Models for SnAgCu Solder Alloys," *Proceedings of the 61st IEEE Electronic Components and Technology Conference* pp. 701-705, 2011.

[73] W. M. Chen, P. McCloskey, and S. C. O'Mathuna, "Isothermal Aging Effects on the Microstructure and Solder Bump Shear Strength of Eutectic Sn37Pb and Sn3.5Ag Solders," *Microelectronics Reliability,* vol. 46, no. 5, pp. 896-904, 2006.

[74] R. Gagliano, "Shear Testing of Solder Joints: The Effect of Various Parameters on the Maximum Shear Stress of Eutectic Tin-Lead Solder," *Advanced Materials for the 21st Century: Proceedings of the 1999 Julia R. Weertman Symposium,* pp. 107-116, 1999.

[75] M. Hasnine, M. Mustafa, J. C. Suhling, B. C. Prorok, M. J. Bozack, and P. Lall, "Characterization of Aging Effects in Lead Free Solder Joints Using Nanoindentation," *Peoceedings of the 63rd IEEE Electronic Components and Technology Conference,* pp. 166-178, 2013.

[76] S. W. R. Lee, Y.-K. Tsui, X. Hunag, and E. C. C. Yan, "Effects of Room Temperature Storage Time on the Shear Strength of PBGA Solder Balls," *International Mechanical Engineering Congress and Exposition*, pp. 259-262, 2002.

[77] Y. Miyazawa and T. Ariga, "Influences of Aging Treatment on Microstructure and Hardness of Sn-(Ag, Bi, Zn) Eutectic Solder Alloys," *Materials Transactions,* vol. 42, no. 5, pp. 776-782, 2001.

[78] M. Mustafa, Z. Cai, J. C. Suhling, and P. Lall, "The Effects of Aging on the Cyclic Stress-Strain Behavior and Hysteresis Loop Evolution of Lead Free Solders," *Proceedings of the 61st IEEE Electronic Components and Technology Conference*, pp. 927-939, 2011.

[79] J. Wilde, A. R. Fix, and W. Nüchter, "Microstructural Changes of Lead-Free Solder Joints During Long-Term Ageing, Thermal Cycling and Vibration Fatigue," *Soldering & Surface Mount Technology*, vol. 20, no. 1, pp. 13-21, 2008.

[80] M. Motalab, M. Mustafa, J. C. Suhling, J. Zhang, J. Evans, M. J. Bozack, and P. Lall, "Correlation of Reliability Models Including Aging Effects with Thermal Cycling Reliability Data," *Proceedings of the 63rd IEEE Electronic Components and Technology Conference*, pp. 986-1004, 2013.

[81] J. Zhang, Z. Hai, S. Thirugnanasambandam, J. L. Evans, M. Bozack, R. Sesek, Y. Zhang, and J. C. Suhling, "Correlation of Aging Effects on Creep Rate and Reliability in Lead Free Solder Joints," *Journal of SMT,* vol. 25, no. 3, pp. 19-28, 2012.

[82] T. Lee and H. Ma, "Aging Impact on the Accelerated Thermal Cycling Performance of Lead-Free BGA Solder Joints in Various Stress Conditions," *Proceedings of the 62nd IEEE Electronic Components and Technology Conference*, pp. 477-482, 2012.

[83] L. Yin, M. Meilunas, B. Arfaei, L. Wentlent, and P. Borgesen, "Effect of Microstructure Evolution on Pb-Free Solder Joint Reliability in Thermomechanical Fatigue," *Proceedings of the 62nd IEEE Electronic Components and Technology Conference*, pp. 493-499, 2012.

[84] T. Zhang, J. Evans, C. Mitchell, Z. Z. Li, E. Crandall, a. J. Ridenour, and F. Xie, "Reliability of Lead-Free BGA with SnPb Solder Paste for Harsh Environments," *Proceedings of SMTA/CAVE Symposium on AIMS Harsh Environment Electronics*, 2009.

[85] M. Hongtao, J. C. Suhling, P. Lall, and M. J. Bozack, "Reliability of the Aging Lead Free Solder Joint," *Peoceedings of the 56th IEEE Electronic Components and Technology Conference,* pp. 849-864, 2006.

[86] Z. Yifei, C. Zijie, J. C. Suhling, P. Lall, and M. J. Bozack, "The Effects of Aging Temperature on SAC Solder Joint Material Behavior and Reliability," *Proceedings of the 58th IEEE Electronic Components and Technology Conference*, pp. 99-112, 2008.

[87] R. J. Coyle, P. P. Solan, A. J. Serafino, and S. A. Gahr, "The Influence of Room Temperature Aging on Ball Shear Strength and Microstructure of Area Array Solder Balls," *Proceedings of the 50th IEEE Electronic Components and Technology Conference*, pp. 160-169, 2000.

[88] T.-K. Lee, H. Ma, K.-C. Liu, and J. Xue, "Impact of Isothermal Aging on Long-Term Reliability of Fine-Pitch Ball Grid Array Packages with Sn-Ag-Cu Solder Interconnects: Surface Finish Effects," *Journal of Electronic Materials,* vol. 39, no. 12, pp. 2564-2573, 2010.

[89] M. A. Whitmore, A. C. Chilton, and W. B. Hampshire, "Fatigue Failure in a Model SMD Joint," *Soldering & Surface Mount Technology,* vol. 1, no. 3, pp. 21-24, 1989.

[90] L. Ming, K. Y. Lee, D. R. Olsen, W. T. Chen, B. T. C. Tan, and S. Mhaisalkar, "Microstructure, Joint Strength and Failure Mechanisms of SnPb and Pb-Free Solders in BGA Packages," *IEEE Transactions on Electronics Packaging Manufacturing,* vol. 25, no. 3, pp. 185-192, 2002.

[91] J.-M. Koo and S.-B. Jung, "Effect of Displacement Rate on Ball Shear Properties for Sn–37Pb and Sn–3.5Ag BGA Solder Joints During Isothermal Aging," *Microelectronics Reliability,* vol. 47, no. 12, pp. 2169-2178, 2007.

[92] R. Darveaux, "Shear Deformation of Lead Free Solder Joints," *Proceedings of the 55th Electronic Components and Technology Conference*, pp. 882-893, 2005.

[93] J. R. Oliver, J. Liu, and Z. Lai, "Effect of Thermal Ageing on the Shear Strength of Lead-Free Solder Joints," *Proceedings of the International Symposium on Advanced Packaging Materials Processes, Properties and Interfaces*, pp. 152-157, 2000.

[94] H. L. J. Pang, K. H. Tan, X. Q. Shi, and Z. P. Wang, "Microstructure and Intermetallic Growth Effects on Shear and Fatigue Strength of Solder Joints Subjected to Thermal Cycling Aging," *Materials Science and Engineering: A,* vol. 307, no. 1, pp. 42-50, 2001.

[95] T. Lee, B. Zhou, and T. R. Bieler, "Impact of Isothermal Aging and Sn Grain Orientation on the Long-Term Reliability of Wafer-Level Chip-Scale Package Sn–Ag–Cu Solder Interconnects," *IEEE Transactions on Components, Packaging and Manufacturing Technology,* vol. 2, no. 3, pp. 496-501, 2012.

[96] R. C. J. Smetana, P. Read, R. Popowich, D. Fleming, and T. Sack, "Variations in Thermal Cycling Response of Pb-Free Solder Due to Isothermal Preconditioning," *Proceedings of SMTA International Conference*, pp. 641-654, 2011.

[97] L. Anand, "Constitutive Equations for Hot-Working of Metals," *International Journal of Plasticity,* vol. 1, no. 3, pp. 213-231, 1985.

[98] S. B. Brown, K. H. Kim, and L. Anand, "An Internal Variable Constitutive Model for Hot Working of Metals," *International Journal of Plasticity,* vol. 5, no. 2, pp. 95-130, 1989.

[99] J.-P. Clech, "An Obstacle-Controlled Creep Model for Sn-Pb and Sn-Based Lead-Free Solders," *Proceedings of SMTA International Conference,* 2004.
[100] Y. Hong, P. Deane, P. Magill, and K. L. Murty, "Creep Deformation of 96.5Sn-3.5Ag Solder Joints in a Flip Chip Package," *Peoceedings of the 46th IEEE Electronic Components and Technology Conference,* pp. 1136-1142, 1996.
[101] X. Q. Shi, Z. P. Wang, Q. J. Yang, and H. L. J. Pang, "Creep Behavior and Deformation Mechanism Map of Sn-Pb Eutectic Solder Alloy," *Journal of Engineering Materials and Technology,* vol. 125, no. 1, pp. 81-88, 2002.
[102] S. Wiese, M. Roellig, and K. Wolter, "Creep of Eutectic SnAgCu in Thermally Treated Solder Joints," *Proceedings of the 55th IEEE Electronic Components and Technology Conference*, vol. 2, pp. 1272-1281, 2005.
[103] H. Ma, J. C. Suhling, Y. Zhang, P. Lall, and M. J. Bozack, "The Influence of Elevated Temperature Aging on Reliability of Lead Free Solder Joints," *Proceedings of the 57th IEEE Electronic Components and Technology Conference*, pp. 653-668, 2007.
[104] J. H. Lau, "Solder Joint Reliability of Flip Chip and Plastic Ball Grid Array Assemblies under Thermal, Mechanical, and Vibrational Conditions," *IEEE Transactions on Components, Packaging, and Manufacturing Technology: Part B,* vol. 19, no. 4, pp. 728-735, 1996.
[105] W. K. Jones, Y. Q. Liu, M. A. Zampino, and G. L. Gonzalez, "The at-Temperature Mechanical Properties of Lead-Tin Based Alloys," in *Microelectronic Interconnections and Assembly*, Springer Netherlands, pp. 53-58, 1998.
[106] Y. L. W. K. Jones, M. A. Zampino, G. Gonzalez, and M. Shah, "Design and Reliability of Solders and Solder Interconnections," *TMS Annual Meeting,* 1997.
[107] X. Q. Shi, W. Zhou, H. L. J. Pang, and Z. P. Wang, "Effect of Temperature and Strain Rate on Mechanical Properties of 63Sn/37Pb Solder Alloy," *Journal of Electronic Packaging,* vol. 121, no. 3, pp. 179-185, 1999.
[108] F. Lang, H. Tanaka, O. Munegata, T. Taguchi, and T. Narita, "The Effect of Strain Rate and Temperature on the Tensile Properties of Sn–3.5Ag Solder," *Materials Characterization,* vol. 54, no. 3, pp. 223-229, 2005.
[109] L. H. Dai and S.-W. R. Lee, "Characterization of Strain Rate-Dependent Behavior of 63sn-37Pb Solder Alloy," *Proceedings of ASME InterPACK*, pp. 307-313, 2001.
[110] H. Nose, M. Sakane, Y. Tsukada, and H. Nishimura, "Temperature and Strain Rate Effects on Tensile Strength and Inelastic Constitutive Relationship of Sn-Pb Solders," *Journal of Electronic Packaging,* vol. 125, no. 1, pp. 59-66, 2003.
[111] W. J. Plumbridge and C. R. Gagg, "Effects of Strain Rate and Temperature on the Stress–Strain Response of Solder Alloys," *Journal of Materials Science: Materials in Electronics,* vol. 10, no. 5, pp. 461-468, 1999.
[112] J. H. L. Pang, B. S. Xiong, and F. X. Che, "Modeling Stress Strain Curves for Lead-Free 95.5Sn-3.8Ag-0.7Cu Solder," *Proceedings of the 5th International Conference on Thermal and Mechanical Simulation and Experiments in Microelectronics and Microsystems,* pp. 449-453, 2004.
[113] J. G. Harper, L. A. Shepard, and J. E. Dorn, "Creep of Aluminum under Extremely Small Stresses," *Acta Metallurgica,* vol. 6, no. 7, pp. 509-518, 1958.
[114] F. Garofalo and D. B. Butrymowicz, "Fundamentals of Creep and Creep-Rupture in Metals," *Physics Today,* vol. 19, no. 5, pp. 100-102, 1966.

[115] L. Anand, "Constitutive Equations for the Rate-Dependent Deformation of Metals at Elevated Temperatures," *Journal of Engineering Materials and Technology,* vol. 104, no. 1, pp. 12-17, 1982.
[116] F. X. Che, H. L. J. Pang, W. H. Zhu, W. Sun, and A. Y. S. Sun, "Modeling Constitutive Model Effect on Reliability of Lead-Free Solder Joints," *Proceedings of the 7th International Conference on Electronic Packaging Technology,* pp. 1-6, 2006.
[117] M. Pei and J. Qu, "Constitutive Modeling of Lead-Free Solders," *Proceedings of International Symposium on Advanced Packaging Materials: Processes, Properties and Interfaces,* pp. 45-49, 2005.
[118] K. Mysore, G. Subbarayan, V. Gupta, and R. Zhang, "Constitutive and Aging Behavior of Sn3.0Ag0.5Cu Solder Alloy," *IEEE Transactions on Electronics Packaging Manufacturing,* vol. 32, no. 4, pp. 221-232, 2009.
[119] M. Motalab, Z. Cai, J. C. Suhling, and P. Lall, "Determination of Anand Constants for SAC Solders Using Stress-Strain or Creep Data," *Proceedings of IEEE ITherm,* pp. 910-922, 2012.
[120] N. Bai, X. Chen, and H. Gao, "Simulation of Uniaxial Tensile Properties for Lead-Free Solders with Modified Anand Model," *Materials & Design,* vol. 30, no. 1, pp. 122-128, 2009.
[121] M. Amagai, M. Watanabe, M. Omiya, K. Kishimoto, and T. Shibuya, "Mechanical Characterization of Sn–Ag-Based Lead-Free Solders," *Microelectronics Reliability,* vol. 42, no. 6, pp. 951-966, 2002.
[122] Y. Kim, H. Noguchi, and M. Amagai, "Vibration Fatigue Reliability of BGA -IC Package with Pb-Free Solder and Pb–Sn Solder," *Microelectronics Reliability,* vol. 46, no. 2, pp. 459-466, 2006.
[123] M. L. Huang and L. Wang, "Effects of Cu, Bi, and in on Microstructure and Tensile Properties of Sn-Ag-X(Cu, Bi, in) Solders," *Metallurgical and Materials Transactions A,* vol. 36, no. 6, pp. 1439-1446, 2005.
[124] M. Matahir, L. Chin, K. Tan, and A. Olofinjana, "Mechanical Strength and Its Variability in Bi-Modified Sn-Ag-Cu Solder Alloy," *Journal of Achievement in Materials and Manufacturing Engineering,* vol. 46, pp. 50-56, 2011.
[125] R. S. Pandher, B. G. Lewis, R. Vangaveti, and B. Singh, "Drop Shock Reliability of Lead-Free Alloys - Effect of Micro-Additives," *Proceedings of the 57th IEEE Electronic Components and Technology Conference*, pp. 669-676, 2007.
[126] Z. Zhenqing, W. Lei, X. Xiaoqiang, W. Qian, and L. Jaisung, "The Influence of Low Level Doping of Ni on the Microstructure and Reliability of SAC Solder Joint," *Proceedings of International Conference on Electronic Packaging Technology & High Density Packaging,* pp. 1-5, 2008.
[127] I. d. Sousa, D. W. Henderson, L. Parry, S. K. Kang, and D. Shih, "The Influence of Low Level Doping on the Thermal Evolution of SAC Alloy Solder Joints with Cu Pad Structures," *Proceedings of the 56th IEEE Electronic Components and Technology Conference*, pp. 1454-1461, 2006.
[128] J. H. Lee, S. Kumar, H. J. Kim, Y. W. Lee, and J. T. Moon, "High Thermo-Mechanical Fatigue and Drop Impact Resistant Ni-Bi Doped Lead Free Solder," *Proceedings of the 64th IEEE Electronic Components and Technology Conference*, pp. 712-716, 2014.

[129] T. Yeung, H. Sze, K. Tan, J. Sandhu, C. Neo, and E. Law, "Material Characterization of a Novel Lead-Free Solder Material — SACQ," *Proceedings of the 64th IEEE Electronic Components and Technology Conference*, pp. 518-522, 2014.
[130] L. Sun and L. Zhang, "Properties and Microstructures of Sn-Ag-Cu-X Lead-Free Solder Joints in Electronic Packaging," *Advances in Materials Science and Engineering,* vol. 2015, no. 639028, 2015.
[131] M. Sadiq, R. Pesci, and M. Cherkaoui, "Impact of Thermal Aging on the Microstructure Evolution and Mechanical Properties of Lanthanum-Doped Tin-Silver-Copper Lead-Free Solders," *Journal of Electronic Materials,* vol. 42, no. 3, pp. 492-501, 2013.
[132] H. Lee, Y. Chen, T. Hong, K. Shih, and C. Hsu, "Microstructural Evolution of Sn-3.5Ag Solder with Lanthanum Addition," *International Conference on Electronic Packaging Technology & High Density Packaging,* pp. 617-622, 2009.
[133] H. Hao, Y. Shi, Z. Xia, Y. Lei, and F. Guo, "Microstructure Evolution of SnAgCu Lead-Free Solders under High Temperature Aging," *Journal of Electronic Materials,* vol. 37, no. 1, pp. 2-8, 2008.
[134] D. Witkin, "Influence of Microstructure on Mechanical Behavior of Bi-Containing Pb-Free Solders," *Proceedings of IPC APEX EXPO Conference and Exhibition,* vol. 1, pp. 540-560, 2013.
[135] A. Delhaise, D. Perovic, and P. Snugovsky, "The Effects of Bi and Aging on the Microstructure and Mechanical Properties of Sn-Rich Alloys," *Proceedings of the International Conference on Soldering and Reliability,* 2015.
[136] R. R. Chromik, R. P. Vinci, S. L. Allen, and M. R. Notis, "Measuring the Mechanical Properties of Pb-Free Solder and Sn-Based Intermetallics by Nanoindentation," *JOM,* vol. 55, no. 6, pp. 66-69, 2003.
[137] X. Deng, N. Chawla, K. K. Chawla, and M. Koopman, "Deformation Behavior of (Cu, Ag)–Sn Intermetallics by Nanoindentation," *Acta Materialia,* vol. 52, no. 14, pp. 4291-4303, 2004.
[138] F. Gao, H. Nishikawa, T. Takemoto, and J. Qu, "Mechanical Properties Versus Temperature Relation of Individual Phases in Sn–3.0Ag–0.5Cu Lead-Free Solder Alloy," *Microelectronics Reliability,* vol. 49, no. 3, pp. 296-302, 2009.
[139] Y. D. Han, H. Y. Jing, S. M. L. Nai, L. Y. Xu, C. M. Tan, and J. Wei, "Temperature Dependence of Creep and Hardness of Sn-Ag-Cu Lead-Free Solder," *Journal of Electronic Materials,* vol. 39, no. 2, pp. 223-229, 2010.
[140] M. Hasnine, J. C. Suhling, B. C. Prorok, M. J. Bozack, and P. Lall, "Exploration of Aging Induced Evolution of Solder Joints Using Nanoindentation and Microdiffraction," *Peoceedings of the 64th IEEE Electronic Components and Technology Conference,* pp. 379-394, 2014.
[141] M. Hasnine, J. C. Suhling, B. C. Prorok, M. J. Bozack, and P. Lall, "Nanomechanical Characterization of SAC Solder Joints - Reduction of Aging Effects Using Microalloy Additions," *Peoceedings of the 65th IEEE Electronic Components and Technology Conference,* pp. 1574-1585, 2015.
[142] M. Hasnine, J. C. Suhling, B. C. Prorok, M. J. Bozack, and P. Lall, "Anisotropic Mechanical Properties of SAC Solder Joints in Microelectronic Packaging and Prediction of Uniaxial Creep Using Nanoindentation Creep," *Experimental Mechanics,* vol. 57, no. 4, pp. 603-614, 2017.

[143] S. Lotfian, J. M. Molina-Aldareguia, K. E. Yazzie, J. Llorca, and N. Chawla, "Mechanical Characterization of Lead-Free Sn-Ag-Cu Solder Joints by High-Temperature Nanoindentation," *Journal of Electronic Materials,* vol. 42, no. 6, pp. 1085-1091, 2013.
[144] V. M. F. Marques, C. Johnston, and P. S. Grant, "Nanomechanical Characterization of Sn–Ag–Cu/Cu Joints—Part 1: Young's Modulus, Hardness and Deformation Mechanisms as a Function of Temperature," *Acta Materialia,* vol. 61, no. 7, pp. 2460-2470, 2013.
[145] V. M. F. Marques, B. Wunderle, C. Johnston, and P. S. Grant, "Nanomechanical Characterization of Sn–Ag–Cu/Cu Joints—Part 2: Nanoindentation Creep and Its Relationship with Uniaxial Creep as a Function of Temperature," *Acta Materialia,* vol. 61, no. 7, pp. 2471-2480, 2013.
[146] H. Rhee, J. P. Lucas, and K. N. Subramanian, "Micromechanical Characterization of Thermomechanically Fatigued Lead-Free Solder Joints," *Journal of Materials Science: Materials in Electronics,* vol. 13, no. 8, pp. 477-484, 2002.
[147] M. Sadiq, J.-S. Lecomte, and M. Cherkaoui, "Individual Phase Mechanical Properties at Different Temperatures of Sn–Ag–Cu Lead-Free Solders Incorporating Special Pileup Effects Using Nanoindentation," *Journal of Electronic Packaging,* vol. 137, no. 3, pp. 031005-031005-5, 2015.
[148] Y. Sun, J. Liang, Z.-H. Xu, G. Wang, and X. Li, "Nanoindentation for Measuring Individual Phase Mechanical Properties of Lead Free Solder Alloy," *Journal of Materials Science: Materials in Electronics,* vol. 19, no. 6, pp. 514-521, 2008.
[149] J. L. Hay and G. M. Pharr, "Instrumented Indentation Testing," *Mechanical Testing and Evaluation*, vol. 8, 2000.
[150] K. O. Kese, Z. C. Li, and B. Bergman, "Method to Account for True Contact Area in Soda-Lime Glass During Nanoindentation with the Berkovich Tip," *Materials Science and Engineering: A,* vol. 404, no. 1, pp. 1-8, 2005.
[151] M. Cabibbo, D. Ciccarelli, and S. Spigarelli, "Nanoindentation Hardness Measurement in Piling up SiO_2 Coating," *Physics Procedia,* vol. 40, pp. 100-112, 2013.
[152] G. J. S. Chou, "Microstructure Evolution of Snpb and SnAg/Cu BGA Solder Joints During Thermal Aging," *Proceedings of the 8th International Advanced Packaging Materials Symposium*, pp. 39-46, 2002.
[153] R. L. J. M. Ubachs, P. J. G. Schreurs, and M. G. D. Geers, "Microstructure Evolution of Tin-Lead Solder," *IEEE Transactions on Components and Packaging Technologies,* vol. 27, no. 4, pp. 635-642, 2004.
[154] U. Sahaym, B. Talebanpour, S. Seekins, I. Dutta, P. Kumar, and P. Borgesen, "Recrystallization and Ag_3Sn Particle Redistribution During Thermomechanical Treatment of Bulk Sn–Ag–Cu Solder Alloys," *IEEE Transactions on Components, Packaging and Manufacturing Technology,* vol. 3, no. 11, pp. 1868-1875, 2013.
[155] M. Maleki, J. Cugnoni, and J. Botsis, "Isothermal Ageing of SnAgCu Solder Alloys: Three-Dimensional Morphometry Analysis of Microstructural Evolution and Its Effects on Mechanical Response," *Journal of Electronic Materials,* vol. 43, no. 4, pp. 1026-1042, 2014.
[156] A. U. Telang, T. R. Bieler, J. P. Lucas, K. N. Subramanian, L. P. Lehman, Y. Xing, and E. J. Cotts, "Grain-Boundary Character and Grain Growth in Bulk Tin and Bulk Lead-Free Solder Alloys," *Journal of Electronic Materials,* vol. 33, no. 12, pp. 1412-1423, 2004.

[157] P. Kumar, B. Talenbanpour, U. Sahaym, C. H. Wen, and I. Dutta, "Microstructural Evolution and Some Unusual Effects During Thermo-Mechanical Cycling of Sn-Ag-Cu Alloys," *Proceedings of IEEE ITherm*, pp. 880-887, 2012.
[158] P. Chauhan, S. Mukherjee, M. Osterman, A. Dasgupta, and M. Pecht, "Effect of Isothermal Aging on Microstructure and Creep Properties of SAC305 Solder: A Micromechanics Approach," *Proceedings of ASME InterPACK*, pp. V001T07A009, 2013.
[159] W. Yang, R. W. Messler, and L. E. Felton, "Microstructure Evolution of Eutectic Sn-Ag Solder Joints," *Journal of Electronic Materials,* vol. 23, no. 8, pp. 765-772, 1994.
[160] C. Tz-Cheng, Z. Kejun, R. Stierman, D. Edwards, and K. Ano, "Effect of Thermal Aging on Board Level Drop Reliability for Pb-Free BGA Packages," *Proceedings of the 54th IEEE Electronic Components and Technology Conference*, vol. 2, pp. 1256-1262, 2004.
[161] S. Ahat, M. Sheng, and L. Luo, "Microstructure and Shear Strength Evolution of SnAg/Cu Surface Mount Solder Joint During Aging," *Journal of Electronic Materials,* vol. 30, no. 10, pp. 1317-1322, 2001.
[162] W. K. Choi and H. M. Lee, "Effect of Soldering and Aging Time on Interfacial Microstructure and Growth of Intermetallic Compounds between Sn-3.5Ag Solder Alloy and Cu Substrate," *Journal of Electronic Materials,* vol. 29, no. 10, pp. 1207-1213, 2000.
[163] A. M. Z. Akhtar, K. H. Wirda, I. S. R. Aisha, and I. Mahadzir, "Microstructure Evolution at the Solder Joint During Isothermal Aging," *Proceedings of the 36th International Electronics Manufacturing Technology Conference,* pp. 1-5, 2014.
[164] M. Berthou, P. Retailleau, H. Frémont, A. Guédon-Gracia, and C. Jéphos-Davennel, "Microstructure Evolution Observation for SAC Solder Joint: Comparison between Thermal Cycling and Thermal Storage," *Microelectronics Reliability,* vol. 49, no. 9, pp. 1267-1272, 2009.
[165] W. C. Oliver and G. M. Pharr, "An Improved Technique for Determining Hardness and Elastic Modulus Using Load and Displacement Sensing Indentation Experiments," *Journal of Materials Research,* vol. 7, no. 6, pp. 1564-1583, 1992.
[166] D. Tabor, *The Hardness of Metals*, Oxford University Press, 2000.
[167] M. Motalab, Z. Cai, J. C. Suhling, J. Zhang, J. L. Evans, M. J. Bozack, and P. Lall, "Improved Predictions of Lead Free Solder Joint Reliability That Include Aging Effects," *Proceedings of the 62nd IEEE Electronic Components and Technology Conference,* pp. 513-531, 2012.
[168] M. Motalab, M. Mustafa, J. C. Suhling, J. Zhang, J. Evans, M. J. Bozack, and P. Lall, "Correlation of Reliability Models Including Aging Effects with Thermal Cycling Reliability Data," *Proceedings of the 63rd IEEE Electronic Components and Technology Conference,* pp. 986-1004, 2013.
[169] D. Herkommer, J. Punch, and M. Reid, "A Reliability Model for SAC Solder Covering Isothermal Mechanical Cycling and Thermal Cycling Conditions," *Microelectronics Reliability,* vol. 50, no. 1, pp. 116-126, 2010.
[170] G. Z. Wang, Z. N. Cheng, K. Becker, and J. Wilde, "Applying Anand Model to Represent the Viscoplastic Deformation Behavior of Solder Alloys," *Journal of Electronic Packaging,* vol. 123, no. 3, pp. 247-253, 2001.
[171] D. Bhate, D. Chan, G. Subbarayan, T. C. Chiu, V. Gupta, and D. R. Edwards, "Constitutive Behavior of Sn3. 8Ag0. 7Cu and Sn1. 0Ag0. 5Cu Alloys at Creep and Low Strain Rate Regimes," *IEEE Transactions on Components and Packaging Technologies,* vol. 31, no. 3, pp. 622-633, 2008.

[172] M. Motalab, Z. Cai, J. C. Suhling, and P. Lall, "Determination of Anand Constants for SAC Solders Using Stress-Strain or Creep Data," *Proceedings of ITherm,* pp. 910-922, 2012.
[173] N. J. Chhanda, J. C. Suhling, and P. Lall, "Experimental Characterization and Viscoplastic Modeling of the Temperature Dependent Material Behavior of Underfill Encapsulants," *Proceedings of ASME InterPACK* no. 44625, pp. 749-761, 2011.
[174] M. Mayo and W. Nix, "A Micro-Indentation Study of Superplasticity in Pb, Sn, and Sn-38 Wt% Pb," *Acta Metallurgica,* vol. 36, no. 8, pp. 2183-2192, 1988.
[175] M. Mayo, R. Siegel, A. Narayanasamy, and W. Nix, "Mechanical Properties of Nanophase TiO_2 as Determined by Nanoindentation," *Journal of Materials Research,* vol. 5, no. 5, pp. 1073-1082, 1990.
[176] P. Borgesen, "Microstructurally Adaptive Constitutive Relations and Reliability Assessment Protocols for Lead Free Solder," in "SERDP Project WP-1752 Final Report," 2015.
[177] I. Dutta, "A Constitutive Model for Creep of Lead-Free Solders Undergoing Strain-Enhanced Microstructural Coarsening: A First Report," *Journal of Electronic Materials,* vol. 32, no. 4, pp. 201-207, 2003.
[178] I. Dutta, P. Kumar, and G. Subbarayan, "Microstructural Coarsening in Sn-Ag-Based Solders and Its Effects on Mechanical Properties," *JOM,* vol. 61, no. 6, pp. 29-38, 2009.
[179] P. Kumar, Z. Huang, S. C. Chavali, D. K. Chan, I. Dutta, G. Subbarayan, and V. Gupta, "Microstructurally Adaptive Model for Primary and Secondary Creep of Sn-Ag-Based Solders," *IEEE Transactions on Components, Packaging and Manufacturing Technology,* vol. 2, no. 2, pp. 256-265, 2012.
[180] G. E. Dieter and D. J. Bacon, *Mechanical Metallurgy*, 3rd ed., Mc Graw-Hill New York, 1986.
[181] R. Boistelle and J. P. Astier, "Crystallization Mechanisms in Solution," *Journal of Crystal Growth,* vol. 90, no. 1, pp. 14-30, 1988.
[182] R. E. Smallman, *Modern Physical Metallurgy*, 4th ed., Elsevier, 2016.
[183] D. A. Porter, K. E. Easterling, and M. Sherif, "Phase Transformations in Metals and Alloys, (Revised Reprint)," CRC press, 2009.
[184] Y. D. Han, H. Y. Jing, S. M. L. Nai, C. M. Tan, J. Wei, L. Y. Xu, and S. R. Zhang, "A Modified Constitutive Model for Creep of Sn–3.5Ag–0.7Cu Solder Joints," *Journal of Physics D: Applied Physics,* vol. 42, no. 12, p. 125411, 2009.
[185] A. Syed, "Updated Life Prediction Models for Solder Joints with Removal of Modeling Assumptions and Effect of Constitutive Equations," *Proceedings of the 7th EuroSimE Conference*, pp. 1-9, 2006.
[186] A. Schubert, R. Dudek, , E. Auerswald,, A. Gollbardt, Michel B., and H. Reichl, "Fatigue Life Models for SnAgCu and SnPb Solder Joints Evaluated by Experiments and Simulation," *Proceedings of the 53rd Electronic Components and Technology Conference*, pp. 603-610, 2003.
[187] B. Zahn, "Solder Joint Fatigue Life Model Methodology for 63Sn37Pb and 95.5 Sn4Ag0.5Cu Materials," *Proceedings of the 53rd IEEE Electronic Components and Technology Conference*, pp. 83-94, 2003.
[188] W. W. Lee, L. T. Nguyen, and G. S. Selvaduray, "Solder Joint Fatigue Models: Review and Applicability to Chip Scale Packages," *Microelectronics Reliability*, Vol. 40, pp. 231-244, 2000.

[189] S. Ridout, and C. Bailey, "Review of Methods to Predict Solder Joint Reliability under Thermo-Mechanical Cycling," *Fatigue & Fracture of Engineering Materials and Structures*, Vol. 30, pp. 400-412, 2007.
[190] C. Basaran, and H. Tang, "A Damage Mechanics Based Fatigue Life Prediction Model for Solder Joints," *Journal of Electronic Packaging*, Vol. 125, pp. 120-125, 2003.
[191] G. Gustafsson, I. Guven, V. Kradinov, and Madenci, E., "Finite Element Modeling of BGA Packages for Life Prediction," *Proceedings of the 50th IEEE Electronic Components and Technology Conference*, pp. 1059-1063, 2000.
[192] J. H. L. Pang, T. I. Tan, and S. K. Sitaraman, "Thermo-Mechanical Analysis of Solder Joint Fatigue and Creep in a Flip Chip on Board Package Subjected to Temperature Cycling Loading," *Proceedings of the 48th IEEE Electronic Components and Technology Conference*, pp. 878-883, 1998.
[193] D. A. Shnawah,M. F. M. Sabri, and I. A. Badruddin, "A Review on Thermal Cycling and Drop Impact Reliability of SAC Solder Joint in Portable Electronic Products," *Microelectronics Reliability*, Vol. 52, pp. 90-99, 2012.
[194] H. Liu, J. Zhang, S. Chen, M. Du, N. Feng, and Q. Wang, "Board Level Thermal Cycle Reliability of BGA for a New Type of Pad Structure with OSP Surface Finish," 2007, *Proceedings of 2007 ICEPT Conference*, pp.1-3, 2007
[195] S. Y. Yu, Y. M. Kwon, J. Kim, T. Jeong,, S. Choi, and K. W. Paik, "Studies on the Thermal Cycling Reliability of BGA System-in-Package (SiP) with an Embedded Die," *IEEE Transactions on Components, Packaging and Manufacturing Technology*, vol. 2, pp. 625-633, 2012.
[196] V. Vasudevan, and X. Fan, "An Acceleration Model for Lead-Free (SAC) Solder Joint Reliability Under Thermal Cycling," *Proceedings of the 58th IEEE Electronic Components and Technology Conference*, pp. 139-145, 2008.
[197] R. Darveaux, "Effect of Simulation Methodology on Solder Joint Crack Growth Correlation," *Proceedings of the 50th IEEE Electronic Components and Technology Conference*, pp. 1048-1058, 2000.
[198] Micromeasurements, "Strain Gage Installation Guideline and Checklist".
[199] Munshi. Basit, and J. C. Suhling, and X. Fan, "Thermal Cycling Reliability of Aged PBGA Assemblies- Comparision of Weibull Failure data and Finite Element Model Predictions ," *Proceedings of the 59th IEEE Electronic Components and Technology Conference*, pp. 1141-1158, 2015.
[200] Munshi. Basit, M. Motalab, J. C. Suhling, and P. Lall, "The Anand Parameters for SAC Solders after Extreme Aging," *Proceedings of the ITherm 2016*, pp. 440-447, 2016.
[201] S. Ahmed, J. C. Suhling, and P. Lall, "The Anand Parameters of Agin Resistant Doped Solder Alloys," *Proceedings of the ITherm 2017*, pp. 1416-1424, 2017.
[202] M. S. Alam, KM. R. Hassan, J. C. Suhling, and P. Lall, "High Temperature Aging Effects in SAC and SAC+X Lead Free Solders," *Proceedings of the 69th IEEE Electronic Components and Technology Conference*, pp. 1815-1825, 2019.
[203] M. S. Alam, KM. R. Hassan, J. C. Suhling, and P. Lall, "Mechanical Characterization and Microstructural Evolution of SAC and SAC+X Lead Free Solders Subjected to High Temperature Aging," *Proceedings of the ITherm 2019*, pp. 319-328, 2019.

[204] M. S. Alam, KM. R. Hassan, J. C. Suhling, and P. Lall, "High Temperature Mechanical Behavior of SAC and SAC+X Lead Free Solders," *Proceedings of the 68th IEEE Electronic Components and Technology Conference*, pp. 1781-1789, 2018.
[205] Jing. Wu, M. S. Alam, KM. R. Hassan, J. C. Suhling, and P. Lall, "Investigation and Comparison of Aging Effects in SAC+X Solders Exposed to High Temperatures," *Proceedings of the 70th IEEE Electronic Components and Technology Conference*, pp. 492-503, 2020.
[206] J. Liang, N. Dariavach, P. Callahan, D. Shangguan, "Metallurgy and Kinetics of Liquid-Solid Interfacial Reaction during Lead-Free Soldering," *Materials Transactions Components and Technology Conference*, Vol. 47, No. 2, pp. 317-325, 2006.

Appendix

A.1 Variation of Temperature inside the Temperature Chamber

Specimen Temperature (°C)	Controller Temperature (°C)		Specimen Temperature (°C)	Controller Temperature (°C)
35	39.9		140	159.5
40	45.6		145	165.2
45	51.3		150	170.9
50	57.0		155	176.6
55	62.7		160	182.3
60	68.4		165	188.0
65	74.1		170	193.7
70	79.8		175	199.4
75	85.5		180	205.1
80	91.2		185	210.8
85	96.9		190	216.5
90	102.6		195	222.2
95	108.3		200	227.9
100	114.0		205	233.6
105	119.7		210	239.3
110	125.4		215	244.9
115	131.1		220	250.6
120	136.7		225	256.3
125	142.4		230	262.0
130	148.1		235	267.7
135	153.8		240	273.4

Table A.1 Calibrated Temperature Table